Emerging stable isotope techniques in hydrothermal research: new methods applied to carbonates and hydrous minerals in ore deposits and geothermal fields

A thesis

submitted in fulfilment

of the requirements for the degree

of

Doctor of Philosophy in Earth Sciences

at

The University of Waikato

by

John Arthur Mering

THE UNIVERSITY OF
WAIKATO
Te Whare Wānanga o Waikato

2019

ABSTRACT

Over the last 70 years, stable isotopes have provided critical insight into the processes governing transfer of mass and energy through geologic systems. Significantly, isotopic signals in minerals reflect conditions of crystallisation, and subsequent alteration history. In hydrothermal systems, isotope tools have been applied to interpret fluid origin, temperature, and interaction with host rock. The research carried out here makes use of emerging techniques to measure hydrogen, oxygen, carbon, and clumped isotopes in carbonates and hydrous minerals. This work encompasses three themes:

(i) Development of new laser spectroscopy approaches for measuring δ^2H and $\delta^{18}O$ in hydrous minerals
(ii) Testing carbonate clumped isotope thermometry in geothermal fields and mineral deposits
(iii) Application of carbonate and hydrous mineral isotope tools in epithermal precious metal deposits

A novel approach to measure δ^2H and $\delta^{18}O$ in hydrous minerals is presented in Chapters 3-4. Measurement was carried out on phyllosilicates, hydrous sulphates, and multimineralic whole rock assay pulps using a custom-built thermal dehydration-dehydroxylation Off-Axis Integrated Cavity Output Spectroscopy (TD-OA-ICOS) system. The δ^2H methodology presented is equal to isotope ratio mass spectrometry in terms of speed and precision, but considerably lower in cost. This work represents the first hydrogen isotope measurements made by a laser spectroscopy system for serpentine, muscovite, sericite, talc, and biotite.

The TD-OA-ICOS method was subsequently applied to measure $\delta^{18}O$ in microvolumes of water, gypsum hydration water, and the hydroxyl component of phyllosilicate minerals (Chapter 4). Intramineral oxygen isotope fractionation values in kaolinite and muscovite, determined by comparison of $\delta^{18}O_{OH}$ measured by TD-OA-ICOS with $\delta^{18}O_{silicate}$ measured by fluorination, are similar to existing constraints. Refinement of this approach should be carried out to test the relationship between formation temperature and intramineral oxygen isotope fractionation in clay minerals.

TD-OA-ICOS was applied to reconstruct δ^2H in well-constrained epithermal areas, exemplified by case studies at the Comstock Lode, USA (Chapter 4) and Miocene-aged adularia-sericite Au-Ag deposits at Waihi and Karangahake on the North Island (Chapter 6). Taking mineral-specific fractionation factors into account, whole rock hydrogen isotope measurements indicate relatively homogeneous fluids of meteoric origin were involved in alteration at each deposit. Accurate reconstruction of fluid δ^2H requires constraints upon the balance of illite and chlorite in samples. Mineral δ^2H is useful for fingerprinting paleo latitude or altitude of source fluids, as evidenced by results from Comstock, which were ~60 ‰ lower for δ^2H, relative to Waihi and Karangahake. It is apparent that mineral δ^2H has greater utility towards understanding mixing in systems where fluids are isotopically distinct. The low cost, safety, and simplicity of operation of TD-OA-ICOS should also make the method attractive for manufacturers and regulatory agencies wishing to use hydrogen and oxygen isotopes to determine the geographic origin of consumer products containing hydrous minerals.

Paleotemperature constraints around ore deposits are essential for characterising the relationship between advection, fluid circulation, and metal transport. In Chapter 5, carbonate clumped isotope thermometry (Δ_{47}) is applied to identify temperature gradients in geothermal fields and hydrothermal ore deposits. This technique, based on quantification of thermodynamically sensitive ^{13}C-^{18}O bond abundance in carbonates, provides new capability to determine fluid $\delta^{18}O$, overcoming a problem which has undermined interpretation of carbonate isotope data in hydrothermal settings for more than 60 years. Geothermal fields (Wairakei, Ngatamariki, Broadlands-Ohaaki) in the Taupo Volcanic Zone, New Zealand served as natural laboratories to test the validity of clumped isotope calibrations in high temperature settings up to 300 °C. Taking local fluid $\delta^{18}O$ into account, results indicate modern TVZ calcites precipitated in equilibrium with produced geothermal waters.

The clumped isotope technique was subsequently applied in epithermal (Waihi, NZ), skarn (Antamina, Peru), and carbonate-hosted (Mount Isa, Australia) metal deposits. Results highlight the potential for clumped isotopes to delineate the heat footprint around mineral deposits that contain carbonates. Further refinement of the clumped isotope method offers new potential to evaluate characteristics of ore deposit genesis, with respect to temperature, fluid source, and depth. This will prove

especially useful in enigmatic carbonate-hosted hydrothermal settings, where temperature and hydrology are unresolved. Paired oxygen isotope and carbonate clumped isotope measurements at Waihi demonstrate that $\delta^{18}O$ of hydrothermal calcite is primarily influenced by rock temperature, with variation in fluid composition due to water-rock exchange exerting secondary control. While calcite precipitates both in and out of phase with precious metals in epithermal areas (e.g. Waihi), clumped isotope signals reflect the overall thermal structure, providing a new avenue to identify hotter upwelling zones, where boiling drives deposition of Au, Ag and other metals. Ultimately, the findings presented herein are useful to workers in hydrothermal settings, with interest in mineral exploration and geothermal resource development, and are broadly applicable across the geologic sciences in topics ranging from paleoenvironmental studies to interpretation of basin histories.

You have to forget your last marathon before you try another.

-Frank Shorter (Olympic Marathon Gold Medallist, 1972)

ACKNOWLEDGMENTS

Claire, thank you for embarking on this journey with me! I love you! You encouraged me throughout. You made me appreciate the successes and helped me overcome the setbacks. I could not have done it as gracefully without you. To Mom, Dad, Ellen, and Karl, thanks for supporting this crazy quest. You guys are everything.

I would like to thank Shaun Barker for encouraging me to make the journey to New Zealand, and take on this project. Your guidance and support from start to finish is truly irreplaceable. I cannot state enough how much I have learned in the process, and how grateful I am for having had this opportunity.

I would like acknowledge the support of Adrian Pittari and Adam Hartland who served as cosupervisors on this project. I would like to also thank Kevin Faure (GNS) and Daniel Layton-Matthews (Queen's University) for serving as examiners. Their comments significantly improved the quality of this thesis.

One of the highlights of this project was working in the clumped isotope lab at the University of Washington. I thank Kate Huntington for having the opportunity to visit and learn from her group. Andy Schauer provided essential mentoring in the lab and Julia Kelson provided assistance with clumped isotope data interpretation.

A number of other individuals provided project input, without which this research would not have been possible. Waikato technicians Peter Jarman, Kirsty Vincent, Annette Rodgers, and Anjana Rajendram provided logistical support. With respect to the clumped isotope investigation, Stuart Simmons provided geothermal samples from the TVZ, and Greg Dipple contributed carbonate from Antamina, and Carlin Au deposits in Nevada. Access to the Becker Collection of Comstock samples was made possible via Erik Melchiorre (California State University, San Bernardino). Mark Simpson (GNS) provided samples from Karangahake. Access to Waihi core and assay pulps was made possible by OceanaGold. Hydrogen isotope reference minerals were provided by April Vuletich (Queen's University), John Dilles (Oregon State University), Zach Sharp (University of New Mexico), and Haiping Qi (United States Geological Survey). Robert van Hale (University of Otago)

carried out IRMS validation of hydrous minerals. Peter Kamp involved me in useful discussions pertaining to North Island geology. Troy Baisden provided insight on operation of the OA-ICOS water vapour analyser used in this study. I would like to acknowledge my fellow hydrothermal research students Ben Andrew, Rosie Hughes, Rocky Barker, Ryan Lee, and Oliver McLeod for providing camaraderie in the lab, at conferences, and during the daily office grind. This work was funded by an MBIE grant (Gold Exploration Models: C05X1405).

A Ph.D. would not be possible without great friends. Joss Ratcliffe, Lara Hepp, Andy Pearson, Steph Mangan, Ben Norris, Francesca Spinardi, Ryan Jones, Tim Stewart, Yu-Shen Liu, and many others were there for bike adventures, spontaneous trips to Lake Tarawera, and countless other great moments. I'm excited to see where we all end up! Special thanks goes to the Homebrew Hombres of Hamilton and Homebrew Hombres International for moral and liquid support. The Hamilton Hawks running club was there most days to keep me on my feet (literally). Major shout out to the 2018 NRR Senior Men for a weekend to remember. Cheers Rodrigo, Jake, Jai, Brad, Lachlan, Logan, and Theunis! A number of friends made the trip out to New Zealand over the last three years. To Erin, Ellie, David, Tristan, Zach, Brady, Cindy, Greg, Viv, and Stefan, thanks for stopping by! It was great to have you guys here.

This Ph.D. is one chapter of what I hope continues to be a life of learning and personal development. I wouldn't have made it here without exceptional mentors early on. I feel especially indebted to the geology team at Pomona College for helping me fall in love with rocks. Thanks Jade Star, Bob, Linda, Eric, and Rick!

TABLE OF CONTENTS

Chapter IV

Measuring hydrogen and oxygen isotopic signals in ore deposits using thermal dehydroxylation OA-ICOS: results from the Comstock Lode, USA

Chapter V

Taking the temperature of hydrothermal ore deposits using clumped isotope thermometry

Chapter VI

Exploring carbon, oxygen, and hydrogen isotopic variation in epithermal systems using laser spectroscopy: insights from Waihi and Karangahake

Chapter VII

Concluding remarks

LIST OF FIGURES

LIST OF TABLES

LIST OF TERMS

α	fractionation factor, where $\alpha_{a\text{-}b} = R_a/R_b$
CDES	Carbon Dioxide Equilibration Scale: heated gas normalisation scheme for carbonate clumped isotopes
CF-IRMS	Continuous Flow IRMS
CVZ	Coromandel volcanic zone
δ	delta: isotope ratio in sample normalised to international reference (e.g. $\delta^{18}O$)
Δ	capital delta: difference in isotopic fractionation between coexisting phases, where $\Delta_{a\text{-}b} = \delta_a - \delta_b \approx 1000\ln\alpha_{a\text{-}b}$
IRMS	Isotope Ratio Mass Spectrometer
LAS	Laser Absorption Spectroscopy
LGR	Los Gatos Research
OA-ICOS	Off-Axis Integrated Cavity Output Spectroscopy
Pa	Pascal: unit of pressure, where 1 Pa = 1 N/m^2
‰	per mil
ppm	parts per million
ppmv	parts per million by volume
R	ratio of heavy and light isotopes in a sample (e.g. $^{13}C/^{12}C$)
VPDB	Vienna Pee Dee Belemnite
VSMOW	Vienna Standard Mean Ocean Water
TC/EA	high temperature conversion elemental analyser: commonly used in conjunction with IRMS (i.e. TC/EA-IRMS)
T_h	fluid inclusion homogenization temperature
Torr	unit of pressure, defined as 133.3224 Pa
TVZ	Taupo volcanic zone
µL	microliter
µm	micrometre
USGS	United States Geological Survey
WVISS	Water Vapor Isotope Standard Source: unit designed for water vapour introduction into OA-ICOS instrument

CHAPTER I

Introduction

1.1 OPENING REMARKS

Although fluid-rock interactions are ubiquitous on Earth, the development and preservation of ore deposits is rare. The scarcity of many metals in the crust and upper mantle is attributed to partitioning of heavier elements into the Fe-Ni rich core early in Earth history (Goldschmidt, 1937; McDonough and Sun, 1995). Metals accessible today are thought to have largely been delivered during meteoritic bombardment events following the initial accretion of Earth (Brenan and McDonough, 2009). In order to explain the unique conditions involved in the transport and concentration of metals, the study of ore deposits is inherently interdisciplinary, merging the fields of geochemistry, geophysics, structural geology, sedimentology, and geobiology. It is with this mind-set that mineral exploration has become a significant driving force towards applying new analytical methodologies relevant to understanding fluid history in geologic systems (Cameron et al., 2004; Kyser et al., 2015).

As resource demand rises, exploration for new mineral deposits becomes an increasingly challenging endeavour. From 1960 to present, world population grew from 3 billion to greater than 7 billion, while production of key metals rose by approximately a factor of four (Lusty and Gunn, 2014; Kesler and Simon, 2015; Meinert et al., 2016; U.S. Census Database). Although most easily extractable resources have been mined, estimates of yet to be discovered mineral deposits are up to 40 times greater than current reserves (Meinert et al., 2016). Historic increases in commodity prices have provided capital to enable discovery of new deposits, which are commonly remote, buried, and may contain disseminated resources (Cameron et al., 2004; Lusty and Gunn, 2014). New discoveries are made possible by interdisciplinary collaboration, and adoption of new technologies tailored to understand the physical characteristics of deposits (Lusty and Gunn, 2014; Kyser

et al., 2015). The body of work contained herein supports this, by demonstrating the application potential of emerging stable isotope methods to reconstruct fluid and temperature signals in ore deposits and modern geothermal areas.

In the following chapters, new methodology employing Off-Axis Integrated Cavity Output Spectroscopy (OA-ICOS) is developed that enables rapid low-cost measurement of hydrogen and oxygen isotope ratios in hydrothermal clay minerals (Chapters 3-4). Carbonate clumped isotope thermometry is applied in high temperature ore settings (Chapter 5). Laser-based (i.e. OA-ICOS) approaches (e.g. Barker et al., 2011) are also applied to measure oxygen and carbon isotope ratios in carbonates in epithermal Au-Ag deposits (Chapter 6). The findings presented here are useful to workers in hydrothermal settings, with interest in mineral exploration and geothermal resource development, and are broadly applicable across the Earth sciences in topics ranging from paleoenvironmental reconstruction to interpretation of basin histories.

1.2 RESEARCH SCOPE

This thesis builds upon a legacy of research demonstrating that stable isotope ratios in minerals are sensitive indicators of fluid source, water-rock interaction, and temperature in ore deposits and geothermal fields (e.g. Ohmoto, 1972; Taylor, 1973; O'Neil and Silberman, 1974; Taylor and O'Neil, 1977; Bethke and Rye, 1979; Marumo et al., 1980; Dilles et al., 1992; Giggenbach, 1992; Nesbitt, 1996; Criss et al., 2000; Barker et al., 2013). Recent advances in stable isotope measurement, including the advent of laser spectroscopy (Baer, 2002; Barker et al., 2013), and carbonate clumped isotope thermometry (e.g. Eiler et al., 2007) provide new avenues to quantify hydrogen, carbon, and oxygen isotope ratios in minerals, and reconstruct temperature gradients around ore bodies. However, these new techniques (Figure 1.1) are largely untested in hydrothermal settings. The methods applied, and geologic settings investigated in this thesis, are outlined in Figures 1.1-1.2. Case examples include geothermal, epithermal, skarn, and carbonate hosted deposits in New Zealand, North America, South America, and Australia (Figure 1.2). Three research areas were identified that focus upon:

(i) Development of new laser spectroscopy techniques to measure isotopic signals in hydrous minerals

(ii) Application of clumped isotope thermometry to reconstruct thermal gradients around ore deposits

(iii) Testing of carbonate and hydrous mineral techniques in ore deposits (Figure 1.2)

The motivation underlying these research themes is provided below.

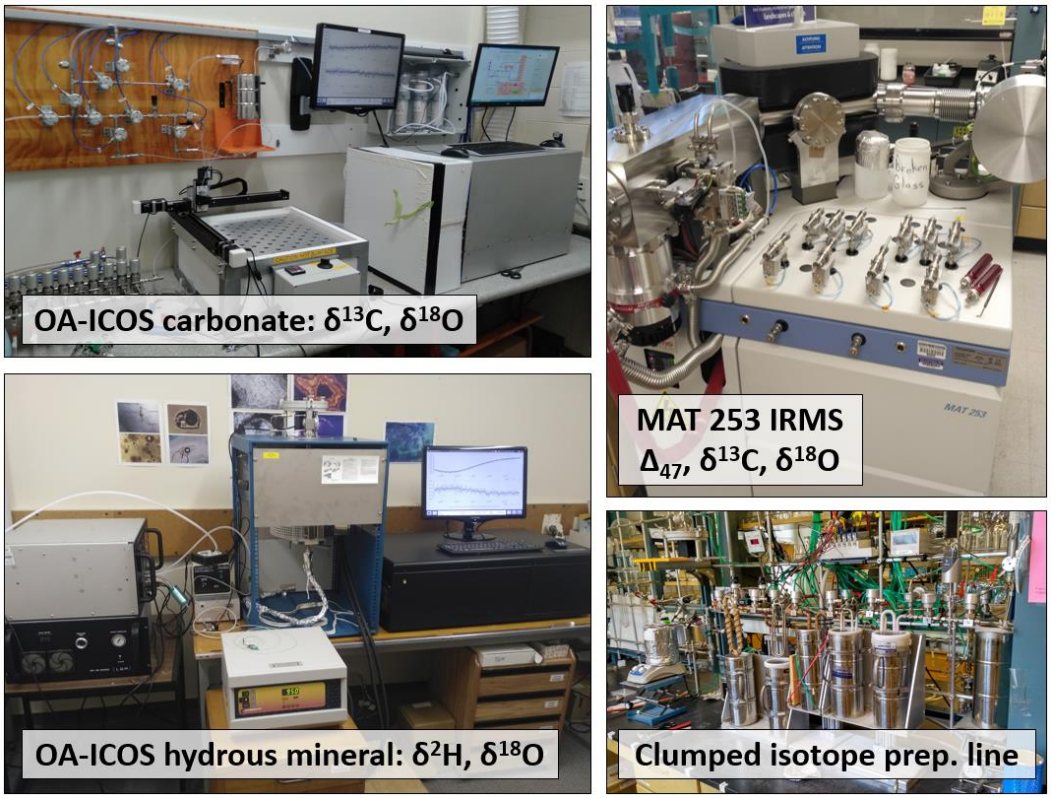

Figure 1.1: key methods applied in this thesis. Upper left: isotope ratios in carbonates were measured using an OA-ICOS system at the University of Waikato. Lower left: OA-ICOS water isotope instrument at Waikato. Upper right: carbonate clumped isotopes were measured using an IRMS at the University of Washington. Lower right: clumped isotope sample preparation setup.

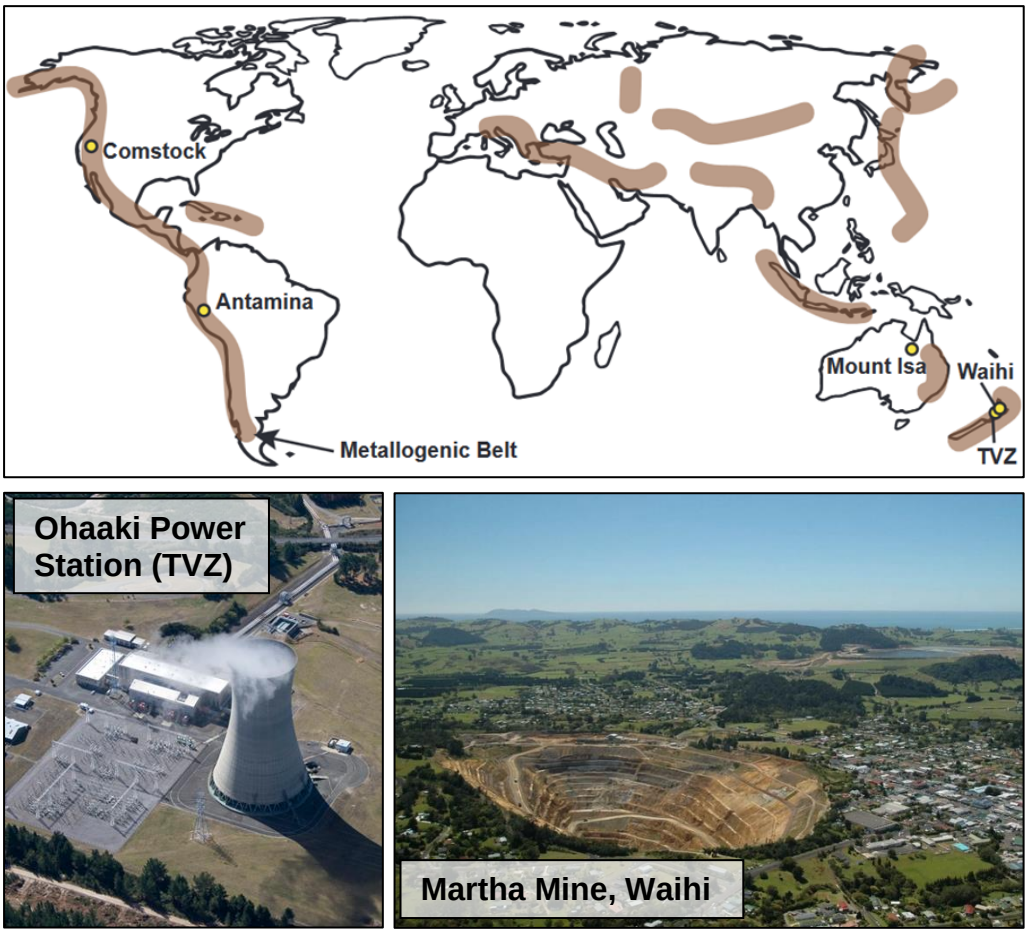

Figure 1.2: top panel: principal hydrothermal areas investigated in this thesis, relative to global distribution of major collisional arc metallogenic belts. Modified from Richards (2013). Lower left: Ohaaki geothermal power station. Lower right: Martha Pit at Waihi epithermal Au-Ag deposit.

1.2.1 Motivation

Area 1: Laser spectroscopy method development

Rationale: hydrous minerals (e.g. clays, micas, hydrous sulphates) archive hydrogen and oxygen signatures of hydrothermal fluids. Hydrogen isotope measurements in minerals have high potential value as an indicator of fluid-rock interaction, due to the abundance of H in aqueous fluid relative to rocks, which are typically less than 10 % H_2O by weight. The internal oxygen isotope fractionation between Si-O and OH sites has potential as a single mineral geothermometer in clay minerals (e.g. Bechtel and Hoernes, 1990). However, the cost, time, and technical

challenges associated with quantitatively extracting and measuring the hydrogen and oxygen isotope compositions of hydrous minerals has limited the scope of application in hydrothermal investigations (Barker et al., 2013; Kyser et al., 2015). New lower cost technology should enable more widespread access to measurement platforms, and encourage experimental work to improve interpretation of hydrous mineral data in ore deposit studies. Specifically, mineral-fluid hydrogen isotopic exchange is not well defined for some classes of hydrous mineral over temperatures relevant to hydrothermal studies.

Area 2: Carbonate clumped isotope thermometry

Rationale: temperature constraints around ore deposits are essential for characterising the relationship between advection, fluid circulation, and metal transport. Here, carbonate clumped isotope thermometry, a non-traditional isotope geothermometer, is applied to identify temperature gradients in geothermal fields and hydrothermal ore deposits. This technique has the potential to overcome shortcomings associated with presently available methods for reconstructing temperature, including fluid inclusion homogenisation, clay mineral associations, and mineral pair isotope thermometers. Importantly, clumped isotope methods can be applied to separate the effects of temperature and fluid composition upon carbonate oxygen isotope signatures, an issue which has impeded interpretation of hydrothermal mineral oxygen isotope results for more than 60 years (Engel et al, 1958). This enables more precise characterisation of the sources fluids involved in ore formation.

Area 3: Stable isotope approaches in mineral exploration

Rationale: In most classes of hydrothermal metal deposit, clays and carbonate minerals are extensive both near orebodies, and within the distal propylitic alteration footprint, making these minerals useful for spatially extensive assessment of fluid isotope properties. In this thesis, $\delta^{2}H$ in phyllosilicates and $\delta^{13}C$ and $\delta^{18}O$ in carbonates were measured in well-constrained epithermal areas using laser spectroscopy in order to evaluate whether gradients in isotopic values exist around large epithermal veins that can be used to vector towards Au-Ag mineralisation. These techniques are sufficiently rapid and inexpensive to be used in the mineral

exploration industry. This work provides an in-depth assessment of the relative utility of clay and carbonate isotope archives in hydrothermal ore deposit exploration.

Method testing in New Zealand

The North Island of New Zealand provides a well-constrained natural laboratory for method testing. The tools developed in this thesis are highlighted by case studies in the active Taupo volcanic zone (TVZ) and Miocene-aged adularia-sericite Au-Ag deposits, within the now extinct Coromandel volcanic zone (CVZ). The TVZ (Figure 1.3) is an extensional region dominated by rhyolitic-andesitic volcanism (Simmons and Brown, 2007; Simmons et al., 2016). Geothermal fields are active within the central TVZ (Rowland and Sibson, 2004; Rowland and Simmons 2012; Simmons et al., 2016b). Clumped isotope calibration was tested at three geothermal fields within the central TVZ (Figure 1.3).

The collisional tectonic setting in New Zealand produced over 50 low sulphidation epithermal deposits during the Miocene (Figure 1.4), which follow the now-extinct Coromandel volcanic zone (CVZ) arc (Brathwaite and Faure, 2002; Christie et al., 2007). Clumped isotope thermometry and OA-ICOS methods are applied at Waihi, the highest Au producing epithermal deposit within the Hauraki Goldfields. A large set of exploration drilling samples were made available by partnership with OceanaGold, the principal operator at Waihi, enabling research presented in chapters 5-6. Hydrogen isotopic variation is also measured at the nearby Karangahake deposit in Chapter 6. Samples were measured as whole rock assay pulps, which are homogenised composite sections of drill core, or as mineral separates.

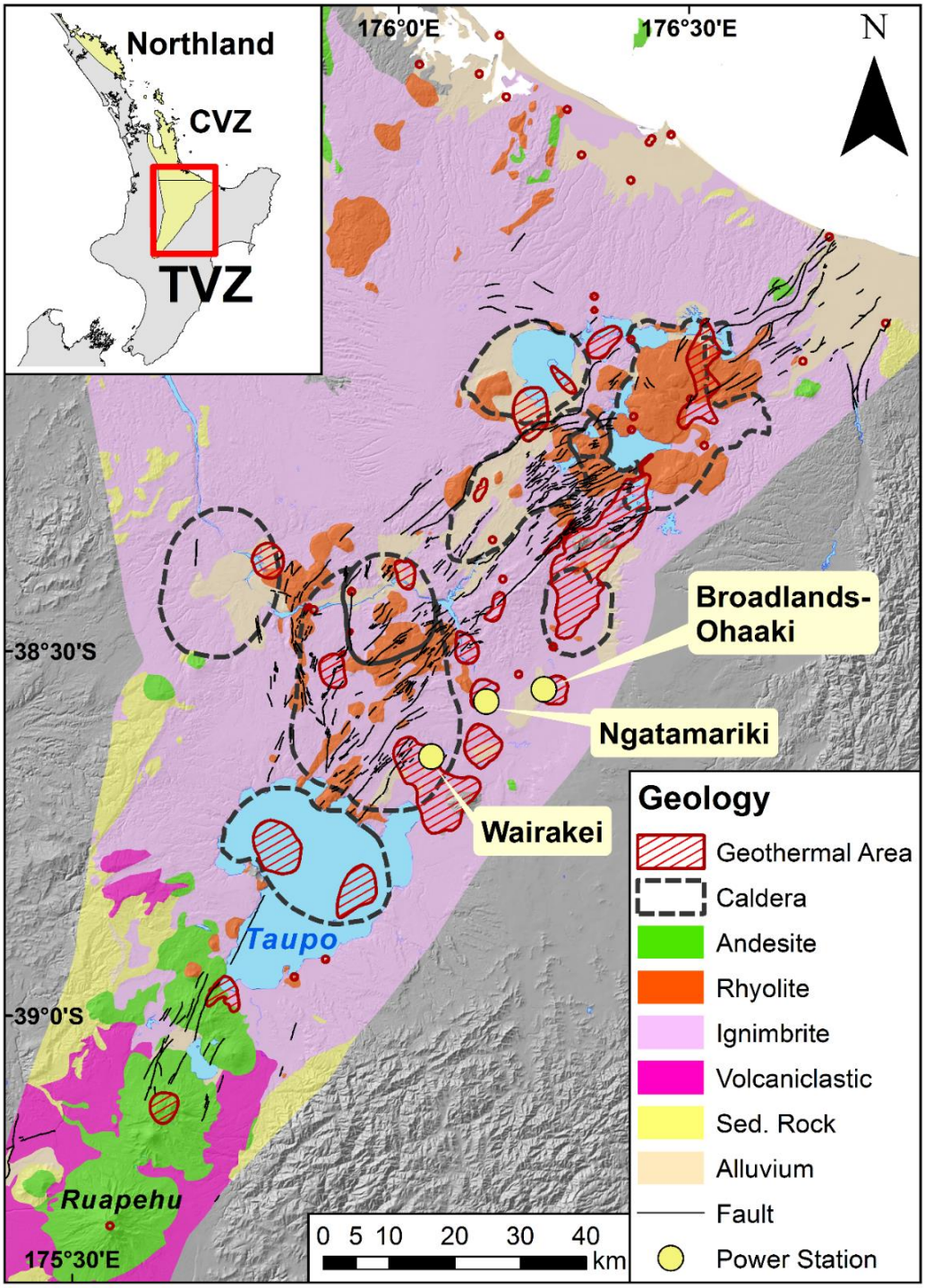

Figure 1.3: geologic setting of the active Taupo volcanic zone, North Island, New Zealand. Clumped isotope measurements were carried out at the Wairakei, Ngatamariki, and Broadlands-Ohaaki geothermal fields. This map was drawn from publically available shapefiles developed for exploration purposes by NZ Petroleum and Minerals.

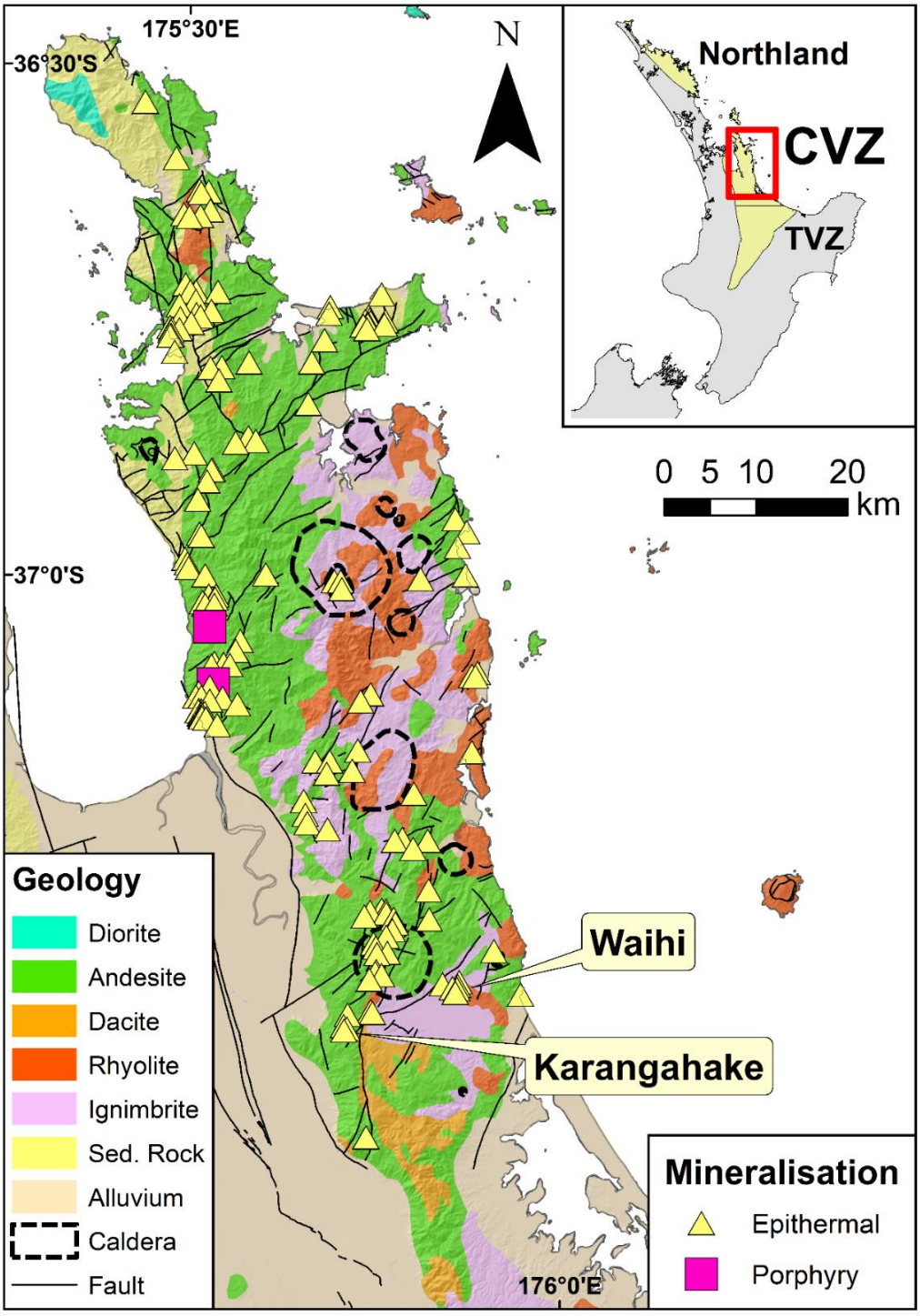

Figure 1.4: geologic setting of the Coromandel Peninsula. The Waihi and Karangahake low sulphidation epithermal deposits lie at the southern end of the Hauraki goldfield, a 200 km long region of hydrothermal mineralization, related to the now-extinct Coromandel volcanic zone. Au-Ag mineralization occurs in andesite and rhyolite hosed quartz veins. Metal deposits become progressively younger from N-S, with hydrothermal activity at Waihi and Karangahake occurring in the late Miocene. This map was drawn from publically available shapefiles developed for exploration purposes by NZ Petroleum and Minerals.

1.2.2 Research questions

Key research questions were developed to guide inquiry in the research areas outlined previously. These are listed below.

Area 1: Measuring δ^2H and $\delta^{18}O$ in hydrous minerals by laser spectroscopy

> ***Q 1.1:*** *What is the best achievable precision, accuracy, and measurement speed for δ^2H and $\delta^{18}O$ in hydrous minerals using an OA-ICOS platform?*
>
> ***Q 1.2:*** *How do the OA-ICOS methods developed here compare to established IRMS approaches?*
>
> ***Q 1.3:*** *How can measurement of hydrous mineral isotope signals by laser spectroscopy aid ore deposit investigations?*

Area 2: Clumped isotope thermometry in hydrothermal investigations

> ***Q 2.1:*** *What is the sensitivity of clumped isotope temperature reconstructions relative to other temperature constraints in geothermal fields and ore deposits (e.g. fluid inclusions, clay mineralogy)?*
>
> ***Q 2.2:*** *Where should Δ_{47} be applied to address gaps in knowledge in terms of reconstructing thermal history?*

Area 3: Stable isotope approaches in exploration

> ***Q 3.1:*** *Do explanations of carbonate growth temperature at modern geothermal areas (e.g. TVZ) apply to corresponding epithermal areas (e.g. Waihi)?*
>
> *Specifically, do $\delta^{13}C$, $\delta^{18}O$, and clumped isotope signals at low sulphidation epithermal areas reflect changes in fluid source or temperature, and to what extent can these be applied to exploration of epithermal deposits?*

Q 3.2: *Does δ^2H change across a given epithermal area, and to what extent is variation attributed to fluid source, temperature, and mineralogy?*

1.2.3 Research approach

An OA-ICOS method was developed to measure δ^2H and $\delta^{18}O$ in phyllosilicates, hydrous sulphates, and multimineralic whole rock assay pulps (Chapters 3-4). There is little precedent for calibrating and reporting hydrous mineral results by OA-ICOS (Q 1.1), and performance relative to IRMS is not established (Q 1.2). The application potential of the method is tested (Q 1.3) with measurement of hydrous mineral standards (Chapters 3-4), and on epithermal sample sets (Chapters 4 and 6).

In Chapter 5, clumped isotope calibration relationships are tested at high temperature (150-300 °C) in modern geothermal samples from the Taupo volcanic zone (Q 2.1). Subsequently, the first carbonate clumped isotope measurements for epithermal (Waihi), carbonate-hosted (Mount Isa), and skarn (Antamina) deposits are reported. In settings where fluid sources (i.e. magmatic vs. meteoric) are unresolved, the clumped isotope approach provides a new path to determine the $\delta^{18}O$ of fluid (Q 2.2). In this work, areas for methodological improvement are identified that should enable more routine application of clumped isotopes in hydrothermal studies (Q 2.2).

Paired oxygen and clumped isotope measurements in TVZ geothermal calcite (Chapter 5), and in carbonates at Waihi (Chapters 5-6), allow for better understanding of the influence of temperature upon of carbonate $\delta^{18}O$ in natural samples (Q 3.1). A wealth of knowledge from active geothermal systems in the TVZ is available for comparison (Q 3.1). The hydrogen isotope signals at epithermal deposits (Waihi, Karangahake, Comstock) are evaluated with respect to clay alteration assemblages (e.g. illite, smectite, chlorite, kaolinite) and fluid source (Q 3.2).

1.3 THESIS OUTLINE

The research carried out in this thesis is presented in four chapters. These are outlined below.

Chapter III: **Rapid and precise measurement of the hydrogen isotope composition in phyllosilicates by thermal dehydroxylation laser spectroscopy**

Here, results are reported from testing of a thermal dehydroxylation platform, paired with an OA-ICOS analyser for δ^2H measurement in clay minerals. The first laser spectroscopic measurements of δ^2H in several classes of hydrous mineral (serpentine, muscovite, talc, biotite) are reported. A section of this work was published in *Analytical Chemistry* in 2018.

Chapter IV: **Measuring hydrogen and oxygen isotopic signals in ore deposits using thermal dehydroxylation OA-ICOS: results from the Comstock Lode, USA**

The analytical platform developed in Chapter 3 is reconfigured to measure oxygen isotopic signals in mineral-bound water, and the hydroxyl fraction of phyllosilicate minerals. Application potential is tested with whole rock measurements of propylitically altered materials from the historically significant Comstock Ag deposit.

Chapter V: Taking the temperature of hydrothermal ore deposits using clumped isotope thermometry

Here results are presented from the TVZ and 3 ore deposits. Discussion is provided on best practise for clumped isotope calibration and fluid $\delta^{18}O$ reconstruction in high temperature geologic settings. A summary of this work was published in *Economic Geology* in 2018.

Chapter VI: Exploring carbon, oxygen, and hydrogen isotopic variation in epithermal systems using laser spectroscopy: insights from Waihi and Karangahake

The δ^2H analytical platform developed in Chapters 3-4 is deployed at two epithermal deposits in the Hauraki goldfields, NZ. Additionally, carbon and oxygen isotope measurements of hydrothermal calcite are reported at the Waihi epithermal deposit, using recently developed OA-ICOS carbonate analytical technique. The results presented in this chapter demonstrate potential for using OA-ICOS to track fluid source and thermal signatures in epithermal areas.

CHAPTER II

Literature Review

2.1 ORE DEPOSIT BACKGROUND

2.1.1 Ore deposit classification

Ore deposits are geochemical anomalies (Kyser et al., 2015), manifest as localised areas where desirable elements are enriched by up to 10,000 times above background concentrations (Tilling et al., 1973; Crocket, 1991; Butterman and Amey, 2005). Deposits form over a range of depths and temperatures, with fluid chemistry varying widely in terms of salinity, pH, and redox potential (Table 2.1, Figure 2.1). Figure 2.1 depicts common intrusion-related ore deposits in cross section, including high sulphidation and low sulphidation epithermal zones, and deeper seated porphyries. Comprehensive reviews of magmatic ore deposit styles, relevant to this thesis, are provided in multiple works (e.g. Hedenquist and Lowenstern, 1994; Simmons et al., 2005; Zhu et al., 2011; Richards, 2013).

The lifetime of an ore-generating hydrothermal system varies, but is most often limited by availability of heat and fluid (White and Hedenquist, 1990; Criss et al., 1991; Simmons et al., 2005). Ore-generating hydrothermal systems are most commonly situated along volcanic arcs, which provide strong temperature gradients required to circulate fluids (e.g. Richards, 2013). The fluids involved in hydrothermal transport of metals are a mixture of H_2O and various other gases (e.g. CO_2, H_2S, CH_4). Fluids migrate through fractures or circulate slowly, passing through smaller interstitial pore spaces (White and Hedenquist, 1990; Simmons et al., 2005; Simmons and Brown, 2007). Fluids drive dissolution of existing mineral assemblages and precipitation of replacement minerals (e.g. Giggenbach, 1981). Variations in fluid chemistry and temperature result in distinct haloes of alteration around ore bodies. In exploration, identification of haloes is critical to deposit discovery (e.g. Zhu et al., 2011).

A number of techniques are employed to identify evidence of hydrothermal alteration at a range of scales, from individual mineral grains to outcrops and deposits. By far, the oldest and simplest approaches involve field mapping, and visual logging of textural and structural associations that are indicative of fluid flow and alteration. Highly effective lithogeochemical and geophysical tools, developed over the last century, have expanded the scope of exploration practice (Kyser et al., 2015).

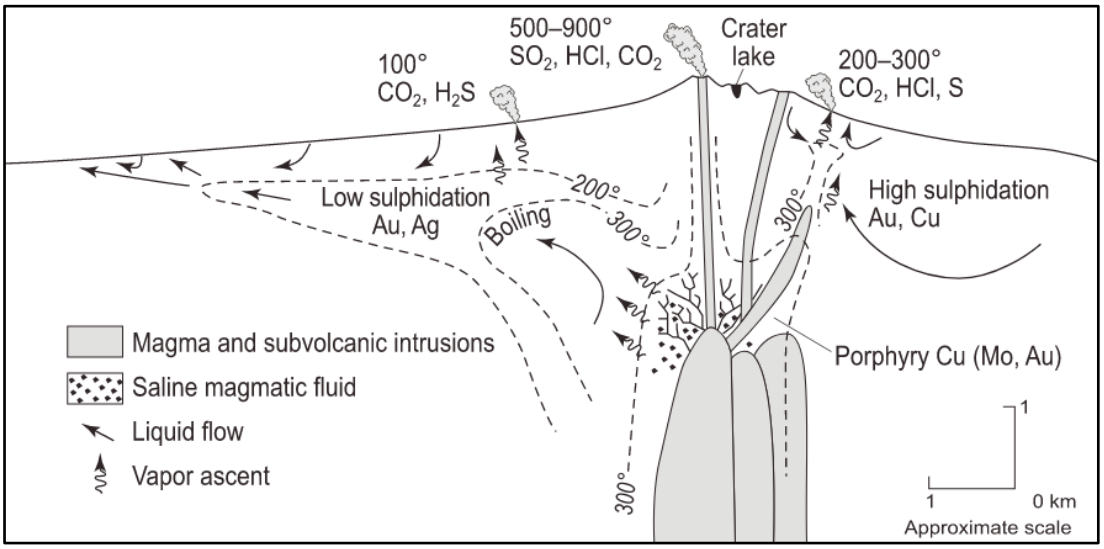

Figure 2.1: schematic cross section of relevant Au and Cu deposits in epithermal and porphyry settings. High sulphidation, acid sulphate type epithermal deposits occur near volcanoes, while low sulphidation deposits develop in near-neutral pH fluids, distal to an intrusion. Figure from Hedenquist and Lowenstern (1994).

Table 2.1: Hydrothermal systems and metal deposition

Deposit	Metals	T (ºC)	Depth (km)	Fluid	Geologic Setting
Epithermal - high S	Au-Cu, Ag-Pb	<300	Near surface to >1.5	Moderate-low salinity, early acidic condensate	Shallow depths proximal to a volcanic vent. Fumaroles, mud pots, acid springs form active surface features.
Epithermal - low S	Au (Ag, Pb-Zn)	150 to 300	Near surface to 1-2	Low salinity, gas-rich, neutral pH	Metal deposition in veins, within volcanic host rock.
Porphyry	Cu±Mo±Au, Mo, W or Sn	300 to >600	2-5	Hypersaline	Adjacent to intrusion in shallow magma bodies beneath stratovolcanoes
Skarn	Fe, Cu, Sn, W, Mo, Au, Ag, Pb-Zn	400 to 600	1-5	Moderate-high salinity	Adjacent to magmatic intrusion in carbonate host rock
Pluton-related veins	Sn, W, Mo±Pb-Zn, Cu, Au	350 to 450	Varies	Low-moderate salinity	Fractures / intrusions associated with shallow magmatic bodies beneath stratovolcanoes
Massive sulfide	Zn-Pb-Ag (Cu or Au)	<300	Seafloor	Salinity closely matches seawater	Back-arc seafloor vents, black smokers

Adapted from Hedenquist and Lowenstern (1994) and Richards (2013)

2.1.2 Epithermal mineralisation

A major component of this thesis involves testing in epithermal deposits, and modern geothermal analogues. The term epithermal was first used by Lindgren (1933). He proposed a mineral deposit classification scheme based upon temperature and depth. Epithermal deposits form in the upper crust, at less than 1-2 km depth, at low temperature (<300° C) and pressure (Henley and Ellis, 1983; Simmons et al., 2005). Because mineralisation occurs at relatively shallow depths, at active plate margins, long-term preservation of is low; the majority of discovered deposits formed during the Cenozoic (Simmons et al., 2005; Sillitoe, 2015).

Epithermal deposits are categorized based upon oxidation state of the fluids in the system (e.g. Arribas, 1995; Sillitoe and Hedenquist, 2003; Simmons et al., 2005). High sulphidation alteration occurs in settings where there is rapid ascent of deep hydrothermal fluid into the epithermal zone. The fluid does not undergo significant evolution, and is acidic due to entrained magmatic volatiles, including SO_2, H_2S, CO_2 and HCl (Simmons et al., 2005). Low pH fluid chemistry drives intensive leaching, leading to characteristic vuggy silica (Arribas, 1995; Simmons et al., 2005). In low sulphidation systems, fluids have neutral to alkaline pH, and do not circulate near magmatic heat sources (Simmons et al., 2005). Sulphur is reduced, often occurring as H_2S (Simmons et al., 2005). Common alteration and vein minerals include quartz, illite, adularia, albite, chlorite, calcite, and pyrite (Simmons and Browne, 2000). Silica sinters are typical surface manifestations (e.g. Hedenquist et al., 2000; Hamilton et al., 2018). The geothermal energy sector has provided a wealth of data on the physical and chemical conditions associated with epithermal mineralization (e.g. Simmons and Christenson, 1994; Simmons and Browne, 2000; Simmonds et al., 2005). The epithermal areas investigated in this thesis (Waihi, Karangahake, Comstock) fall into the low sulphidation category.

2.1.3 Stable isotopes in hydrothermal research

Early on it was recognised that the crust, mantle, ocean, atmosphere, and biosphere were distinct with respect to major elemental composition. By the 1960s, it became apparent that isotopic abundances of major light elements (i.e. O, C, H, S) also varied between reservoirs. Furthermore, isotopic composition of these elements

reflected changes in temperature, mineralogy, and biological involvement (e.g. Taylor and Barnes, 1997; Sharp, 2017). Stable isotope measurements of light elements thus provide detailed information pertaining to the transfer of mass and energy from one reservoir to another (Taylor, 1978; Taylor and Barnes, 1997; Waring et al., 1998; Kyser et al., 2015). Comprehensive reviews on the history of isotope techniques in the geologic sciences are provided in several volumes (e.g. De Groot, 2004; Hoefs, 2009; Sharp, 2017).

Within the context of hydrothermal ore deposit investigations, isotope ratios in minerals record the passage of exogenous fluids, which transport and concentrate metals of economic interest (Taylor, 1974; Taylor, 1978; Waring et al., 1998; Kyser et al., 2015). Historically, stable isotope measurements have been applied in mineral deposit investigations in order to:

(i) Identify the sources of hydrothermal fluids
(ii) Evaluate fluid-rock exchange, in order to determine the intensity and extent of fluid flow
(iii) Reconstruct temperature gradients
(iv) Define redox conditions

Stable isotope techniques have been applied in a number of studies relating to ore mineralisation or hydrothermal fluid flow (e.g. Ohmoto, 1972; O'Neil and Silberman, 1974; Taylor, 1974; Bethke and Rye, 1979; Dilles et al., 1992; Nesbitt, 1996; Criss et al., 2000; Barker et al., 2013), with updated summaries provided in Taylor and Barnes (1997) and elsewhere (e.g. Shanks, 2001; Barker and Dipple, 2019). Historic hydrogen ($\delta^{2}H$) and oxygen ($\delta^{18}O$) isotope studies in intrusion related ore deposits (e.g. epithermal and porphyry) demonstrate circulation of fluids around intrusions drives mineralisation, and that patterns of isotopic depletion, indicative of water-rock exchange, can be mapped in host rock over a range of scales (e.g. Taylor, 1973; Taylor, 1978; Criss and Taylor, 1983; Criss et al., 2000). Key examples from the Comstock Lode (Figure 2.2) and the Idaho Batholith (Figures 2.3) are depicted on the following pages.

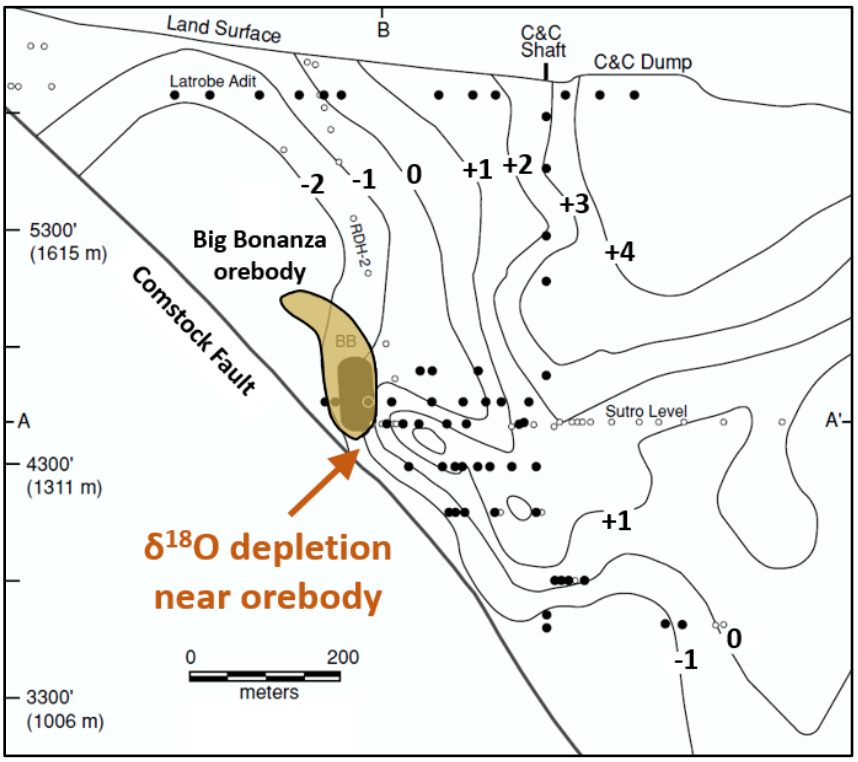

Figure 2.2: Oxygen isotope contouring across the Comstock Lode deposit indicates distinct zonation related to the intensity of fluid flow. The oxygen isotope signature of host rock becomes progressively lower near the Big Bonanza orebody. Fresh or minimally altered rock exhibits $\delta^{18}O$ between 5 and 9 ‰ VSMOW, while samples between -4 and +3 ‰ indicate extensive alteration by flow of meteoric hydrothermal fluid. Cross section of $\delta^{18}O$ alteration modified from Figure 5 in Criss et al., 2000.

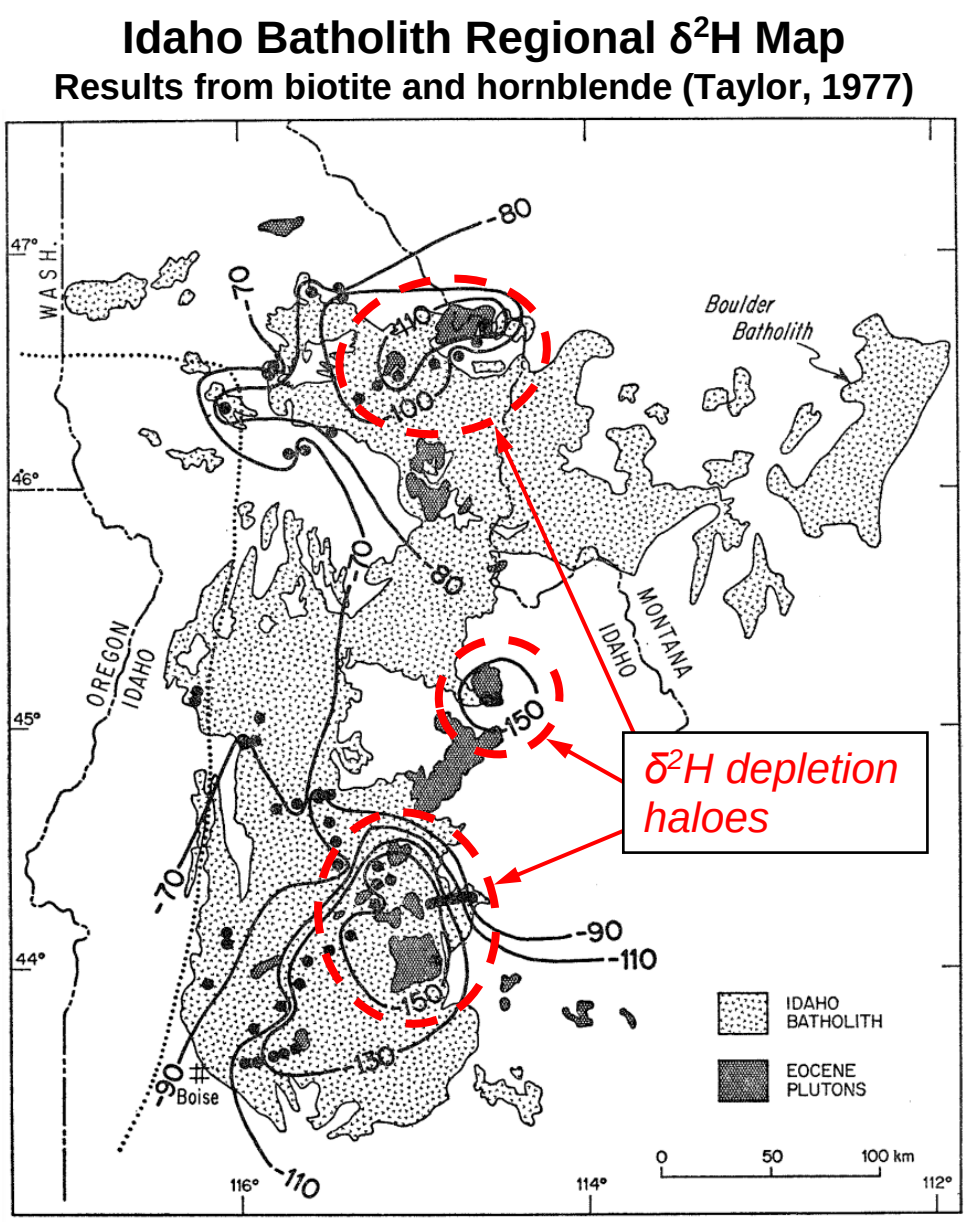

Figure 2.3: map of the Idaho batholith, with δ^2H contours drawn from measurements of biotites and hornblendes. The Idaho Batholith is a Cretaceous-Paleogene granitic body that extends over 25,000 square km in Central Idaho, USA. Regional scale contouring of δ^2H, measured in mineral separates, reveals zones of depletion around granitic plutons (Taylor, 1977; Criss and Taylor, 1983). Hydrogen isotope signals in minerals around Eocene plutons are shifted to more negative values reflecting intense hydrothermally-driven circulation of meteoric fluids. Figure from Taylor, 1977.

These pioneering works carried out in North America identify zones of isotopic depletion around ore deposits as indicative of higher intensity fluid flow. When applied across districts, it is suggested that stable isotope tools are capable of providing alteration targets that may extend beyond conventional indicators of fluid flow, including textural and mineral associations (Criss et al., 2000; Barker et al., 2013). Isotopic haloes around deposits are interpreted to reflect the duration of fluid circulation and intensity of alteration. In some cases, the size of the isotope alteration footprint may be related to the overall size of the deposit and can be used to estimate resource potential (Criss and Taylor, 1983; Waring et al., 1998). The isotopic alteration patterns observed at Comstock and the Idaho batholith reflect several key tenets of stable isotope theory, including: the isotopic value ranges of terrestrial fluids, mineral-fluid exchange of isotopes (i.e. water-rock), and equilibrium fractionation. These are introduced in the following sections.

2.2 STABLE ISOTOPE CONCEPTS

2.2.1 Stable isotope notation

Delta notation is the universal method for reporting stable isotope data (McKinney et al., 1950; Craig, 1957). The δ value reflects the relative enrichment, or depletion, of rare isotopes in a material, in parts per thousand, or per mil (‰), relative to internationally agreed upon reference standards (Craig, 1957). This scheme is useful because most isotope ratios in nature are comparable to three significant digits. The value for enrichment or depletion of a given isotope is reported as:

$$\delta = (R_{sample}/R_{standard} - 1) * 1000 \quad (2.1)$$

The R term is the ratio of rare and common isotopes for a given system (e.g. $^{18}O/^{16}O$, $^{13}C/^{12}C$). Hydrogen isotope ratios ($^{2}H/^{1}H$) in waters are reported relative to Vienna Standard Mean Ocean Water (VSMOW) (e.g. Coplen et al., 1983; Coplen, 2011). VSMOW is the primary reference for oxygen isotope ratios ($^{18}O/^{16}O$, $^{17}O/^{16}O$). Carbon isotope ratios ($^{13}C/^{12}C$) are reported relative to the value of a Cretaceous-aged belemnite fossil from the Pee Dee (VPDB) formation (Coplen et al., 1983).

The isotope fractionation factor "α" represents the partitioning of isotopes between two phases, or the ratio of isotopes in one phase relative to the other coexisting phase. The general form for α is defined in the following for generic phases "a" and "b", with measured isotope ratios (R):

$$\alpha_{a\text{-}b} = R_a/R_b \qquad (2.2)$$

Notably, the expression of fractionation (i.e. 1000lnα), varies significantly with respect to temperature for isotope measurements in many species of minerals (e.g. O'Neil et al., 1969). Relevant mineral-fluid temperature fractionation relationships are outlined in the following sections for clays, carbonates and silicates.

2.2.2 Isotope thermometry

Oxygen isotope thermometry

One of the major driving forces towards developing stable isotope techniques has been to understand the temperature at which minerals form in the crust. The temperature dependent relationship governing isotope exchange between fluids and minerals (e.g. quartz, calcite) was established early in the history of stable isotope geochemistry (Urey et al., 1951; Epstein et al., 1953). In conventional oxygen isotope thermometry, the $\delta^{18}O_{mineral}$ parameter is measured, but $\delta^{18}O_{water}$ must be known, or reasonably estimated, in order to define temperature. Below, the relationship between mineralization temperature, $\delta^{18}O_{water}$, and $\delta^{18}O_{carbonate}$ is given for a commonly used calcite-water thermometer (Kim and O'Neil, 1997):

$$1000 \times \ln\alpha(\text{Calcite-}H_2O) = (18.03 \times 10^3)/T - 32.42 \qquad (2.3)$$

Temperature (T) is in Kelvin

Commonly used oxygen isotope mineral-water fractionation relationships for carbonates and silicates are plotted in Figure 2.4.

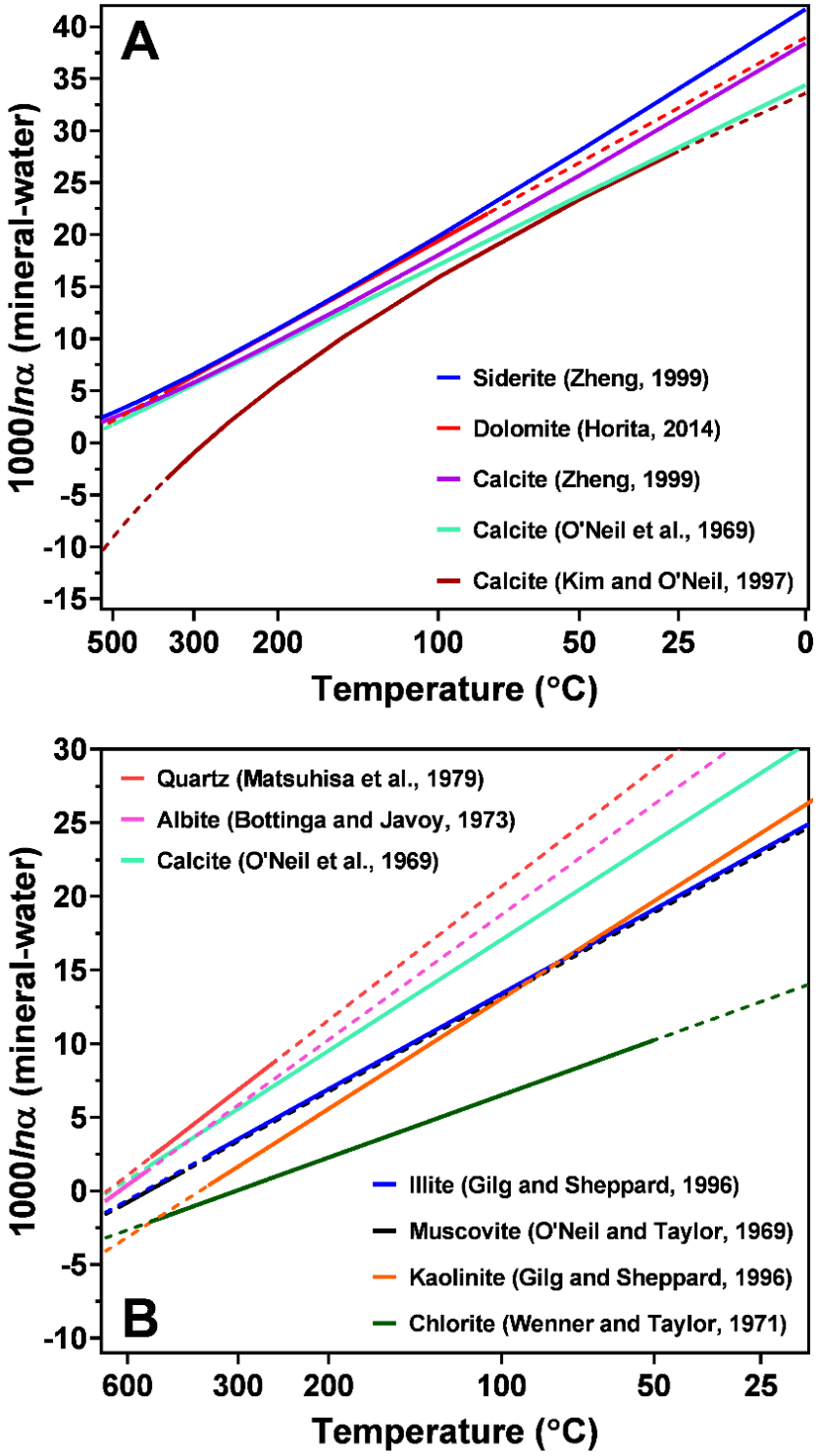

Figure 2.4: common oxygen isotope fractionation relationships governing mineral-water exchange with respect to temperature. Panel A: carbonate mineral $\delta^{18}O$ fractionation. Panel B: fractionation factors for a range of silicates and calcite.

In hydrothermal settings, the significant variations between meteoric, magmatic, and metamorphic fluid make estimation of fluid $\delta^{18}O$ problematic in many cases. To circumvent the limitations of the oxygen isotope geothermometry, mineral pair isotope thermometers have been developed, based on the knowledge that minerals forming in equilibrium from a common fluid fractionate isotopes differently (Figure 2.4). As an example, the quartz-calcite thermometer (Chiba et al., 1989) is defined below:

$$\Delta_{Quartz\text{-}Calcite} = 0.38\times 10^6/T^2 \quad (2.4)$$

Clumped isotope thermometry

Although mineral pair thermometers are widely utilised, it is often difficult to prove that two phases (e.g. quartz-calcite) formed contemporaneously from a common fluid. Single-mineral isotope thermometers, made possible by recent analytical advances, are a promising but largely untested alternative. Clumped isotope (e.g. Eiler, 2007, Huntington et al., 2011) and triple oxygen isotope techniques (e.g. Sharp et al., 2016; Hayles et al., 2018) overcome some of the limitations posed by traditional thermometry approaches by providing a thermodynamically sensitive means for reconstructing fluid temperature in a single mineral (Schauble et al., 2006; Eiler et al., 2007; Dennis et al., 2011). The clumped isotope method applied in Chapter 5 of this thesis is based on the exchange of isotopes between isotopologues of carbonate-containing groups (Schauble et al., 2006). In the following equation, cooler temperatures favour the forward reaction:

$$Ca^{12}C^{18}O^{16}O_2 + Ca^{13}C^{16}O_3 = Ca^{\mathbf{13}}\mathbf{C}^{\mathbf{18}}\mathbf{O}^{16}O_2 + Ca^{12}C^{16}O_3 \quad (2.5)$$

clumped isotope

The clumped isotope value (Δ_{47}) can be related to the temperature of ambient fluid at the time of mineralization, where lower temperatures are associated with a greater abundance of ^{13}C-^{18}O bonds (Figure 2.5). For reference, the natural abundances of isotopologues of CO_2 are provided in Table 2.2.

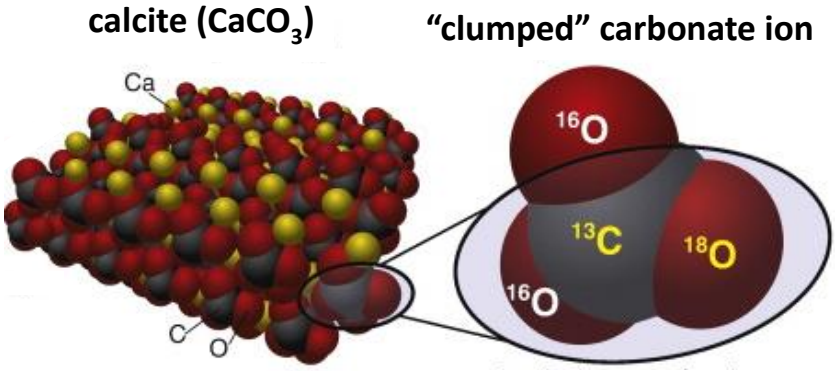

From: Huntington and Lechler, 2015

Figure 2.5: carbonate clumped isotope thermometry is a measure of thermally dependent ^{13}C-^{18}O bond abundance. Figure modified from Huntington and Lechler, 2015.

Table 2.2: Average natural abundance of CO_2 isotopologues

Mass	Isotopologue*	Abundance
44	$^{12}C^{16}O_2$	98.40 %
45	$^{13}C^{16}O_2$	1.11 %
	$^{12}C^{16}O^{17}O$	748 ppm
46	$^{12}C^{18}O^{16}O$	0.40 %
	$^{13}C^{17}O^{16}O$	8.40 ppm
	$^{12}C^{17}O_2$	0.142 ppm
47	**$^{13}C^{18}O^{16}O$**	**44.4 ppm**
	$^{12}C^{17}O^{18}O$	1.50 ppm
	$^{13}C^{17}O_2$	1.60 ppm
48	$^{12}C^{18}O_2$	3.96 ppm
	$^{13}C^{17}O^{18}O$	16.8 ppb
49	$^{13}C^{18}O_2$	44.5 ppb

Based on Eiler, 2007

*Rare multiply substituted isotopologues are underlined

In contrast to conventional carbon and oxygen isotopes, clumped isotope values are normalised relative to a stochastic isotope distribution. In practice, stochastic isotope distributions are measured on CO_2 gas standards that are heated at 1000 °C for at least two hours (Dennis et al., 2011). The Δ_{47} value is defined in Equation 2.8, where R_{45}*, R_{46}*, R_{47}* are values for a stochastic distribution of carbon and oxygen isotopes in a given sample of CO_2 gas (Eiler, 2007). Interlab comparison of clumped isotope results is accomplished by utilisation of the Carbon Dioxide Equilibration Scale (CDES) (Dennis et al., 2011). When CO_2 passes through the ionising source of an IRMS, CO_2^+ ions are variably fragmented. The CDES scale provides a universal reconstruction of this effect, which may be applied to any instrument. The CDES is established through routine analysis of CO_2 equilibrated at different temperatures.

$$\Delta_{47} = [(R_{47}/R_{47}^*) - (R_{46}/R_{46}^*) - (R_{45}/R_{45}^*) + 1] \times 1000 \quad (2.6)$$

$$R_{45}^* = R_{13} + 2 \times R_{17}$$
$$R_{46}^* = 2 \times R_{18} + 2 \times R_{13} \times R_{17} + (R_{17})^2$$
$$R_{47}^* = 2 \times R_{13} \times R_{18} + 2 \times R_{17} \times R_{18} + R_{13} \times (R_{17})^2$$

Despite the potential advantages conferred by using clumped isotopes for single mineral thermometry, the method is largely untested in hydrothermal settings. Technically challenging sample preparation, and time consuming measurement (~3 hours per analysis), has limited the number of studies applying the method in high temperature geologic settings. Additional work is needed to test the validity of clumped isotope calibrations in high temperature geologic systems, and identify the long term preservation potential of clumped isotope signatures in the geologic record. Specifically, it is not resolved whether clumped isotope measurements in hydrothermal carbonates, and deep basinal settings, reflect peak alteration (metamorphic) temperatures, or cooling history that postdates the thermal maximum. Chapter 5 in this thesis explores these themes with results reported from modern geothermal and epithermal (i.e. fossil geothermal) sites on the North Island of New Zealand, as well as results from skarn and carbonate hosted base metal deposits, where peak temperatures are thought to have exceeded 300 °C.

2.2.3 Isotopic variation in terrestrial reservoirs

Figure 2.6 provides an overview of the range of fluids and processes governing hydrogen and oxygen isotope exchange in hydrothermal fluids. Evaluation of mixing and water-rock interaction can used to quantify the contributions of local meteoric water, metamorphic, or magmatic waters in a system. On Earth, meteoric water $\delta^{18}O$ spans from -55.5 to ~0 ‰ VSMOW (Gonfiantini, 1984; Coplen, 1988), while sedimentary brines and magmatic waters are between ~5 and 10 ‰ (Kesler et al., 1997), and metamorphic fluids are as heavy as 30 ‰ (e.g. Giggenbach, 1992; Kesler et al., 1997).

With respect to $\delta^{2}H$, magmatic waters span between approximately -80 and -40 ‰, and basinal brines may extend above 0 ‰ (Giggenbach, 1992; Kesler et al., 1997). Meteoric waters range from -428 ‰ for Antarctic precipitation (i.e. SLAP) up to 0 ‰ for seawater (e.g. Gonfiantini, 1984; Coplen, 1988). The isotopic signature of meteoric water varies globally, with higher latitudes and elevations typically receiving lighter precipitation. Evaporation causes waters to plot along lines of shallower slope, reflecting preferential enrichment of $\delta^{18}O$, relative to $\delta^{2}H$. In meteoric water that has not been fractionated by evaporation, the Global Meteoric Water Line (GMWL) is used to represent trends in hydrogen and oxygen isotope ratios (Craig, 1961):

$$\delta^{2}H = 8 * \delta^{18}O + 10 \qquad (2.7)$$

The amount of fluid passing through a hydrothermal system can be parameterised as a water-rock ratio. Kinetic equations describing fluid-rock exchange have been developed for this purpose (e.g. Criss et al., 1987; Dipple and Ferry, 1992). Water-rock ratio calculations, based upon oxygen isotope exchange, assume that the isotopic value of fluid differs from that of the original host rock (Criss et al., 1987; Bowman et al., 1994). Greater separation in isotope values for rock and fluid allow for accurate determination of fluid-rock exchange and interpretation of alteration intensity and fluid volume. Typically, hydrothermal fluids develop enriched $\delta^{18}O$, as a result of water-rock interaction (e.g. Criss et al., 1987; Taylor and Barnes, 1997). Simultaneously, host rock is altered, attaining more ^{18}O depleted signatures.

Isotopic exchange between fluids and host rock is invoked to explain $\delta^{18}O$ depletion haloes around some hydrothermal areas (e.g. Comstock), and $\delta^{18}O$ enrichment of waters in geothermal fields above local meteoric values (Criss et al., 2000).

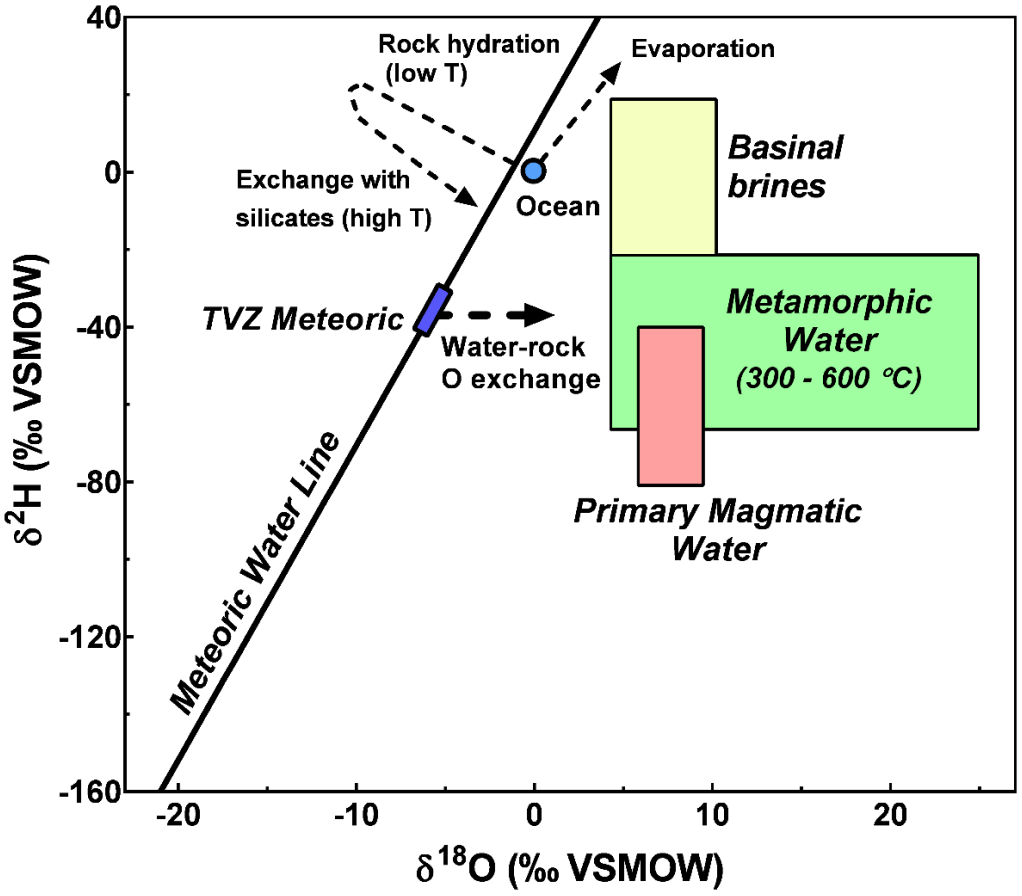

Figure 2.6: idealised plot of H and O isotopic value ranges of terrestrial waters. Meteoric waters exhibit variability in $\delta^{18}O$ and $\delta^{2}H$, with respect to latitude, moisture source, and elevation. Crustal rocks are typically ^{18}O enriched relative to ocean water, while meteoric waters are depleted. Water-rock interactions result in isotopically heavier hydrothermal fluids. The range of $\delta^{18}O$ and $\delta^{2}H$ in waters feeding geothermal fields in the modern TVZ is highlighted in blue. Figure drawn from previously defined fluid isotope ranges (e.g. Gonfiantini, 1984; Giggenbach, 1992b; Kesler et al., 1997).

2.2.4 Carbonates in hydrothermal settings

Carbonates are highly sensitive to fluid properties of the hydrothermal systems in which they form. Specifically, $\delta^{13}C$ and $\delta^{18}O$ signatures provide a measure of fluid source (e.g. H_2O and CO_2) and temperature. In recent case studies, stable isotopes

have been applied to exploration scenarios in carbonate hosted ore settings (e.g. Barker et al., 2013; Lepore, 2013; Vaughan et al., 2016; Beinlich et al., 2019). In Carlin-type Au deposits, localised zones of $\delta^{18}O$ depletion in carbonate host rock are indicative of elevated fluid flux and greater mineralisation potential (Arehart and Donelick, 2006; Barker et al., 2013; Vaughn et al., 2016).

Precipitation of carbonates in geothermal and epithermal settings is attributed to the balance of pH, *p*CO2, temperature, and brine composition (Fournier, 1985). Processes that lower pCO_2 in epithermal systems, such as boiling, and mixing with low-CO_2 fluids (Figure 2.7), enable carbonate deposition (Zheng, 1990; Zheng and Hoefs, 1993; Simmons and Christenson, 1994). Carbon dioxide is removed from solution during boiling, where fluid pressure abruptly drops, resulting in platy or bladed calcites (Simmons and Christenson, 1994). Carbonate deposition in the propylitic environment is also determined by availability of requisite cations (e.g. Ca^{2+}), sourced from dissolution of wall-rock minerals (e.g. calcic feldspars). Above ~100 °C, CO_2-rich fluids dissolve calcic wall rock minerals (e.g. plagioclase), resulting in an abundance of Ca^{2+} ions in solution (Giggenbach, 1981; Simmons and Christenson, 1994). Calcite subsequently precipitates, replacing the dissolved wall rock minerals. Simplified equations describing the dissolution of anorthite in a CO_2 rich aqueous fluid (equation 6.1) and subsequent precipitation of calcite (equation 6.2) are presented below:

$$CaAl_2Si_2O_8 + CO_2 + H_2O = Ca^{2+} + Al_2O_3 + 2SiO_2 + HCO_3^- + H_2O \quad (2.8)$$

$$Ca^{2+} + HCO_3^- = CaCO_3 + H^+ \quad (2.9)$$

There is abundant evidence demonstrating the cumulative influence of these processes in modern analogue geothermal fields in the Taupo volcanic zone (TVZ), New Zealand (Simmons and Christenson, 1994; Simmons and Browne, 2000).

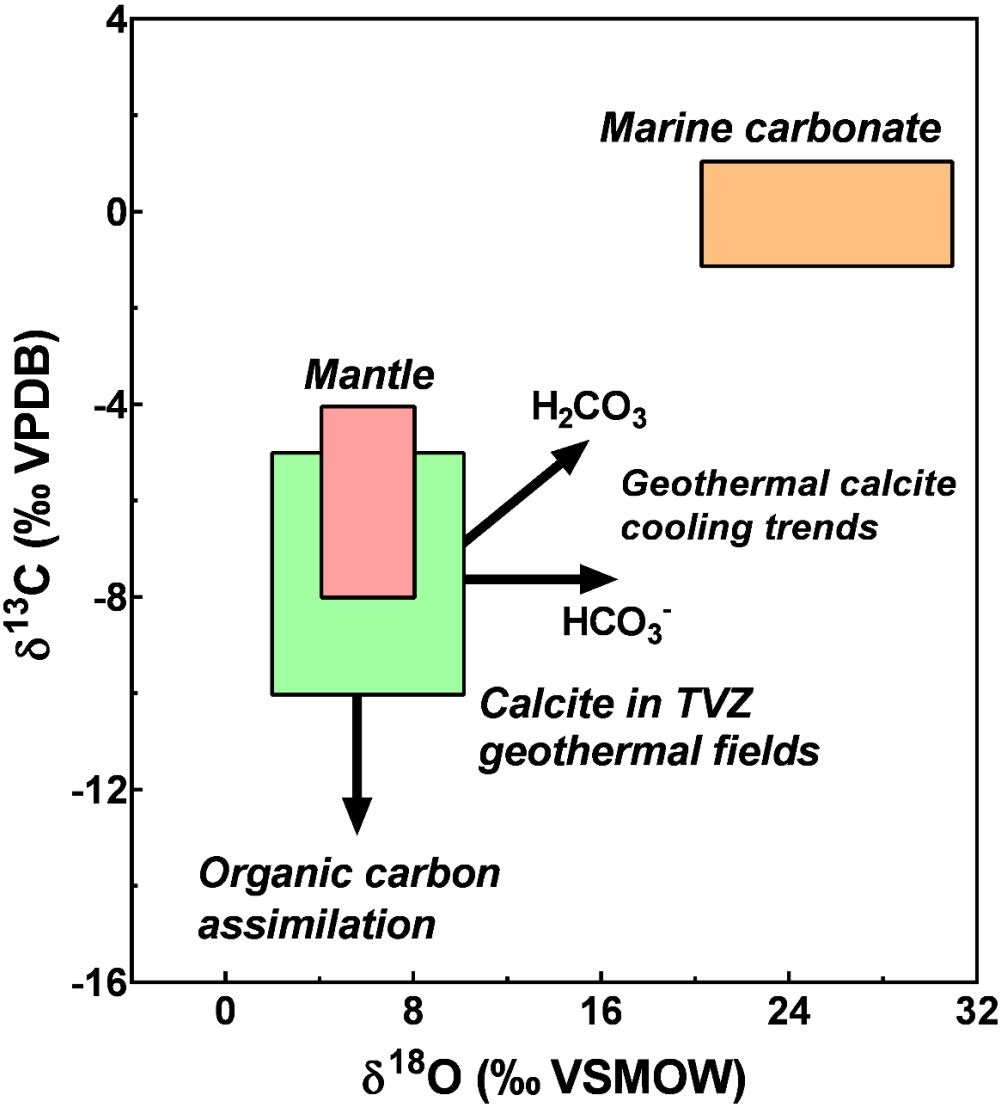

Figure 2.7: plot of carbon and oxygen isotopic value ranges in carbonates of both marine (orange) and magmatic (red) origin. The value range for measurements of $\delta^{13}C$ and $\delta^{18}O$ in TVZ carbonates is bounded by the green box. Variations in $\delta^{18}O$ reflect both fluid history (source and water-rock interactions) and temperature, while $\delta^{13}C$ is primarily linked to the sources of carbon. Carbonate isotope ranges after Swain et al. (2015). Values of TVZ calcite and trends for H_2CO_3 and HCO_3^- from Simmons and Christenson (1994).

The $\delta^{13}C$ signatures in hydrothermal carbonates enable interpretation of CO_2 source (e.g. magmatic vs. sedimentary organic), and are sensitive to dissolved inorganic carbon (DIC) species in fluids (Ohmoto, 1972; Robinson, 1975; Zheng and Hoefs, 1993). Carbon sourced from magmatic CO_2 will typically range between approximately -4 and -8 ‰ on the VPDB scale, while sedimentary organic carbon

may be lower than -20 ‰ (Figure 2.7). In fluid-dominated systems (i.e. modern geothermal and epithermal), positive covariation of $\delta^{18}O$ and $\delta^{13}C$ reflects calcite precipitation from a CO_2 rich fluid.

2.2.5 Isotope measurements in clay minerals

Clay minerals are generated during weathering and hydrothermal alteration (Giggenbach, 1981; Inoue, 1995). In hydrothermal investigations, clays provide a measure of alteration intensity, and are isotopically sensitive to fluid sources (e.g. Criss and Taylor, 1983). In most classes of ore deposit, clays are extensive both near the locus of mineralisation, and within the distal propylitic footprint (Inoue, 1995), making these minerals an attractive analytical target for reconstruction of fluid $\delta^{2}H$ and $\delta^{18}O$. In propylitic environments, the dissolution of hostrock is accompanied by the precipitation of clay and zeolite minerals, which vary depending upon temperature, pH, and available ions in solution (Giggenbach, 1981).

In clays, oxygen is distributed between tetrahedral sites (e.g. Si–O–Si, Al–O–Si, Al–O–Al, Si–O–Mg) and octahedral sites (i.e. OH), while hydrogen is present at the octahedral site (Figure 2.8). A limited body of work has attempted to understand oxygen isotope fractionation between tetrahedral and octahedral sites in clays (Savin and Epstein, 1970; Hamza and Epstein 1980; Bechtel and Hoernes 1990; Girard and Savin, 1996). Bechtel and Hoernes (1990) demonstrated that intramineral oxygen isotope fractionation in hydrothermal illite reflected both temperature and fluid $\delta^{18}O$. They note, however, that analyses are impeded in cases in which materials contain appreciable amounts of Fe, which interferes with extraction of OH.

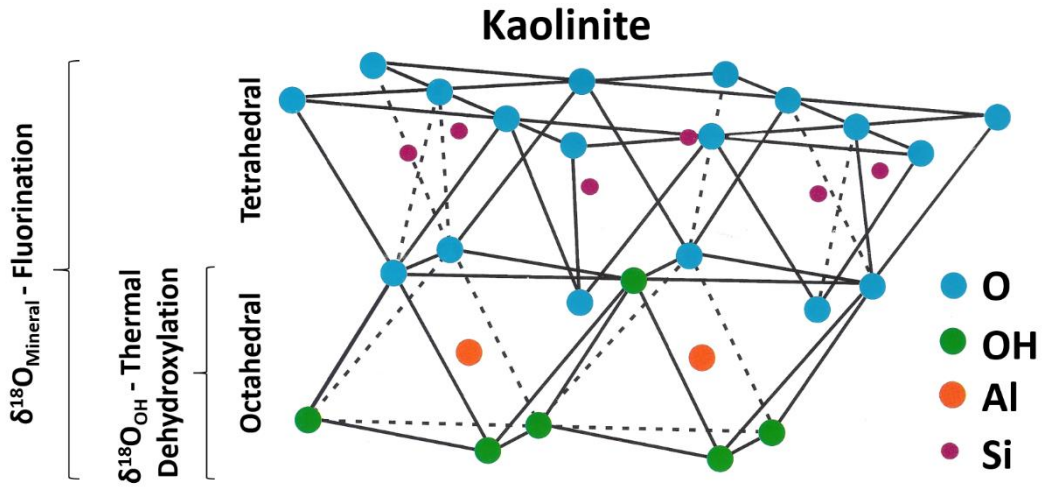

Figure 2.8: structure of kaolinite. Oxygen in clay minerals is partitioned into tetrahedral (Si-O) and octahedral (OH) sites. Kaolinite exhibits the simplest structure, with successive sheets joined together by H-bonds. In this work, the δ^2H and $\delta^{18}O$ signatures of OH groups are measured by thermal dehydroxylation laser spectroscopy. Fluorination-based IRMS techniques are required in order to extract and measure $\delta^{18}O_{silicate}$. Figure modified after Grim (1962) and Geatches (2011).

While equilibrium fractionation relationships are well constrained for oxygen isotopes in silicates and carbonates (e.g. O'Neil, 1969; Kim and O'Neil, 1997), the relationship between temperature, fluid δ^2H, and mineral δ^2H is not settled for many common clay mineral species (Savin and Hsieh, 1988; Faure et al., 2002). Most calibration studies are sample limited, and as Figure 2.9 demonstrates there is considerable disagreement in published clay-water fractionation relationships (Figure 2.9). Variable results likely stem from the small sample sets used in fractionation studies, and inherent difficulty associated with attaining mineral-fluid equilibrium in laboratory settings. In studies based upon modern geothermal samples (i.e. Marumo et al., 1980) and lab-based chlorite work (Graham et al., 1987), hydrogen isotope mineral-fluid fractionation varied minimally with respect to temperature. More work is needed to definitively constrain temperature effects upon clay-water δ^2H fractionation above 100 °C.

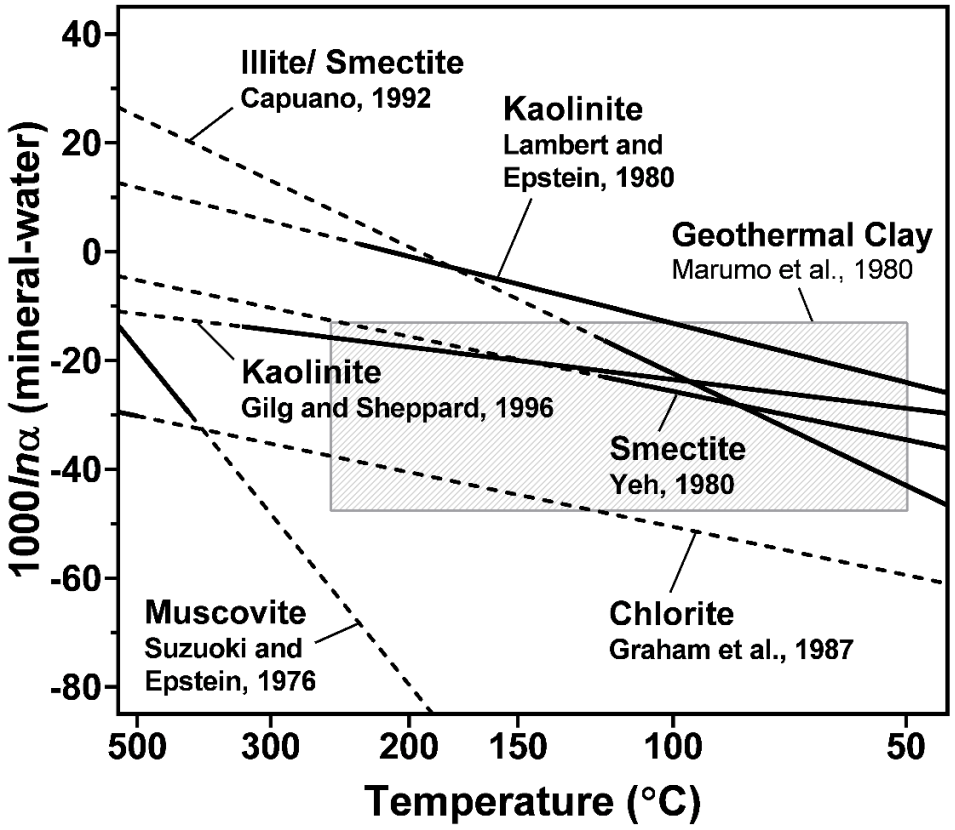

Figure 2.9: hydrogen isotope mineral-water fractionation factors in common clay minerals associated with ore deposits. Solid lines denote calibration range bounded by samples. Dashed lines are extrapolations. Grey box encloses kaolinite, chlorite, and sericite (illite) samples measured in the active Ohnuma geothermal area of Japan at temperatures between 50 and 250 °C.

In light of the present uncertainty regarding published clay-water fractionation relationships, the Ohnuma geothermal clay geothermal dataset (i.e. Marumo et al., 1980) is a natural choice to guide interpretation of whole rock δ^2H data collected at epithermal sites in this thesis (i.e. Waihi, Karangahake, Comstock). In the Ohnuma study, hydrogen isotope measurements were performed upon kaolinite, illite, and chlorite minerals, and associated fluids from geothermal wells at temperatures between 50 to 250 °C (Figure 2.10). Measurements of illite were on average 26 ‰ lower than geothermal H_2O, while kaolinite and dickite were 20 ‰ lower (Marumo et al., 1980). At Ohnuma, measurements of chlorite were 35 ‰ lower, on average, than measured H_2O values in geothermal fluid (Marumo et al., 1980). These results are similar to experimental constraints for chlorite (e.g. Graham et al., 1987) and kaolinite (e.g. Gilg and Sheppard, 1996), and constraints from New Zealand

geothermal areas (e.g. Hedenquist and Browne, 1989). Chlorites collected from the modern epithermal analogue at Waiotapu in the TVZ exhibit δ^2H between -70 and -80 ‰; water $\delta^{18}O$ in modern fluids ranges from -40 to -30 ‰ for local precipitation and deep chlorite water upflow, respectively (Hedenquist and Browne, 1989). Based on these constraints, it is reasonable to infer that chlorite may attain an equilibrium δ^2H signature that is ~5-15 ‰ lower than an illite clay forming under similar conditions.

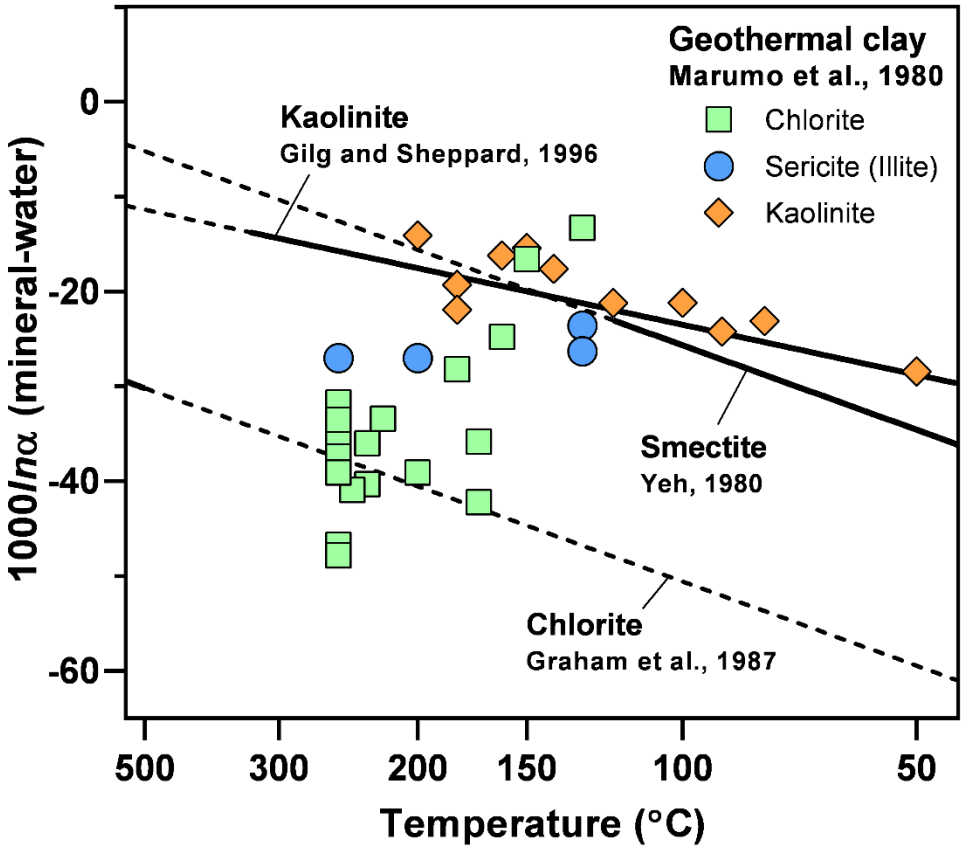

Figure 2.10: hydrogen isotope mineral-water fractionation factors in common clay minerals. The coloured points represent chlorite, sericite (illite) and kaolinite measurements of clays from the Ohnuma geothermal area, Japan, reported in Marumo et al., 1980. The Ohnuma geothermal clay-water relationships are applied in this thesis to reconstruct δ^2H of hydrothermal fluid at the Waihi, Karangahake, and Comstock epithermal sites.

Hydrogen isotopic constraints in hydrous minerals have the potential to identify fluids involved in alteration and ore emplacement. However, equilibrium isotope fractionation relationships in clays are not fully constrained for many minerals (Figure 2.9-2.10). The TD-OA-ICOS methodology applied herein (Chapters 3, 4, 6) provides groundwork to support more expansive application in natural systems.

2.2.6 Stable isotope measurement technology

Isotope ratio mass spectrometry

A variety of tools are available to measure isotopic abundances in minerals. Dual inlet isotope ratio mass spectrometry (IRMS) forms the basis for quantifying stable isotope values (McKinney et al., 1950; Urey et al., 1951; Craig, 1957). Figure 2.11 provides a schematic diagram of a generic dual inlet isotope ratio mass spectrometer, configured for measuring CO_2. Recent advances in mass spectrometry allow for accurate quantification of the rare multiply substituted isotopologues of CO_2 (Table 2.2), including mass-47 (e.g. $^{13}C^{18}O^{16}O$) applied in carbonate clumped isotope thermometry (i.e. Δ_{47}).

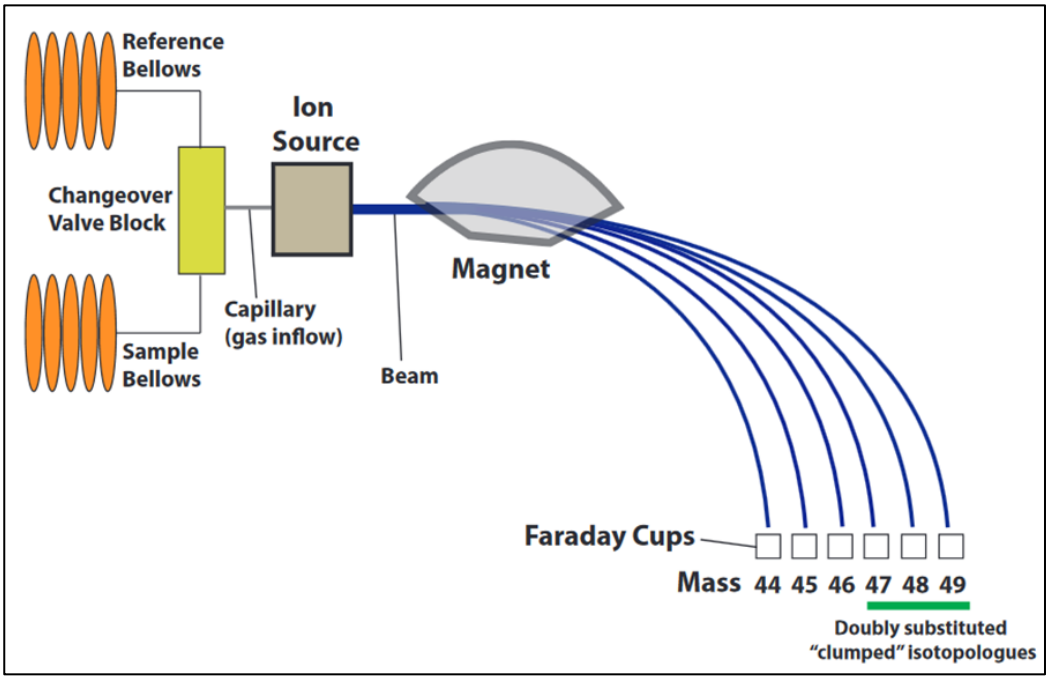

Figure 2.11: schematic of the major components in a dual inlet IRMS configured for measuring CO_2. Solid geologic samples are gasified by acidification or thermal conversion. An ionizing filament in the source confers a charge on the gas molecules. The ionized molecules leaving the source passes through a sector magnet, which splits the beam. Sample gas mass/charge is measured against reference gas of known isotopic value, with analyses alternating between sample bellows and reference bellows. In this example, faraday resistors are configured to measure masses 44-49.

Although dual inlet isotope ratio mass spectrometers provide the highest level of analytical precision, long measurement times make these systems less useful in

many applications. The continuous flow (CF) approach to IRMS offers advantages over dual inlet for applications in which many samples must be measured (Brenna et al., 1997; Sharp et al., 2001). In CF-IRMS, pulses of sample gas are purified and concentrated by transit through a gas chromatograph (GC) en route to an IRMS (e.g. Brenna et al., 1997). Isotope ratios are determined from peak area ratios for individual isotopologues.

Laser spectroscopy

Advances in laser spectroscopy present new platforms to assess hydrogen, carbon, and oxygen isotopes in ore deposits (e.g. Barker el., 2013; Mering and Barker, 2018). Measurement is accomplished by introducing gas into a mirrored optical cavity, which contains a diode laser and photodetector (Figure 2.12). Previous application of Off-Axis Integrated Cavity Output Spectroscopy (OA-ICOS) demonstrated measurement capability of $\delta^{13}C$ and $\delta^{18}O$ in carbonate minerals, at precisions of approximately ±0.3-0.6 ‰ (Barker et al., 2011; Barker et al., 2013; Beinlich et al., 2017). The carbonate OA-ICOS approach has been applied to measure isotopic variation around carbonate-hosted mineral deposits (e.g. Barker et al, 2013, Beinlich et al., 2019). Many of the principles of isotopic analysis via laser spectroscopy remain similar to those of traditional mass spectrometry, including conversion of mineral samples to gas (e.g. $CaCO_3$ to CO_2), and the analysis of standards of known isotopic composition in order to report sample values relative to international isotope ratio scales (i.e. VSMOW, VPDB). In this thesis, OA-ICOS techniques are developed for measurement of $\delta^{2}H$ and $\delta^{18}O$ in hydrous minerals (Chapters 3-4), and applied to measure hydrous minerals and carbonates in epithermal areas (Chapters 4 and 6).

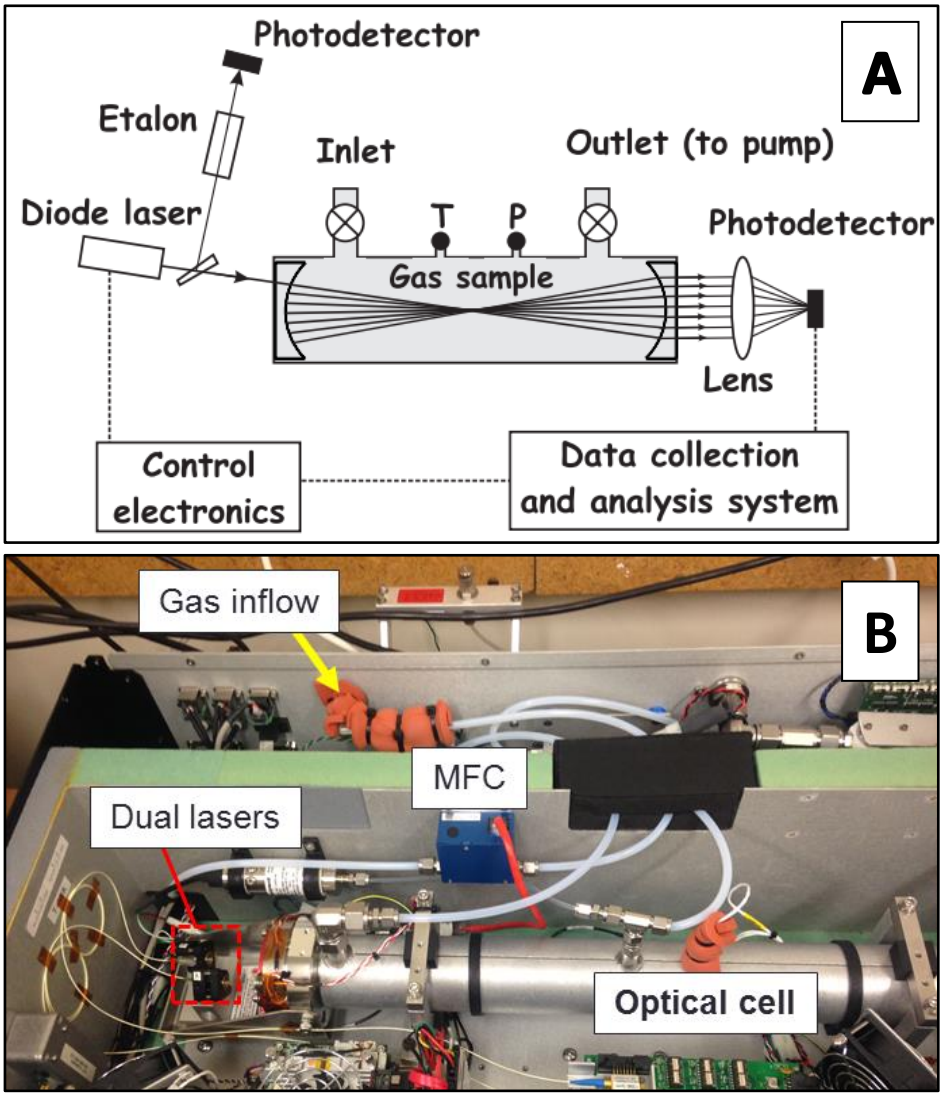

Figure 2.12: LGR OA-ICOS system. The laser is pulsed through the cell, and the mixing ratios for isotopologues (e.g. $^{1}H_{2}{}^{16}O$, $^{1}H^{2}H^{16}O$, $^{1}H_{2}{}^{18}O$) are calculated from absorption spectra (i.e. ringdown time), which can in turn be applied to calculate isotope ratio values. Panel A: conceptual OA-ICOS design (www.lgrinc.com). Panel B: OA-ICOS water isotope analyser at University of Waikato used in this research.

CHAPTER III

Rapid and precise measurement of the hydrogen isotope composition in phyllosilicates by thermal dehydroxylation laser spectroscopy

---

In the following chapter, an analytical method is described for measuring hydrogen stable isotope ratios ($^2H/^1H$) in hydrous minerals and sub-µL liquid waters using an Off Axis Integrated Cavity Output Spectroscopy (OA-ICOS) water vapour isotope analyser. Hydrogen isotope measurements (δ^2H) made using a laser absorption spectroscopy platform are reported here for the first time for mica (muscovite, talc, biotite) and serpentine minerals. Discussion is provided on the best protocol for achieving high precision, accuracy, and speed, while limiting sample requirements. A version of this work was published in 2018 in the journal *Analytical Chemistry*. The work presented herein (including published data) was collected by John Mering. The protocols described herein were designed by John Mering in consultation with Shaun Barker (co-author and research supervisor). The paper, including figures and tables, was drafted by John Mering, with feedback from Shaun Barker. Funding for this project was provided by a New Zealand Ministry of Business, Innovation and Employment research grant (Gold Exploration Models: C05X1405). Reference materials were contributed by John Dilles (Oregon State University), Kurtis Kyser (Queen's University), Zach Sharp (University of New Mexico), and Haiping Qi (United States Geological Survey). Robert Van Hale (University of Otago) performed IRMS verification of hydrous minerals. Peter Jarman (University of Waikato) provided assistance with construction and maintenance of hardware. The citation for the published work is as follows:

Mering, J.A., and Barker, S.L.L., 2018, Precise Measurement of the Hydrogen Isotope Composition of Phyllosilicates by Continuous Flow Off-Axis Integrated Cavity Output Spectroscopy: Analytical Chemistry, v. 90, p. 2852–2859, doi:10.1021/acs.analchem.7b04992.

ABSTRACT

New methodology is presented for analysing hydrogen isotope ratios ($^2H/^1H$) in phyllosilicate minerals by laser absorption spectroscopy. Measurements were carried out using an OA-ICOS instrument operated in a continuous flow configuration. Water was extracted from minerals in a high temperature quartz column and advanced to the analyser in a dry air carrier gas stream. The first δ^2H measurements by a laser system are reported for serpentine, muscovite, sericite, talc, and biotite. Kaolinite, gypsum, and small volumes of water are also measured. Materials, excluding biotite, were calibrated to within 1.5 ‰ of IRMS-measured δ^2H values, with an average precision of 1.1 ‰. Biotite δ^2H measurements were up to 10 ‰ higher than established IRMS values, inferred to be due to partial reduction of evolved waters by Fe in the high temperature column. Recommendations are provided for overcoming redox interference for measurements of biotite, and other ferrous materials, by OA-ICOS. Rapid, precise, and accurate analyses were carried out on water volumes as low as 0.25 μL extracted from minerals. With the exception of talc, the time required for thermal dewatering and measurement is 140 seconds, which translates into a throughput of up to 6 mineral samples per hour, including replicates. By demonstrating high precision, rapid throughput, low cost, and ease of operation, we provide a tool that should enable researchers at institutions with limited funding to routinely measure δ^2H in hydrous minerals. The protocols presented herein should also be useful to commercial users seeking to produce high density isotope datasets relevant to exploration of hydrothermal ore deposits and geothermal fields.

3.1 INTRODUCTION

3.1.1 Hydrogen stable isotopes in geologic investigations

Hydrogen stable isotope archives in minerals provide a means to reconstruct fluid history in both surficial and subsurface deposits of geologic and environmental interest. Historically, a number of workers have measured δ^2H signatures in clays, micas and serpentine minerals to study fluid flow in hydrothermal settings (Taylor, 1974; Marumo et al., 1980; Criss and Taylor, 1983; Criss and Taylor, 1986; Giggenbach, 1992a; Nesbitt, 1996; Vennemann and O'Neil, 1996; Marumo and Hattori, 1999; Shanks, 2001). Hydrogen isotope values in minerals are routinely measured in both active (Marumo et al., 1980; Criss and Taylor, 1979; Giggenbach, 1992b; Shanks, 2001) and ancient hydrothermal environments (Taylor, 1974; Criss and Taylor, 1983; Criss and Taylor, 1986) to map fluid flow and temperature gradients (Criss and Taylor, 1986; Nesbitt, 1996; Criss et al., 2000). Important settings for these investigations encompass modern geothermal fields (Marumo et al., 1980; Criss and Taylor, 1980; Giggenbach, 1992b), submarine spreading centres (Marumo and Hattori, 1999; Shanks, 2001), ancient hydrothermal ore deposits (Taylor, 1974; Criss and Taylor, 1983; Criss and Taylor, 1986; Nesbitt, 1996; Barker et al., 2013) and sedimentary basins (Capuano, 1992; Schimmelmann et al., 2006). From an economic standpoint, these systems are relevant to geothermal energy development, mineral deposit studies (Criss and Taylor, 1983; Criss and Taylor, 1986; Nesbitt, 1996; Barker et al., 2013), and hydrocarbon exploration (Capuano, 1992; Schimmelmann et al., 2006).

Collectively, researchers have benefitted from advances in stable isotope measurement technology over the last 60 years. Yet, despite improvements in speed, precision, and accuracy (Coleman et al., 1982; Vennemann and O'Neil, 1993; Sharp et al., 2001), costs of hardware and consumables associated with Isotope Ratio Mass Spectrometry (IRMS) remain high. Herein, we demonstrate that continuous flow Off-Axis Integrated Cavity Output Spectroscopy (OA-ICOS) is a viable, lower cost, platform for rapidly quantifying hydrogen isotope ratios in hydrous minerals.

3.1.2 Laser spectroscopic approaches for measuring δ^2H in hydrous materials

Although Laser Absorption Spectroscopy (LAS) instruments, including OA-ICOS, are now widely used for isotopic measurement of water samples (Lis et al., 2008; Penna et al., 2012), they are rarely utilized to measure hydrous solids. LAS manufacturers do not provide "off the shelf" sample preparation systems for rapidly extracting water from hydroxyl bearing minerals, and other solids (e.g. organic compounds). Data handling software, for processing and calibrating results is also not available at this time. Consequently, work utilizing LAS to measure δ^2H in solid materials has been largely relegated to proof of concept papers. Trial work has focused on measurements of gypsum (Hodell et al., 2012; Gázquez et al. 2015; Evans et al., 2015; Gázquez et al., 2017), fluid inclusions (Affolter et al., 2014), organic compounds (Koehler and Wassenaar, 2012), and kaolinite (Bauska et al., 2017), in which water was extracted either offline (Hodell et al., 2012; Gázquez et al. 2015; Evans et al., 2015), or in continuous flow (Koehler and Wassenaar, 2012; Affolter et al., 2014; Oerter et al., 2017; Bauska et al., 2017). Two recent Cavity Ringdown Spectroscopy (CRDS) protocols, utilizing thermogravimetric analysers, enable interpretation of isotope signals across slowly evolved water peaks in gypsum, goethite and clay minerals (Bauska et al., 2017; Oerter et al., 2017). However, complex hardware, and processing times of up to 90 minutes for clays, render these techniques less useful for applications in which higher sample throughput is required, including mineral exploration. Mapping isotopic variation across mineral deposits in three dimensions can provide useful information on paleohydrothermal fluid source (e.g. Criss et al., 2000; Barker et al., 2013). In order to match the pace of exploratory programs, isotope measurement throughput on the scale of 10s-100s of measurements in a day is desirable.

Herein, documentation is provided of a methodology that enables routine measurement of δ^2H ratios of hydrous minerals using readily available and reliable equipment. A comprehensive discussion of hardware operation and data processing is provided to enable users of laser absorption spectrometers to rapidly analyse, and accurately calibrate, δ^2H signals in minerals. Measurements were performed using a Los Gatos Research (LGR) OA-ICOS analyser (San Jose, CA, USA), but the principles described here should be applicable to users of other LAS systems. Tests were carried out on common hydrous minerals, including serpentine, muscovite,

sericite, kaolinite, talc, biotite, and gypsum. The analytical setup described here is characteristically simpler than Thermal Conversion Elemental Analysis (TC/EA) IRMS systems, but still capable of delivering precise and rapid hydrogen isotope ratio measurements.

3.2 METHODS

3.2.1 Hardware setup

Isotopic analyses were conducted using a LGR OA-ICOS Triple Isotope Water Analyzer (IWA-45EP), and a custom-built sample preparation line at the University of Waikato, Hamilton, New Zealand. Minerals are dewatered in a high temperature column, and the resulting water vapour pulse is transferred to the optical cell in the analyser in a dry air carrier gas stream. A pressurized dry air cylinder was used as the carrier gas source, but any dry and oil free compressed air source would be suitable. The OA-ICOS instrument, contains a high finesse optical cell, which operates on the principle of cavity enhanced absorption. The analyser is described in literature (Baer et al., 2002; Lis et al., 2008; Gupta et al., 2009; Barker et al., 2011; Penna et al., 2012; Koehler and Wassenaar, 2012). Measurement is accomplished by introducing H_2O vapour into the cell, which contains highly reflective mirrors, a diode laser, and photodetector. The laser is pulsed through the cell, and the absorption spectra of water isotopologues are measured. Mixing ratios for $H_2{}^{16}O$, HDO, $H_2{}^{18}O$, and $H_2{}^{17}O$ are calculated from absorption spectra, and corrected to account for cavity temperature, pressure, laser path length, and ringdown time (Baer et al., 2002; Lis et al., 2008; Gupta et al., 2009; Barker et al., 2011; Koehler and Wassenaar, 2012; Penna et al., 2012). Concentrations of isotopologues were measured in parts per million by volume (ppmv) at 1 Hz.

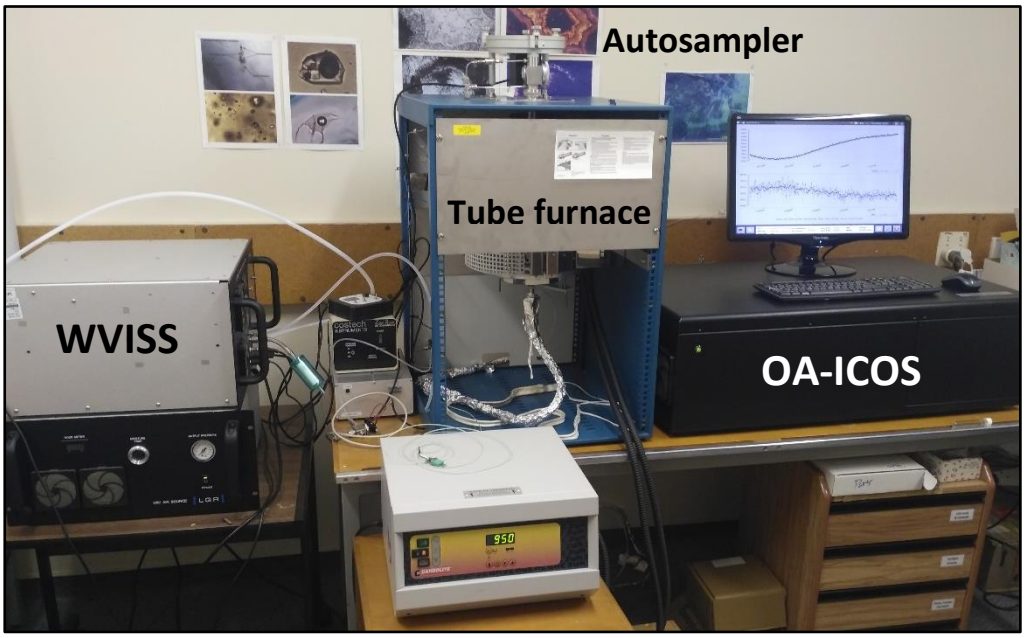

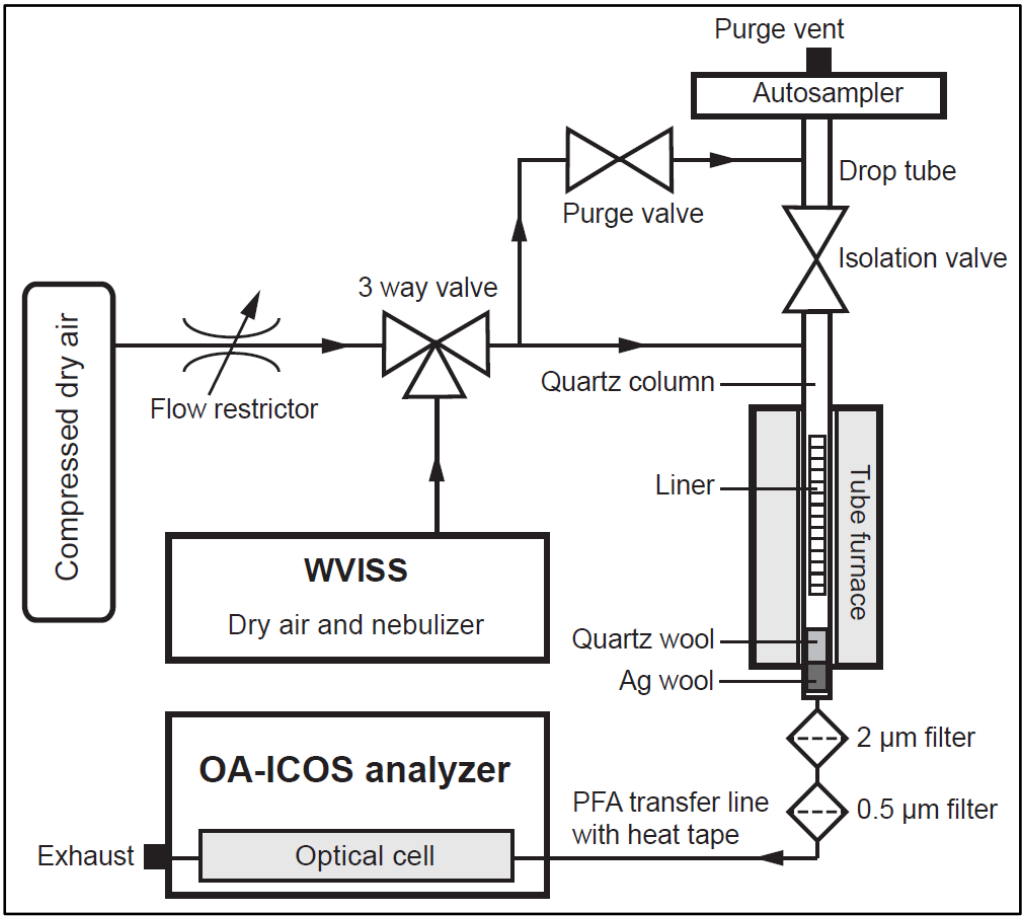

Figure 3.1: hardware setup of the mineral dehydration line and LGR OA-ICOS analyser used for measurement of hydrogen isotope signatures in hydrous minerals at the University of Waikato. Minerals were dewatered in a quartz tube, heated between 945 and 1000 °C.

The mineral dehydration line, depicted in Figure 3.1, was designed to facilitate high sample throughput and minimise memory. The dehydration line features a high temperature quartz column, emplaced in a Carbolite (Hope, UK) tube furnace, paired with a Costech Zero Blank (Valencia, CA, USA) carousel autosampler. The autosampler is triggered using an Arduino (Somerville, MA, USA) single-board microcontroller, which generates a 1 second contact closure. A USB access port on the controller allows users to adjust the timing of the autosampler drop interval. Mineral powders are dewatered in the column, at temperatures between 945 and 1000 °C. For straightforward maintenance, a quartz liner was installed to sequester used capsules and mineral powder. The liner rests upon 3 indentations in the hottest interval of the quartz column. The base of the liner is closed, and the wall of the liner is perforated to allow the flow of water vapour and carrier gas through to the analyser. Plugs of quartz wool and silver wool are emplaced at the base of the column to preclude the transit of mineral powder, and sulphur-bearing compounds, into the analyser. No other packing (e.g. quartz chips, Cr_2O_3) was utilized. A pair of 2-µm and 0.5-µm filters (Valco Instruments Co., Inc., USA) were installed below the column, upstream of the OA-ICOS unit, to prevent clogging of the internal filter in the analyser.

During the course of the study, filters in the prep line occasionally became coated by sulphur compounds. Sulphur build-up occurred during analyses of hydrothermally altered rocks, which contained pyrite, and hydrous sulphates. This issue was mitigated by including a silver wool trap in the column packing, and by routinely changing the inline filters and quartz liner. Maintenance on the liner and filters was carried out after approximately 1 g of mineral powder had been analysed. The filters and liner can be changed in less than 10 minutes, while the column is at normal operating temperatures. The column is connected directly to the analyser by a 1/4 inch diameter, 75 cm long PFA tube. The tube is wrapped in heat tape, and is maintained at 95 °C during analyses.

A combination of greater heating of transfer lines, shortened transfer tubing, and a carrier gas pressure setting high enough to achieve turbulent flow resulted in the best precision and the smallest memory effect. Analysis of a synthetic gypsum sample demonstrated a reduction in memory of up to 20 percent on the first analysis in a series of replicates as a result of heating. A variety of flow and pressure settings

were considered. The standard rate of carrier gas flow from the column into the optical cell is approximately 110 ml/min. Although it was possible to maintain a normal pressure of 40.3 torr (5372.9 Pa) in the OA-ICOS cell at lower flow rates, measurements of hydrogen isotope ratios were considerably less precise. At a flow setting of 60 ml/min, analytical uncertainty of δ^2H, represented by 1 standard deviation of the mean (1σ) of replicate measurements, was consistently greater than 5 ‰, and above 10 ‰ in several cases.

In the tests reported here, the hydrogen isotope (δ^2H) values of minerals and liquid waters were measured by OA-ICOS for materials that covered an expansive range of values, from 0 to -189 ‰ VSMOW. Hydrogen isotope ratios ($^2H/^1H$) were normalized to the VSMOW scale, using reference materials with known δ^2H values, established by IRMS. New hydrogen isotope mineral standards were measured by TC/EA-IRMS at the University of Otago. A list of the materials evaluated by OA-ICOS in this study is provided in Table 3.1.

Table 3.1: Materials measured by OA-ICOS in this study

Standard	Type	IRMS δ^2H (‰ VSMOW)
Hydrous mineral		
G-18502	Muscovite	-23.8
USGS 58	Muscovite	-28.4
Talc-1	Talc	-41.6
G-18499	Muscovite	-51.1
Kga-1b	Kaolinite	-50.5
Georgia Clay	Kaolinite	-59.0
MISASA	Sericite	-59.1
NBS 30	Biotite	-65.7 (-53.4)[a]
ATG-1	Serpentine	-81.4
USGS 57	Biotite	-91.5
BuD 96014	Biotite	-158.4
Serp-HS-1	Serpentine	-135.3
WS-1	Serpentine	-162.4
Gy-Ajax	Gypsum	-
Gy-HS-1	Gypsum	-
BB42	Illite-chlorite in rock pulp	-
H_2O – 0.5 µL silver capsules		
VSMOW	Water	0.0
USGS W 62001	Water	-41.1
USGS W 32615	Water	-60.0
USGS 47	Water	-150.2
GISP	Water	-189.7
H_2O – pulses via WVISS		
USGS W 67400	Water	1.2
Waikato Distilled	Water	-52.8
LGR #3A	Water	-96.4
USGS 43156	Water	-112.8

[a] The original offline IRMS value of NBS 30 is -65.7 ‰ (IAEA Reference Sheet: NBS-30). The updated value by TC/EA-IRMS is -53.4 ‰ (Qi et al., 2017)

3.2.2 Operation

Mineral powders were weighed into 5×9 mm silver foil capsules in sets of 3 to 7 replicates. Water standards were introduced in either crimped silver capillary tubes, or as pulses delivered from the LGR manufactured Water Vapor Isotope Standard Source (WVISS) to the reaction column. Prior to analyses, powders were dried at 190 °C for 5 hours, in a vacuum oven. To limit uptake of water after drying, samples were transferred from the vacuum oven to the autosampler in heated metal trays, with a total exposure time to open air of 3 minutes or less. Up to 49 capsules may be loaded at a time, which translates into 7-16 unique samples or standards, accounting for replicates.

A typical analysis session begins with a 4 minute dry air purge of the autosampler, followed by a 3-5 minute stabilization phase in order to achieve a background water vapour concentration of less than 250 ppmv. During stabilization, dry carrier gas flows through the autosampler, reaction tube, and analyser. Samples are dropped into the quartz column in 140 second intervals. The throughput reported here is comparable to the measurement cycle on a continuous flow IRMS platform. The sample throughput is significantly faster than rates reported for offline LAS measurements of gypsum hydration water (Hodell et al., 2012; Gázquez et al. 2015; Evans et al., 2015; Gázquez et al., 2017), trial measurements of organic compounds by continuous flow OA-ICOS, where samples were dropped at 8 minute intervals (Koehler and Wassenaar, 2012), and recent online CRDS mineral dewatering experiments, involving thermogravimetric analysers (Bauska et al., 2017; Oerter et al., 2017).

Analyses are manifest as discreet peaks over a low background H_2O concentration. Peak maxima for 0.5 μL water pulses liberated from minerals or water capsules were generally between 10,000 and 12,000 ppmv. The response time required for a water vapour pulse to reach the analyser is typically 18 to 22 seconds for liquid waters in silver capillary tubes, and 20 to 30 seconds for mineral powders in silver foil capsules. The maximum water concentration in the OA-ICOS cell is attained during the first 25 seconds following the start of the peak. Recovery from the maximum water vapour concentration down to the baseline occurs more slowly. Water concentrations within the analytical cell are usually within 200 ppmv of the baseline, 70 seconds after the peak maximum. For most analyses, the background vapour concentration between peaks varied by less than 100 ppmv. During standby periods, the entire system is pumped down to 500 mTorr (66.7 Pa), using the internal pump on the analyser, to preserve dry internal conditions.

3.2.3 Data processing – concentration correction

Measurements of isotopologue mixing ratios by OA-ICOS are influenced by the total H_2O vapour concentration in the optical cell. This was assessed, and corrected for, by measuring water standards over a range of concentrations, using the WVISS, as has been done in prior work (Lis et al., 2008; Penna et al., 2012; Koehler and Wassenaar, 2012; Affolter et al., 2014). The WVISS is comprised of a heated

nebulizer spray chamber and a dry air source. The mixing ratio of dry air and vapour from the nebulizer chamber is governed by a mass flow controller, and the pressure setting on the nebulizer spray chamber. Following the principle of identical treatment for samples and standards (Werner and Brand, 2001), the WVISS was run through the autosampler and furnace (Figure 3.1). Conducting reference water vapour through the heated column is advantageous as it provides a tool for rapidly assessing column and transfer line efficiency. Positioning the WVISS upstream of the hot column also allowed for a shorter transfer line to the analyser, which reduced intersample memory.

Concentration dependency of the analyser was assessed by introducing water standards over a range of settings (Figures 3.2-3.3). Water standards are vaporised and diluted with dry air in an LGR manufactured WVISS. Concentration dependency of OA-ICOS isotopologue measurements, termed "HDO bias" in previous work (Koehler and Wassenaar, 2012), is defined as the difference between measured and expected deuterium abundance for a reference water at a given H_2O concentration. For the analyser used in this study, the typical HDO bias correction was applied to water results that spanned 3,000 to 13,500 ppm (Figure 3.3).

The LGR OA-ICOS system provides reliable results over relatively long timeframes. The WVISS bias correction was assessed 7 times in the course of a month (July 2017), and found to be stable during that interval. Isotope bias should be assessed on a monthly basis, or more frequently if significant changes are made to the sample preparation hardware.

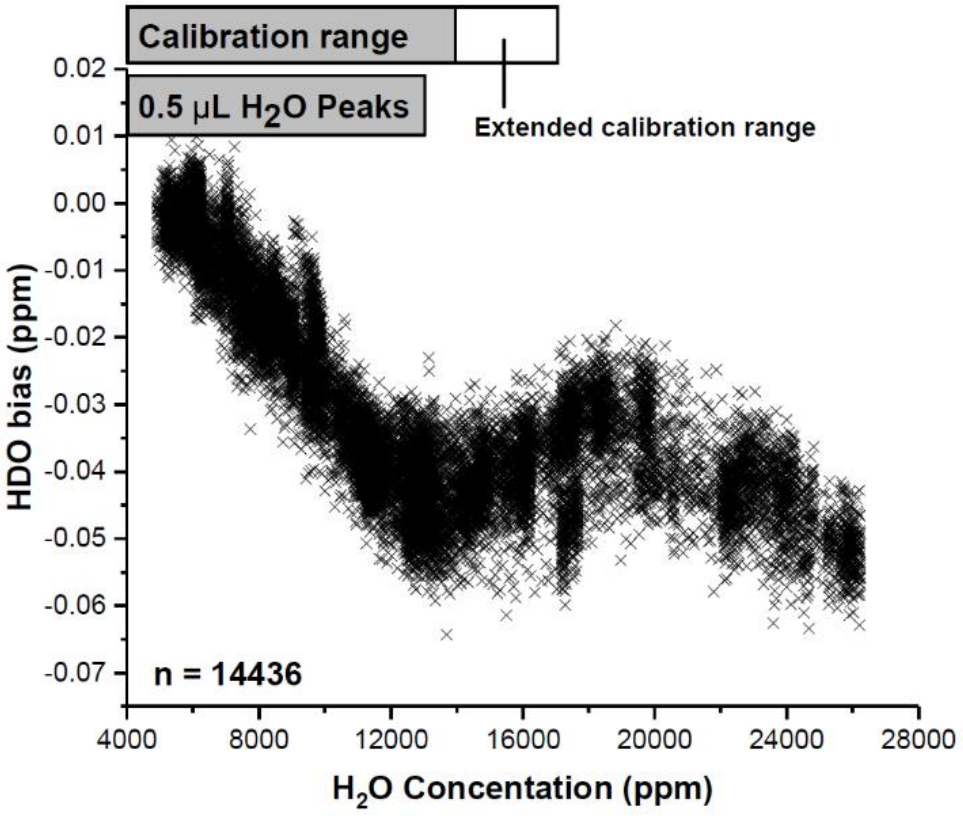

Figure 3.2: composite plot of HDO concentration dependency of the OA-ICOS analyser up to 26,000 ppm. HDO bias is the difference between measured and predicted HDO concentration at a given H_2O concentration. Predicted HDO values are calculated from the $^2H/^1H$ values reported for a given H_2O standard. The plot of bias vs. H_2O concentration shown here was developed from 4 USGS water standards, with δ^2H values of 1.25, -60, -112.8, and -399 ‰, run through the LGR WVISS.

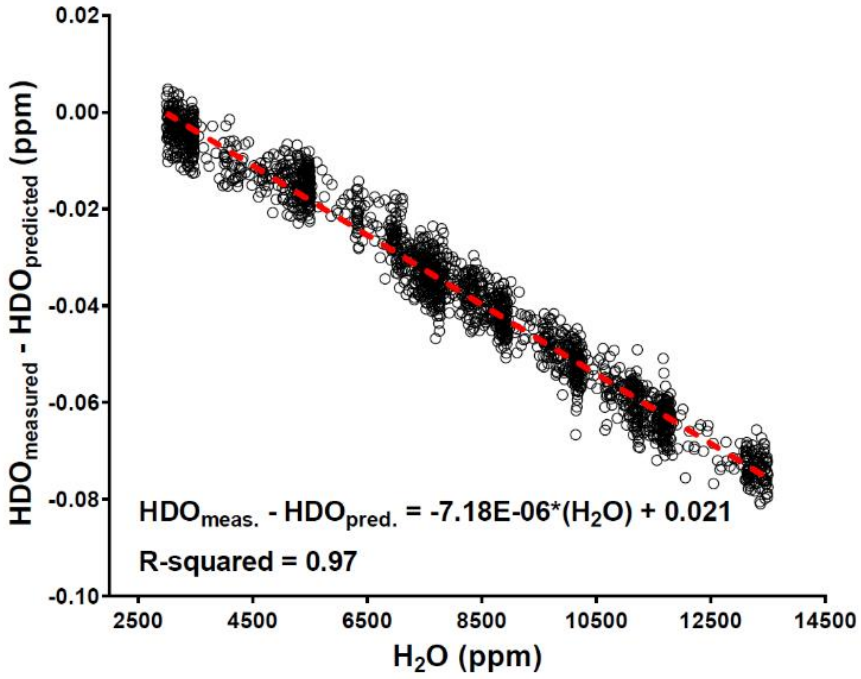

Figure 3.3: typical relationship for H_2O-HDO concentration dependency between 3,000 to 13,500 ppm. Data was collected using a liquid water standard (Waikato Distilled).

3.2.4 Data processing – peak area integration

The continuous flow approach decreases analytical time, but introduces similar challenges to those encountered with continuous flow IRMS. In a typical dewatering sequence, small isotope chromatography effects have been identified due to the more rapid transfer of light isotopologues from the hot column to the analyser (Koehler and Wassenaar, 2012; Affolter et. al., 2014). Consequently, the apparent $^2H/^1H$ value of a vapour pulse is initially lower than its reported value for a given material (Figure 3.4). As the peak progresses, the $^2H/^1H$ ratio increases. Chromatographic effects are overcome by calculating a composite $^2H/^1H$ ratio, which is comprised of the integrated areas beneath isotopologue peaks for HDO and $H_2{}^{16}O$.

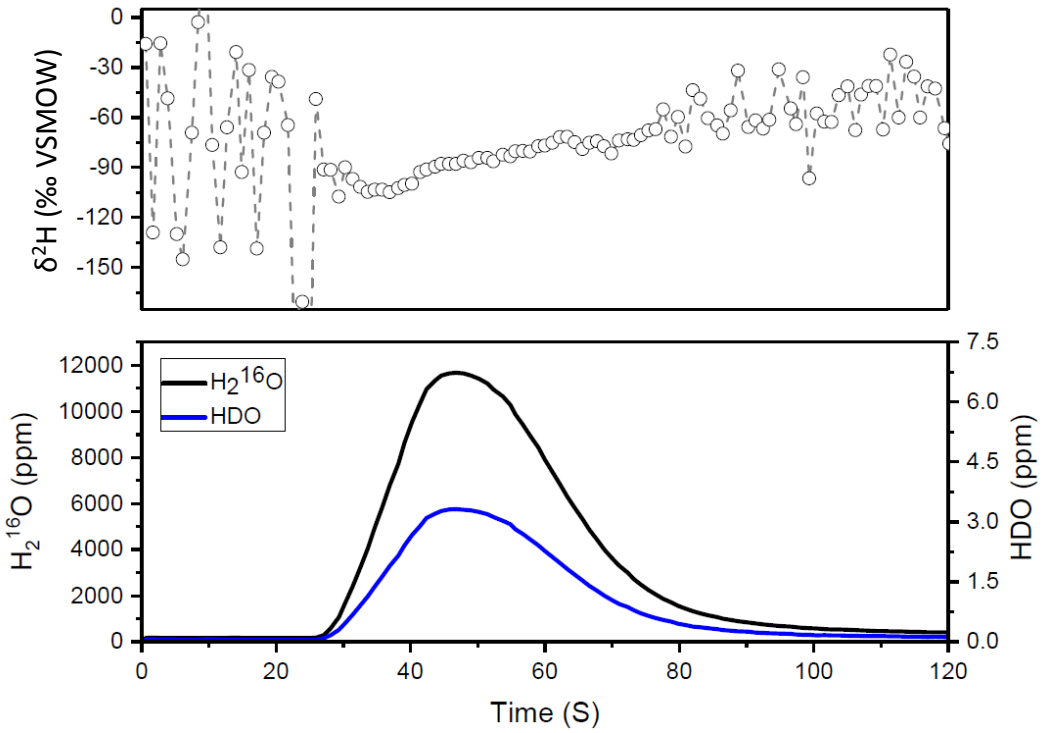

Figure 3.4: plot of instantaneous δ^2H values with respect to water concentration in the optical cavity for a single vapour pulse generated from serpentine (ATG-1). Hydrogen isotopes are more ^2H depleted at the onset of the water peak, but trend towards more enriched values as the peak progresses, owing to small chromatographic effects, which delay the arrival of heavier isotopologues. Peak areas are integrated in order to calculate isotope ratios for samples.

Isotopologue peak areas were integrated in order to calculate composite isotope ratios ($^2H/^1H$) for samples. Two peak integration methods are compared in Figure 3.5. In method 1, peaks are defined via a concentration trigger, with no background correction (Figure 3.5, left panel). 3,000 ppm H_2O was selected as a concentration threshold because the OA-ICOS analyser does not precisely measure rare isotopologues (i.e. HDO) at lower water vapour concentrations. In the second integration approach (Figure 3.5, right panel), peaks were integrated across 120 second time windows, with baseline values subtracted. The 120 second period spans 30 seconds before and 90 seconds after maxima. The ratio of processed peak areas for HDO and $H_2{}^{16}O$ was applied to calculate sample $^2H/^1H$ values. Processed data using both peak integration approaches is presented in Figure 3.5. The VSMOW calibration relationship was similar for either approach.

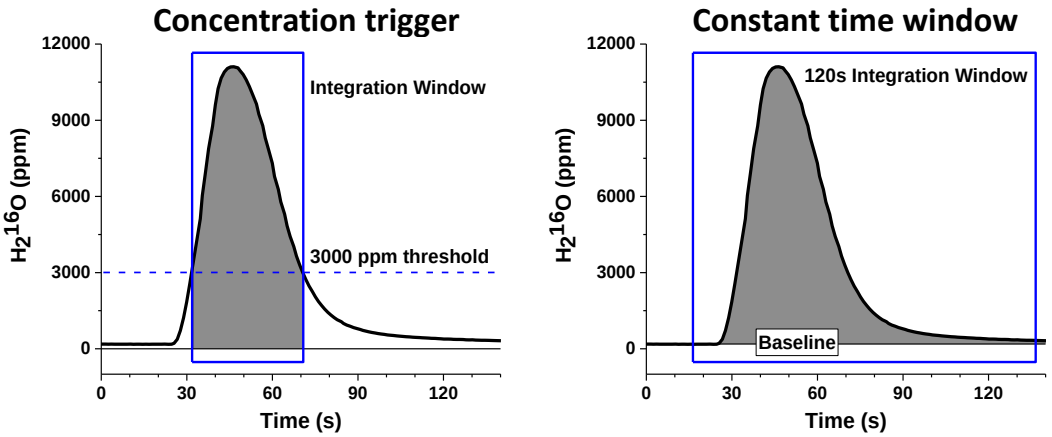

Figure 3.5: integration was carried using a 3,000 ppm concentration trigger, and no baseline (left panel), or across a 120 second fixed window above a baseline value (right panel). The Peak Analyzer tool in OriginPro® was used to process HDO bias corrected isotopologue data. The baseline in the right panel was defined using an asymmetric least squares relationship in OriginPro®. Excel tables used for standard peak processing and calculation of HDO concentration are provided in the digital appendix.

The ratio of processed peak areas for HDO and $H_2{}^{16}O$ was applied to calculate sample $^2H/^1H$ values, as has been done elsewhere for water isotope measurements by continuous flow LAS (Koehler and Wassenaar, 2012; Affolter et al., 2014; Bauska et al., 2017). Here, the trapezoidal method for peak integration was applied to HDO and $H_2{}^{16}O$ isotopologue data. Integration was carried out using the Peak Analyzer tool in the OriginPro® software package. Peaks were defined via a concentration trigger, with no background correction. A concentration threshold of 3,000 ppm H_2O was selected because the OA-ICOS analyser does not precisely measure rare isotopologues (i.e. HDO) at lower water vapour concentrations (Koehler and Wassenaar, 2012). Alternative peak processing that included baseline correction (Figure 3.5, right panel), were also carried out, but determined to be unnecessary, as demonstrated by the close agreement of data generated using either approach for a series of mineral sample measurements, shown in Figure 3.6.

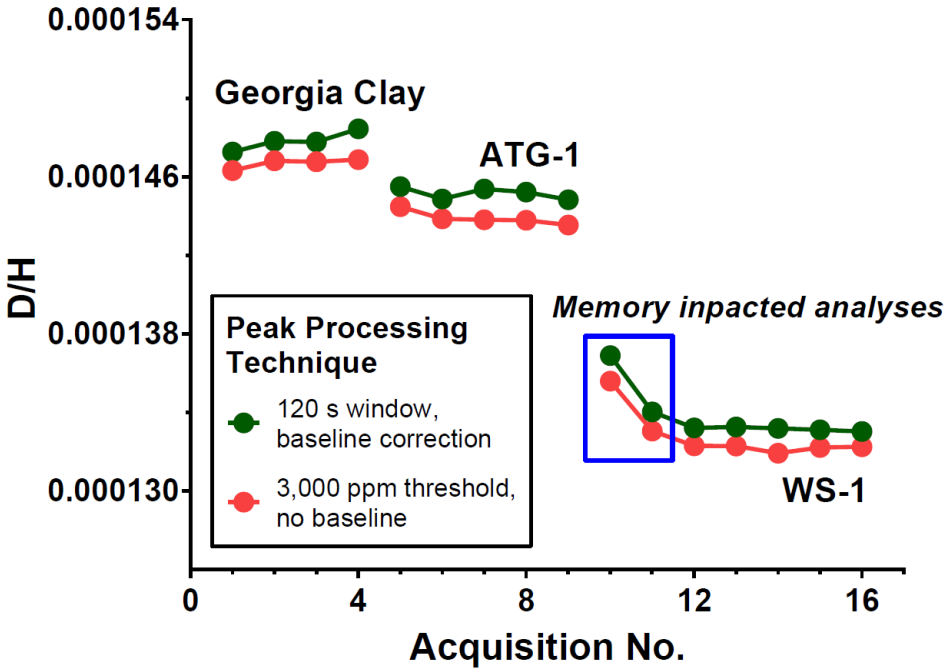

Figure 3.6: hydrogen isotope ratios calculated using two peak integration approaches for kaolinite (Georgia Clay) and serpentine (ATG-1, WS-1). HDO and H216O peak areas were determined using either a time window and baseline, or 3,000 ppm concentration threshold, without baseline. Intersample memory impacts the first 1-2 replicates for analyses of WS-1. Isotope results are similar using either data processing approach.

For a set of analyses of a given material, the first 1-2 replicates are often discarded due to memory effects imposed by the previous standard or sample. The latter hydrogen isotope measurements, not impacted by intersample memory, are averaged. For comparison, up to 10 analyses are rejected due to memory for isotopic measurements of liquid waters using laser spectroscopy (e.g. Penna et al., 2012). A supplemental description of memory effects associated with the hydrous mineral method developed here is provided in Appendix A. Analytical uncertainty is calculated as 1 standard deviation of the mean (1σ) of a group of averaged replicate measurements. To account for VSMOW scale compression, raw hydrogen isotope values ($^2H/^1H$) were calibrated to the VSMOW scale using linear transfer functions generated from standards measured by IRMS in the general form: $\delta^2H_{expected} = {}^2H/^1H_{measured} \times slope + intercept$. Slopes and intercepts of regressions were calculated with 95% confidence intervals in GraphPad Prism® statistical software. Calibration lines were subjected to ANOVA testing. The similarity of calibration regression slopes generated from different types of reference materials was then

tested in Prism using a technique similar to ANCOVA. Calibration lines were compared using a two tailed P-value, which tested the null hypothesis that the slopes were equal.

3.3 RESULTS AND DISCUSSION

3.3.1 Precision

Results for mineral and water standards are presented in Table 3.2. Mineral analyses, excluding biotite, are accurate within 1.2 ‰ of IRMS-measured δ^2H values, on average. Reference water vapour pulses delivered to the analyser via the tube furnace exhibit average accuracy of within 1.7 ‰ of established values. Biotite results, were enriched for deuterium, relative to established values. Excluding biotite, the average precision of OA-ICOS measurements across all material types reported in Table 3.2 is 1.1 ‰. Kaolinite, muscovite, serpentine, sericite, gypsum, and talc were measured at average precisions ranging from 0.4 to 2.2 ‰, while the analytical uncertainty of biotite ranged from 2.1 to 3.7 ‰. The average uncertainty for analyses of water standards is 0.8 ‰. The precision and accuracy of analyses reported here, mark a significant improvement for rapid LAS measurements of hydrogen extracted from solid compounds, with routine precisions comparable to continuous flow IRMS. IRMS labs typically measure δ^2H in hydrous solids with uncertainties of 2 ‰, or better (Vennemann and O'Neil, 1993; Sharp et al., 2001; Qi et al., 2017). In comparison, 5 measurements of organic materials and gypsum in an earlier proof of concept OA-ICOS paper were reported with 1σ uncertainties ranging from 2 to 5 ‰ (Koehler and Wassenaar, 2012).

Table 3.2: Analytical results for hydrous minerals and small volumes of water

Standard	IRMS value	OA-ICOS δ^2H result	1σ	Run time	Calibration standards
Serpentine					
Serp-HS-1	-135.3	-134.3	1.6	140 s	WS-1, G-18502
WS-1	-162.4	-160.6	1.0	140 s	ATG-1, USGS 58
Kaolinite					
Kga-1b	-50.5	-49.7	0.7	140 s	WS-1, G-18502
	-50.5	-51.9	1.9	140 s	ATG-1, USGS 58
	-50.5	-50.8	1.0	140 s	WS-1, G-18502
	-50.5	-50.2	2.2	140 s	WS-1, G-18502
Georgia Clay	-59.0	-58.0	1.5	360 s	ATG-1, USGS 58
	-59.0	-60.4	0.4	140 s	ATG-1, USGS 58
Muscovite					
G-18502	-23.8	-27.5	0.9	140 s	ATG-1, USGS 58
G-18499	-51.1	-49.9	0.4	140 s	ATG-1, USGS 58
	-51.1	-51.4	1.7	140 s	WS-1, G-18502
Sericite					
Misasa	-59.1	-57.5	1.6	360 s	ATG-1, USGS 58
Biotite					
NBS 30	-53.4	-52.3	2.1	360 s	ATG-1, USGS 58
USGS 57	-91.5	-82.8	3.3	360 s	ATG-1, USGS 58
BuD96014	-158.4	-148.0	3.7	360 s	ATG-1, USGS 58
Talc					
Talc-1	-41.6	-44.1	1.2	720 s	Waikato Distilled
	-41.6	-40.0	1.9	720 s	Waikato Distilled
Gypsum					
Gy-Ajax	-	-62.7	1.3	360 s	ATG-1, USGS 58
Gy-HS-1	-	-114.5	1.2	360 s	ATG-1, USGS 58
VSMOW	0.0	-2.7	0.3	360 s	W 32615, USGS 47
W 62001	-41.1	-40.7	1.0	360 s	VSMOW, USGS 47
W 32615	-60.0	-60.6	1.0	360 s	VSMOW, USGS 47
	-60.0	-61.9	1.0	360 s	VSMOW, USGS 47
GISP	-189.5	-191.5	1.0	360 s	W 32615, USGS 47
Waikato Distilled	-52.8	-50.0	0.6	180 s	W 67400, W 43156
LGR #3A	-96.4	-95.2	0.6	180 s	W 67400, W 43156

[a] The original offline IRMS value of NBS 30 is -65.7 ‰. The updated value by TC/EA-IRMS is -53.4 ‰ (Qi et al., 2017)

3.3.2 Routine calibration

A representative VSMOW scale calibration for minerals ($\delta^2H_{expected}$ = slope × $^2H/^1H_{measured}$ + intercept) analysed by OA-ICOS is presented in Figure 3.7. Calibration relationships developed using water standards are presented in Figure 3.8. The calibration for minerals (Figure 3.7) was not statistically different from water standards introduced as pulses from the WVISS during the same timeframe (P=0.61). The calibration equation for water standards introduced to the furnace in silver crimped silver capillary tubes generally differed with a steeper slope and lower intercept, relative to both minerals and waters introduced as vapour pulses.

In a series of measurements that included both silver tube water and mineral standards, the slope of the regression defined by minerals ($\delta^2H_{expected}$ = 6738691 ± 98772 × $^2H/^1H_{measured}$ – 1041 ± 14) was statistically different (P<0.001) from the line defined by water capsules ($\delta^2H_{expected}$ = 7607035 ± 47476 × $^2H/^1H_{measured}$ – 1164 ± 7). This offset in calibration translates into a decrease in accuracy of ~3 ‰, when minerals are calibrated using silver tube water standards, or vice versa. In general, material specific calibrations were consistent over relatively lengthy periods of time. After a dehydration column was replaced in July 2017, minerals analysed on separate days also had statistically similar (p=0.121) VSMOW-scale calibration slopes, ranging from 6827418 to 7047573.

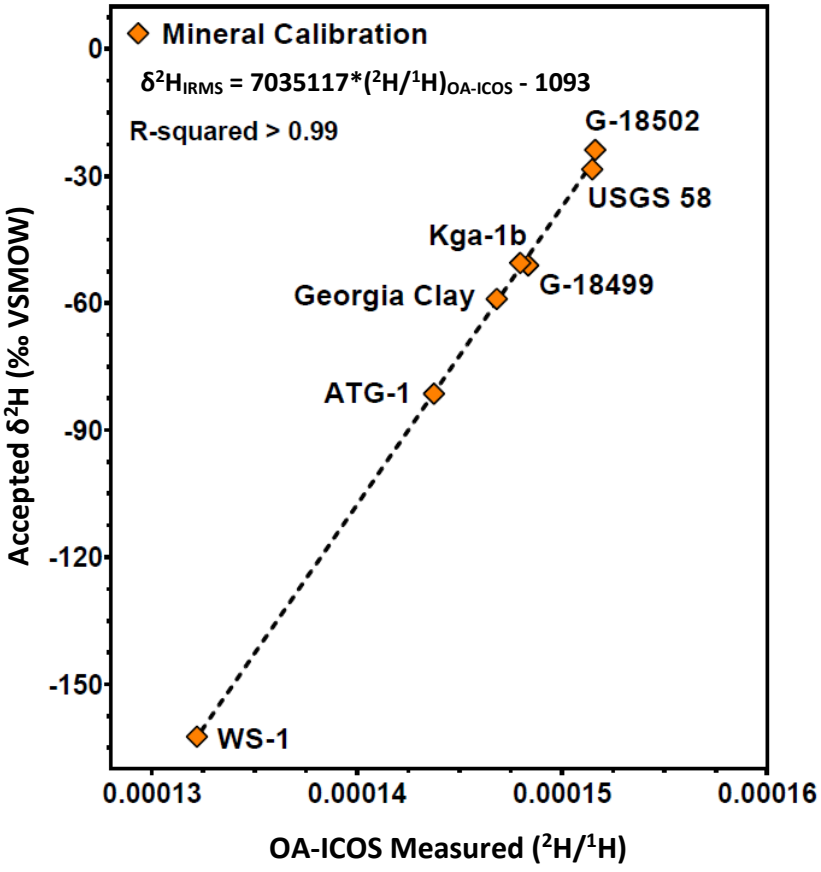

Figure 3.7: representative calibration line for hydrous minerals measured by OA-ICOS. The calibration relationship displayed includes serpentine (WS-1, ATG-1), kaolinite (Georgia Clay, Kga-1b), and muscovite (G-18499, USGS 58, G-18502). A highly linear calibration relationship for H_2O liberated from these minerals indicates that these materials may be used interchangeably.

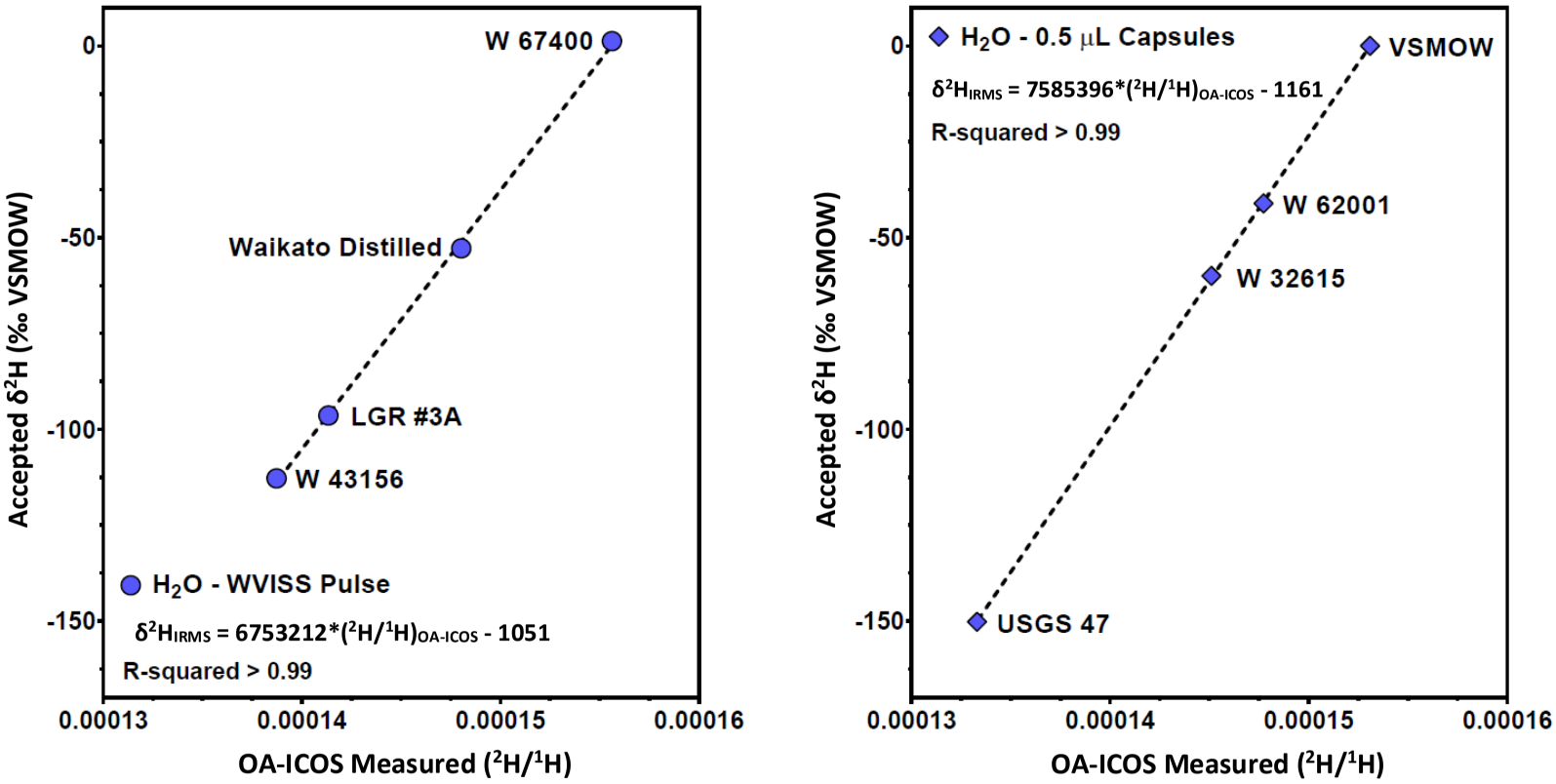

Figure 3.8: representative calibration lines for water isotope standards. Waters were introduced into the reaction column either as pulses from the WVISS (left panel), or in sealed silver capillary tubes (right panel). A small matrix effect associated with water capsules in sealed tubes results in a steeper calibration line (right panel). The relationship for water pulses from the WVISS is similar to mineral-based calibrations.

Operators wishing to calibrate phyllosilicates with reference waters should introduce vapour pulses through the furnace, using the WVISS unit, or comparable vaporization hardware. A one point standardization procedure, developed using the WVISS, provided δ^2H calibration that was accurate to within 2.3 ‰ of values measured externally by IRMS, for analyses of minerals with values ranging from -23.8 to -81.4 ‰. However, moderate scale compression was observed for materials significantly outside this range, highlighting the need for two point calibration lines (Figure 3.8) in most applications.

Although less accurate for calibrating minerals, crimped silver tube waters provide a means to analyse high salinity fluid samples. The tube furnace used in this study is less susceptible to salt blockage than septa-based injection systems (Skrzypek and Ford, 2014), and nebulizer units (i.e. WVISS). In the experimental setup used here, 1-2 μL of brine, introduced in crimped silver tubes, may be analysed in ~5-15 minutes, depending upon the number of replicates desired.

3.3.3 Recommendations for analysing biotite and other Fe-bearing minerals

Biotite minerals were measured at lower precision and accuracy relative to other results reported here. The OA-ICOS δ^2H result for NBS 30 of -52.3 ‰, is significantly more positive than the offline IRMS value of -65.7 ‰ (IAEA Reference Sheet for International Measurement Standards: NBS-30). This finding, in which OA-ICOS results indicate a more deuterium-enriched hydrogen isotope ratio than corresponding offline IRMS measurements (Figure 3.9), has previously been documented for continuous flow IRMS systems (Qi et al., 2014). In a recent compilation of analyses of NBS 30 by six TC/EA IRMS labs, the average value was -53.4 ‰ (Qi et al., 2017), which is comparable to the OA-ICOS value reported here.

Although the causes of positive δ^2H anomalies in measurements of biotite by OA-ICOS are not definitively known, it has been postulated that in hot continuous flow extractions, high-Fe biotite (e.g. NBS 30) can impede analyte transfer (Qi et al., 2014; Qi et al., 2017). With TC/EA systems, full conversion from H_2O to H_2 is inhibited by the formation of ^2H depleted metal hydrides (Qi et al., 2014), which impose a deuterium-enriched signature on the analyte hydrogen gas. While we do not rule out metal hydride formation in our analytical setup, we also propose

oxidation of Fe by H_2O (i.e. reduction of H_2O to H_2) as a potential cause for unexpectedly high δ^2H measurements in biotite, relative to established IRMS values (Richet et al., 1977; Simon et al., 2011). In a set of heating experiments, the δ^2H signature of water released from NBS 30 at temperatures between 973 and 1073 °C, ranged from -25 to -51 ‰, while δ^2H of by-product H_2 gas ranged from -218 to -256 ‰ (Simon et al., 2011). Any H_2 gas generated by reduction of H_2O in the presence Fe is effectively lost in the OA-ICOS method because the analyte measured is water vapour.

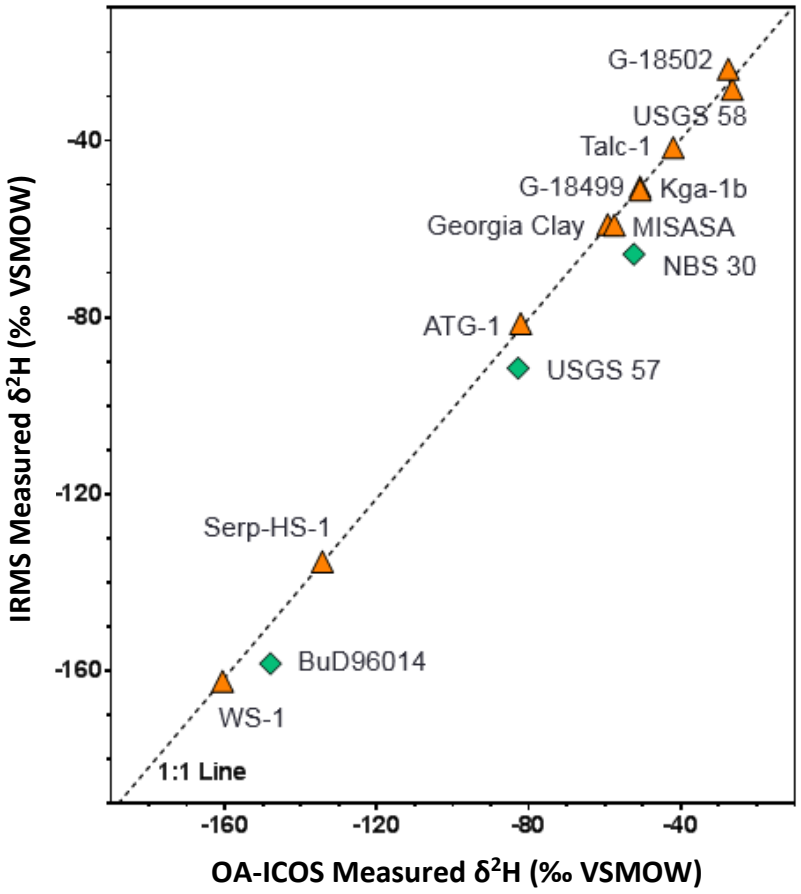

Figure 3.9: long term aggregate calibrations of hydrous minerals measured by both OA-ICOS and IRMS. Note that for serpentine (WS-1, Serp-HS-1, ATG-1), kaolinite (Kga-1b, Georgia Clay), Muscovite (USGS 58, G-18502, G-18499), and talc (Talc-1), results for both IRMS and OA-ICOS are similar. Biotite samples (green diamonds), which contain variable amounts of Fe, are shifted to the right of the 1:1 line of equal calibration by up to 12 ‰.

Remnant Fe compounds in the reaction column may impose a reducing effect during several subsequent analyses. This occurred when a sericite (MISASA) was measured following NBS 30 (Figure 3.10). We analysed the sericite standard 7

times. During the first 4 analyses, the memory effect from NBS 30 was discernible. Results of the final three analyses of MISASA were similar to IRMS values. We report a mean of -57.5 ± 1.6 ‰, which is comparable to reported IRMS values, which range from -56.0 to -59.1 ‰ (Zhang et al., 2000).

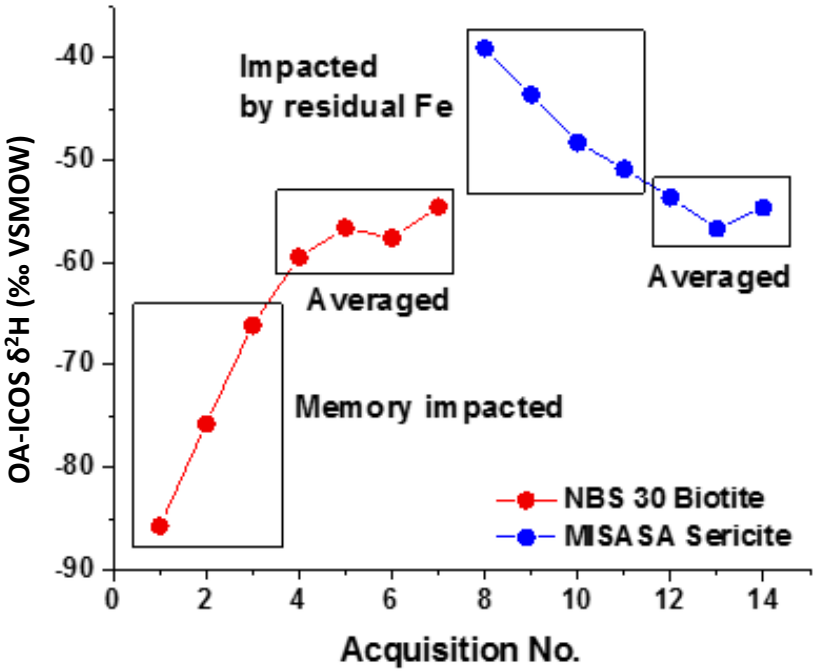

Figure 3.10: analytical sequence of biotite (NBS-30) followed by sericite (MISASA). The first three analyses of NBS-30 are impacted by water vapour memory imposed by a previous sample. The first three measurements of sericite exhibit a positive isotope bias due to remnant Fe from biotite in the high temperature dehydration column. Water vapour memory effects were reduced by heating transfer lines and filters in subsequent work. Interference imposed by iron containing samples may be mitigated by inclusion of copper oxide packing in the dehydration column.

Complications associated with fractionation during mineral dehydration appear to be restricted to biotite. This is an issue that will collectively need to be addressed by users wishing to measure biotite and other Fe-rich minerals using online high temperature dehydration systems coupled with LAS units. Crushing biotite, and other iron-bearing samples to smaller grain sizes has been demonstrated to increase accuracy with TC/EA analyses (Qi et al., 2014; Qi et al., 2017). With continuous flow OA-ICOS, finer mineral powders may facilitate more rapid dehydration, minimizing fractionation in the hot column. Incorporating an oxidant into column

packing (e.g. CuO), may also minimize reduction of waters evolved from high Fe samples. Memory associated with remnant Fe can be eliminated by cleaning the quartz liner in the dehydration column after biotite analyses.

3.3.4 Sample mass requirements

A yield function was developed by analysing a kaolinite standard (Kga-1b), over a range of masses. Kga-1b has an established water content of 13.7 % (Pruett and Webb, 1993). Mineral water content, calculated from dry mineral mass, correlated linearly with H_2O peak area for aliquots of kaolinite between 1.80 to 4.80 mg (Figure 3.11, left panel). This range corresponds with sample water volumes between 0.25 and 0.66 µL H_2O.

Precise and accurate δ^2H measurements were recorded for water concentrations from 0.25 to 0.55 µL (Figure 3.11, right panel). This range of water volumes correlates with H_2O peak maxima in the OA-ICOS analyser between 6,305 and 14,094 ppmv. The 0.66 µL (4.8 mg) kaolinite analysis in Figure 3.11 generated a peak water concentration of 16,870 ppmv. This peak is significantly above the concentration correction range for this study, which spanned from 3,000 to 13,500 ppmv (SI). Although mineral powders were typically analysed at masses equivalent to 0.4 to 0.5 µL H_2O, the yield test presented here indicates that routine analyses can be performed using as little as 0.25 µL H_2O. Accurate concentration correction should be possible for smaller peaks between 3,000 and 6,000 ppmv, which coincide with water pulses of ~0.1 to 0.2 µL.

3.3.5 Sample drying tests

Effective removal of adsorbed and interlayer water in clays is a necessary treatment step prior to analysing the hydrogen isotope signature of structural hydroxyl (VanDeVelde et al., 2013; Bauer and Vennemann, 2014; Lonero, 2017). The efficacy of drying techniques for hydrogen isotope analyses of clays is a topic of ongoing discussion in the isotope geochemistry community (VanDeVelde et al., 2013; Bauer and Vennemann, 2014). Here, two drying approaches were compared for serpentine (WS-1), muscovite (G-18502), kaolinite (Kga-1b), and a crushed whole rock sample (BB42) from the Martha Gold Mine, Waihi, NZ (Table 3.3). The

crushed sample is from an interval of drill core, containing illite and smectite clays. In the first approach, materials were dried at 110 °C in a conventional oven for 24 hours. In approach 2, samples powders were dried at 190 °C in a vacuum oven for 5 hours (VanDeVelde et al., 2013). The yield function in Figure 3.11 was used to calculate the mineral structural water weight percent for these tests.

For muscovite, kaolinite, and serpentine, water content varied by 0.3 weight percent, or less, from established mineral values, regardless of drying treatment. However, for the powdered whole rock sample (BB42), the drying approach significantly impacted results. For BB42, drying for 24 hours at 110 °C in a conventional oven resulted in a 53 percent decrease in H_2O yield. Vacuum oven treatment resulted in a 57 percent decrease in H_2O yield, and provides a more rapid preparation approach that effectively minimizes the interference of interlayer and adsorbed water upon the isotopic signal of hydroxyl.

3.3.6 Column temperature

The broadness of peaks, expressed as a ratio of area / height (Table 3.3), correlated with established mineral thermal dehydration curves (Nutting, 1943). For kaolinite, serpentine, and the illite-smectite rock powder (BB42), peak dimensions were similar. These materials typically undergo full dehydration below 700 °C. Peaks for muscovite, and other micas, are characteristically broader than the clays assessed. For muscovite, the majority of weight loss occurs above 500 °C (Nutting, 1943). While it was possible to analyse muscovite at 140 second intervals, talc samples dehydrated more slowly, and were analysed at 12 minute intervals to allow for water concentrations in the analyser to return to a low baseline. Normal talc retains hydroxyl up to 730 °C, and dehydration continues up to 930 °C (Nutting, 1943).

Table 3.3: Assessment of mineral drying techniques

Mineral	Treatment	H_2O (wt. %)	1σ	H_2O Area (ppmv×s)	H_2O Max (ppmv)	Area / Height	$^2H/^1H$ (×1E-04)
WS-1 (serpentine)	No drying	12.4	0.2	299003	11186	26.7	1.325
H_2O = 12.2 %[a]	24 hrs at 110 °C	12.2	0.5	290967	10883	26.7	1.314
	5 hrs at 190 °C, vacuum	12.1	0.2	282312	10594	26.6	1.320
Kga-1b (kaolinite)	No drying	13.7	0.2	329589	12208	27.0	1.471
H_2O = 13.7 %[b]	24 hrs at 110 °C	13.4	0.2	317902	11819	26.9	1.472
	5 hrs at 190 °C, vacuum	13.7	0.4	323548	11944	27.1	1.476
BB42 (crushed rock)	No drying	11.5	0.3	480021	17047	28.2	1.472
illite / smectite	24 hrs at 110 °C	5.4	0.1	256436	9507	27.0	1.427
	5 hrs at 190 °C, vacuum	4.9	0.7	233691	8720	26.8	1.441
G-18502 (musco-vite)	No drying	-	-	391854	11610	33.8	1.523
H_2O = 4.3 %[a]	24 hrs at 110 °C	4.1	0.0	382672	10989	34.8	1.518
	5 hrs at 190 °C, vacuum	4.2	0.0	399230	11563	34.5	1.518

[a] Calculated from TC/EA results, University of Otago
[b] Pruett and Webb, 1993

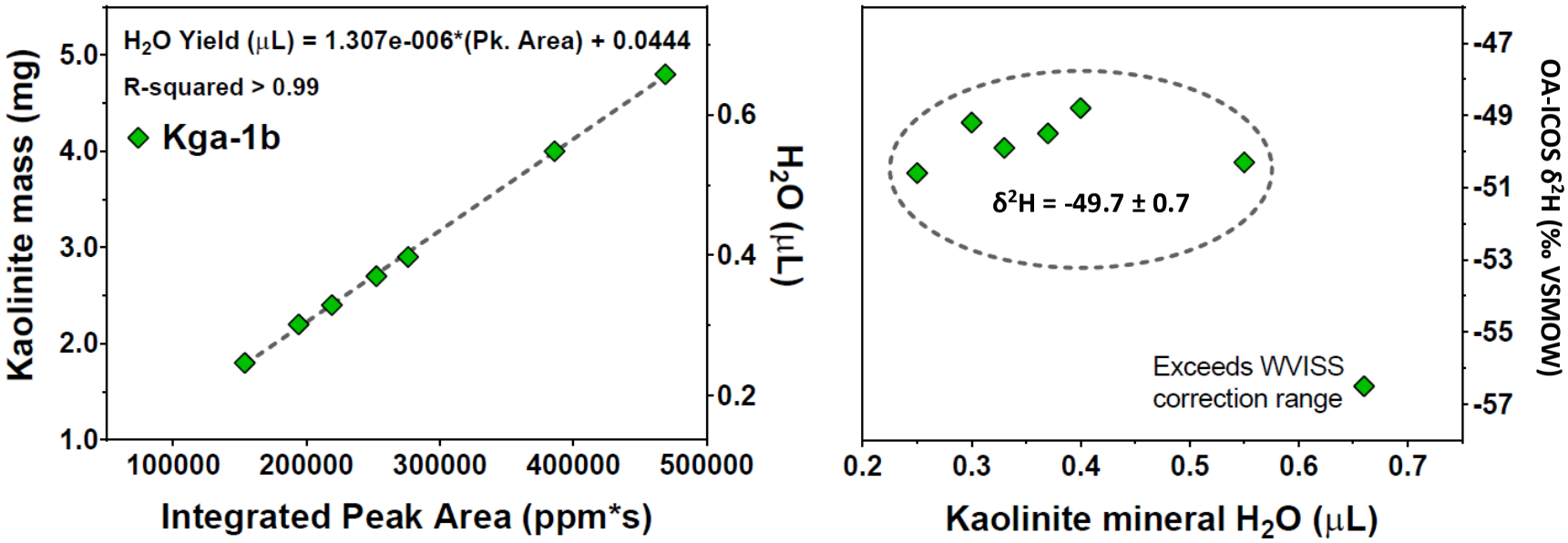

Figure 3.11: Left panel: yield relative to integrated peak area for the Kga-1b kaolinite standard. A linear relationship facilities calculation of H_2O content in samples. Right panel: the relationship between sample water content and hydrogen isotope ratio for the Kga-1b kaolinite standard (δ^2H_{IRMS} = -50.5 ‰). Accurate results were obtained for analyses across a range of water volumes evolved from kaolinite. The highest value is above the WVISS concentration correction range. Kga-1b yield standards were dried for 5 hours at 190 °C in a vacuum oven.

The analyses presented in this work were conducted between 950 and 1000 °C, but the column temperature should be adjusted to suit the analytical needs of the user. For measurements of muscovite, biotite, and talc, a hotter column may be desirable in order to achieve more rapid water extraction. During the course of the study, sulphur compounds condensed at the base of the column and at the first inline filter, where temperatures were below 150 °C. The sulphur is sourced from hydrothermal rock powders (i.e. BB42, Table 3.3), and anhydrite, which accumulated in the column during gypsum analyses. Although thermal decomposition of sulphate in anhydrite is not predicted to occur at 1000 °C, the reaction can proceed at lower temperatures in the presence of additives, including silica and kaolinite (Swift et al., 1976). The quartz column, liner, and silica wool packing may have enabled this. For many clays, and hydrous sulphates, operating at temperatures below 900 °C may be advantageous.

3.4 CONCLUSIONS

In this work, OA-ICOS is demonstrated as a rapid means to measure hydrogen isotope values in minerals. The setup tested here successfully measured water liberated from phyllosilicate and hydrous sulphate minerals at volumes as low as 0.25 μL, at greater precision and speed than has been reported previously for continuous flow LAS measurement of gypsum hydration water (Koehler and Wassenaar, 2012). High precision was maintained, while carrying out measurements at 140 second intervals, at an effective rate of 6 samples in an hour, including replicates. This throughput is comparable to, or slightly faster, than modern TC/EA IRMS systems. The analytical setup also provides a straightforward means to analyse high salinity fluids, encased in crimped silver tubes (e.g. Qi et al., 2010). When compared with IRMS, and recent continuous flow CRDS-based work (Bauska et al., 2017), the hardware configuration, calibration, and maintenance times are significantly shorter for the OA-ICOS protocol outlined here. The methodology presented here is also less expensive than IRMS, and may be implemented for less than $100,000 USD at list prices for the analytical instrumentation, preparation line, and data processing software. Ultimately, because the hardware is straightforward to maintain, and operation costs are low, this method should allow more individuals and institutions to measure hydrogen isotope

ratios in minerals and bulk geologic samples. In particular, assessment of hydrogen isotope signals in minerals is of interest in the mining and geothermal industries, yet is infrequently utilized outside of academic venues due to the cost and time associated with analyses.

Chapter IV

Measuring hydrogen and oxygen isotopic signals in ore deposits using thermal dehydroxylation OA-ICOS: results from the Comstock Lode, USA

This chapter presents a new analytical method for measuring the oxygen isotope ratio in hydrous minerals using thermal dehydroxylation OA-ICOS. Isotope measurements (δ^2H, $\delta^{18}O$) were made using a laser absorption spectroscopy platform operated with nitrogen carrier gas. In this work, oxygen isotopes are measured on microvolumes of water, gypsum, and clay minerals. The application potential of the method is tested by measurement of δ^2H and $\delta^{18}O$ in altered andesite from the Comstock Ag-Au deposit, Nevada, USA. Comstock materials are from the historically significant Becker Collection, which was sampled in 1882 in preparation of USGS Monograph 3. Access to the Becker Collection was possible through cooperation with Erik Melchiorre (California State University, San Bernardino). This work is unpublished.

Geology of the Comstock lode and the Washoe district
USGS Monograph 3: George Becker, 1882

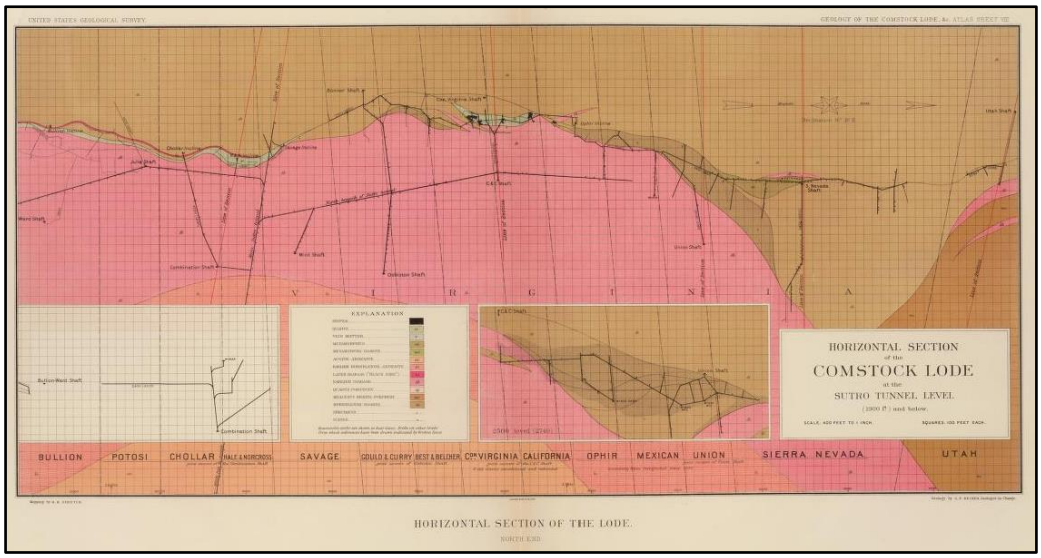

mapsofthepast.com

ABSTRACT

The hydrogen and oxygen isotopic values of hydrous minerals are sensitive to the fluids in the systems in which they form. Here, an OA-ICOS system operated with nitrogen carrier gas is described that is capable of simultaneous measurement of δ^2H and $\delta^{18}O$ in water vapour pulses liberated from clays and gypsum. Hydroxyl oxygen isotope values (i.e. $\delta^{18}O_{OH}$) in kaolinite, muscovite, and serpentine were measured at typical precisions of 0.2 to 2.0 ‰. An internal OH to Si-O fractionation of 1.0149 was determined for a weathering-derived kaolinite (Kga-1b, Macon, Georgia, USA). To exemplify application potential in hydrothermal settings, whole rock powders from the Comstock Lode Ag-Au epithermal deposit (Nevada, USA) were measured. Oxygen isotopes ($\delta^{18}O$) in H_2O extracted from Comstock samples ranges from -6.1 to 7.1 ‰. This range is similar to prior whole rock fluorination results (-3.0 to 6.7 ‰). Comstock whole rock δ^2H results are between -126 and -160 ‰. Taking mineral-water fractionation into account, Comstock δ^2H values are consistent with alteration by meteoric-derived H_2O that has undergone minimal hydrogen isotopic exchange. Spectral interferences on the OA-ICOS system were more common when using nitrogen as a carrier gas, possibly due to the presence of H_2S, which was generated from whole rock samples containing pyrite. Hardware and data processing solutions to address interference are identified. With improvements in sample processing and gas clean-up, the outlined method should be useful in studies of intramineral oxygen isotope fractionation in hydrous minerals, with the potential to improve understanding of fluid source in hydrothermal areas. The low cost, safety, and simplicity of operation should also make the method attractive for manufacturers and regulatory agencies wishing to use hydrogen and oxygen isotopes to determine the geographic origin of consumer products (e.g. cosmetics and food additives) containing hydrous minerals.

4.1 INTRODUCTION

4.1.1 Background

Hydrogen and oxygen isotopes in hydrous minerals provide insight into fluid history in geologic systems. In particular, clay minerals are generated during weathering and hydrothermal alteration. In hydrothermal investigations, clays provide a measure of alteration intensity, and are isotopically sensitive to fluid sources (e.g. Criss and Taylor, 1983). Isotope values in hydrous minerals have been measured in modern geothermal fields (Marumo et al., 1980), hydrothermal ore deposits (Taylor, 1974; Criss and Taylor, 1983) and sedimentary basins (Capuano, 1992; Schimmelmann et al., 2006). While a considerable body of work exists interpreting whole mineral oxygen isotope values in phyllosilicates, as determined by fluorination (e.g. Savin, 1967; Sharp, 1990), measurement of hydroxyl water (i.e. $\delta^{18}O_{OH}$) in clays has been limited to several trial studies (e.g. Bechtel and Hoernes, 1990; Girard and Savin, 1996). The OA-ICOS analytical setup developed in Chapter 3 presents a new platform with which to measure $\delta^{18}O_{OH}$ in phyllosilicate minerals.

Oxygen isotope values in hydrous minerals have been determined by either fluorination, partial fluorination, or thermal dehydroxylation. Fluorination involves reaction of sample material with a fluorinating agent (e.g. BrF_5) in order to extract oxygen from Si-O bonds (Clayton and Mayeda, 1963; Sharp, 1990; Girard and Savin, 1996). Methods for extraction were initially slow and required large bulk samples, exceeding 10 mg (e.g. Clayton and Mayeda, 1963). Methodological updates, including laser fluorination (Sharp, 1990), decreased sample requirements and measurement time for geologic materials. The general format for fluorination of kaolinite is given in the following reaction (Girard and Savin, 1996):

$$Al_2Si_2O_5(OH)_4 + 9F_2 \rightarrow 2AlF_3 + 2SiF_4 + 4HF + 4.5O_2 \quad (4.1)$$

The isotopic ratio of the resulting oxygen gas is measured using an IRMS, with some setups requiring conversion to CO_2 prior to measurement (de Groot, 2004).

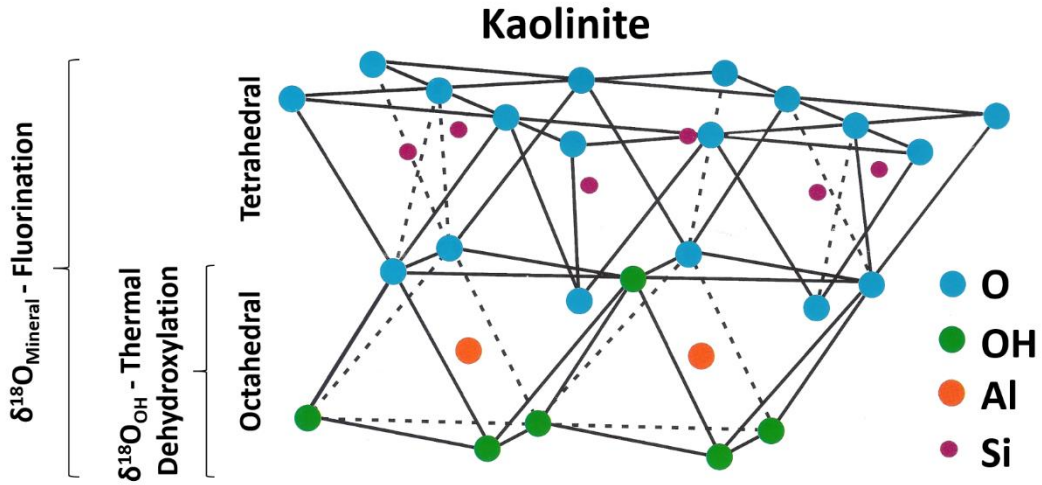

Figure 4.1: oxygen in clay minerals is divided into tetrahedral (Si-O) and octahedral (OH) sites. Kaolinite exhibits the simplest structure, with successive sheets joined together by H-bonds. The majority of historic work has implemented fluorination-based IRMS techniques in order to extract and measure the whole mineral $\delta^{18}O$. In this chapter, $\delta^{18}O_{OH}$ is measured by thermal dehydroxylation OA-ICOS. A body of work indicates that oxygen isotope fractionation between tetrahedral and octahedral sites has potential application as a single mineral isotope thermometer. Figure modified after Grim (1962) and Geatches (2011).

High temperature fluorination approaches provide a measure of bulk $\delta^{18}O$ values in minerals, but cannot resolve differences between oxygen contained in tetrahedral sites and hydroxyl water (Figure 4.1). Oxygen in hydrous silicate minerals (e.g. clays) is divided between tetrahedral (i.e. Si–O–Si, Al–O–Si, Al–O–Al, Si–O–Mg) and octahedral (i.e. OH) sites. Hydrogen is exclusively contained within octahedral group. In clays, the OH component represents a considerable component of the mineral oxygen budget, ranging from 45 % in kaolinite to ~17 % in illite minerals. A limited amount of work has attempted to classify the oxygen isotope fractionation factors for each site using experimental (Savin, 1967; Hamza and Epstein 1980; Bechtel and Hoernes 1990; Girard and Savin, 1996) or computational approaches (Zheng, 1993). To isolate and measure hydroxyl water, partial fluorination (e.g. Savin, 1967; Hamza and Epstein, 1980; Bechtel and Hoernes, 1990) and thermal dehydroxylation were employed (e.g. Bechtel and Hoernes, 1990; Girard and Savin, 1996). These studies were carried out on illite, chlorite, muscovite, biotite, phlogopite, and kaolinite. Partial fluorination reactions are accomplished by reacting an excess of F_2 gas at low temperature (<200 °C). Thermal dehydroxylation involves heating to accomplish destruction of the octahedral site, generating water

vapour by the following reaction (Taylor, 1962):

$$2(OH^-) \rightarrow H_2O_g + O^{2-} \quad (4.2)$$

It should be noted that the thermal dehydroxylation approach generates both H_2O and a free oxygen (Equation 4.2). The comparability of thermal dehydroxylation and partial fluorination measurements have been determined in two studies (Bechtel and Horns, 1990; Girard and Savin, 1996). In some instances partial fluorination resulted in an oxygen excess, indicating partial decomposition of Si-O bonds. Girard and Savin (1996) found that thermal dehydroxylation did not provide consistent results on coarse grained kaolinite samples, but was generally more reliable than partial fluorination. Bechtel and Hoernes (1990) demonstrate that measuring both tetrahedral and OH sites within hydrothermal illite allows for interpretation of the temperature signal and isotope signature of fluid. They note, however, that analyses are impeded in cases in which materials contain appreciable amounts of Fe, which interferes with extraction of OH. They define the following illite-based thermometer:

$$1000\ln\alpha_{\text{illite-OH}} = -0.076t + 30.42 \ (t \text{ in } ^oC) \quad (4.3)$$

Laser Absorption Spectroscopy (LAS) instruments provide new tools for measuring isotope signals in H_2O liberated from hydrous minerals. LAS instruments are now widely used for isotopic measurement of water samples (Lis et al., 2008; Penna et al., 2012), but are not routinely utilised to measure isotopic abundances in hydrous solids (e.g. hydrous minerals, fluid inclusions, organic matter). LAS measurements of oxygen and hydrogen isotopes in gypsum hydration waters were first reported in 2012 (Hodell et al., 2012; Koehler and Wassenaar, 2012). Since that time, Cavity Ringdown Spectroscopy (CRDS) has been applied to measure δ^2H and $\delta^{18}O$ in hydrous sulphates to reconstruct water budgets in several paleoclimate studies (e.g. Hodell et al., 2012; Evans et al., 2015; Gázquez et al., 2017). Two recent CRDS methodology papers employed thermogravimetric analysers to measure δ^2H, $\delta^{18}O$, and $\delta^{17}O$ signals across slowly evolved water peaks from gypsum, kaolinite, goethite and opal (Bauska et al., 2017; Oerter et al., 2017). These techniques have promise for measuring isotopic variation in heterogeneous hydrous samples. However, processing times of up to 90 minutes for clays, render these techniques

less useful for applications in which rapid results are desired, including mineral exploration, and in commercial laboratories that operate on a high throughput basis.

Here, the Off Axis Integrated Cavity Output Spectroscopy (OA-ICOS) mineral dehydroxylation method described in Chapter 3 (i.e. Mering and Barker, 2018) is applied to simultaneously measure hydrogen and oxygen isotopes in hydrous minerals. The approach developed here is inexpensive to implement and is capable of carrying out measurements in under three minutes. However, considerable uncertainties exist with respect to best practice for preparing and routinely measuring mineral separates and bulk geologic samples (such as those produced during mineral exploration, often referred to as assay pulps) using this emerging technique. These are addressed here in a series of tests performed using a Los Gatos Research (LGR) OA-ICOS instrument (San Jose, CA, USA). Testing was carried out on common hydrous minerals, including serpentine, muscovite, kaolinite, and gypsum, which were previously utilised to demonstrate δ^2H measurement potential in Chapter 3 and published work (Mering and Barker, 2018). Subsequently, measurements were carried out on samples from the Comstock Lode Ag deposit in Nevada, USA. A comprehensive discussion of hardware, and best practice for applying hydrous mineral OA-ICOS techniques in hydrothermal ore deposit studies, is provided to enable continued development of this approach.

4.1.2 Sample types

The calibration relationship for a set of water standards was determined, and applied to measure the hydroxyl $\delta^{18}O$ values of the hydrous minerals tested in the previous chapter. A list of the materials evaluated by OA-ICOS in this study is provided in Table 4.1.

The N_2 carrier gas methodology was applied to measure hydrothermal whole rock samples from the Comstock epithermal Ag-Au deposit. The deposit formed during the Miocene from a large meteoric hydrothermal fluid gyre (Criss et al., 2000). Mining during the late nineteenth and early twentieth centuries yielded approximately 200M oz Ag and 8M oz Au (Eaton et al., 1998). Altered andesite whole rock powders of samples collected from Comstock (Becker, 1882) have been measured for $\delta^{18}O$ using standard fluorination techniques (e.g. Criss et al., 2000),

and δ^2H (Vikre, 1989). Oxygen isotope measurements at Comstock indicate distinct zonation, which is thought to be related to the intensity of hydrothermal alteration (e.g. Criss et al., 2000). Here, hydrogen and oxygen isotope signals are measured in 12 propylitically altered andesite whole rock samples with $\delta^{18}O$ fluorination values between -3 and 6.7 ‰ VSMOW.

Table 4.1: Materials measured by thermal dehydration-dehydroxylation OA-ICOS

Name	Type	Locality	Reference
Minerals			
WS-1	Serpentine	Cassiar, BC, CA	Mering and Barker, 2018
Serp-HS-1	Serpentine	Huckleberry Range, WA, USA	Mering and Barker, 2018
Kga-1b	Kaolinite	GA, USA	Mering and Barker, 2018
G-18499	Muscovite	China	Mering and Barker, 2018
G-18502	Muscovite	China	Mering and Barker, 2018
USGS 58	Muscovite	China	Qi et al., 2017
Gy-Ajax	Gypsum	Ajax Chemicals	Mering and Barker, 2018
Becker Collection	Whole rock, altered andesite	Comstock Lode, Ag-Au epithermal	Becker, 1882; Criss et al., 2000
Water standards			
Waikato Distilled	Water	Internal Standard	Mering and Barker, 2018
USGS W-43156	Water	USGS Standard	https://isotopes.usgs.gov/
USGS W-67400	Water	USGS Standard	https://isotopes.usgs.gov/
USGS 47	Water (Ag capsule)	USGS Standard	https://isotopes.usgs.gov/
USGS 48	Water (Ag capsule)	USGS Standard	https://isotopes.usgs.gov/
USGS W-32615	Water (Ag capsule)	USGS Standard	https://isotopes.usgs.gov/
USGS W-62001	Water (Ag capsule)	USGS Standard	https://isotopes.usgs.gov/

4.2 METHODS

In this work, the potential for the OA-ICOS instrument to measure oxygen isotopes in small volumes of water liberated from mineral separates and whole rock powders was tested. Isotopic analyses were conducted using a LGR OA-ICOS instrument

operated in continuous flow mode, and a custom sample preparation line at the University of Waikato, following a modified protocol described in the previous chapter (i.e. Mering and Barker, 2018). Mineral powders are dried in a vacuum oven at 195 °C for 5 hours, following published protocol (Mering and Barker, 2018). Samples are dehydroxylated in a quartz column, maintained at 945 °C. Plugs of quartz wool and silver wool are emplaced at the base of the column to preclude the transit of mineral powder, and sulphur-bearing compounds, into the analyser. A 10-μm filter (Valco Instruments Co., Inc., USA) is installed below the column, upstream of the OA-ICOS unit, to prevent clogging of the internal filter in the analyser. Concentrations of isotopologues are measured in parts per million by volume (ppmv) at 1 Hz. Samples are dropped into the quartz column in 180 second intervals. In order to achieve identical treatment of samples and standards, water peaks from the associated Water Vapor Isotope Standard Source (WVISS) are delivered through the heated quartz column. In the hardware setup operated here, intersample isotope memory between adjacent samples is typically small, requiring no more than 3 replicate measurements to overcome the effect. Heating the sample processing hardware and reductions to the surface area of transfer tubing improved intersample memory (Oerter et al., 2017; Mering and Barker, 2018).

In prior work, it was observed that at high temperature (>550 °C), the oxygen isotope signature of H_2O vapour became equilibrated with ambient O_2, attaining a final $\delta^{18}O$ signature greater than +20 ‰ VSMOW, regardless of starting water oxygen isotope value (Kohler and Wassenaar, 2012). In that work, use of an O_2 free carrier gas (e.g. N_2) was suggested as a potential means analyse $\delta^{18}O$ in H_2O liberated from minerals at high temperature. The H_2O-O_2 exchange relationship in the analytical apparatus used in this study is assessed by flowing atmosphere through the heated column into the analyser over a range of temperatures, from 18 to 945 °C. In order to calibrate peaks of water vapour generated during mineral dehydration, reference waters mixed with N_2 carrier gas are streamed from the WVISS through the heated column at 945 °C and normalized to the VSMOW scale.

Mineral sample $\delta^{18}O$ signals measured here are interpreted to reflect the hydroxyl component. In a low-Fe illite, OH represents 17 % of the mineral oxygen budget with the remaining 83 % from tetrahedral sites. For an OA-ICOS measurement of illite, an H_2O yield of ~4.5 weight percent is expected based upon mineral

stoichiometry. In this scenario, the OA-ICOS result reflects of half the hydroxyl O. Notably, fractionation between the evolved H_2O and O_2 species generated during dehydroxylation is thought to be insignificant (Girard and Savin, 1996).

4.3 RESULTS

4.3.1 Carrier gas comparison

Ambient atmosphere was allowed to flow through the dehydroxylation column during a heating ramp cycle from 18 to 945 °C (Figure 4.2). The initial $\delta^{18}O$ value prior to heating the column was -10.8±0.2 ‰ (15 second average). Upon heating, the oxygen isotope values of water vapour are effectively stable up to 300 °C. Between 300 and 650 °C, $\delta^{18}O$ increased from -10.0±0.2 ‰ to -0.3±0.1 ‰, then rose sharply, over the temperature range from 650° up to 945 °C. At the peak temperature of the heating ramp test, the measured $\delta^{18}O$ value was 25.2±0.1 ‰. Over the course of tests conducted using a dry air carrier gas, the measured $\delta^{18}O$ value of mineral samples (i.e. kaolinite, muscovite, serpentine) ranged between 22 and 26 ‰. These results are similar to atmospheric oxygen $\delta^{18}O$ values, indicating that a high degree of exchange is occurring between water liberated from minerals, and oxygen in dry air carrier gas, as observed elsewhere (Koehler and Wassenaar, 2012).

Using the starting and ending $\delta^{18}O$ values as representative of degree of exchange with oxygen during the heating test, the percent of mixing and exchange between each reservoir can be determined (Figure 4.2). Exchange is negligible below 300 °C, and is 52 % at 800 °C. Based upon these results, it may be possible to operate with an air carrier gas at temperatures up to 800 °C, and determine unknown samples, provided that at any given operating temperature the exchange between water vapour and oxygen is consistent.

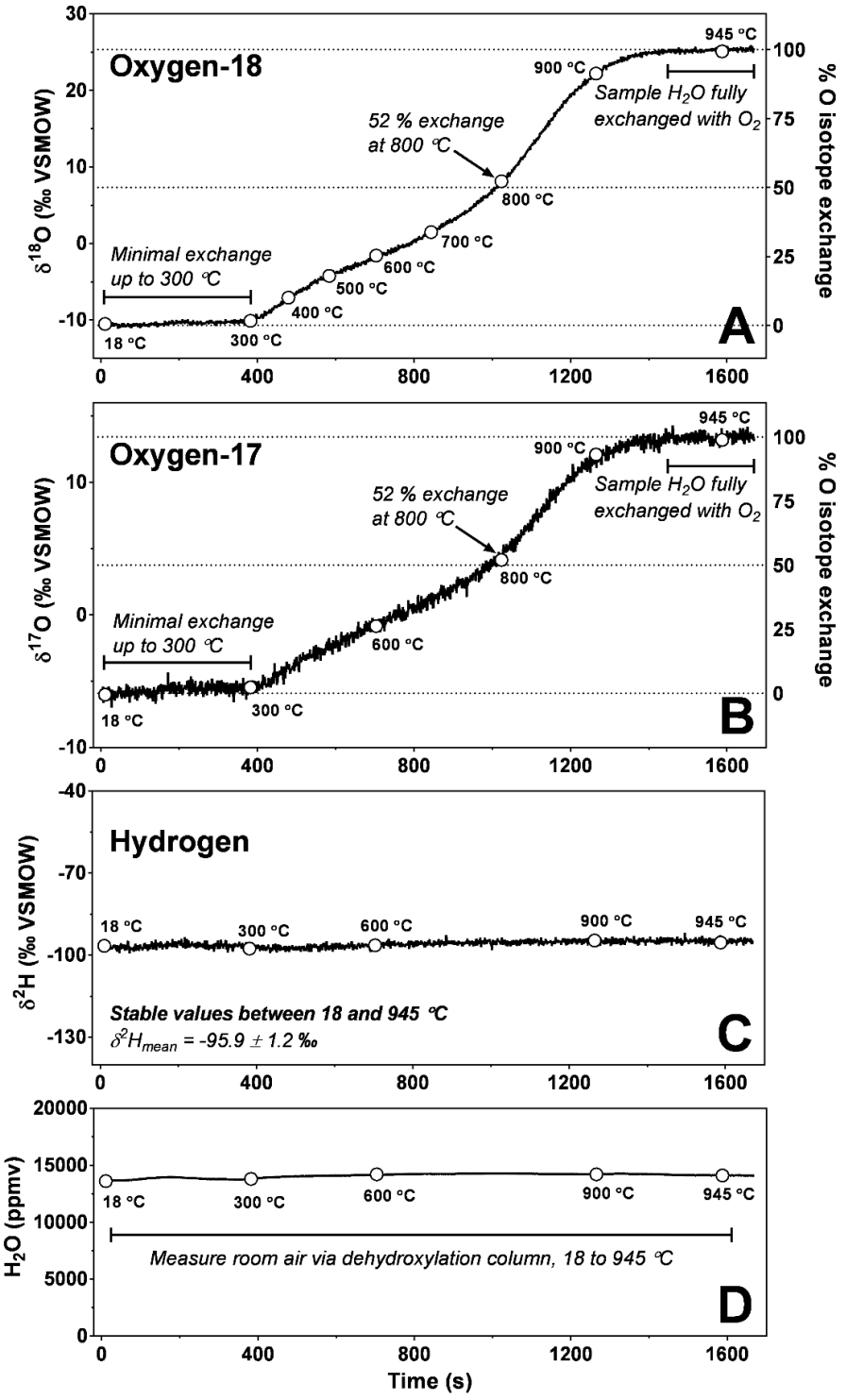

Figure 4.2: heating test carried out by flowing room air through the dehydroxylation column at temperatures between 18 and 945 °C. Oxygen isotope exchange is calculated for $\delta^{18}O$ (Panel A) and $\delta^{17}O$ (Panel B). Hydrogen isotope variation was minimal at any temperature, demonstrating that air is an acceptable carrier gas for $\delta^{2}H$ measurements. The average H_2O concentration during the test was 14,802±182 ppmv (Panel D).

4.3.2 Calibration

VSMOW scale calibration relationships for the N_2 carrier gas configuration were constructed by pulsing reference waters through the heated column (Figure 4.3). The $\delta^{18}O$ calibration slope is ~1.4 indicating moderate scale compression due to a reservoir of oxygen in the heated column partially exchanging with sample H_2O. Potential sources for exchange include quartz in the dehydroxylation column or remnant mineral powder from prior analyses. The Costech Zeroblank autosampler may represent a small dead leak of O_2 within the system. Prior to analyses, the autosampler was purged for 5 minutes, but adjustments to this practice may improve performance. Although a positive pressure of N_2 was maintained in the column during operation, minor diffusion of atmospheric O_2 into the system potentially occurred due to the difference in partial pressure between the room and the dehydration-dehydroxylation assembly. Predictably, the slope of the δ^2H VSMOW calibration relationship determined in this configuration is 1.0, indicating no loss, or exchange of hydrogen, during measurements (Figure 4.3).

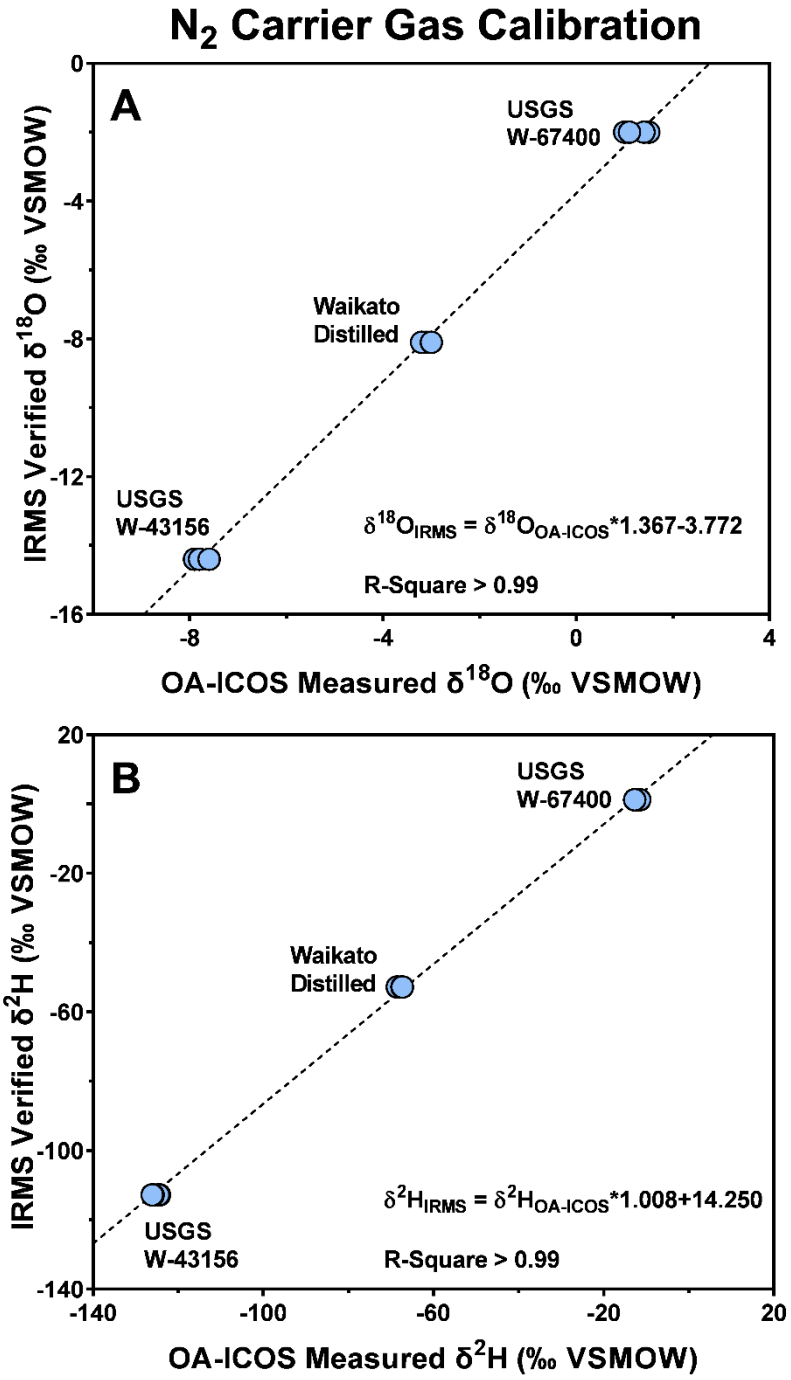

Figure 4.3: calibration relationships for $\delta^{18}O$ (Panel A) and $\delta^{2}H$ (Panel B), determined by pulsing reference waters through the heated column at 945 °C in a nitrogen carrier gas.

4.3.3 Oxygen isotope mineral results

Oxygen isotope results are presented for serpentine, kaolinite, muscovite, and Comstock whole rock samples in Table 4.2. Peak areas were integrated and normalized to the VSMOW scale using the transfer function presented in Figure 4.3. Water peaks generated by heating Comstock powders are extremely enriched for ^{18}O during the first 5-20 seconds (Figure 4.4). Early positive $\delta^{18}O$ values on analytical peaks are also observed for serpentine mineral separates.

Mineral analyses of kaolinite, muscovite, serpentine, and gypsum were measured at average $\delta^{18}O$ precisions of ±1.2 ‰, while the precision of measurements of water standards in crimped silver capillary tubes (0.5 μL) is ±0.8 ‰. Water vapour pulses generated by the WVISS are considerably more precise at ±0.2 ‰, on average. The oxygen isotope precision recorded here is lower than reported oxygen isotope results for hydrous sulphates by Cavity Ringdown Spectroscopy (e.g. Bauska et al., 2017), and whole mineral $\delta^{18}O$ results by fluorination (e.g. Sharp, 1990). Although not considered here, grain size has been demonstrated to affect dehydroxylation results (Girard and Savin, 1996). Comparative work with different size fractions may prove informative.

Table 4.2: OA-ICOS oxygen isotope results measured with an oxygen free N_2 carrier gas. Results are processed using either the full analytical peak or the right hand side.

Sample	Est. $\delta^{18}O$[a]	n	$\delta^{18}O$ Full Pk.	±1σ	$\delta^{18}O$ Rt. Half Pk.	±1σ
Water - WVISS pulse						
USGS W-67400	-2.0	4	-2.0	0.3	-2.3	0.7
Waikato Distilled	-8.1	9	-8.1	0.2	-8.1	0.2
USGS W-43156	-14.4	5	-14.4	0.2	-14.4	0.2
Water - Ag capsule						
USGS 48	-2.2	9	-2.3	1.0	-	-
USGS W-62001	-6.3	9	-6.1	0.5	-	-
USGS W-32615	-9.3	10	-9.8	0.9	-	-
USGS 47	-19.8	8	-19.7	0.9	-	-
Serpentine						
WS-1 (Cassiar)	-	4	7.5	2.4	6.0	1.2
Serp-HS-1 (Huckleberry)	-	4	9.6	1.7	7.1	1.1
Kaolinite						
Kga-1b (Macon, GA)	21.5	3	13.2	1.0	13.5	0.8
Muscovite						
G-18499	-	2	2.9	0.9	1.6	0.3
G-18502	9.7	3	10.1	1.6	4.8	0.4
USGS 58	-	3	3.5	0.7	1.1	0.8
Gypsum						
Gy-Ajax	-	7	-1.9	0.4	-	-
Comstock Lode Ag-Au deposit (NV, USA): hydrothermally altered andesite						
71638	6.7	1	10.9	1.4	7.1	0.8
71639	4.4	1	5.0	1.4	1.2	0.8
71390	2.4	1	3.2	1.4	0.5	0.8
71598	1.6	1	2.5	1.4	-2.3	0.8
71603	1.6	1	-6.7	1.4	-6.1	0.8
71643	1.3	1	11.9	1.4	4.1	0.8
71612	-0.8	1	9.0	1.4	1.8	0.8
71424	-2.3	1	10.1	1.4	3.0	0.8
71619	-2.6	1	7.6	1.4	0.9	0.8
71642	-2.9	1	4.4	1.4	-2.0	0.8
71647	-2.1	1	8.6	1.4	0.9	0.8
71570	-3.0	1	1.5	1.4	-3.7	0.8

[a] Established values for waters are TC/EA-IRMS (USGS Reston Lab; Mering and Barker, 2018). Prior Comstock δ18O by whole rock fluorination IRMS (Eaton et al., 1998). G-18502 and KGa-1b measured by fluorination (Longstaffe, 2019)

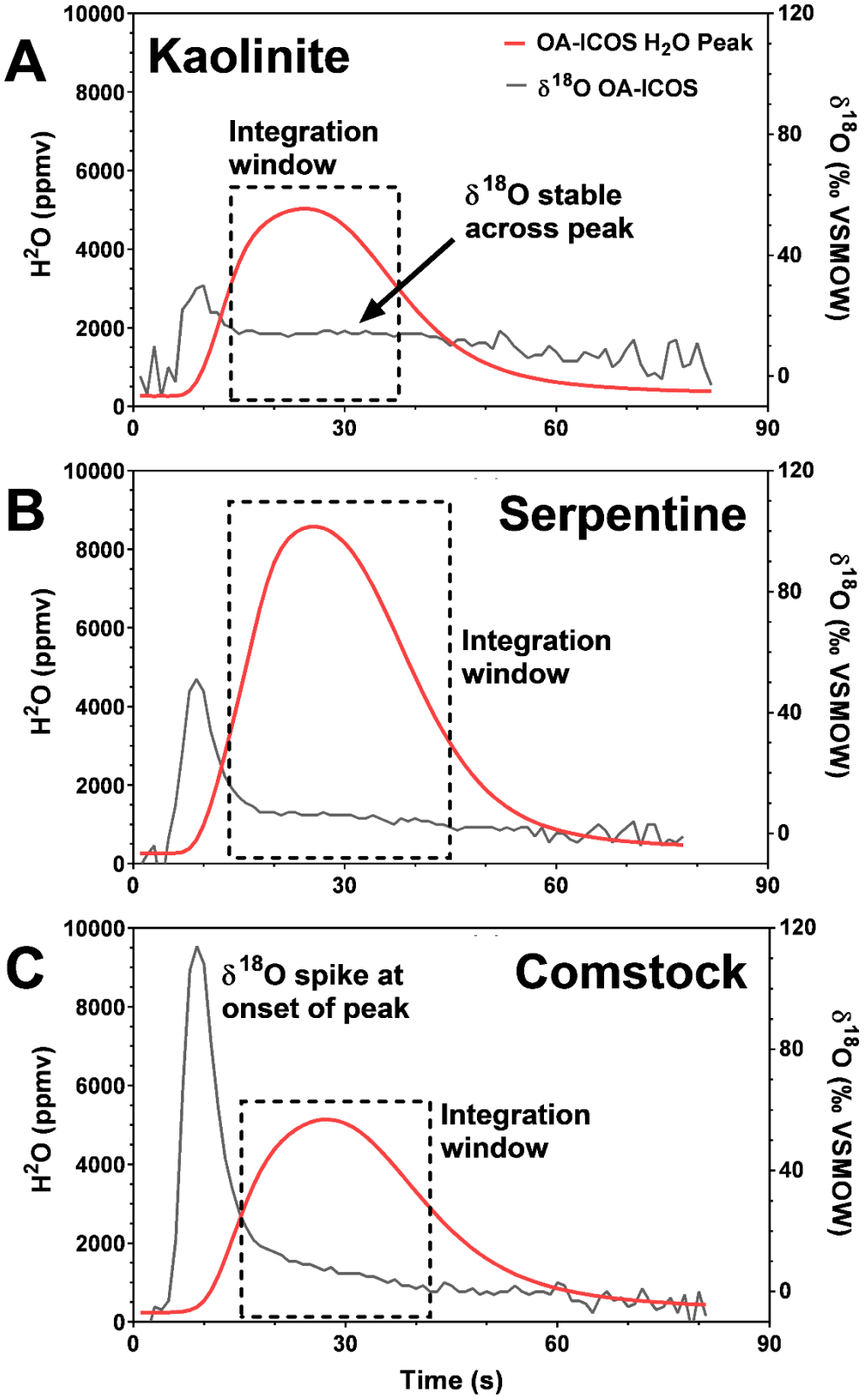

Figure 4.4: water vapour concentrations and $\delta^{18}O$ values for analytical peaks generated by thermal dehydroxylation of mineral powders. A: kaolinite (Kga-1b) exhibited stable $\delta^{18}O$ values on both the left and right sides of peaks. B: serpentine (Serp-HS-1) water has a high abundance of ^{18}O early in the peak. C: Comstock samples generated water peaks that are ^{18}O enriched during the first 10-20 seconds.

4.3.4 Hydrogen isotope mineral results

Calibrated hydrogen isotope results for three mineral separates and Comstock powders are presented in Figure 4.5 and Table 4.3. Analyses were carried out using identical hardware, but with different carrier gases (dry air and N_2). The δ^2H measurements of mineral separates and whole rock pulps are comparable within ±4.5 ‰ using either carrier gas. Comstock samples measured using dry air are -133 ‰ on average (-121 to -160 ‰). In the N_2 gas configuration, Comstock samples are -132 ‰ (-118 to -150 ‰). The average precision for hydrogen isotope results measured with a N_2 background is ±1.5 ‰. This is slightly lower than the typical precision achieved with air carrier gas, which is often ±1 ‰, or better.

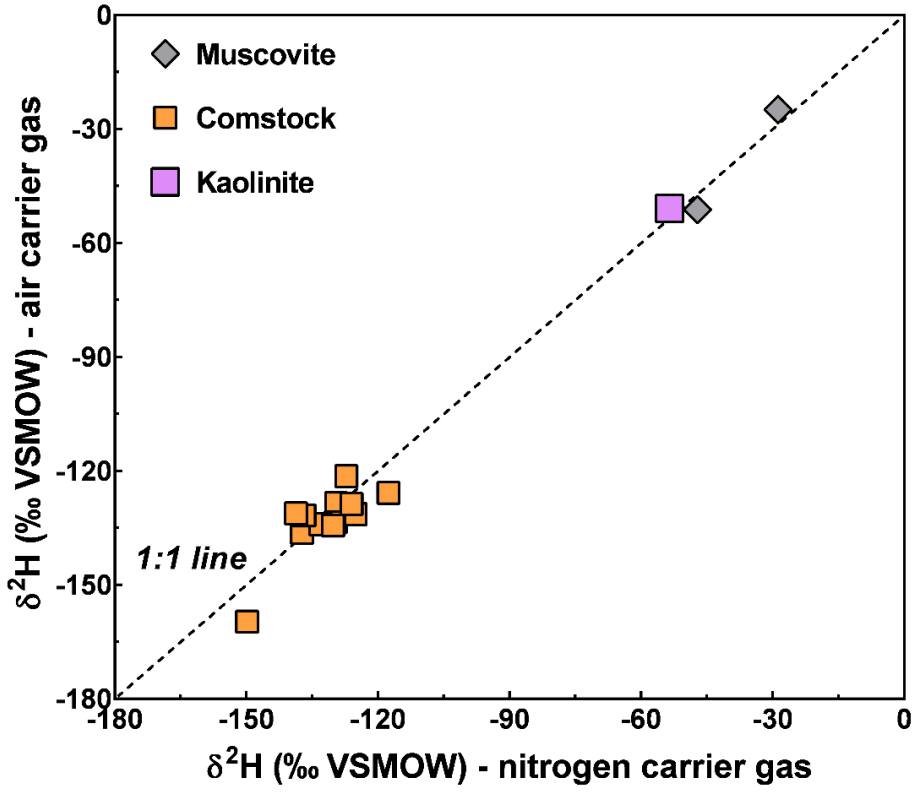

Figure 4.5: calibrated δ^2H measurements of Comstock whole rock pulps, 2 muscovite minerals (G-18499, G-18502), and kaolinite (Kga-1b). Samples were calibrated against serpentine and muscovite standards (WS-1, Serp-HS-1, USGS 58). Measurements were made using N_2 carrier gas (horizontal axis) and dry air (vertical axis). Results collected using air or N_2 gas are comparable within ±4.5 ‰.

Table 4.3: Mineral hydrogen isotope result comparison. Mineral separates and whole rock pulps were measured using dry air and N_2 carrier gases. Results are processed and calibrated using either the full analytical peak or the right hand side.

Sample	δ^2H Oxygen Free N_2 Gas			δ^2H Dry Air Gas		
	Raw[b]	Mineral Cal.[c]		Raw[b]	Mineral Cal.[c]	
(Est. δ^2H[a])	Full Peak	Full Peak	Rt. Half	Full Peak	Full Peak	Rt. Half
Kaolinite						
Kga-1b *(-50)*	-80	-53	-54	-63	-51	-48
Muscovite						
G-18499 *(-51)*	-74	-47	-48	-63	-51	-52
G-18502 *(-24)*	-56	-29	-25	-41	-25	-25
Comstock Lode Ag-Au deposit (NV, USA): hydrothermally altered andesite						
71638	-154	-130	-126	-129	-129	-127
71639	-153	-130	-127	-134	-134	-132
71390	-143	-118	-117	-127	-126	-125
71598	-149	-125	-123	-132	-131	-129
71603	-173	-150	-154	-156	-160	-158
71643	-162	-137	-131	-136	-136	-135
71612	-158	-133	-129	-134	-134	-133
71424	-153	-127	-117	-123	-121	-118
71619	-162	-137	-123	-132	-132	-130
71642	-151	-126	-121	-130	-129	-127
71647	-166	-139	-131	-132	-131	-129
71570	-155	-130	-124	-134	-134	-132

[a]Established values for minerals are by TC/EA-IRMS (Mering and Barker, 2018).

[b]δ^2H using LGR factory calibration.

[c]δ^2H values calibrated using mineral standards (USGS 58, Serp-HS-1, WS-1).

4.4 DISCUSSION

4.4.1 Interference

Analysis of Comstock whole rock powders highlight previously identified issues associated with interference during measurement of some minerals by thermal dehydroxylation (e.g. Bechtel and Hoernes, 1990; Bauska, 2017; Mering and Barker, 2018). The positive isotope spikes at the start of peaks observed here (Figure 4.4) cannot be explained by chromatographic effects (e.g. Koehler and Wassenaar, 2012), which should result in lower $\delta^{18}O$ for initial water (left side of

peak) produced during analyses. Early ^{18}O enrichment of waters produced by high temperature dehydration-dehydroxylation of whole rock powders may be due to destruction of carbonate (Bauska et al., 2017), or oxidation of ferrous materials (e.g. Bechtel and Hoernes, 1990). The reactions, which are predicted to occur in the heated column during mineral dehydroxylation, are summarized below in equations 4.4-4.8.

Thermal dehydroxylation of silicates yields water, O_2 gas, and by-product silicate residue. The dehydration reaction of kaolinite is shown in equation 4.4:

$$KAl_2Si_2O_5(OH)_4 \rightarrow SiO_2 + Al_2Si_2O_5 + 2H_2O(g) + O_2(g) \quad (4.4)$$

Decarbonation of calcite (and other carbonates) generates CO_2 (equation 4.5). In the high temperature column, CO_2 has the potential to exchange oxygen isotopes with H_2O released from hydrous minerals (equation 4.6). Notably, the $\delta^{18}O$ of early H_2O produced from Comstock samples exceeds 100 ‰, which is 70-90 ‰ above most terrestrial carbonate $\delta^{18}O$.

$$CaCO_3 \rightarrow CaO + CO_2(g) \quad (4.5)$$

$$^{12}C^{18}O^{16}O(g) + H_2{}^{16}O(g) \rightarrow H_2{}^{18}O^{16}O(g) + {}^{12}C^{16}O_2(g) \quad (4.6)$$

Oxidation of pyrite: at high temperature, pyrite progressively decomposes producing pyrrhotite (equation 4.7). The reaction progresses to generate reduced Fe and S_2 gas, with complete destruction of pyrite occurring by 800 °C, well below the 945 °C operating temperature for this study (Boyabat et al., 2004; Young, 2016; Oliveira et al., 2018). Simultaneously, Fe is oxidised by H_2O (Young, 2016), elevating the $\delta^{18}O$ value of the water vapour stream passing through to the analyser (equation 4.8).

$$FeS_2 \rightarrow FeS_{(1-x)} + (1-x)S_2(g) \quad (4.7)$$

$$Fe + H_2{}^{16}O(g) \rightarrow Fe^{16}O + H_2(g) \quad (4.8)$$

In this study, sulphurous gases (e.g. S_2, H_2S) are trapped by Ag wool at the base of the dehydroxylation column. Samples containing iron bearing minerals (e.g. pyrite) may have caused some early water vapour (left side peak) to become reduced. During preliminary trials using nitrogen carrier gas, the dehydroxylation column was operated without silver wool packing. In this setup, interfering gases (e.g. H_2S) were occasionally produced during measurements of gypsum and whole rock mineral powders (clay ± pyrite). With the addition of Ag wool packing, by-product sulphur gases were trapped upstream of the analyser, enabling measurement of fractionated water peaks depicted in the lower panel of Figure 4.4.

4.4.2 Analytical issues and solutions

Issues with measurement arising from working on heterogeneous samples may be addressed by modification of hardware, sample preparation, and data processing. The primary challenges identified include:

(i) spectral interference imparted by H_2S
(ii) deposition of S compounds on filters
(iii) fractionation of $\delta^{18}O$ signatures caused by Fe becoming partially oxidised.

These challenges primarily occur in sulphide containing samples. Packing silver wool into the column provided an effective sulphur trap, but does not prevent sample water liberated from minerals from reacting with metals to produce oxides. If sulphides are prevalent in samples, isolation of clay minerals via standard clay separate procedures (i.e. deflocculation, settling, and centrifugation) may improve quality of data. If carbonates are present, treatment of rock pulps with dilute HCl may be necessary prior to analysis (e.g. Bauska et al., 2017).

4.4.3 Alternative data processing methodology

Interference by Fe containing mineral species may also be partly, or fully, dealt with by calculating peak area ratios (e.g. $^{18}O/^{16}O$) for the right hand side of peaks, with the left side excluded. Right hand peak area integration is carried out under the assumption that for samples containing Fe, the majority of oxidation impacts early

H_2O during the first 20 seconds of a peak (Figure 4.4, bottom panel). Isotope results calculated using either full peak or right side of peak integration approaches are compared in Tables 4.2-4.3 and Figure 4.6. Notably, samples that do not contain Fe (e.g. Kaolinite, diaspore Comstock sample, reference waters) exhibit similar oxygen isotope calibration relationships regardless of whether the right side or entire peak is evaluated. However, $\delta^{18}O$ values computed from right hand peak area ratios for Comstock whole rock samples, as well as two serpentine mineral separates (i.e. WS-1, Serp-HS-1), are lower than corresponding full peak values that included measurements from the left (ascending) side of peaks. No apparent difference in calibrated $\delta^{2}H$ values was observed using the right half peak protocol as compared with standard full peak integration (Table 4.3).

One of the potential setbacks of the right-hand approach is a reduction of measurements for a sample water pulse by ~50 percent. If the right half peak integration method is implemented, a lower flow rate may be necessary in order to increase the duration of peaks, and thereby achieve a more robust dataset. In a trial, a throttle valve was installed on the pump exhaust of the OA-ICOS analyser. By doing this, it was possible to reduce flow from ~110 ml/min to 60 ml/min while maintaining the manufacturer specified target pressure in the optical cell of 40.3 torr.

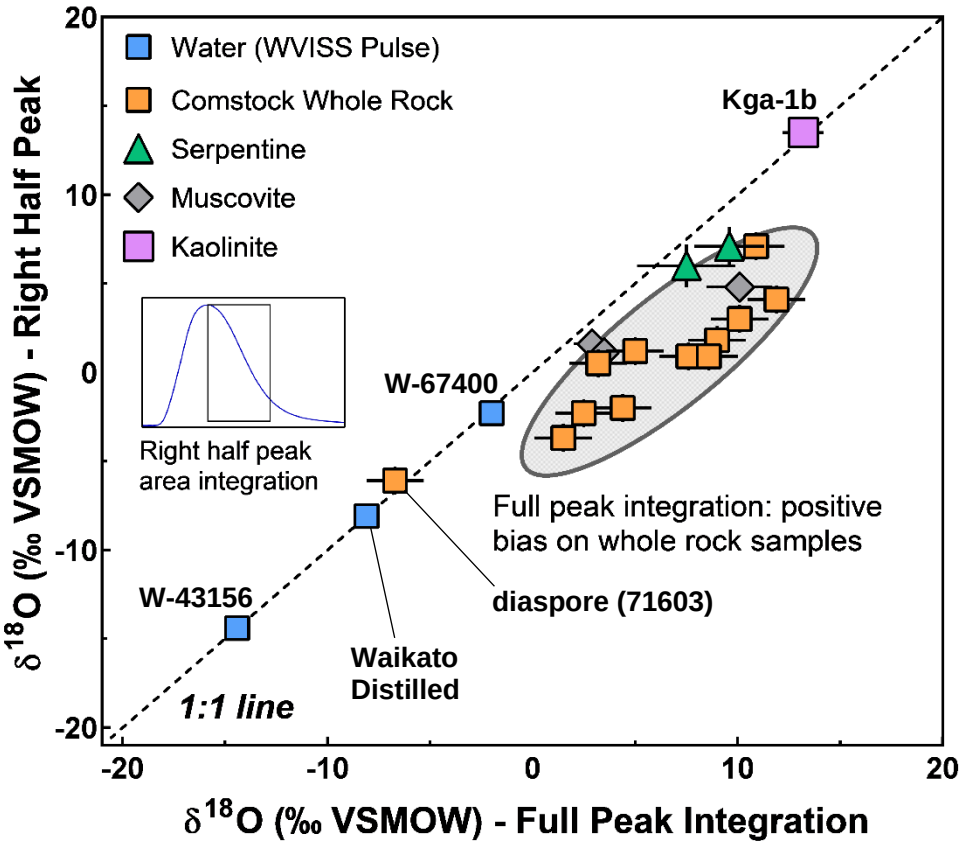

Figure 4.6: comparison of $\delta^{18}O$ results determined using either full peak (horizontal axis) or right half peak integration (vertical axis). Interference by ferrous materials may impart a positive shift upon some whole rock materials when the left side of a peak is included in the isotope ratio calculation. Right half peak processing generated $\delta^{18}O$ results for the majority of Comstock samples, which are on average 5 ‰ lower. Notably, kaolinite (Kga-1b) and one diaspore-containing Comstock sample (71603) exhibited similar values regardless of peak integration method.

4.4.4 Characterizing fluid isotope values at the Comstock Lode

Hydrogen

At Comstock, $\delta^{2}H$ whole rock values, measured by OA-ICOS (dry air configuration) range from -160 to -121 and are -133 ‰ on average (Figure 4.7). The measurements are moderately ^{2}H depleted relative to $\delta^{2}H$ results for quartz vein fluid inclusions (-109 ± 20 ‰) reported in two previous papers (O'Neil and Silberman, 1974; Vikre, 1989). Hydrogen isotope values in clay minerals that are

lower than fluid inputs are explained by mineral-water fractionation relationships. Illite clays are expected to attain δ^2H values that are 26 ‰ lower than corresponding fluid values over temperatures between 130 and 250 °C, while chlorite and epidote exhibit fractionation of -30 to -40 ‰, relative to parent fluid (e.g. Marumo et al., 1980; Graham et al., 1987). Sample 71603 was most isotopically negative (-160 ‰) of the Comstock materials measured. This sample exhibited an XRD signature consistent with diaspore (AlO(OH)) and kaolinite, indicating some degree of argillic alteration. Based on limited fractionation information, diaspore is predicted attain a δ^2H value that is up to 80 ‰ lower than local fluid (Zheng, 1998), indicating that the depleted signature measured in 71603 primarily reflects variation in mineralogy, while fluid may have been relatively constant.

Based upon application of fractionation information for geothermal clay (i.e. Marumo et al., 1980) and diaspore (Zheng, 1998), reconstructed fluid values in samples are slightly enriched relative to meteoric values and measurements of fluid inclusions in quartz veins (Figure 4.7). Provided that mineralogy and clay-water isotope fractionation can be reconstructed, δ^2H values may reflect minor contribution of magmatic fluids in the system (approximately -80 to -40 ‰); given the relative uncertainty in clay-water hydrogen isotope fractionation, these interpretations should be considered preliminary. In higher latitude hydrothermal locales, where there is even greater separation in the values of meteoric and magmatic fluid, current constraints upon mineral-water fractionation factors may be sufficient to unambiguously fingerprint magmatic inputs, or meteoric-induced shifts to primary hydrous minerals in hostrock (see example from Idaho Batholith in Chapter 2, Figure 2.3).

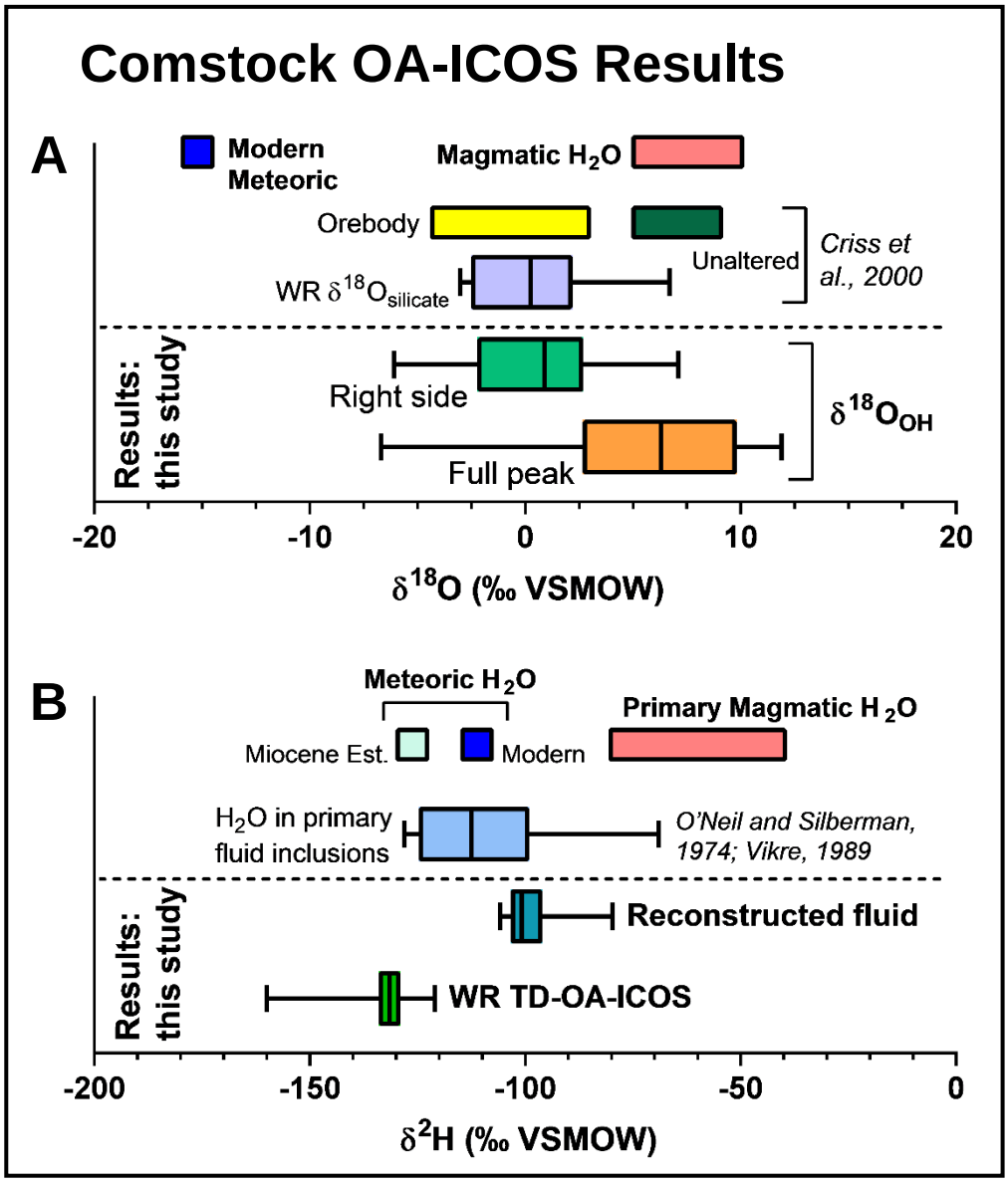

Figure 4.7: Comstock whole rock thermal dehydroxylation OA-ICOS results (this study) plotted relative to prior isotopic constraints upon mineral and fluid values. Panel A: TD-OA-ICOS $\delta^{18}O_{OH}$ values determined using the "right side" peak integration approach are lower than "full peak" results, and similar to the value range reported for whole rock fluorination $\delta^{18}O_{silicate}$ (i.e. Eaton et al., 1998; Criss et al., 2000). $\delta^{18}O_{OH}$ values are more enriched than local meteoric H_2O, but lower than $\delta^{18}O$ in local unaltered volcanic rock or magmatic H_2O. Panel B: whole rock TD-OA-ICOS δ^2H values and reconstructed fluid δ^2H. The Comstock fluid δ^2H values reconstructed here are slightly enriched relative to local meteoric H_2O, and overlap measurements of H_2O extracted from primary quartz fluid inclusions (O'Neil and Silberman, 1974; Vikre, 1989). Reconstructed fluid values are more depleted than magmatic H_2O. Modern meteoric fluid δ^2H and $\delta^{18}O$ from the OIPC (Bowen, 2019). Miocene estimate for meteoric δ^2H from Vikre, 1989. Isotope value ranges for primary magmatic H_2O from Taylor and Barnes, 1997.

Comstock results were processed using both full peak and right side peak integration approaches (Figures 4.6). The spike in ^{18}O abundance at the onset of analytical peaks due to redox effects and/or decarbonation requires further investigation. Notably, $\delta^{18}O_{OH}$ results processed using the right side approach overlap with whole rock $\delta^{18}O_{silicate}$ results (Figure 4.7), determined by fluorination (Criss et al., 2000).

The overlap of $\delta^{18}O_{OH}$ (right side integration) with $\delta^{18}O_{silicate}$ is notable given that a dehydroxylation value reflects a small proportion of the oxygen isotope budget in a sample. Argillic and propylitic alteration zones at Comstock contain variable amounts of quartz and pyrite, and hydrous alteration products including illite, chlorite, smectite, epidote, kaolinite, and diaspore (Vikre, 1989). Water yields for Comstock samples measured here range from 1.4 to 7.2 % by weight, and are 2.9±1.5 % on average. Assuming a single alteration phase (i.e. illite or chlorite), a water yield of 2.9 % would indicate a whole rock sample that is 64 % illite or 26 % chlorite, with the remaining fraction comprised of nominally anhydrous minerals (e.g. quartz, feldspars). Regardless, the fraction of O measured as H_2O by thermal dehydroxylation is secondary compared with the composite whole rock fluorination $\delta^{18}O$ signal, which includes O released from OH, and the remaining nonhydrous silicate fraction (e.g. quartz, feldspar, tetrahedral sites in clays). Hence, comparison of whole rock fluorination ($\delta^{18}O_{silicate}$) and thermal dehydroxylation ($\delta^{18}O_{OH}$) results should be made cautiously.

4.4.5 Intramineral oxygen isotope fractionation

Internal oxygen isotope fractionation within hydrous minerals is not well studied. TD-OA-ICOS results for muscovite and kaolinite were paired with fluorination constraints to evaluate intramineral fractionation (phyllosilicate-OH). Results for kaolinite (Kga-1b) and muscovite (G-18502) are similar to values obtained in previous studies using either partial fluorination or thermal dehydroxylation IRMS (Figure 4.8). The measured $\delta^{18}O_{mineral}$ value of Kga-1b by fluorination is 21.5 ‰ (Longstaffe, 2019), which indicates phyllosilicate-OH fractionation of 8 ‰. The measured internal fractionation of muscovite (G-18502) is 4.9 ‰. Overall, these

values overlap with results for kaolinite and muscovite reported previously (e.g. Hamza and Epstein, 1980; Meheut et al., 2007; Seligman and Bindeman, 2019).

One of the potential advantages of quantifying intramineral fractionation is the potential for single mineral thermometry (e.g. Bechtel and Hoernes, 1991). In this context, robust interpretation of site-specific oxygen isotope signals in whole rock samples at Comstock is not possible because the whole rock fluorination and thermal dehydroxylation results are not mineral specific. However, emerging targeted mineral dehydration approaches (e.g. Bauska et al., 2018), which allow for continuous measurement of mineral dehydration products over a temperature ramp may better suited towards untangling hydrous mineral isotope signals in bulk samples containing more than one hydrous mineral species.

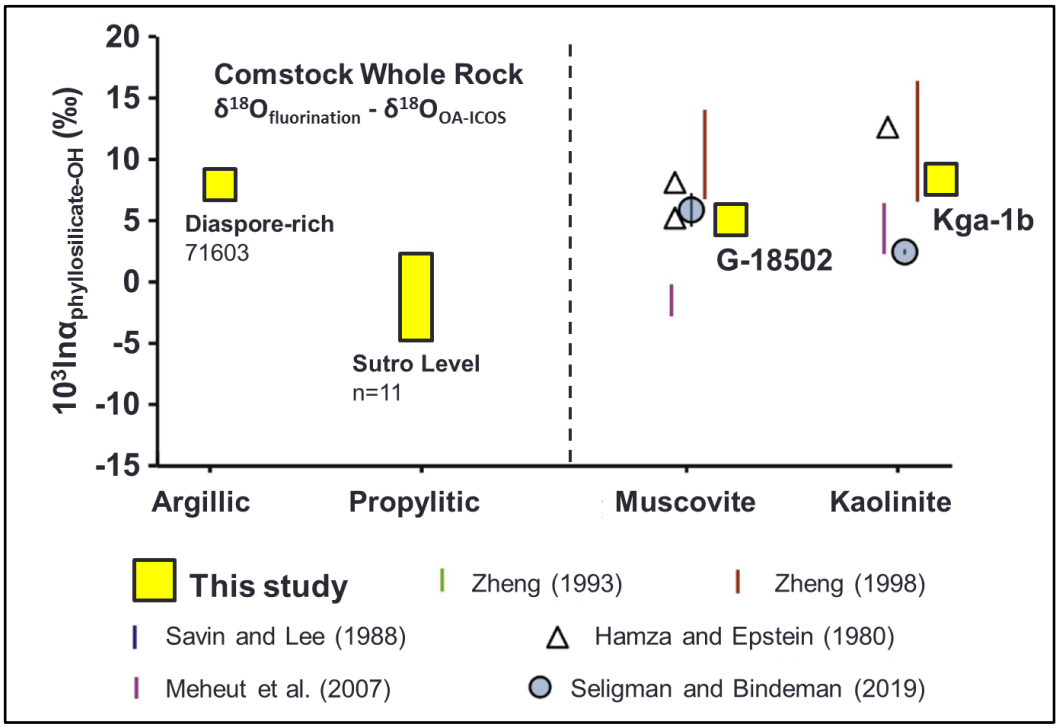

Figure 4.8: Oxygen isotope results compared for silicate and OH in muscovite, kaolinite, and Comstock Lode whole rock samples. Figure adapted from Seligman and Bindeman, 2019.

4.4.6 Using OA-ICOS to reconstruct fluid history in hydrous minerals

The results presented here demonstrate the feasibility of using high temperature dehydration-dehydroxylation, paired with OA-ICOS, to measure the hydrogen and

oxygen isotope signatures in hydrous minerals (Figure 4.9). For the gypsum measured (Gy-Ajax: δ^2H = -62.7 ‰, $\delta^{18}O$ = -1.88 ‰), application of recently updated $\alpha_{gypsum\text{-}water}$ relationships (Gázquez et al., 2017) indicate mineral formation from a water near the meteoric water line (δ^2H = -44.7 ‰, $\delta^{18}O$ = -5.36 ‰). The results for serpentine and kaolinite reflect geographic origin and geologic setting. The Huckleberry Range serpentine (Serp-HS-1, WA, USA) exhibits higher δ^2H and $\delta^{18}O$ relative to the Cassiar serpentine (WS-1, BC, CA). These findings are consistent with a significant meteoric water component involved in serpentinization, with lower fluid and mineral values at the higher latitude Cassiar site.

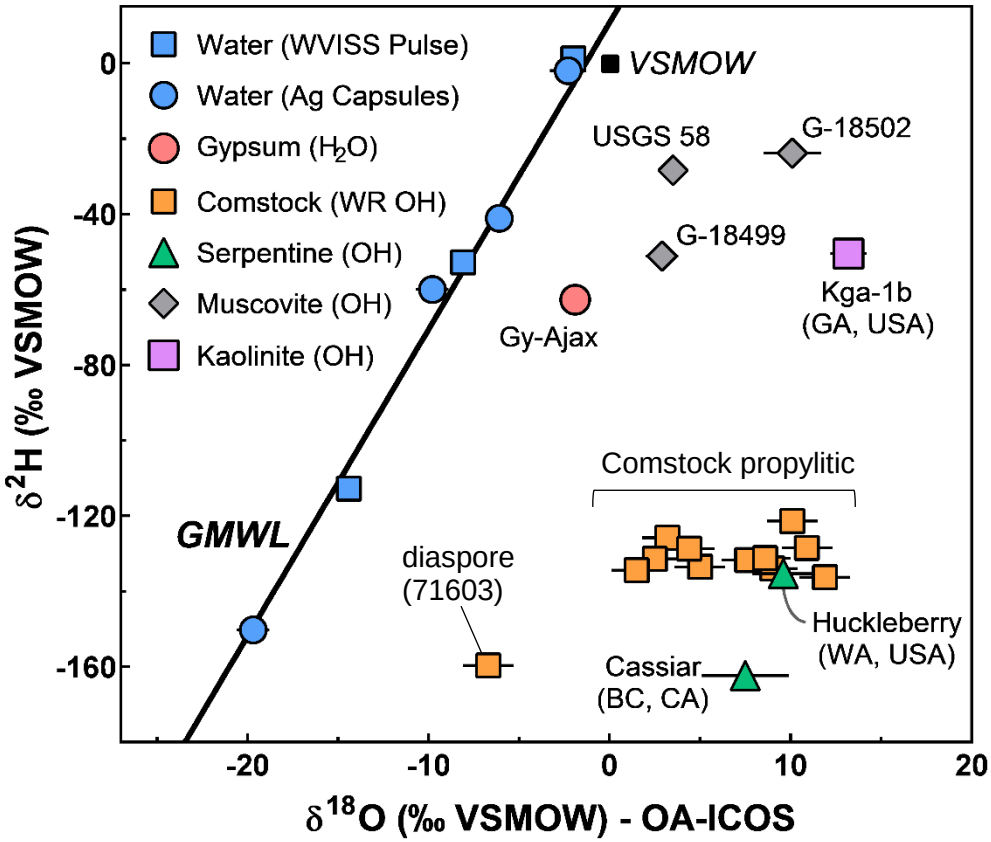

Figure 4.9: measured OA-ICOS $\delta^{18}O$ results (full peak integration method) for hydrous minerals and waters plotted against δ^2H values. Measurement of δ^2H and $\delta^{18}O$ in minerals enhances understanding fluid origin in geologic systems. The gypsum $\delta^{18}O$ value is for mineral hydration water. Serpentine, muscovite, kaolinite, and Comstock results are measurements of hydroxyl $\delta^{18}O$. Reference waters were introduced as either Ag capsules into the high temperature column or as pulses of water from the WVISS. The Global Meteoric Water Line (GMWL) and VSMOW are plotted for comparison.

In mineral deposit studies, OA-ICOS provides a low cost alternative to IRMS for rapid characterization of δ^2H and $\delta^{18}O_{OH}$. This analytical capability may prove useful in studies where δ^2H has been applied historically to reconstruct fluid source in epithermal and porphyry environments (e.g. Taylor, 1974; Dilles et al., 1992). Hydrogen isotope measurements in clays may have exploration potential in uranium deposits. The method developed here may be useful towards evaluating radiation induced alteration of δ^2H in phyllosilicates (Kotzer and Kyser, 1995; Truche et al., 2018). Recent work in Canada identified a halo of clays trapping radiogenic H_2 around the Cigar Lake uranium deposit (Truche et al. 2018). Additional work is needed to determine whether the δ^2H of trapped gases are in equilibrium with mineral hydroxyl.

4.4.7 Fingerprinting the origin of clay products using stable isotopes

The method demonstrated here should be readily useful for hydrogen and oxygen measurements in hydrous materials for which there is interest in tracking product origin. Clays, and other hydrous minerals, have an annual trade value in excess of $10B USD (USGS, 2019). Clays are mined for use in building materials, drilling muds, paper products, food additives, and a variety of personal products. In the food and cosmetics industries, there is a need to verify the origin of clays to limit the possibility of sourcing ingredients from deposits that contain unwanted, and potentially dangerous, impurities (e.g. Buzon, 2016). With many isotope labs lacking the necessary hardware, expertise, sample preparation facilities, and analytical standards, commercial measurement of δ^2H and $\delta^{18}O$ in clay minerals is often costly, ranging from $50 to greater than $100 per measurement. The results reported in this study open the possibility of using $\delta^{18}O_{OH}$, combined with δ^2H, to identify geographic origin (e.g. British Columbia vs. Georgia) of clay products (Figure 4.9). The low cost of measuring $\delta^{18}O_{OH}$, and absence of dangerous fluorination, make TD-OA-ICOS an attractive tool for use by manufacturers and regulatory agencies.

4.5 CONCLUSIONS

The OA-ICOS approach demonstrated here is capable of measuring oxygen isotope ratios in small volumes of water and hydrous minerals. Potential issues with early peak fractionation may be overcome by preparing clay separates or adjusting the peak integration procedure. The hardware setup is suitable for measurement of pure mineral separates, including gypsum, kaolinite, muscovite, and serpentine. At Comstock, variation in whole rock δ^2H is attributed to mineralogical differences, with propylitic assemblages exhibiting more enriched values (-121 to -136 ‰) than a diaspore-rich sample (-160 ‰). Taking mineral-fluid fractionation factors into account, whole rock hydrogen isotope measurements imply a relatively homogeneous fluid of meteoric origin was involved in alteration at the Comstock Lode. A lack of reliable published intramineral oxygen isotope fractionation factors impedes advanced interpretation of the $\delta^{18}O_{OH}$ data at Comstock. The method should be deployable for measurement in epithermal and porphyry deposits, although further testing is needed in order to develop a platform capable of reliably measuring $\delta^{18}O_{OH}$ in assay pulps. The ability to simultaneously measure oxygen and hydrogen isotopes in hydrous minerals may also prove useful for verification of the geographic origin of clays used in consumer products.

CHAPTER V

Taking the temperature of hydrothermal ore deposits using clumped isotope thermometry

In the following chapter, a carbonate clumped isotope investigation is reported for a set of geothermal and hydrothermal ore deposit calcite and dolomite samples. Analyses were carried out in the IsoLab at the University of Washington, Seattle, USA. A manuscript based on this work was published in *Economic Geology* (2018). The results presented in this chapter, and in the manuscript, were collected by John Mering. This chapter, and the published manuscript, were written by John Mering, with support from collaborators. Notably, these individuals contributed samples (Shaun Barker, Stuart Simmons, Benjamin Andrew, Gregory Dipple), guidance on clumped isotope methodology (Katherine Huntington, Andrew Schauer, Julia Kelson), analytical support (Andrew Schauer), and feedback on the structure of the manuscript (Shaun Barker, Stuart Simmons, Kate Huntington). Samples from Waihi were made available by partnership with OceanaGold. The work was funded by the New Zealand Ministry of Business, Innovation and Employment (Gold Exploration Models: C05X1405). The citation for the publication of this work is the following:

Mering, J.A., Barker, S.L.L., Huntington, K.W., Simmons, S., Dipple, G., Andrew, B., and Schauer, A., 2019, Taking the temperature of hydrothermal ore deposits using clumped isotope thermometry: Economic Geology, v. 113, p. 1671 – 1678, doi: 10.5382/econgeo.2018.4608

ABSTRACT

Better tools are needed to map the thermal structure of ore deposits. Here, carbonate clumped isotope thermometry is applied for the first time in epithermal, skarn, and carbonate hosted deposits to identify the conditions involved in metal transport and deposition. Clumped isotope temperature calibrations were tested by measurement of carbonates from three geothermal fields in the Taupo Volcanic Zone (TVZ), New Zealand that record growth temperatures between 130 and 310 °C. Results for modern TVZ calcites were paired with known fluid $\delta^{18}O$ values, and indicate precipitation in equilibrium with produced geothermal waters. Measurements carried out at the Waihi low sulfidation deposit in New Zealand, the Antamina polymetallic skarn in Peru, and the Mount Isa sediment hosted Pb-Zn and Cu deposit in Queensland Australia demonstrate that clumped isotope values are sensitive to temperature gradients defined using other methods. At Waihi, an andesite hosted deposit, temperature controls the majority of variation in carbonate mineral $\delta^{18}O$. At Mount Isa, ~300-400 °C temperatures were recorded in a 1.5 Ga orebody, which are consistent with fluid inclusion values, highlighting the longevity of clumped isotope archives in dolomite minerals. These results demonstrate the potential for clumped isotopes to delineate the heat footprint around deposits that contain carbonates, and more effectively disentangle magmatic and meteoric fluid $\delta^{18}O$ signals.

5.1 INTRODUCTION

5.1.1 Thermometry in hydrothermal settings

Advection in the upper crust derives from fluid circulation in hydrothermal systems, which are associated with magmatic intrusions and the formation of hydrothermal ore deposits. In ore-forming systems, hydrothermal solutions attain metals at depth, then rise through buoyancy to deposit economic minerals where pressure and temperature decrease (e.g. epithermal), or in response to fluid-rock interaction (e.g. skarn). Accurate reconstructions of fluid temperature in hydrothermal systems are applied to delineate thermal gradients, which drive metal uptake, transport, and deposition. The resulting understanding of thermal structure, exemplified in Figure 5.1, underpins development of ore deposit models used in mineral exploration programs (e.g. Heinrich et al., 1996; Ferry and Gerdes, 1998).

There are shortcomings to virtually all techniques which are applied to reconstruct temperature in ore deposits. The interpretation of fluid inclusion homogenization thermometry (T_h) is complicated in cases in which inclusions are absent or are not primary (e.g. many epithermal deposits, Carlin-type sediment hosted Au), and accurate temperature interpretations of fluid inclusions require definition of the pressure (i.e. depth) of formation (Roedder, 1984). Although demonstrably useful, mineral pair isotope thermometers often reflect neither the conditions of crystallization nor closure temperature, and require the assumption that mineral phases precipitate in equilibrium, which is often difficult to prove (e.g. Giletti, 1986). Notably, clay mineral relationships (Figure 5.2) provide qualitative evidence of thermal regime, but are characteristically insensitive (Essene and Peacor, 1995; Simmons and Browne, 2000).

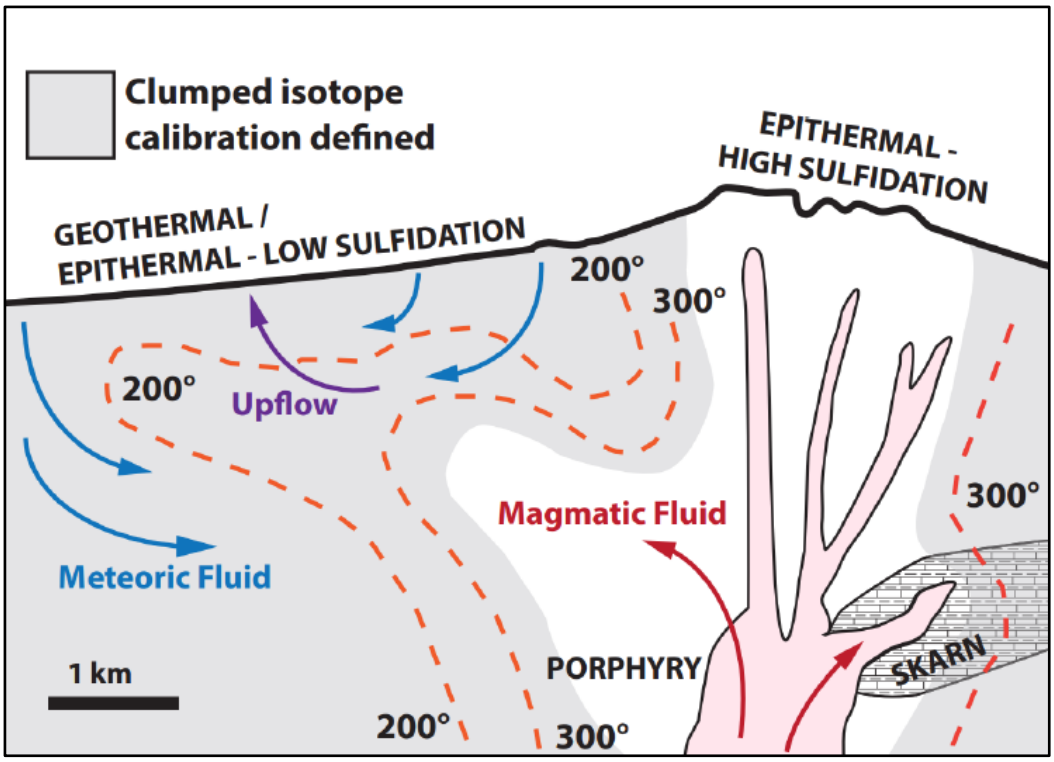

Figure 5.1: schematic of convective fluid flow based upon the porphyry and vein controlled Au-Ag deposit model presented in Hedenquist and Lowenstern (1994). Hydrothermal mineral deposits occur near hot zones, and temperature decreases significantly, moving away from ore bodies to reflect the local geotherm. Epithermal (e.g. Waihi) and geothermal (e.g. TVZ) systems occur at temperatures below 300 °C, while porphyry deposits occur at greater depths, in association with intrusions. Skarns (e.g. Antamina) develop where magma intrudes carbonate host rock. Recent developments in clumped isotope methodology, extend the range of calibrations up to 350 °C, which is suitable for hydrothermal ore deposit investigations.

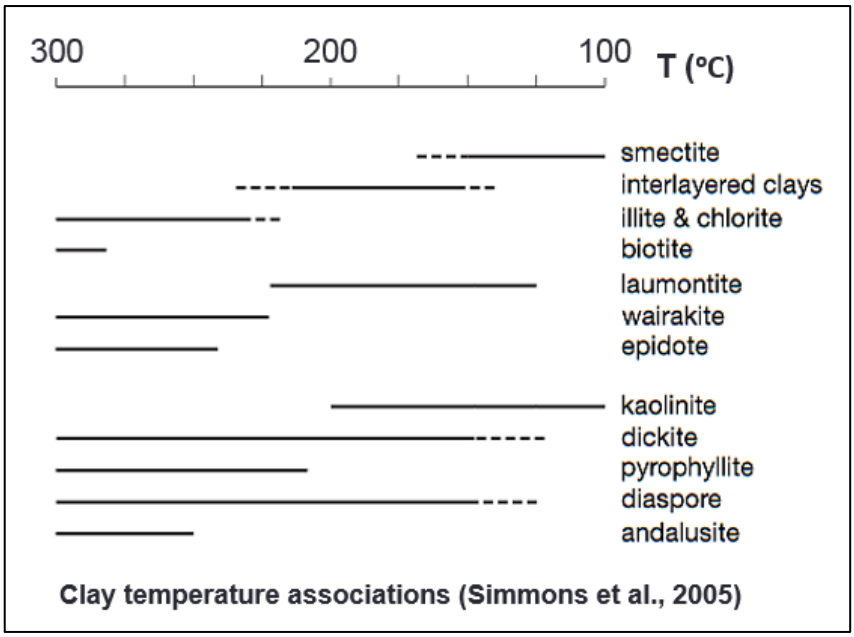

Figure 5.2: clay mineral associations commonly applied to infer temperature ranges in hydrothermal settings. From Figure 4 in Simmons et al., 2005.

5.1.2 Carbonate clumped isotopes

Carbonate clumped isotope thermometry, which quantifies the thermodynamically dependent abundance of ^{13}C-^{18}O bonds, expressed as Δ_{47}, has the potential to accurately determine the temperature at which hydrothermal carbonates form. With this approach, analyses may be carried out on a single carbonate mineral without requiring constraints upon the oxygen isotope value of mineralizing fluid (e.g. Eiler, 2007, Huntington et al., 2011). Clumped isotopes consequently have the potential to separate the effects of temperature and $\delta^{18}O_{water}$ upon $\delta^{18}O_{mineral}$, and more precisely characterize the range of aqueous fluids involved in ore genesis (Dennis et al., 2018). Within deposits, $\delta^{18}O$ inputs range from -20 to up to 0 ‰ VSMOW for meteoric waters, while basinal brines and primary magmatic water range from 5-10 ‰, and metamorphic waters are up to 30 ‰ higher than ocean water (e.g. Giggenbach, 1992b; Kesler et al., 1997).

Over the last decade, clumped isotopes have been applied extensively to sedimentary and biogenic carbonates to address paleoclimate and paleoceanographic questions (Eiler, 2011; Douglas et al., 2014), and to reconstruct uplift histories (e.g. Huntington et al., 2010; Lechler et al., 2013). In the subsurface,

clumped isotopes have been utilized to understand diagenesis (e.g. Dennis and Schrag, 2010), and describe the movement of fluids through fault zones (e.g. Bergman et al., 2013; Luetkemeyer et al., 2016). Recent work has taken up the challenge of assessing the application potential for Δ_{47} to reliably elucidate temperatures in hydrothermal environments (e.g. Sumner, 2014; Lloyd et al., 2017; Lu et al., 2017; Lu et al., 2018; Honlet et al., 2018). New carbonate growth experiments have expanded lab calibration datasets to between 250 °C (Kluge et al., 2015) and 350 °C (Bonifacie et al., 2017). Recent work demonstrates that clumped isotopes are useful towards identifying the fluid source in Mississippi Valley Type (MVT) deposits at temperatures between 40 and 100 °C (Dennis et al., 2018).

5.1.3 Site selection

In this study, carbonate clumped isotope thermometry (Δ_{47}) is applied in modern geothermal fields, representative of low sulphidation mineralization, and a range of ancient ore-forming settings (Table 5.1). Measurements were carried out on scaling and ejecta calcite samples from geothermal wells at the Broadlands-Ohaaki, Ngatamariki, and Wairakei fields, within the Taupo Volcanic Zone (TVZ). The TVZ serves as world-class laboratory for understanding metal transport in hydrothermal environments, with high fluxes of Au, Ag, Cu, Pb, Te, and Zn reported in geothermal fields (Rowland and Simmons, 2012; Simmons et al., 2016a). Measurements were also carried out on vein and propylitic calcite at Waihi, a giant low sulfidation deposit (~8 M oz Au, 40 M oz Ag historic production), which formed during the upper Miocene within the Coromandel Volcanic Arc, North Island, New Zealand (e.g. Brathwaite and Faure, 2002; Christie et al., 2007), and in two ore deposits, where temperatures of mineralization exceed 300 °C. These high-temperature case studies include the Antamina Cu-Zn polymetallic skarn (561 Mt Cu), Western Cordillera, Peru (Escalante et al., 2010), which formed ~10 Ma, and Mount Isa, a 1.5 Ga globally significant sediment-hosted base metal deposit (Pb-Zn-Ag and Cu) in Northwest Queensland, Australia (Heinrich et al., 1989; Hannan et al., 1993).

Table 5.1: Hydrothermal sites investigated using clumped isotope thermometry

Site	System type (Resource)	Location	Age	Samples
Taupo Volcanic Zone	Active geothermal (energy, metals)	North Island, New Zealand	Modern	Calcite from boreholes with known temperatures
Waihi	Low sulfidation epithermal (Au-Ag)	North Island, New Zealand	7-6 Ma	Vein and propylitic calcite in andesite
Antamina	Polymetallic skarn (Cu-Zn)	Western Cordillera, Peru	10 Ma	CRD calcite veins, marble
Mount Isa	Carbonate hosted (Pb-Zn, and Cu)	Queensland, Australia	1.5 Ga	Dolomite veins

5.1.4 Taupo Volcanic Zone, New Zealand – modern geothermal fields

The TVZ is an extensional region dominated by rhyolitic-andesitic volcanism, on the North Island of New Zealand (Simmons and Brown, 2007; Rowland and Simmons, 2012; Simmons et al., 2016). Geothermal fields are active within the central TVZ (Rowland and Sibson, 2004; Rowland and Simmons 2012; Simmons et al., 2016a; Simmons et al., 2016b). Geothermal reservoirs occur at 600 to 3000 m depth in layered volcanic sequences (Rowland and Simmons, 2012). Calcite samples for this study were selected from production wells at the Ngatamariki, Wairakei, and Broadlands-Ohaaki geothermal areas (Figures 5.3-5.4, Tables 5.1-5.2). Fluid inclusion homogenisation (T_h) temperatures reported for these samples range between 140 to 310 °C (Simmons and Christenson, 1994; Christenston et al., 2000; Simmons et al., 2005; Simpson et al., 2014). The typical oxygen isotope values of groundwater and geothermal reservoir water range between -7.0 and -3.0 ‰, but further isotopic enrichment of deep fluids by water-rock reaction has been documented (Simmons and Christenson, 1994; Dempsey et al., 2012).

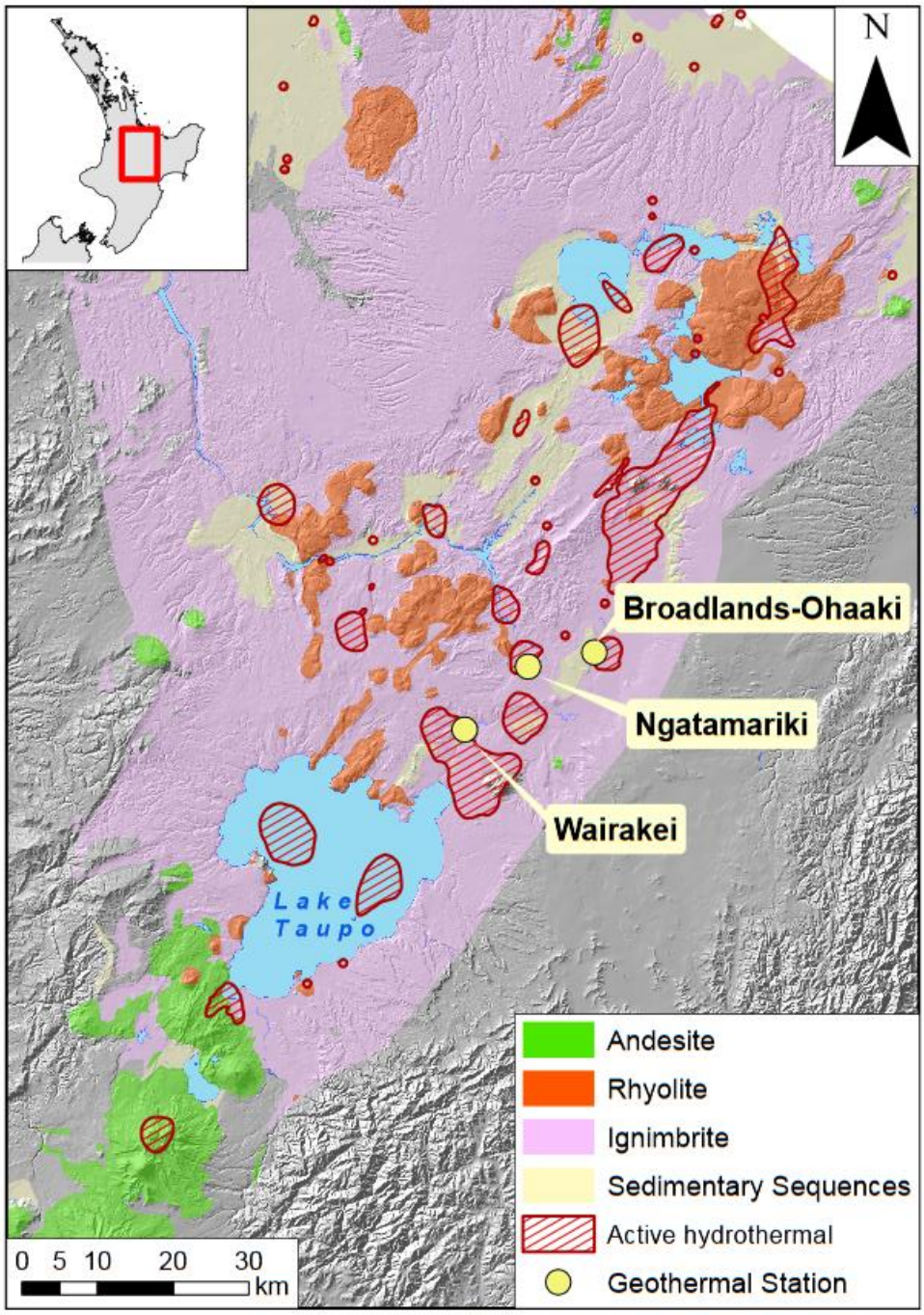

Figure 5.3: geologic setting of the Taupo Volcanic Zone. Geothermal calcite samples were selected from production wells at the Ngatamariki, Broadlands-Ohaaki, and Wairakei geothermal power stations.

Table 5.2: Modern geothermal sample temperature conditions

Sample	Depth (m)	Established T (°C) T_h	Established T (°C) Discharge	Description	Reference
Wairakei					
WK-80	-	-	250[1]	Bladed calcite scale	Clayton and Steiner, 1975; Stewart, 1976; Giggenbach, 1980
Ngatamariki					
Ngatamariki-Breccia	-	138±8	-	Eruption breccia consisting of scale/veins. T_h on platy calcite	Horton et al., 2012; Simpson et al., 2014
Broadlands-Ohaaki					
BR-21-101	101	180±20	135±5	Cuttings	Simmons and Christenson, 1994
BR-6-15-150	150	-	180[1]	Scale	Simmons and Christenson, 1994
BR-13-866	866	284±10	270	Scale	Simmons and Christenson, 1994
BR-27-400	400	240	-	Platy calcite scale	Simmons and Brown, 2000
BR-15-1655	1655	308	290	Scale	Simmons and Christenson, 1994
BR-42-Ejecta	-	245	199	Ejecta	Christenson et al., 2002

[1]Approximate well discharge fluid temperatures for WK-80 and BR-6-15-150 estimated from thermal profiles of Wairakei and Broadlands-Ohaaki geothermal areas

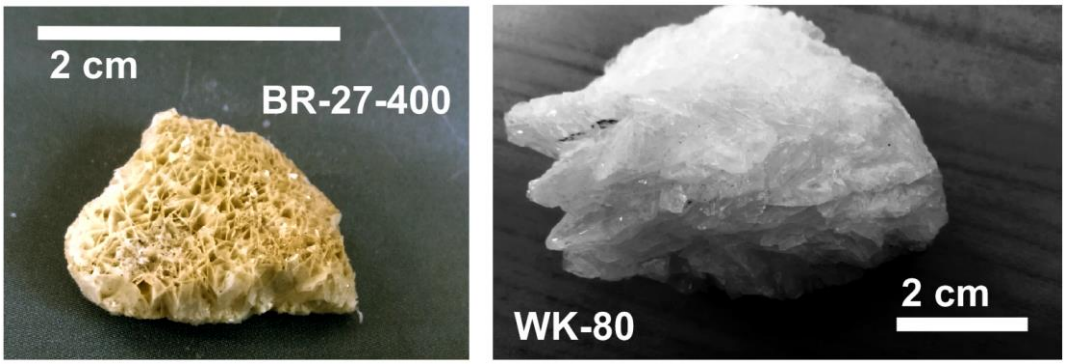

Figure 5.4: examples of calcite scale textures indicative of growth in a boiling geothermal environment. Left: BR-27-400 is a platy calcite from the Broadlands geothermal field. Right: WK-80 is a calcite scale sample collected at Wairakei.

5.1.5 Ore deposit samples

Waihi, New Zealand – Low Sulphidation Au-Ag

During the Miocene, the Coromandel Volcanic Zone (CVZ) was the primary locus of silicic volcanism on the North Island of New Zealand. Within the CVZ, epithermal precious metal deposits (Figure 5.5) formed in volcanic settings that alternated between dominantly andesitic and rhyolitic eruptive styles (Christie et al., 2007). Waihi is the largest Au-Ag deposit, having yielded over 7.7 million ounces of Au, historically (Mauk et al., 2016). Calcite, which is a significant gangue mineral at Waihi, is distributed in mm to cm scale veins, and also occurs as a replacement texture in plagioclase phenocrysts within andesite host rock.

At Waihi, clumped isotope measurements were compared in two sections of drill core. A set of vein calcites was sampled 300-1200 meters NW of the main Au-Ag mineralized quartz veins at the Martha Mine. This transect corresponds with a previously characterized clay mineral transition (illite-dominated to smectite dominated), which is inferred to generally indicate decreasing temperature conditions (i.e. Figure 5.2), moving away from the hotter upflow zone (Bodger, 2015).

Table 5.3: Ore deposit sample descriptions

Sample	Description
Epithermal (Au-Ag) - Waihi, North Island, New Zealand	
UW462-BB23V	Calcite vein, approximately 350 m NW of main ore body at Martha Pit
UW462-BB23R	Replacement calcite, approximately 350m NW of main ore body at Martha Pit
UW462-879V	Calcite vein, 879 m NW of Martha Pit
UW462-BB58V	Calcite vein 1 km NW of Martha Pit
SP0597-V	Calcite vein 300 m NE of Martha Pit
SP0597-R	Replacement calcite, 300 m NE of Martha Pit
Skarn (Cu-Zn) - Antamina, Peru	
4PAA157	Fortuna syn mineral vein
4PAA129	Fortuna syn mineral vein
4PAA178	Fortuna syn mineral vein
4PAA219	Oscarina calcite vein
4PAA119	Distal pre-mineral vein
3PAA273	Distal pre-mineral vein
2PAG172	Marble sample adjacent to skarn contact
Carbonate hosted (Pb-Zn-Ag and Cu) - Mount Isa, Queensland, Australia	
ISA105621150V	Dolomite vein sample, main Cu orebody
ISA105586A150V	Dolomite vein sample, main Cu orebody

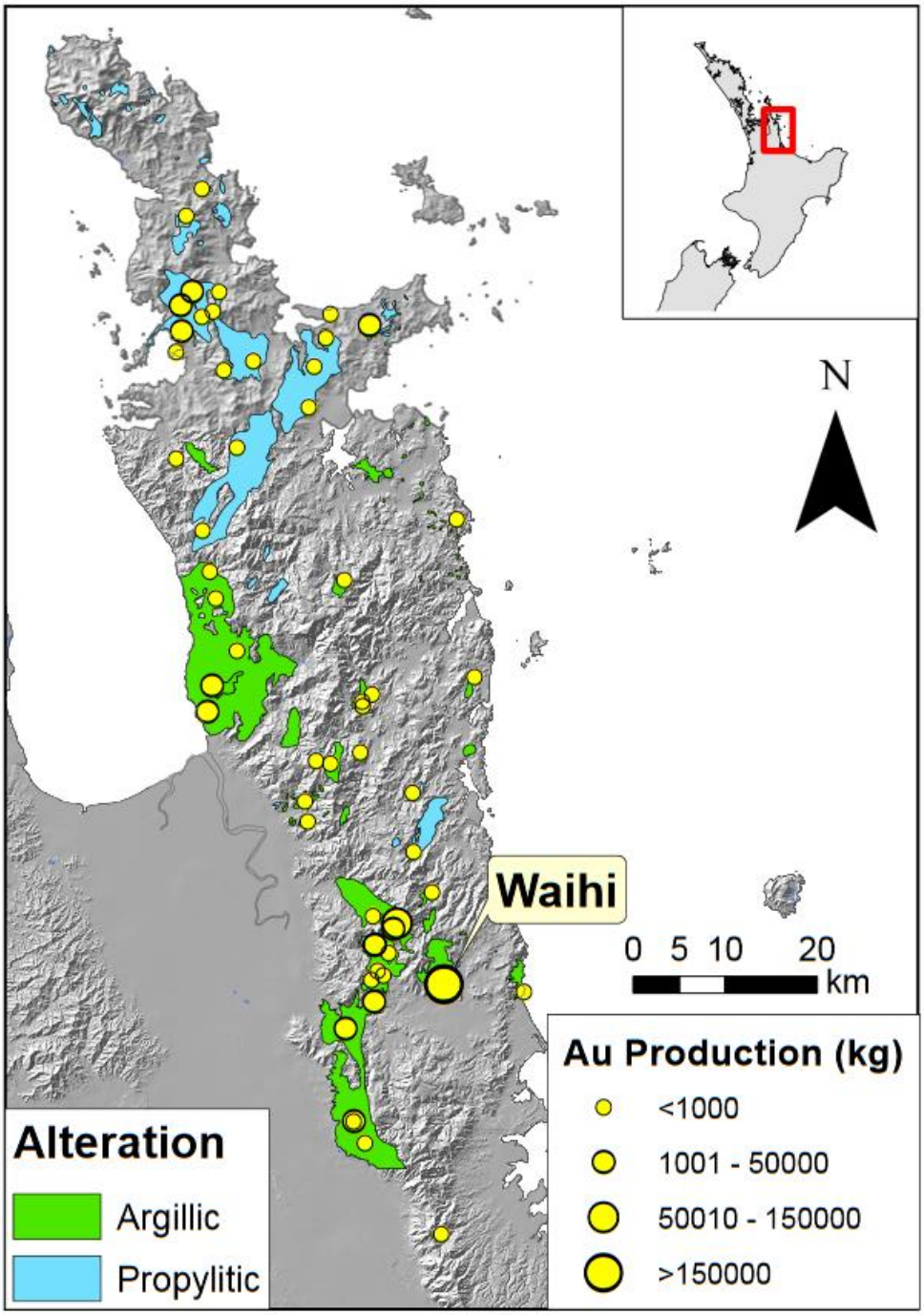

Figure 5.5: Waihi is a giant low sulphidation epithermal Au-Ag deposit, located at the southern end of the Coromandel Peninsula, with over a century of mining history. During the Miocene, the Coromandel volcanic zone (CVZ) was the primary locus of silicic volcanism on the North Island of New Zealand.

Antamina, Peru – polymetallic skarn

Antamina is a giant polymetallic skarn orebody, within the Western Cordillera of the larger Maranon fold and thrust belt, in Peru. The deposit was emplaced circa 10 Ma, where quartz monzonite porphyries intruded Upper Cretaceous sedimentary

sequences (Escalante et al., 2010). The deposit occupies a 4.5x2 km area, and is fully described in Love et al., 2004 and Escalante et al., 2010. A detailed geologic map of the deposit is presented in Figure 1 of Escalante et al., 2010. Samples selected for clumped isotope measurements were taken from three principal zones. Sample 2PAG172 is a marble from the skarn body. Samples 4PAA157, 4PAA129, 4PAA178 are from the Fortuna Transect, an Ag-base metal deposit containing calcite±sulphide veins. Sample 4PAA219 is a calcite vein from the Oscarina intrusion, 1-2 km SW of the Fortuna site, and samples 4PAA119 and 3PAA273 are also distal to the orebody and predate mineralization.

Mount Isa, Australia – sediment hosted base metal

The Isa inlier has undergone a complex history, including development of three unconformity bounded super sequences during the Proterozoic (Jackson et al., 2000). A broadly extensional tectonic regime was terminated by basin inversion during the Isan Orogeny between 1.6 and 1.5 Ga, when Cu mineralization occurred (Bell, 1983, Perkins, 1984; Page and Bell, 1986). Measurements were carried out on two dolomite vein samples peripheral to the main Cu orebody which formed during Cu mineralization, where mineralization temperatures are thought to span 250-350 ℃ (Bell, 1983, Perkins, 1984; Heinrich et al., 1989; Hannan et al., 1993).

5.2 METHODS

Carbonate was extracted from veins using a microdrill. The drill was operated at low speed to minimise the possibility of frictional heating leading to solid state reordering of ^{13}C-^{18}O bonds in samples. Calcite scale samples from geothermal wells were powdered using an agate mortar and pestle. Samples containing 6-8 mg of calcite or dolomite were reacted in a 90 °C phosphoric acid bath, cryogenically purified on a custom built vacuum line, and analysed on a Thermo MAT 253 isotope ratio mass spectrometer (IRMS) at the University of Washington following methodology described in Burgener et al. (2016) and Schauer et al. (2016). The analytical setup is depicted in Figure 5.6. Carbonate and CO_2 gas standards were analysed daily. Carbonate $\delta^{13}C$ values are referenced to VPDB, and $\delta^{18}O$ measurements of carbonate, and calculated aqueous fluid values, are reported

relative to VSMOW (Coplen, 1988). Clumped isotope values (Δ_{47}) are normalized to the Absolute Reference Frame (Dennis et al., 2011), also known as the carbon dioxide equilibrium scale (CDES).

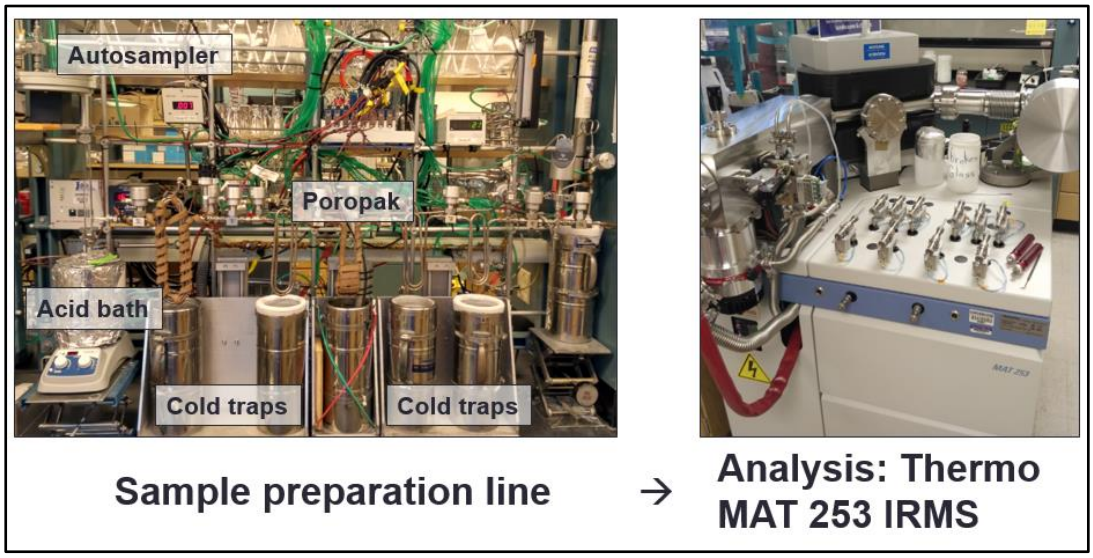

Figure 5.6: clumped isotope sample preparation line and Thermo MAT 253 IRMS at the IsoLab, University of Washington, USA.

The CDES-corrected Δ_{47} values are converted to temperature using the Kluge et al. (2015) relationship recalculated using Brand et al. (2010) ^{17}O correction parameters. This is the only high-temperature (constrained between 25 and 250 °C) carbonate calibration that we can confirm is appropriate for our samples based on agreement of Δ_{47} values for multiple carbonate standards (ETH-1, ETH-2, ETH-3 and ETH-4; Bernasconi et al., 2018) analysed at the University of Washington and at the Imperial College London laboratory in which the Kluge et al. (2015) calibration data were produced. The Kluge et al. (2015) relationship also agrees with the University of Washington calibration of Kelson et al. (2017) in the temperature range for which the latter is constrained (4-85 °C). Uncertainties of Δ_{47} results are reported to 1 standard error (1 s.e.) of the average of a set of replicate measurements. Mount Isa samples, which were measured as single replicates, are reported with an estimated uncertainty based upon the long-term 1 s.e. for a high temperature carbonate standard (ETH-1) analysed at the University of Washington. The calculated $\delta^{18}O$ values of aqueous fluid associated with calcite precipitation are reported using the fractionation factor (α) presented in Kim and O'Neil (1997), while $\delta^{18}O$ fluid values for dolomite at Mount Isa are reported using the relationship presented in Horita (2014).

5.3 RESULTS

Isotope results ($\delta^{13}C$, $\delta^{18}O$, Δ_{47}) are presented in Table 5.4 and Figure 5.7. Calibrated clumped isotope temperatures, and $\delta^{18}O$ fluid values are presented in Table 5.5 and Figures 5.7-5.8.

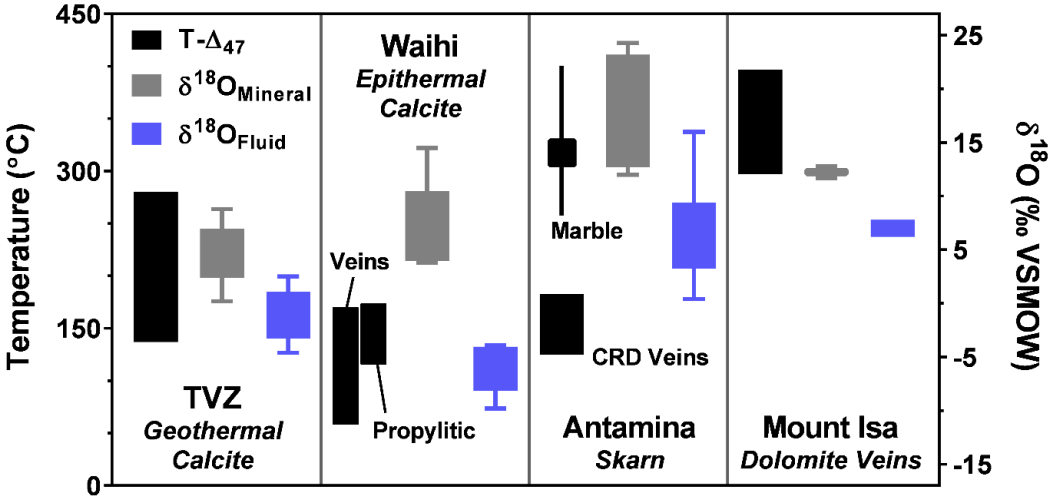

Figure 5.7: clumped isotope results for TVZ geothermal fields and ore deposits. Clumped isotope temperatures, reconstructed using the Kluge et al. (2015) calibration were combined with mineral $\delta^{18}O$ values to reconstruct the $\delta^{18}O$ signatures of aqueous fluid. Samples from TVZ, Waihi, and Antamina are calcite, while Mount Isa veins are dolomite.

5.3.1 TVZ geothermal

Clumped isotope values for modern TVZ geothermal calcites (scale and ejecta), with known formation temperatures between 130 and 310 °C, range from 0.408±0.024 (Ngatamariki) to 0.299±0.008 (BR-13-866) ‰ CDES; these overlap with established thermometer calibrations, as shown in Figure 5.8. Applying the Kluge et al. (2015) calibration, TVZ geothermal calcite clumped isotope temperatures are between 137^{+20}_{-17} and 280^{+17}_{-15} °C (Figure 5.8. Fluid $\delta^{18}O$ values calculated from carbonate oxygen isotopic values and clumped isotope temperatures range from -4.6 to 2.5 ‰ (Table 5.5, Figure 5.7).

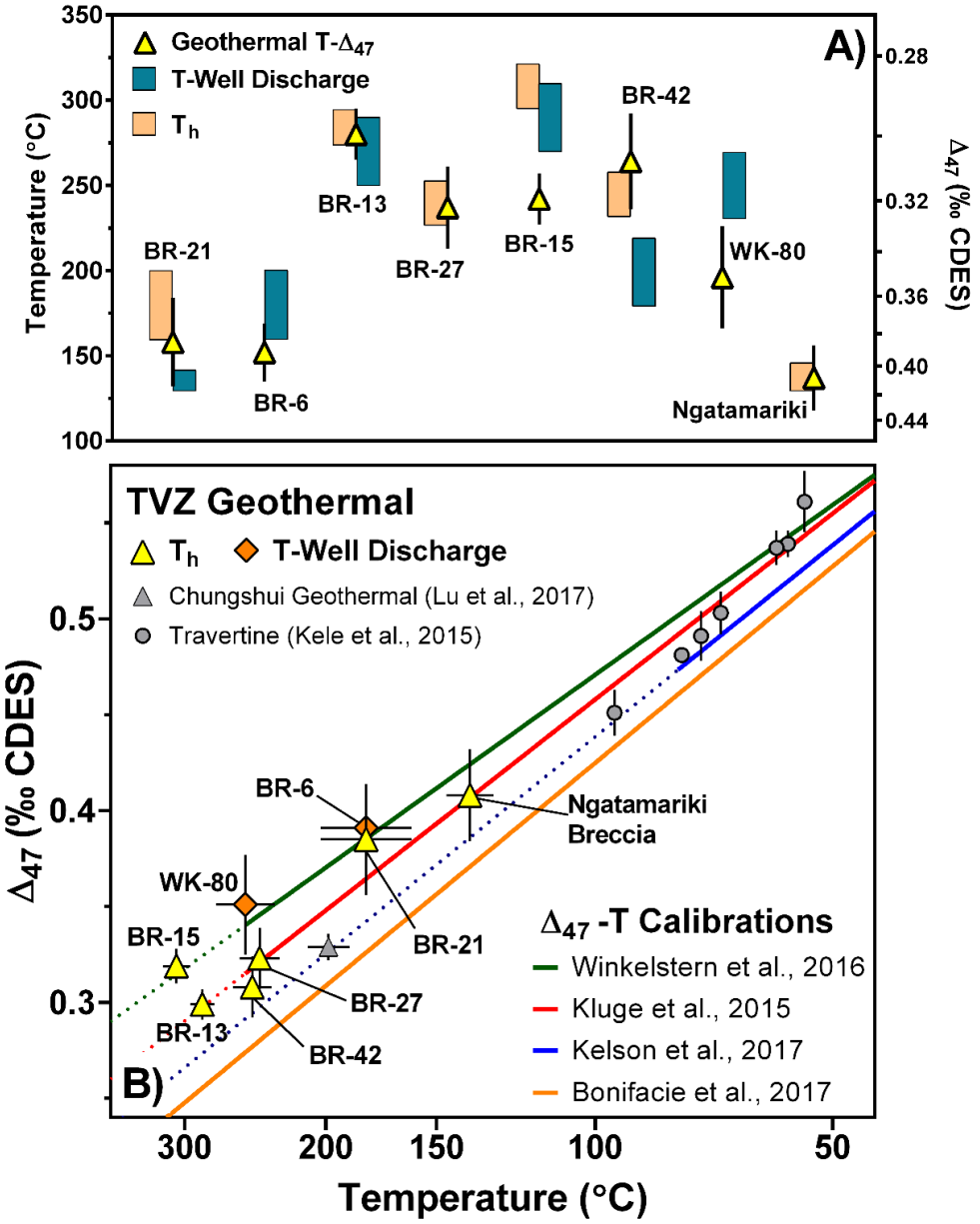

Figure 5.8: Panel A: Geothermal sample clumped isotope results compared to temperature constraints from T_h and well fluid discharge measurements. Samples are sourced from three geothermal fields: Wairakei (WK-80), Broadlands-Ohaaki (BR-6, 13, 15, 21, 27, 42), and Ngatamariki (Breccia). Discharge temperatures that are below clumped isotope and fluid inclusion constraints for carbonates, reflect diminishing enthalpy over the lifecycle of the geothermal field. Panel B: Geothermal calcite growth temperatures plotted against clumped isotope values (Δ_{47}). For comparison, four calibration relationships are shown along with previously reported results for 7 modern hot spring travertines (Kele et al., 2015) and a geothermal calcite (Lu et al., 2017). For calibrations, solid lines indicate the temperature range bounded by samples, while dashed lines are extrapolations.

Table 5.4: Analytical results

Sample	N	$\delta^{13}C_{min.}$	1 σ	$\delta^{18}O_{min.}$	1 σ	Δ_{47}	1 SE
		‰ VPDB		‰ VSMOW		‰ CDES	
TVZ - Geothermal							
WK-80	4	-5.9	0.0	2.5	0.2	0.351	0.026
Ngatamariki-Breccia	6	-6.6	0.0	7.0	0.1	0.408	0.024
BR-21-101	4	-7.1	0.0	6.8	0.1	0.385	0.029
BR-6-15-150	3	-7.1	0.0	8.8	0.1	0.391	0.019
BR-13-866	2	-7.9	0.0	2.6	0.1	0.299	0.008
BR-27-400	3	-9.4	0.0	4.1	0.0	0.323	0.016
BR-15-1655	3	-9.5	0.0	0.2	0.0	0.319	0.009
BR-42-Ejecta	5	-10.2	0.0	2.3	0.1	0.308	0.016
Waihi - Epithermal							
UW462-BB23V	3	-9.0	0.0	4.6	0.1	0.383	0.012
UW462-879V	3	-8.7	0.1	14.5	0.3	0.536	0.014
UW462-BB58V	3	-17.8	0.0	9.1	0.5	0.424	0.027
SP0597-V	3	-8.0	0.0	4.0	0.0	0.373	0.045
UW462-BB23R	3	-8.4	0.0	3.8	0.3	0.369	0.028
SP0597-R	2	-8.4	0.5	4.0	0.2	0.434	0.013
Antamina - Skarn							
4PAA157	3	0.1	0.0	14.4	0.0	0.377	0.035
4PAA129	3	-2.2	0.1	12.0	0.1	0.366	0.020
4PAA178	3	-2.6	0.0	12.7	0.1	0.375	0.038
4PAA219	4	-10.7	0.1	13.4	0.0	0.423	0.044
4PAA119	2	1.9	0.0	23.2	0.0	0.361	0.034
3PAA273	3	0.8	0.1	15.6	0.1	0.373	0.017
2PAG172	3	2.5	0.0	24.3	0.0	0.283	0.027
Mount Isa – Carbonate Hosted							
ISA105621150V	1	-5.3	0.0	11.7	0.0	0.257	0.012
ISA105586A150V	1	-5.5	0.0	12.8	0.0	0.291	0.012

Table 5.5: Calculated clumped isotope temperature and fluid $\delta^{18}O$ values

Sample	T-Δ_{47} Kluge	T range		$\delta^{18}O_{fluid}$[1]	$\delta^{18}O_{fluid}$ range	
	°C	-	+	‰ VSMOW	-	+
TVZ - Geothermal						
WK-80	196	167	233	-3.5	-6.1	-0.7
Ngatamariki-Breccia	137	118	158	-4.6	-6.7	-2.5
BR-21-101	158	132	190	-2.6	-5.2	0.3
BR-6-15-150	152	135	171	-1.2	-3.0	0.7
BR-13-866	280	265	297	2.5	1.6	3.4
BR-27-400	237	212	265	1.1	-0.7	3.0
BR-15-1655	242	227	259	-2.4	-3.4	-1.3
BR-42-Ejecta	264	236	296	1.1	-0.7	3.0
Waihi - Epithermal						
UW462-BB23V	160	148	173	-4.6	-5.8	-3.4
UW462-879V	58	52	65	-7.6	-8.6	-6.5
UW462-BB58V	124	105	146	-3.9	-6.2	-1.5
SP0597-V	170	128	228	-4.3	-8.4	0.4
UW462-BB23R	174	146	208	-4.1	-6.7	-1.2
SP0597-R	116	107	126	-9.8	-11.0	-8.6
Antamina - Skarn						
4PAA157	166	133	208	5.6	2.3	9.3
4PAA129	178	157	203	4.4	2.4	6.5
4PAA178	168	132	215	4.2	0.6	8.2
4PAA219	125	94	163	0.4	-3.3	4.5
4PAA119	183	148	229	16.0	12.6	19.6
3PAA273	170	153	189	7.2	5.5	8.9
2PAG172	317	259	400	26.2	22.8	30.0
Mount Isa - Carbonate Hosted						
ISA105621150V	397	357	446	7.8	6.9	8.8
ISA105586A150V	297	272	326	6.2	5.3	7.2

[1] Fluid $\delta^{18}O$ calculated using the $\alpha_{calcite\text{-}water}$ in Kim and O'Neil (1997). Fluid values at Mount Isa calculated using $\alpha_{dolomite\text{-}water}$ in Horita (2014).

5.3.2 Waihi epithermal

Vein and replacement calcite at Waihi record Δ_{47} values between 0.373±0.045 and 0.536±0.014 ‰ ARF (Table 5.4). The calibrated temperatures for calcite veins near the principal Martha orebody are between 160^{+13}_{-12} and 170^{+58}_{-41} °C, while clumped

isotope temperatures of propylitic carbonate (e.g. groundmass calcite that replaced feldspars) from this area are between 116^{+10}_{-9} and 174^{+34}_{-28} °C (Figures 5.7 and 5.9). Veins ~1 km northwest of the ore body record cooler Δ_{47} temperatures of 58^{+7}_{-6} to 124^{+22}_{-19} °C. Calculated fluid $\delta^{18}O$ values range from -3.9 to -9.8 ‰.

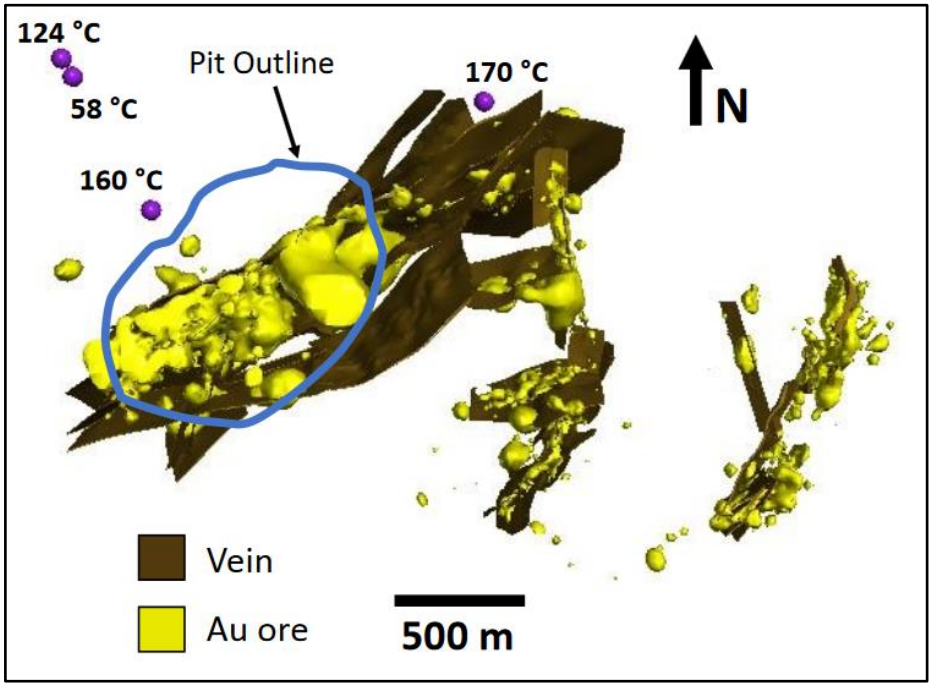

Figure 5.9: sample locations at Waihi, with vein clumped isotope temperatures reported. Samples were selected near the large NE-SW striking Martha vein system, and 300m to 1 km NW of the open pit mine. Yellow regions are defined by Au assay results greater than or equal to 1 ppm.

5.3.3 Antamina results

Samples measured at Antamina include a marble at the skarn contact with a Δ_{47} value of 0.283±0.027, and six Carbonate Replacement deposit (CRD) sulphide-bearing veins, collected ~300 m to 2 km from the intrusion, with values ranging from 0.361±0.034 to 0.423±0.044 (Table 5.4, Figure 5.7). Vein samples formed from cooler fluids outside the thermal front (e.g. the edge of the marble), at temperatures of 125^{+39}_{-30} to 183^{+46}_{-35} °C (Table 5.5). The marble (2PAG172) records an apparent equilibrium clumped isotope temperature of 317^{+82}_{-58} °C, while retaining a $\delta^{18}O$ value of 24.3 ‰, consistent with a sedimentary carbonate oxygen

isotope value for Cretaceous limestone (Banner and Hanson, 1990). The marble temperature reflects reordering of ^{13}C-^{18}O bonds during cooling from higher peak metamorphic temperatures associated with the intrusion (e.g., Dennis and Schrag, 2010; Lloyd et al., 2017).

5.3.4 Mount Isa results

Dolomite vein samples from the northern and southern ends of the Cu orebodies at Mount Isa record Δ_{47} values of 0.291±0.012 to 0.257±0.012, corresponding with temperatures between 297^{+29}_{-25} and 397^{+48}_{-40} °C (Figure 5.7, Table 5.5). Notably, the T-Δ_{47} record at Mount Isa overlaps previously determined temperature estimates for the ore body (~250 to 350 °C) from fluid inclusion homogenization and quartz-chlorite $\delta^{18}O$ thermometry (Heinrich et al., 1989; Hannan et al., 1993). We therefore interpret the record at Mount Isa to reflect the temperature of Cu mineralization, post-peak metamorphism, rather than apparent equilibrium temperatures reflective of the vein cooling history. These results suggest that preservation of high-temperature clumped isotope signals is possible over long (1.5 Ga) timescales.

5.4 DISCUSSION

5.4.1 Clumped isotopes in modern geothermal fields

Carbonate clumped isotope thermometry enables mapping of thermal signatures around ore bodies, at temperatures up to 350 °C (Figure 5.8). The temperatures calculated using the Kluge et al. (2015) calibration are most consistent with direct temperature and fluid inclusion homogenization measurements for the set of modern TVZ geothermal carbonates (Figure 5.8). The calculated fluid $\delta^{18}O$ for TVZ carbonates (-4.6 to 2.5 ‰) indicates moderate enrichment in ^{18}O for several high temperature samples relative to local ground water (-4.5 ‰), implicating fluid-rock reaction and/or some minor input of magmatic water in deep fluids (Simmons and Christenson, 1994; Dempsey et al., 2012). Clumped isotope temperatures were plotted against the difference between $\delta^{18}O_{calcite}$ (measured in this study) and reported $\delta^{18}O_{fluid}$ (Simmons and Christenson, 1994; Dempsey et al., 2012). Notably, this difference, expressed as $1000\ln\alpha_{calcite\text{-}water}$, indicates that TVZ calcite grew

under equilibrium conditions (Figure 5.10). Hence, oxygen isotope values of mineralizing fluids, may be determined with reasonable certainty, by combining clumped isotope temperatures and mineral oxygen isotope values.

Small offsets between well discharge fluid temperature, T_h, and T-Δ_{47} in geothermal samples are not unexpected (Figure 5.8). Prior work at Broadlands-Ohaaki indicates that fluid inclusion homogenization measurements vary by ~20 °C within individual calcite crystals (Simmons and Christenson, 1994). Direct measurements of fluid temperature that postdate carbonate growth may be lower than clumped isotope and T_h values (samples Br-21, Br-42), reflecting loss of enthalpy over the production lifecycle of the wellfield. Potential ^{13}C-^{18}O bond reordering by equilibration with water during sample preparation, may introduce additional uncertainty in measurement.

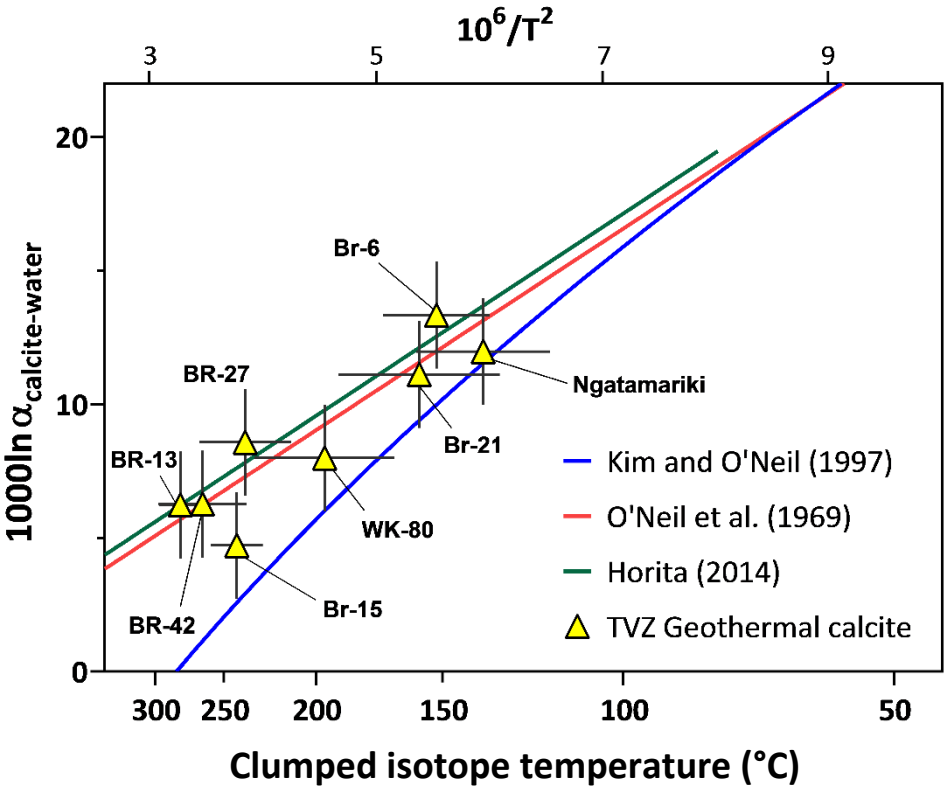

Figure 5.10: plotting Δ_{47} temperatures relative to $\delta^{18}O$ values of calcite and well discharge fluid, defined as $1000\ln\alpha_{calcite\text{-}water}$, indicates that samples reflect equilibrium growth conditions.

Although the choice of temperature calibration (e.g. Kluge et al., 2015 vs. Bonifacie et al., 2017) and fractionation factor (e.g. Kim and O'Neil, 1997 vs. Horita et al., 2014) affect interpretation of absolute temperature (Figure 5.8), and calculated fluid $\delta^{18}O$ (Table 5.5), the methodology used in this study is sufficient to identify thermal gradients, and fluid sources at the deposit scale (Figures 5.7-5.8, 5.11), regardless of calibration used (Figure 5.8). In settings where magmatic, meteoric, and metamorphic fluids are variably mixed (e.g. porphyries and skarns), Δ_{47} enables more accurate quantification of input from these different reservoirs (Figure 5.11). This is in line with recent work, in which T-Δ_{47} was applied to quantify fluid flux from deep sedimentary basins in MVT-style deposits in England (Dennis et al., 2018). In addition to isotope fingerprinting of fluids, clumped isotope thermometry unlocks new potential for single mineral barometry, by combined temperatures with fluid inclusion homogenization results, to define pressure (i.e. depth) within deposits (Roedder and Bodnar, 1980; Honlet et al., 2018).

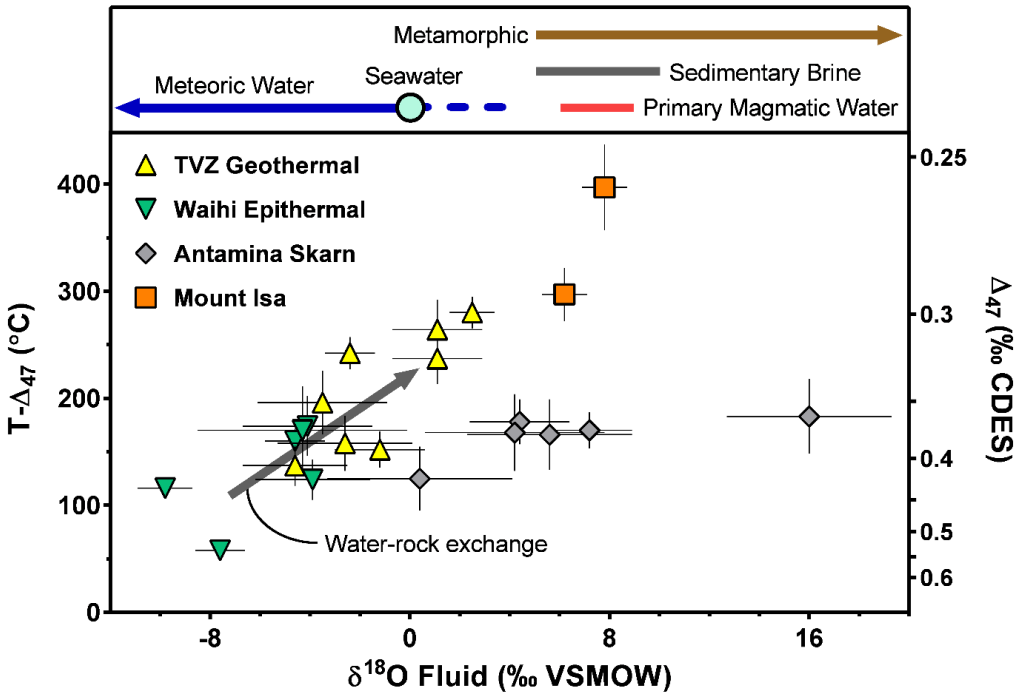

Figure 5.11: calculated fluid $\delta^{18}O$ plotted against calibrated temperatures (left vertical axis) and Δ_{47} values (right vertical axis) for geothermal and ore deposit samples. The apparent enrichment of aqueous fluid $\delta^{18}O$ observed for geothermal samples forming above 200 °C is consistent with limited modification of meteoric water by exchange with host-rock. Temperatures were calibrated using the Kluge et al. (2015) relationship. The $\delta^{18}O$ values of aqueous fluids were determined using fractionation factors for calcite-water (Kim and O'Neil, 1997) and dolomite-water (Horita, 2014). The isotope value ranges for terrestrial fluids reservoirs are from Giggenbach (1992) and Kesler et al. (1997).

5.4.2 Clumped isotopes in mineral exploration

In epithermal deposits, clumped isotopes enable differentiation between carbonate forming near hotter upflow conduits, which convey metal-rich fluids, and lower temperature peripheral veins where metals typically accumulate at subeconomic concentrations. Specifically, in systems where the hostrock is dominantly silicate (e.g. andesite hosted epithermal), the majority of variation in $\delta^{18}O$ of carbonate minerals is influenced by temperature. Notably, temperature, calculated from Δ_{47}, exerts strong control upon calcite $\delta^{18}O$ in the Waihi epithermal samples investigated here. Calcite $\delta^{18}O$ spans a range of ~11 ‰, while the calculated oxygen isotope value of fluid is less variable, ranging between -3.9 and -4.6 ‰ for four samples, while two samples indicate lower fluid values between -7.6 and -9.8 ‰ (Table 5.5). With control upon the $\delta^{18}O$-Δ_{47} relationship at Waihi, $\delta^{18}O_{carbonate}$ can then be used as a geothermometer to vector towards hotter upwelling zones. Applying this approach to a larger suite of samples, for which only $\delta^{18}O$ is known, in part, overcomes the lengthy sample processing time (2-3 hours per replicate analysis) imposed by the clumped isotope methodology used in this study. Such an approach has wide ranging potential in silicate hosted systems, where fluid-rock oxygen isotope exchange is relatively slow; however, in sediment-hosted systems (i.e. carbonate hosted), extensive dissolution and reprecipitation of carbonate hostrock make such an approach less effective. Nevertheless, compared with clay mineral relationships (Figure 5.2), which are insensitive to fine scale temperature variations, the outlined approach should enable more precise and confident temperature reconstructions in epithermal and geothermal environments, such as the volcanic hosted sites investigated here (i.e. Waihi, TVZ).

5.4.3 Methodological considerations

It is postulated that a build-up of H_2O in the sample preparation line periodically induced partial reset of the Δ_{47} signal in sample CO_2 liberated from carbonate by acid digestion. During carbonate sample digestion, CO_2 and a mixture of H_2O and trace gases are released. The gas transits through a dry ice-ethanol slush trap at -72 °C, which removes H_2O, with the CO_2 component sequestered further down in a liquid nitrogen trap. From here, sample gas is passed through a Poropak loop, to remove trace sulphur, organic, and chlorocarbon compounds. In the setup utilised

in this study, a small fraction of water passed through the first ethanol-slush trap and entered the Poropak loop, along with the sample CO_2. Thes effect of partial reset is apparent in higher temperature carbonates, for which the magnitude of Δ_{47} shift will be inherently higher. In Figure 5.12, positive values above sample means potentially imply that CO_2 from high temperature calcite (low Δ_{47}) has become partially equilibrated by H_2O during sample preparation.

Over the course of the study, it became apparent that carbonate samples prepared later in a working day generally recorded Δ_{47} values that are more positive than corresponding sample mean values, potentially due to a build up of H_2O in the preparation line (Figure 5.12). To counter this, the preparation line was baked, flushed with He, and pumped on for 75 minutes prior to each carbonate sample digestion. Samples and standards were measured in a random order, which ensured that early vs. late preparation did not bias results for any specific sample or deposit type. More efficient water freezing methodology, including the implementation of stirling cryocooler technology (e.g. Sakai et al., 2017), and reductions in sample size requirements, may diminish issues associated with partial Δ_{47} reset during sample preparation.

One deep geothermal scale sample from Broadlands-Ohaaki (BR-15-1655) exhibited a clumped isotope temperature of 242 °C, which is below mean values indicated by well fluid (290 °C) and T_h (308 °C). A statistical correction based on lab-specific empirical observations of samples that were partially equilibrated with water during purification yields an adjusted clumped isotope temperature of 308 °C for this sample. The agreement of the adjusted clumped isotope temperature and fluid inclusion temperature support the idea that modification of ^{13}C-^{18}O ordering during CO_2 sample preparation may explain the discrepancy. Monitoring for partial reset of Δ_{47}, to reflect lower apparent temperatures caused by exchange with H_2O during sample preparation, is critical towards reducing uncertainty and obtaining accurate results.

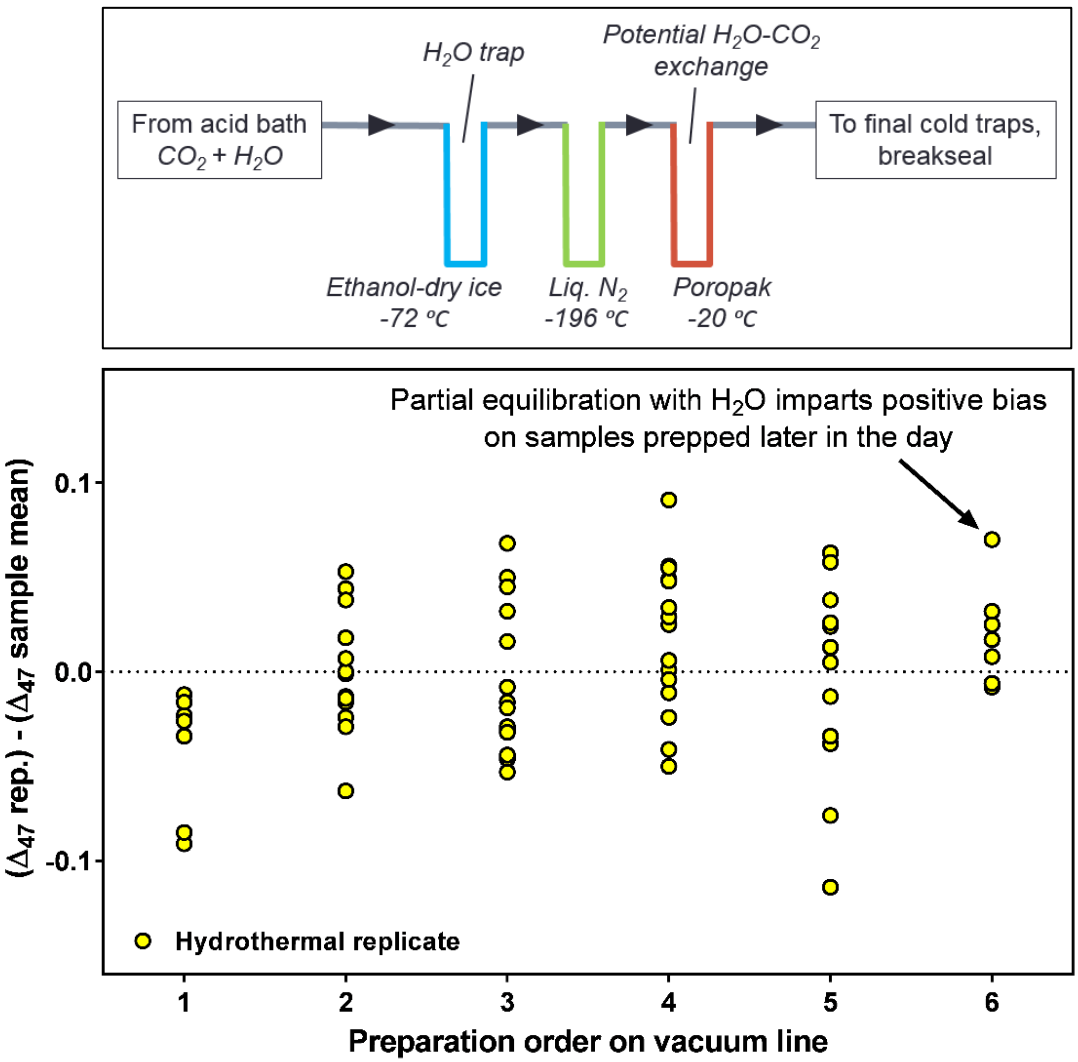

Figure 5.12: Upper panel: schematic of vacuum preparation line, illustrating the location of the Poropak trap, relative to ethanol and liquid N_2 traps. Lower panel: preparation order during the working day (horizontal axis) plotted against the distance from mean Δ_{47} (vertical axis). A value of 0 on the vertical axis indicates that the measured Δ_{47} value for a replicate is equal to the sample mean.

5.4.4 Future directions

Recent analytical developments have significant promise in terms of reducing time, sample size, error, and operational costs, making clumped isotope thermometry a useful tool in ore deposit investigations. The newly developed Long Integration Dual Inlet (LIDI) approach (Müller et al., 2017) lowers sample mass requirements and enables more analyses, providing the means to better overcome uncertainties resulting from intrasample heterogeneity (e.g. Defliese and Lohmann, 2015), which can be problematic when measuring fewer (3-5) replicates. Using the LIDI method,

aliquots of ~100 μg of carbonate are measured in 45 minute cycles (Müller et al., 2017). Issues associated with partial reset of clumped isotope temperatures, due to equilibration with water during sample preparation (Figure 5.12), can potentially be overcome by implementing advanced cryogen-free techniques for purification of CO_2 (e.g. Sakai et al., 2017). Recently developed infrared absorption spectrometers also provide an alternative platform for clumped isotope analyses (Nelson, 2016; Sakai et al., 2017; Prokhorov et al., 2019). Laser instruments may eliminate issues associated contamination imparted by sulphur, hydrocarbon, and chlorocarbon compounds, which frequently occur in hydrothermal carbonates, and interfere with measurement of $^{47}CO_2$. Although comparative studies using laser spectroscopy to measure carbonate clumped isotopes are yet to occur, recent work demonstrated successful Δ_{47} measurement of geothermal CO_2 by an optical instrument (Prokhorov et al., 2019).

5.5 CONCLUSIONS

The results presented here demonstrate that carbonate clumped isotopes provide valid temperature and fluid $\delta^{18}O$ constraints in modern geothermal areas, at temperatures up to ~300 °C. Temperature gradients defined by clumped isotope results in epithermal, skarn, and carbonate hosted settings overlap other studies. Further refinement of the clumped isotope method will provide a new tool to evaluate characteristics of ore deposit genesis, with respect to temperature, fluid source, and depth. This will prove especially useful in carbonate-hosted ore settings (e.g. skarns, Mount Isa, and Carlin-type Au), where temperature, hydrology, and the overall balance of magmatic and meteoric fluid are unclear (Figure 5.11). In epithermal deposits, Δ_{47} represents a new vector to hot upflow zones, where boiling drives deposition of Au, Ag and other metals. Given the demand for clumped isotope capability in academic venues, and growing interest in the mining and geothermal sectors, development of less expensive and more precise measurement platforms is anticipated over the coming years.

CHAPTER VI

Exploring carbon, oxygen, and hydrogen isotopic variation in epithermal systems using laser spectroscopy: insights from Waihi and Karangahake

---

This chapter presents a compilation of carbonate and hydrous mineral isotope data, collected using laser spectroscopy, from the Waihi and Karangahake low sulphidation epithermal deposits, North Island, New Zealand. OceanaGold provided access to whole rock pulp and drill core samples at Waihi. Mark Simpson (GNS) provided access to Karangahake samples.

Martha Pit, Waihi

Maria Vein, Karangahake Goldfield, circa 1919

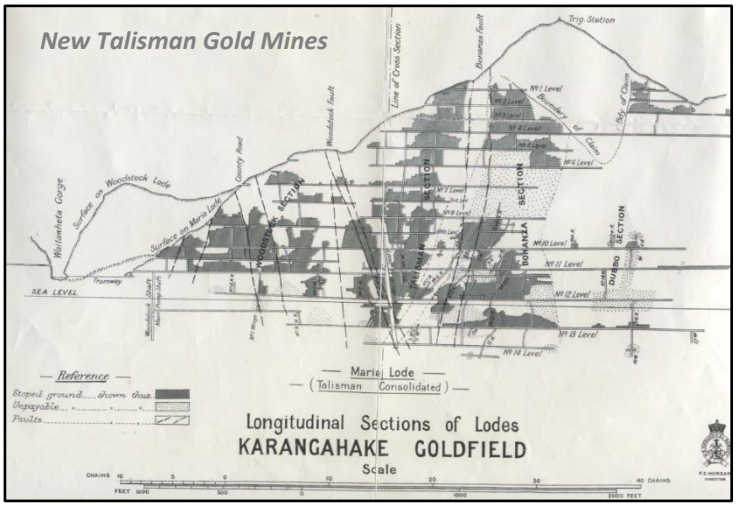

ABSTRACT

Herein, new stable isotope methods are applied to characterise the origin, movement, and temperature of fluids involved in propylitic alteration in low sulphidation epithermal areas. Hydrogen isotope ratios (δ^2H) in phyllosilicates and oxygen and carbon (i.e. $\delta^{18}O$ and $\delta^{13}C$) in carbonates were measured using OA-ICOS laser spectroscopy approaches in order to evaluate whether gradients in isotopic values exist around large epithermal veins that can be used to vector towards mineralisation. These methodologies were specifically developed for measurement of whole rock assay pulps, and are sufficiently rapid and inexpensive to be used in the mineral exploration industry. Measurements were carried out at two major andesite-hosted epithermal Au-Ag deposits within the Hauraki Goldfields, North Island, New Zealand. Measurements of δ^2H in whole rock pulps, and prepared clay separates, reveal that isotope results from the two sample media are identical within error. At Waihi, δ^2H in clay minerals ranges from -82 to -51, and is -68 ‰ on average, corresponding with a mean fluid value of -39 ‰ VSMOW. Variation in calcite $\delta^{18}O$ at Waihi is primarily controlled by temperature. With this understanding, oxygen isotope variation in propylitic calcite can be used to reconstruct temperature ranges within low sulphidation deposits, and likely other deposit types, including porphyry copper. Collectively, these results provide the groundwork to map paleo-hydrothermal fluid source, and temperature gradients, in intrusion-related hydrothermal ore deposits.

6.1 BACKGROUND

6.1.1 Stable isotopes in hydrothermal investigations

The interaction of fluids with host rock results in chemical alteration, dissolution, and replacement of existing assemblages. Evidence of fluid-rock interaction is quantified as alteration using a variety of textural and geochemical approaches. In addition to standard lithogeochemical techniques, stable isotope ratios of alteration minerals have the potential to identify fluid source, fluid volume, and temperature (Dilles et al., 1992; Djouka-Fonkwé et al., 2012). Characterization of isotopic signatures over large spatial extents is useful towards identifying prospective areas with higher fluid to rock ratios (e.g. Criss and Taylor, 1983; Criss et al., 2000; Barker et al., 2013), or elevated temperature (Mering et al., 2018).

Herein, two techniques utilizing OA-ICOS are applied to measure $\delta^{13}C$ and $\delta^{18}O$ in hydrothermal calcite (e.g. Barker et al., 2015) and $\delta^{2}H$ in clay alteration minerals (Chapters 3-4; Mering and Barker, 2018) at the Waihi and Karangahake low sulphidation epithermal deposits on the North Island, New Zealand. Near infrared laser absorption spectroscopy is an emerging technology, with the potential to rapidly quantify isotopic values in drill assay pulps produced during mineral exploration (Barker et al. 2011; Barker et al. 2013; Beinlich et al, 2017). To date, this is the first application study in which the isotope values of epithermal silicates and carbonates have been measured using laser spectroscopy. In most classes of ore deposit, clays and carbonates are extensive both near orebodies, and within the distal propylitic alteration footprint, making these minerals useful for deposit to district scale assessment of fluid isotope properties. Within propylitic zones, feldspars are replaced by calcite, epidote, illite, and prehnite, while biotite and hornblende are often replaced by chlorite and epidote (White and Hedenquist, 1995; Djouka-Fonkwé et al., 2012). The results presented here provide an in-depth assessment on the relative utility of clay and carbonate archives in epithermal exploration. More generally, the use of these approaches to measure fluid source and temperature in propylitic areas is applicable towards exploration of other classes of hydrothermal deposit (e.g. porphyry copper) and characterisation of geothermal reservoirs.

6.1.2 Fluid-mineral relationships in hydrothermal systems

A number of important contributions have been made in terms of applying isotope methods in carbonates and silicates to understand fluid properties in ore systems (e.g. Ohmoto, 1972; O'Neil and Silberman, 1974; Taylor, 1974; Bethke and Rye, 1979; Dilles et al., 1992; Nesbitt, 1996; Criss et al., 2000) and modern geothermal fields (e.g. Marumo et al., 1980; Giggenbach, 1992b; Marumo and Hattori, 1999; Mering et al., 2018). Historic studies in epithermal deposits in North America in the Idaho Batholith and the Comstock Lode indicate host rocks attain depleted $\delta^{18}O$ values near the locus of hydrothermal upwelling. Regionally, $\delta^{2}H$ in minerals has been used to identify distal fluid-rock alteration around epithermal districts at a scale of 10s to 100s of kilometres (e.g. Taylor 1977; Criss and Taylor, 1983). More recently, stable isotopes have been applied to routine exploration scenarios in carbonate hosted ore settings (e.g. Barker et al., 2013; Lepore, 2013; Vaughan et al., 2016; Beinlich et al., 2019). Significantly, isotope applications in exploration have utility towards establishing isotherms (e.g. Mering et al., 2018), and calculating fluid flux magnitudes (e.g. Waring 1998), which result in better understanding of fluid flow pathways.

Carbonates are highly sensitive to fluid properties of the hydrothermal systems in which they form. Specifically, $\delta^{13}C$ and $\delta^{18}O$ provide a measure of fluid source (e.g. H_2O and CO_2) and temperature. Broadly, precipitation of calcite in hydrothermal settings is attributed to the balance of pH, *p*CO2, temperature, and brine composition (Fournier, 1985). Processes that lower pCO_2 in epithermal systems, such as boiling, and mixing with low-CO_2 fluids, enable carbonate deposition (Zheng, 1990; Zheng and Hoefs, 1993; Simmons and Christenson, 1994). Carbonate deposition in the propylitic environment is also determined by availability of requisite cations (e.g. Ca^{2+}), sourced from dissolution of wall-rock minerals (e.g. calcic feldspars). There is abundant evidence demonstrating the cumulative influence of these processes in geothermal fields in the Taupo volcanic zone (TVZ), New Zealand (Simmons and Christenson, 1994; Simmons and Browne, 2000).

Variations in hydrogen isotope values in fluids are interpreted to reflect fluid source and modification by mixing (e.g. magmatic-meteoric), or boiling (e.g. Hedenquist

and Brown, 1989). However, equilibrium isotope fractionation relationships are not well constrained for many clay minerals (See Chapter 2, Section 2.2.5). There is a considerable range in published clay-water fractionation factors. Inconsistent results likely stem from the small sample sets used in clay-water fractionation studies, and inherent difficulty associated with attaining mineral-fluid equilibrium in laboratory settings. More work is needed to definitively identify, or rule out, thermal effects upon clay-water δ^2H fractionation over the temperatures relevant to geothermal and epithermal studies (100-300 °C). Consequently, δ^2H in clays is applied less frequently than $\delta^{18}O$ in carbonates and silicates in hydrothermal investigations. To address this, TD-OA-ICOS is applied here to demonstrate a tool that is capable of rapidly characterising δ^2H variation in ore deposits, and provide groundwork to support more expansive testing in natural systems in the future.

6.1.3 Geologic setting

Samples from epithermal areas on the North Island of New Zealand were selected for measurement. Waihi and Karangahake are the first and third highest producing Au epithermal deposits within the Hauraki Goldfield, with over a century of mining history (Figure 6.1). The structural controls and mineralogical associations relating to Au-Ag ore formation are well documented for these deposits.

The Hauraki Goldfield is host to a series of significant Au-Ag epithermal areas oriented along a 200 km North-South trend (Figure 6.1), which follows the now-extinct Coromandel volcanic zone (CVZ) arc (Brathwaite and Faure, 2002; Christie et al., 2007). Volcanism was active in the CVZ from 18 to 2 Ma, with cessation coinciding with the initiation of the modern Taupo volcanic zone to the south (Briggs et al., 2005; Booden et al., 2012). The lithology of the CVZ consists of Miocene and Pliocene volcanics that overly Jurassic greywacke and argillite of the Manaia Hill Group. Au-Ag mineralization occurs in andesite-dacite-rhyolite hosted quartz veins along steeply dipping fractures (Christie et al., 2007). Mineralization occurs over significant vertical extents at Waihi (575 m) and Karangahake (700 m), relative to other Coromandel epithermal areas (e.g. Golden Cross), where ore is typically distributed over less than 200 m (Brathwaite and Faure, 2002).

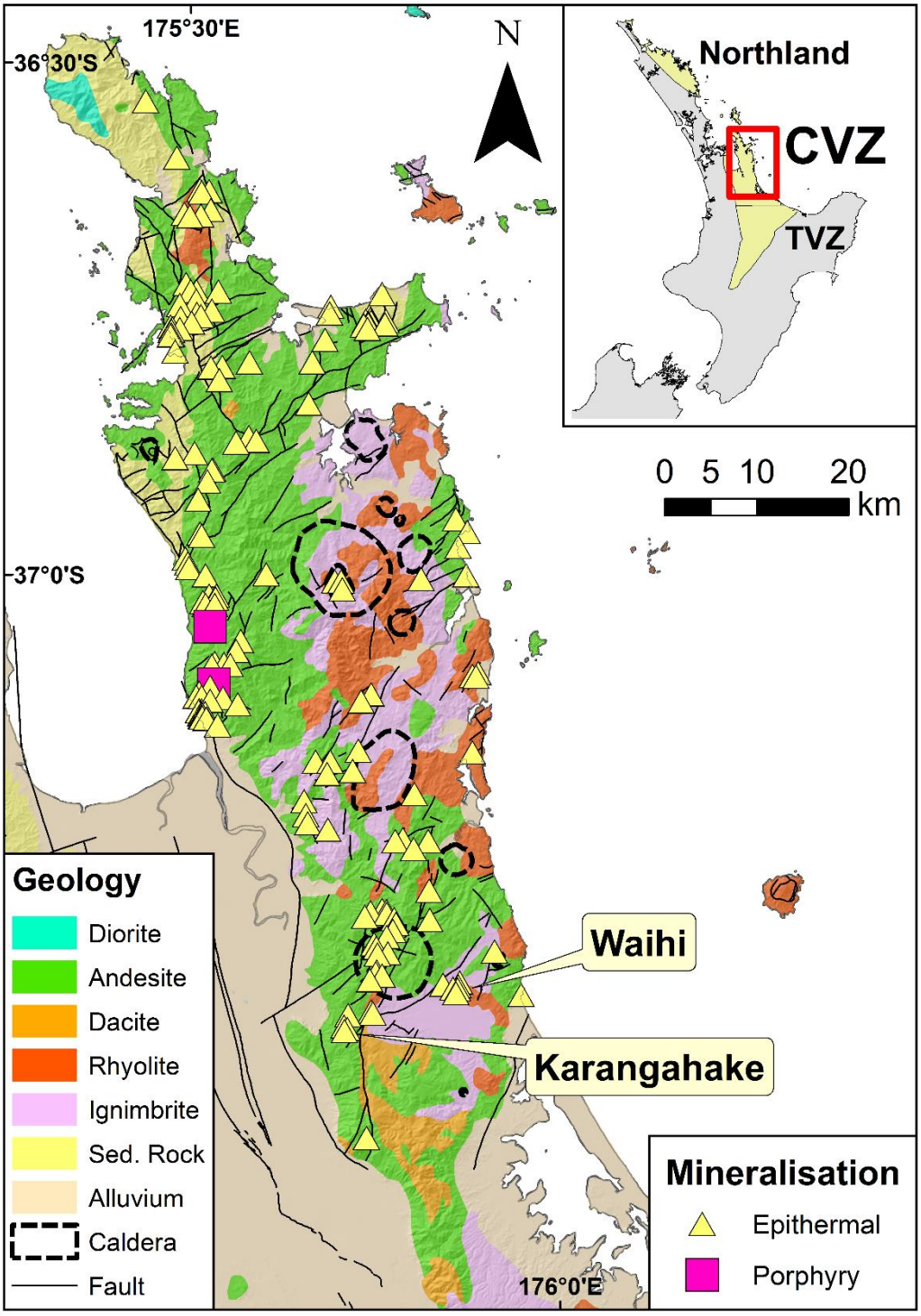

Figure 6.1: location of Waihi and Karangahake within the Hauraki Goldfield. The Hauraki Goldfields contain approximately 50 proven adularia-sericite epithermal Au-Ag deposits, which have been mined for over a century (Booden et al., 2012). Metal deposits become progressively younger from N-S, with hydrothermal activity at Waihi and Karangahake occurring in the late Miocene. This map was drawn from publicly available shapefiles developed for exploration purposes by NZ Petroleum and Minerals.

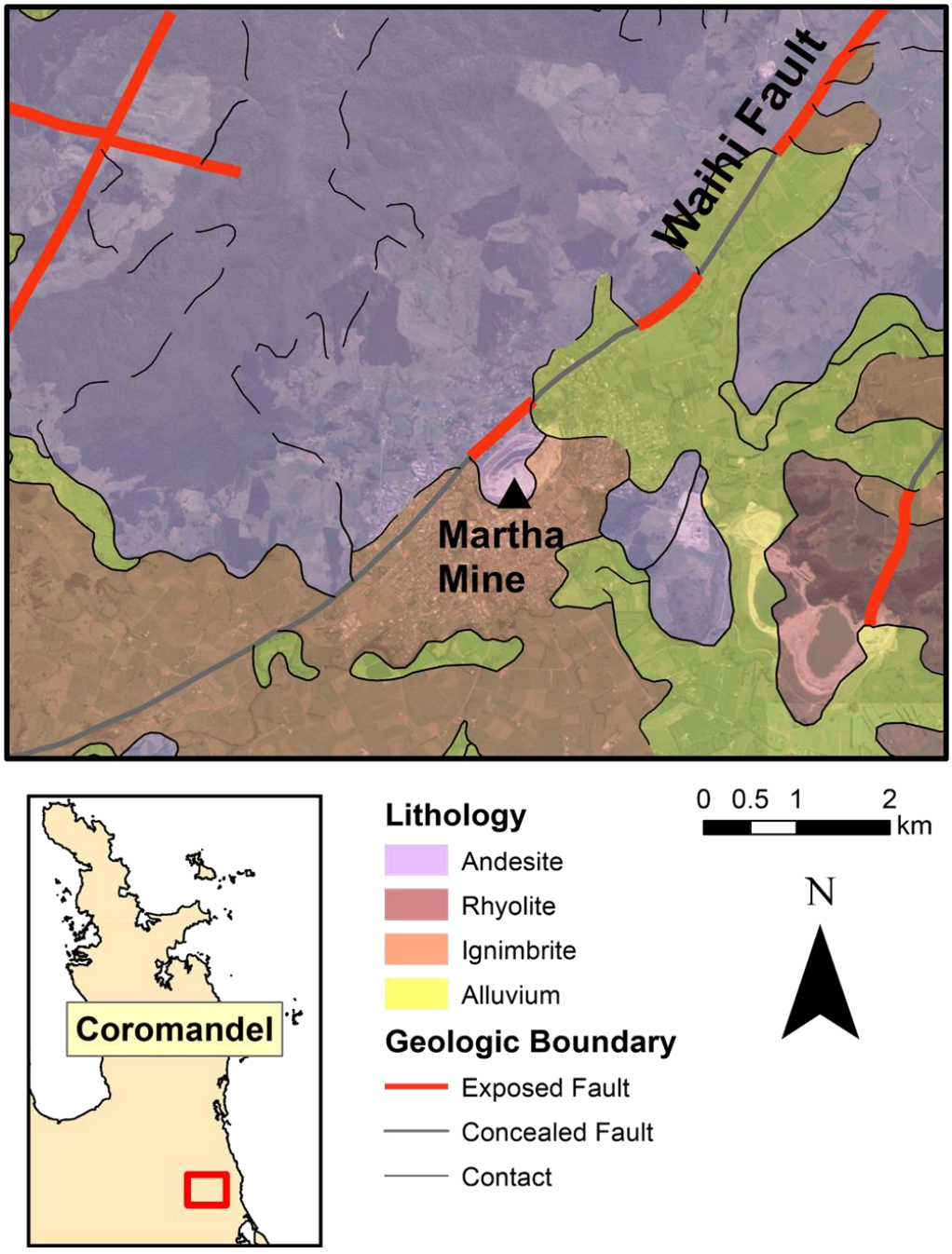

Figure 6.2: local geologic setting of the Waihi area. The Martha deposit has been mined since the late nineteenth century, and developed as an open pit resource since the 1990s. This map was drawn from publicly available shapefiles developed for exploration purposes by NZ Petroleum and Minerals.

Waihi, which covers an area of ~10 square km, is the largest epithermal deposit in the region (Figures 6.1-6.2). Epithermal veins at Waihi are hosted within andesite of the upper Miocene Waipupu Formation, of the Coromandel Group (Brathwaite and Christie, 1996). The history of emplacement of rock, subsequent deformation,

and hydrothermal alteration has been succinctly described (e.g. Brathwaite and Faure, 2002; Christie et al., 2007; Sporli and Cargill, 2011). Early deformation and fracturing was accompanied by intrusion of clastic dikes and sills. Continued local faulting, and emplacement of Au-Ag mineralized quartz veins has been dated at 6.16 ± 0.06 Ma (Booden et al., 2012). The principal host rock units exhibit a shallow SE dip; tilting is thought to predate hydrothermal activity (Sporli and Cargill, 2011).

Temperature at Waihi has been estimated quantitatively using fluid inclusion homogenization thermometry (Brathwaite and Faure, 2002) and clumped isotope thermometry (Mering et al., 2018). Fluid inclusion homogenization (T_h) estimates between ~190 and 300 °C been reported for quartz and platy calcite from mineralized upflow conduits (Brathwaite and Faure, 2002; Simpson, 2017). Clumped isotope thermometry demonstrates that calcite precipitation in propylitic areas outside of upflow zones occurred between ~60 and 180 °C, with temperature varying with respect to both palaeodepth and distance from major fluid conduits (Mering et al., 2018). Qualitative remarks regarding temperature gradients at Waihi have been made by applying clay mineral associations (Brathwaite and Faure, 2002; Bodger, 2015). Previous work at Waihi has characterized the extent of hydrothermal alteration using mineral species and lithogeochemistry (Brathwaite and Faure, 2002; Simpson and Mauk, 2007; Bodger, 2015; Barker et al., 2019). Carbon, oxygen, and hydrogen isotopes have been measured in calcite and quartz in upflow conduits (e.g. Brathwaite and Faure, 2002).

The Martha deposit was first mined in the late nineteenth century, with renewed exploration and production continuing from the 1970s to present. Since 2000, exploration and development has subsequently resulted in additional underground development at the Correnso, Favona, Trio, and Singleton vein systems, adjacent to Martha (Torckler et al., 2006; Christie et al., 2007). The Favona Vein system lies ~2 km east of Martha, and consists of a series of Au-Ag quartz veins, along a NE strike (Simpson and Mauk, 2007). Underground mining at Favona occurred between 2006 and 2014, while production in the adjacent Trio mine began in 2012 (Christie et al., 2007; Simpson and Mauk, 2007). Mining began at Correnso in 2016 and is ongoing, via a series of underground workings.

Karangahake, which is situated ~11 km SW of Waihi is historically the third most productive epithermal area within the Hauraki Goldfields (Christie et al., 2007; Simpson et al., 2019). As at Waihi, Au mineralization at Karangahake occurs within steeply dipping quartz veins, which cut through fractured sections of andesite. Important veins at Karangahake include Maria and Crown, and Welcome, which strike approximately N-S (Simpson et al., 2019). Mineralization has been dated to between 6.9 and 5.7 Ma by $^{40}Ar/^{39}Ar$ methodology (Booden et al., 2012; Simpson et al., 2019). Lithogeochemical characterization of samples is reported elsewhere (Simpson et al., 2019), using a variety of standard techniques including, XRD, EDS, portable XRF, and automated mineral mapping. Samples analysed at Karangahake are from units of green to grey altered porphyritic andesite. Samples are dominantly comprised of quartz-adularia-albite with alteration minerals that include illite, chlorite, smectite, illite-smectite, calcite, and pyrite.

6.1.4 Motivation

This work applies new isotopic methods to evaluate the extent to which carbon, oxygen and hydrogen isotope chemistry reflect thermal conditions and fluid source in well-constrained epithermal areas. At Waihi, deposit-scale (3 x 2 km) measurements of carbon and oxygen in calcite are carried out in samples from 13 boreholes (Figure 6.3). These are paired with hydrogen isotope measurements across a similar spatial extent. Specifically, carbonate isotopes (i.e. $\delta^{13}C$, $\delta^{18}O$) are evaluated at Waihi to identify trends in fluid evolution and/or temperature. Hydrogen isotope results from Waihi, Karangahake, and Comstock (reported in Chapter 4) allow for interpretation of the extent to which $\delta^{2}H$ changes across a given epithermal area, and whether variation is correlated with fluid source, mineralogy, and proximity to mineralised veins.

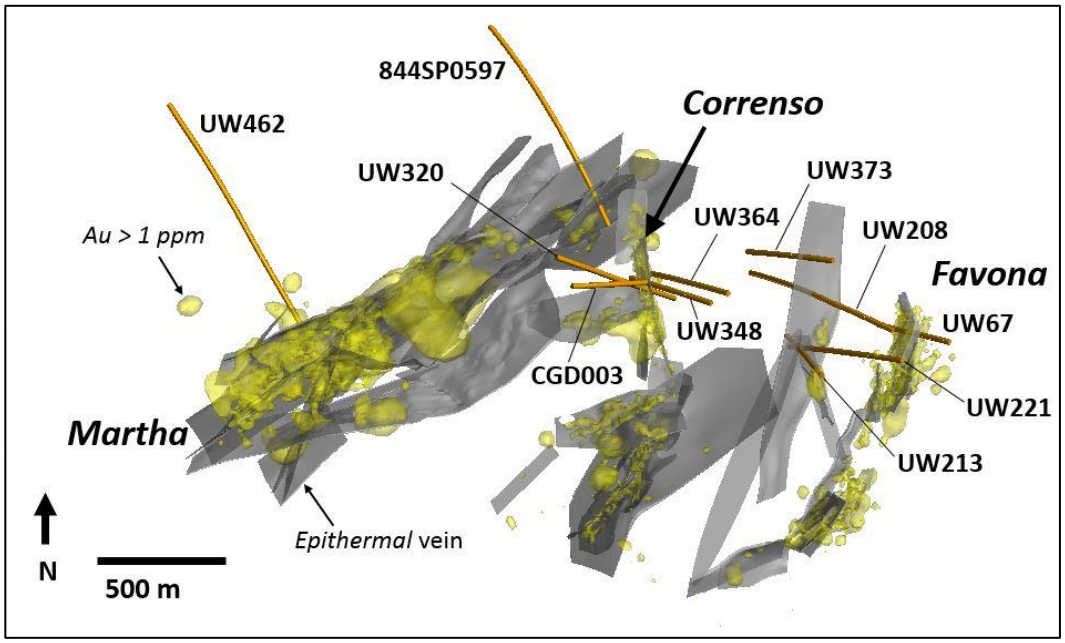

Figure 6.3: vein framework at Waihi with locations of Au grade exceeding 1 ppm. The boreholes sampled here are highlighted in orange. Figure drawn in Leapfrog® from the near mine exploration data archive provided by OceanaGold.

6.2 METHODS

6.2.1 Clay mineral hydrogen isotope OA-ICOS protocol

Hydrogen isotopic abundances were measured in whole rock composite samples and clay separates using a continuous flow laser spectroscopy approach (Mering and Barker, 2018). Mineral powders were weighed into silver capsules, and dried under vacuum for 5 hours at 195 °C. Dried samples were rapidly loaded into a Costech Zeroblank autosampler, which was then purged with dry air for 20 minutes. Hydrous mineral powders were dropped from the autosampler into a heated quartz column, operated at 945 °C. Rapid thermal dehydroxylation in the column generates a water vapour pulse, which is measured using a LGR OA-ICOS instrument (IWA-34 EP), operated in a continuous flow configuration (Mering and Barker, 2018). Hydrogen isotope ratios (i.e. $^{2}H/^{1}H$) are calculated from isotopologue concentration data, and normalized to the VSMOW scale using hydrous mineral reference standards (Table 6.1). Precision of measurements, not impacted by intersample memory, was typically between 0.5 and 1.5 ‰ VSMOW.

Table 6.1: hydrogen isotope reference materials

Standard	δ^2H (‰ VSMOW)	Mineralogy
G-18502	-23.8	muscovite
USGS 58	-28.4	muscovite
Kga-1b	-50.5	kaolinite
G-18499	-51.1	muscovite
Serp-HS-1	-135.3	serpentine
WS-1	-162.4	serpentine

Water content, and approximate δ^2H value in samples, was determined by first analysing single replicates, alongside Kga-1b kaolinite, which has an established H_2O content of 13.7 % by weight. For the yield function, Kga-1b was measured over range of amounts between 1.5 and 4.4 mg, corresponding with 0.2 and 0.6 µL H_2O (see Chapter 3, Section 3.3.4). Subsequently, samples were weighed to achieve 0.2 to 0.5 µL H_2O, and measured in groups of 2-4 replicates. At Waihi, δ^2H was measured in 308 replicate measurements of 127 pulp samples, and 18 prepared clay separates in 10 drillholes. At Karangahake, δ^2H was measured in 52 replicate measurements of 28 clay separate samples.

Correct interpretation of heterogeneous samples (i.e. pulps) requires accurate determination of hydrous mineral composition within samples. Clay mineralogy was measured by XRD on clay separates, and is also available for Martha, Correnso, and Favona from several prior studies (Bodger, 2015; Hughes and Barker, 2018), which made use of XRD and automated mineralogy (i.e. TIMA) protocols (Bodger, 2015; Simpson et al, 2019). Clay separates were prepared by isolating clay sized fractions by disaggregation, deflocculation, and centrifugation of samples. Whole rock pulps were disaggregated in a deflocculant (sodium hexametaphosphate 0.15g/L) solution that was subjected to ultrasonic and centrifuge treatment. The supernatant fraction, containing clay, was pipetted onto glass slides for XRD analysis, and the remaining clay fraction was sequestered for isotope measurement, and dried at 45 °C overnight. The clay residue was subsequently powdered, weighed into silver capsules, and analysed identically to whole rock pulps for δ^2H. The clay separate procedure requires approximately three minutes additional preparation time per sample, but has the added benefit of eliminating issues associated with introducing sulphides, and other Fe bearing materials, into the analytical apparatus (see Chapter 4, Section 4.4.1)

6.2.2 Determining mineral-specific clay-water δ^2H fractionation

In light of the present uncertainty regarding published clay-water fractionation relationships, the Ohnuma geothermal clay geothermal dataset (i.e. Marumo et al., 1980) is a reasonable choice to guide interpretation of whole rock δ^2H data collected at Waihi and Karangahake. In that study, hydrogen isotope measurements were performed upon kaolinite, illite, and chlorite minerals, and associated fluids from geothermal wells at temperatures between 50 to 250 °C. Mineral-specific fractionation factors were developed from geothermal clay results reported in Marumo et al., 1980. Samples containing illite, illite-smectite, and smectite alteration minerals were assigned a mineral-water fractionation of -26 ‰, while samples containing chlorite were assigned mineral-water fractionation of -35 ‰.

6.2.3 Hydrothermal carbonate methodology

Calcite was identified in core and assay pulps by testing reactivity of samples with 10 % HCl. Petrographic characterizations were carried out to identify textures in carbonate veins (e.g. microcrystalline vs. bladed calcite) and the presence of calcite replacing feldspar phenocrysts. Polished mounts observed under cathodoluminescence (CL) light revealed the distribution of calcite in samples.

290 isotope measurements were carried out on 195 pulp, and drilled vein and replacement calcite samples. Samples include 166 whole rock assay pulps, 17 drilled veins, and 6 replacement samples. In addition, 4 vein and 2 replacement samples were measured by IRMS in the previous chapter. Whole rock pulps and drilled powders were weighed to achieve 0.25-1.0 mg $CaCO_3$, and measured using an OA-ICOS system, following protocol outlined elsewhere (Barker et al., 2011; Barker et al., 2013; Beinlich et al, 2017).

Samples were reacted with 102% orthophosphoric acid at 72 °C in exetainer vials for a minimum of two hours prior to analysis. CO_2 was passed through an ethanol-dry ice slush trap to remove water, and the mixing ratios of isotopologues were measured on an LGR CCIA-48 OA-ICOS analyser. Calculated isotope ratios ($^{13}C/^{12}C$, $^{18}O/^{16}O$) are reported as $\delta^{13}C$ and $\delta^{18}O$ values, and calibrated to international scales (VSMOW and VPDB), using reference materials. Calcite

content in pulp samples was determined during stable isotope analysis by quantification of the total CO_2 yield for pulps, relative to yields for high purity calcite analytical standards.

Several correction and standardisation procedures are applied to data. Concentration dependency of the OA-ICOS instrument was corrected for by carrying out gas yield corrections using an in-house carbonate standard analysed over a range of masses from 0.2 to 2.0 mg. A CO_2 gas standard of known isotopic value was measured at regular intervals to correct for drift. Two international carbonate standards (NBS-18, NBS-19), and up to four internal standards (Sigma, WCS, BDH, BN-13) were analysed in order to translate isotope results to international scales. All results are reported in units per mil (‰) on the VPDB scale for carbon isotopes, and VSMOW scale for oxygen isotopes. The isotope values for standards are listed below in Table 6.2.

Table 6.2: Calcite reference materials

Standard	$\delta^{13}C$ (‰ VPDB)	$\delta^{18}O$ (‰ SMOW)
NBS18	-5.01	7.20
NBS19	1.95	28.60
BDH	-24.95	16.49
BN13	1.82	13.72
GNS	-2.04	24.31
Sigma	-14.18	10.22
WCS	-10.27	27.76

Initially, the OA-ICOS carbonate instrument was operated in a semi-online configuration (e.g. Barker et al., 2011). Further modification of this analytical setup was carried out in the second half of the project to develop a more rapid continuous flow configuration, as has been done for isotopic analyses of water extracted from hydrous minerals (see Chapters 3-4; Mering and Barker, 2018). In the final hardware setup, CO_2 was continuously flushed from sample vials into the analytical cell of the OA-ICOS. This setup decreased analytical time from ~6 minutes per sample to ~2 minutes. In both configurations, the typical precision of $\delta^{13}C$ and $\delta^{18}O$, represented by the 1σ of measurements of reference materials, is between 0.2 and 0.4 ‰.

6.3 HYDROGEN ISOTOPE RESULTS AND INTERPRETATION

6.3.1 Analytical results

Hydrogen isotope results are presented in Table 6.3, Figure 6.4 and in Appendix C. Hydrogen isotope values in pulps at Waihi ranged from -80.6 to -50.8 ‰, and are -68.1±6.4 ‰, on average. Hydrogen isotope values in clay separate samples are between -82.3 and -61.3 ‰, and are -72±5.5 ‰, on average. Hydrogen isotope values at Karangahake are similar to Waihi, ranging from between -79.3 and -61.5 ‰, and are -73.6±4.2 ‰, on average. For comparison, Comstock, δ^2H values measured by OA-ICOS are -133.1±9.3 ‰, on average (reported in Chapter 4). In Table 6.3 whole rock hydrogen isotope results and calculated fluid values are presented.

Table 6.3: Hydrogen isotope results in epithermal areas. δ^2H was measured in whole rock assay pulps at Waihi and in clay separates at Waihi and Karangahake. For comparison δ^2H results from Comstock (reported in Chapter 4) are also shown.

Locality		N. Samples	δ^2H (‰ VSMOW)			
			Whole rock[1]			Fluid[2]
			Max.	Min.	Mean	Mean
COMSTOCK		**12**	**-121**	**-160**	**-133**	**-103**
KARANGAHAKE		**28**	**-61**	**-79**	**-74**	**-42**
WAIHI		**131**	**-51**	**-82**	**-72**	**-39**
Martha-NW	UW462	31	-61	-82	-73	-43
Martha-NW	844SP0597	25	-66	-74	-70	-40
Correnso	UW320	20	-68	-76	-72	-42
Favona	UW373	11	-52	-65	-58	-28
Favona	UW208	10	-62	-68	-66	-35
Favona	UW213	6	-61	-69	-65	-34
Favona	UW221	7	-59	-67	-63	-33
Favona	UW67	5	-59	-70	-62	-32
Favona	UW85	16	-51	-75	-68	-38

[1] OA-ICOS measurement

[2] Calculated from chlorite and illite fractionation results (Marumo et al., 1980)

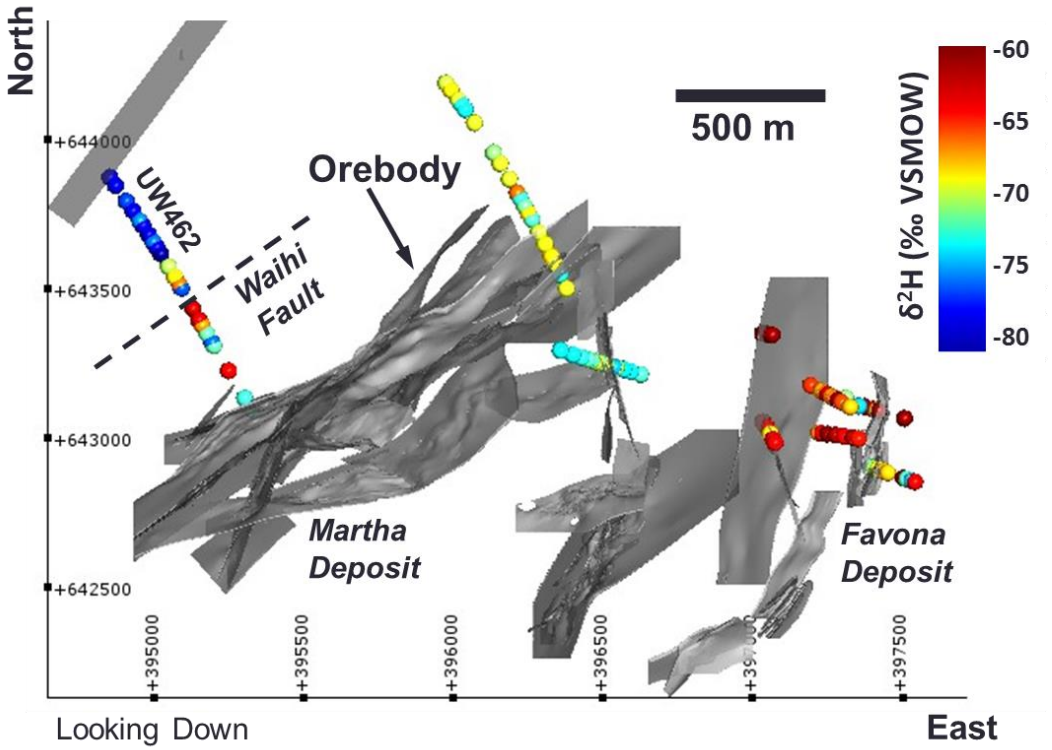

Figure 6.4: hydrogen isotope (δ^2H) variation in hydrous minerals at Waihi. δ^2H is lowest in samples distal to the Martha vein system in the UW462 borehole, and most positive in Favona samples. Hydrogen isotope values increase at the Waihi Fault. Significant vein structures are shown in grey. Drillhole data and vein locations from OceanaGold exploration database. Figure drawn using Leapfrog Geo 3D modelling software.

6.3.2 Results compared for clay separates and whole rock assay pulps

Preparing clay separates of fine fraction materials effectively doubled water yields from samples, but produced similar δ^2H results (Figures 6.5-6.6). In a comparative analysis of pulps and clay separates in 13 samples at Waihi, δ^2H is on average 1.2 ‰ higher for pulps. Water content in clay separates from Waihi and Karangahake are similar, at 5.5±1.1 and 5.2±1.0 weight percent, respectively (Appendix C). Close agreement of δ^2H measurements of pulps and prepared separates indicate that data from either can be used interchangeably at Waihi. For measurements of three pulp samples, δ^2H was ~6 ‰ higher than corresponding clay separates. Observed ^2H enrichment in pulps relative to clay separates may indicate Fe-induced reduction of water in samples containing pyrite (e.g. Mering and Barker, 2018).

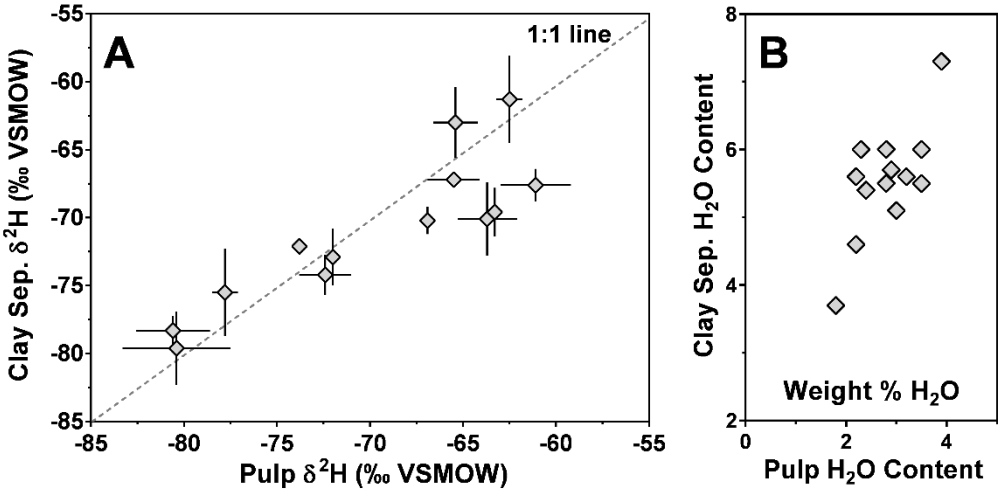

Figure 6.5: Panel A: δ^2H relationship for assay pulp and clay separate samples at Waihi. Close agreement in isotope values for these two sample sets indicate that results may be used interchangeably, unless the utmost accuracy is desired. Panel B: comparison of water content in whole rock pulp and clay separates at Waihi. Preparation of clay separates for hydrogen isotope analysis effectively doubled the water content in samples.

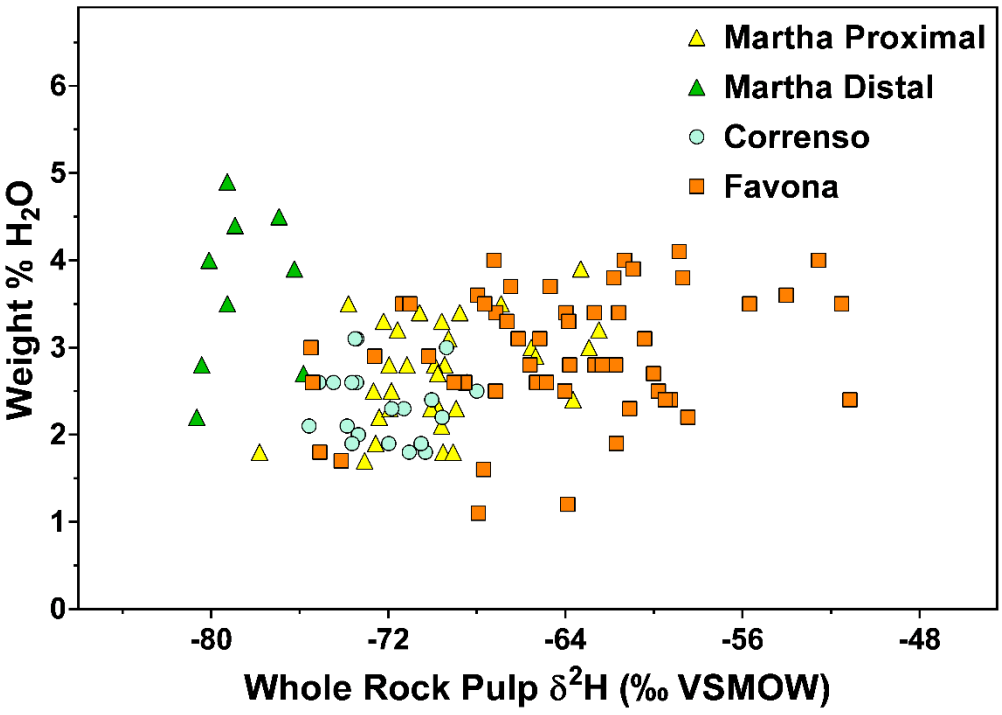

Figure 6.6: comparison of whole rock δ^2H and water content in Waihi assay pulps. Water content in pulps at Waihi ranges from 1.1 to 4.9 weight percent H_2O, and is 2.9±0.7 % on average.

6.3.3 Hydrogen isotope interpretation

At Waihi, Karangahake, and Comstock, whole rock hydrogen isotope signatures are 20-50 ‰ lower than local meteoric waters, or estimates for paleohydrothermal fluid, obtained by measurement of fluid inclusion water (Figure 6.7). This apparent depletion is consistent with prior work on clays collected in modern geothermal areas (e.g. Marumo et al., 1980; Hedenquist and Browne, 1989) and other epithermal sites (e.g. Faure et al., 2002). The application of weighted fractionation factors that take chlorite content into account in samples at Waihi and Karangahake resulted in calculated fluid δ^2H values of -39 and -42 ‰, respectively. The results recorded here overlap with the range of δ^2H values recorded in fluid inclusions in Brathwaite and Faure (2002).

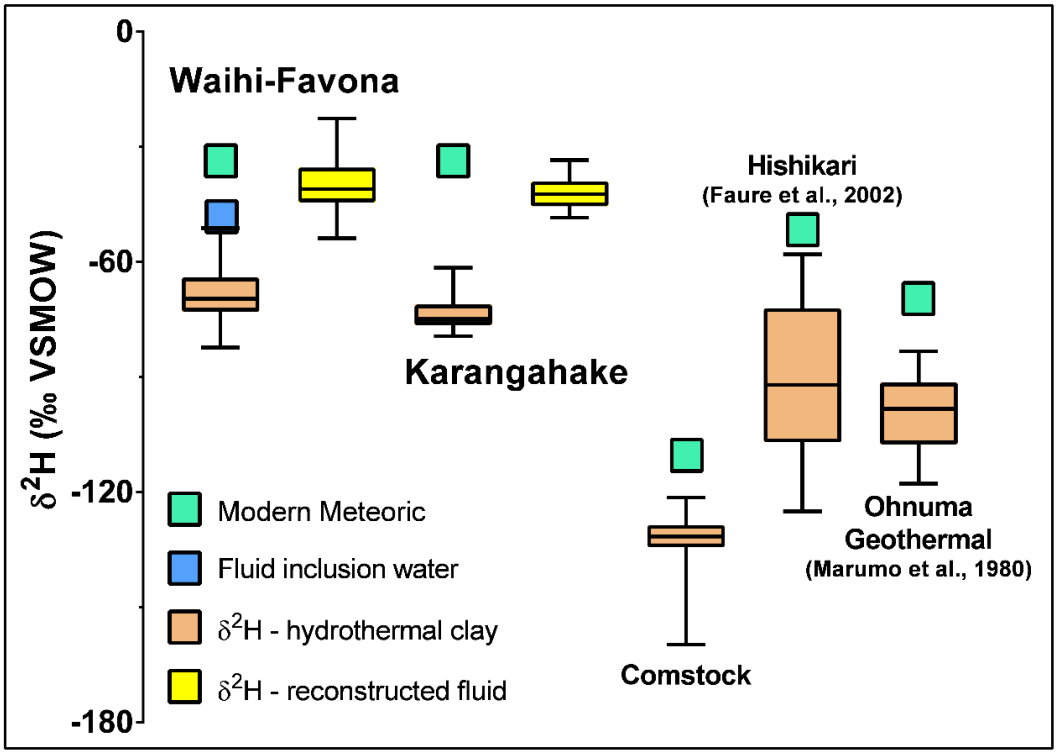

Figure 6.7: δ^2H at epithermal and geothermal areas plotted relative to the values of local meteoric water. The fluid inclusion δ^2H range at Waihi is presented in Brathwaite and Faure (2002). The differences in hydrogen isotope values between each region largely correspond with the isotopic value of local meteoric water. The δ^2H value of modern rainfall at Waihi and Karangahake is -34±6 while precipitation at Comstock is -103±8 ‰, on average (Bowen, 2019).

6.3.4 Mineral δ^2H and hydrothermal fluid

In general, the δ^2H fluid values reconstructed at Waihi and Karangahake are lower than the modern local precipitation value of -34 ‰ (Bowen, 2019). Although the isotopic signature of meteoric fluid feeding these systems is not precisely known, the range of modern values across the North Island provide a reasonable basis for comparison. If precipitation at Waihi and Karangahake were sourced from 360 m above sea level, the modern elevation of Lake Taupo, the resulting δ^2H is expected to shift to -38 (Bowen, 2019). Notably, the average δ^2H of fluid inclusion water in quartz and calcite veins measured at Waihi in a prior study is -48 ‰, and ranges from -29 to -64 ‰, indicating some degree of variability across the system (Brathwaite and Faure, 2002).

At Waihi, some variability is expected between infiltrating meteoric fluid, boiled ascending chloride fluid, and acid sulphate waters. Evaluation of the isotope characteristics of fluids in modern metal producing geothermal areas provide a sense of the range of expected values for the Waihi system. At Waiotapu, the δ^2H values of deep chloride fluids and boiled upflow are ~10 ‰ higher than local precipitation and marginal steam-heated groundwaters (Hedenquist and Browne, 1989). Notably, acid sulphate alteration associated with steam heated shallow groundwater is also ~12 ‰ higher than meteoric fluid (Hedenquist and Browne, 1989). In the shallower Favona deposit at Waihi, mean whole rock δ^2H values in boreholes range from -58 to -68 ‰, corresponding with reconstructed δ^2H_{fluid} values of approximately -28 to -38 ‰. These are isotopically heavier than mean whole rock (-72 ‰), and reconstructed fluid (-39 ‰), across the Waihi deposit (Table 6.3).

In general, it is difficult to reliably identify, or rule out, the presence of magmatic fluid at Waihi and Karangahake using δ^2H. Juvenile mantle water δ^2H is -65±15 ‰, although there is some evidence to suggest that andesitic water at convergent plate margins around the Pacific (e.g. New Zealand) is around -20±15 ‰ due to incorporation of seawater (Giggenbach, 1992b). The relative proximity of either value to that of meteoric fluid at Waihi and Karangahake makes it such that a minor magmatic fluid component will not induce a detectable shift in the overall δ^2H signature of hydrothermal fluid.

6.3.5 Hydrogen isotope results compared to measures of alteration intensity

At Waihi, there is a moderate correlation between the Rb/Sr ratio and whole rock δ^2H (Figure 6.8). Elevated Rb/Sr ratios indicate incorporation of Rb into K sites in alteration minerals, while depletion of Sr reflects destruction of calcic minerals (Plimer and Elliott, 1979; Shah et al., 1994). In Figure 6.8 hydrogen isotope results are paired with whole rock Rb/Sr values determined elsewhere (i.e. Bodger, 2015; Hughes and Barker, 2018). At Waihi, a whole rock δ^2H value more positive than -70 ‰ corresponds with a mean Rb/Sr of value of 3.4, while the average Rb/Sr value is 2.1 for samples with δ^2H below -70 ‰. Higher δ^2H values in Favona samples possibly reflect some alteration by acid sulphate fluid, resulting from interaction with the water table (Simpson and Mauk, 2007).

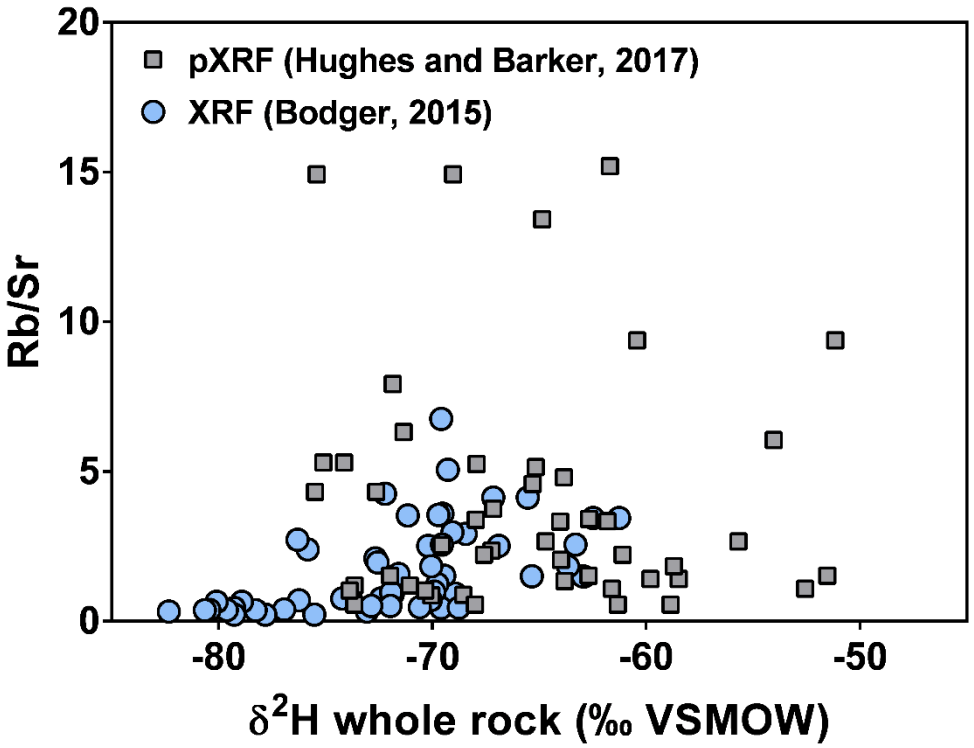

Figure 6.8: plot of measured whole rock hydrogen isotope values (this study) against Rb/Sr data. Elemental results were collected elsewhere using either XRF (Bodger, 2015) or portable XRF (Hughes and Barker, 2017).

A 1 km horizontal borehole drilled NW of the Martha mine (UW462) presents a unique opportunity to evaluate hydrogen isotope signatures across a range of mapped alteration zones, moving away from principal hydrothermal upflow conduits (Figures 6.9-6.10). Whole rock δ^2H, and general trends in clay mineralogy, are depicted in Figure 6.9. Areas of weakly to pervasively silicified rocks, which contain illite and calcite, are proximal to Au-Ag bearing quartz veins. The illite zone grades into a mixed illite-smectite (IS) zone (Bodger, 2015). Within the IS zone, feldspars (i.e. plagioclase) are replaced by calcite and/or illite and adularia, pyroxenes are replaced by chlorite and calcite, and magnetite is replaced by pyrite and titanite (Brathwaite and Faure, 2002; Bodger, 2015). An outer smectite±chlorite zone defines the lowest intensity alteration, where glass in andesitic groundmass has been converted to smectite and chlorite-smectite.

In this case example, the value of whole rock δ^2H is -69.0±5.2 ‰ VMOW (n=19) over the first 576 m, where illite clays are more prevalent. From 576 to 936 m, the mean δ^2H is -79.0±1.9 ‰ VMOW (n=12). The elevated δ^2H value, observed in the first 576 m of sampling, corresponds with elevated concentrations of pathfinder elements (As, Sb), and higher Rb/Sr ratios (Figure 6.10). The K/Al value, defined as a proxy for adularia elsewhere (Hughes and Barker, 2018), is also generally higher in zones of elevated δ^2H. Increased concentrations of pathfinder elements, and evidence of alteration and replacement minerals is consistent with increased volume and/or duration of heated upwelling of fluids with an elevated δ^2H signature. Carbonate isotope variation is discussed along the UW462 trend in the following sections.

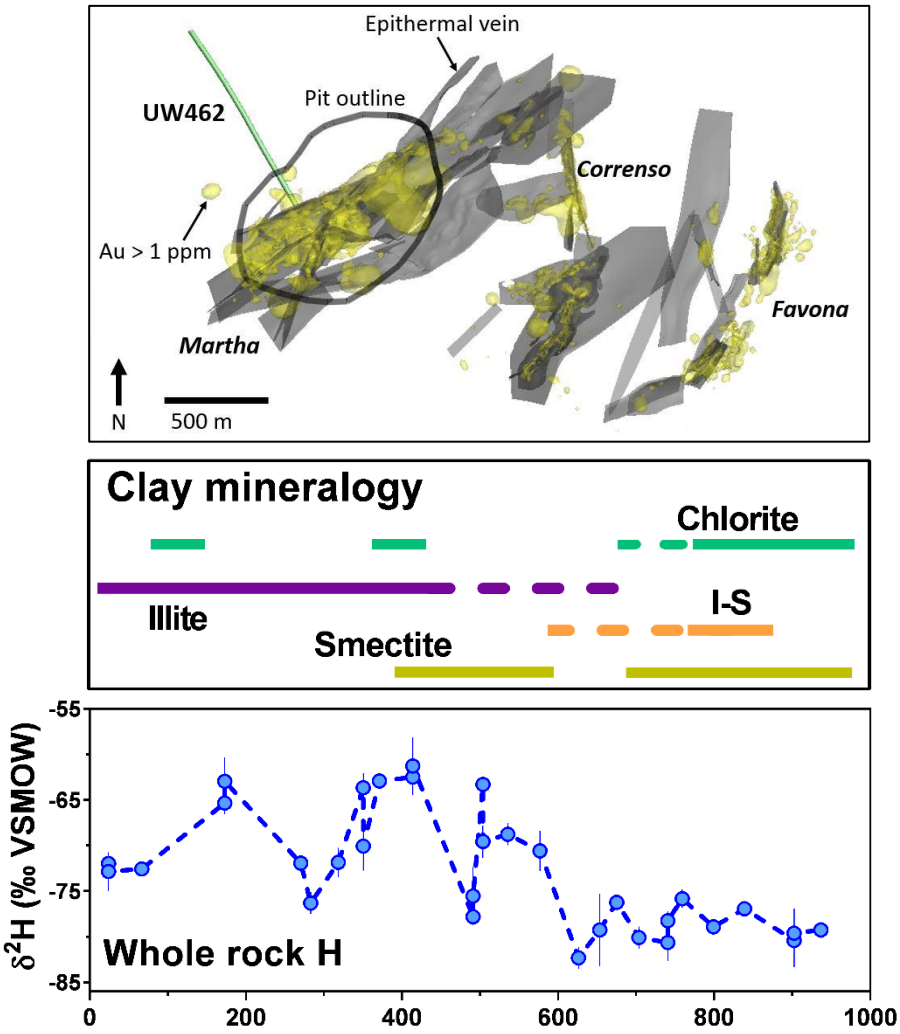

Figure 6.9: the UW462 borehole covers a horizontal extent of ~1 km, and includes both high and low intensity alteration areas. Upper panel: location of the UW 462 borehole. Middle panel: clay mineralogical trends presented in Bodger (2015). Lower panel: whole rock δ^2H measured in this study.

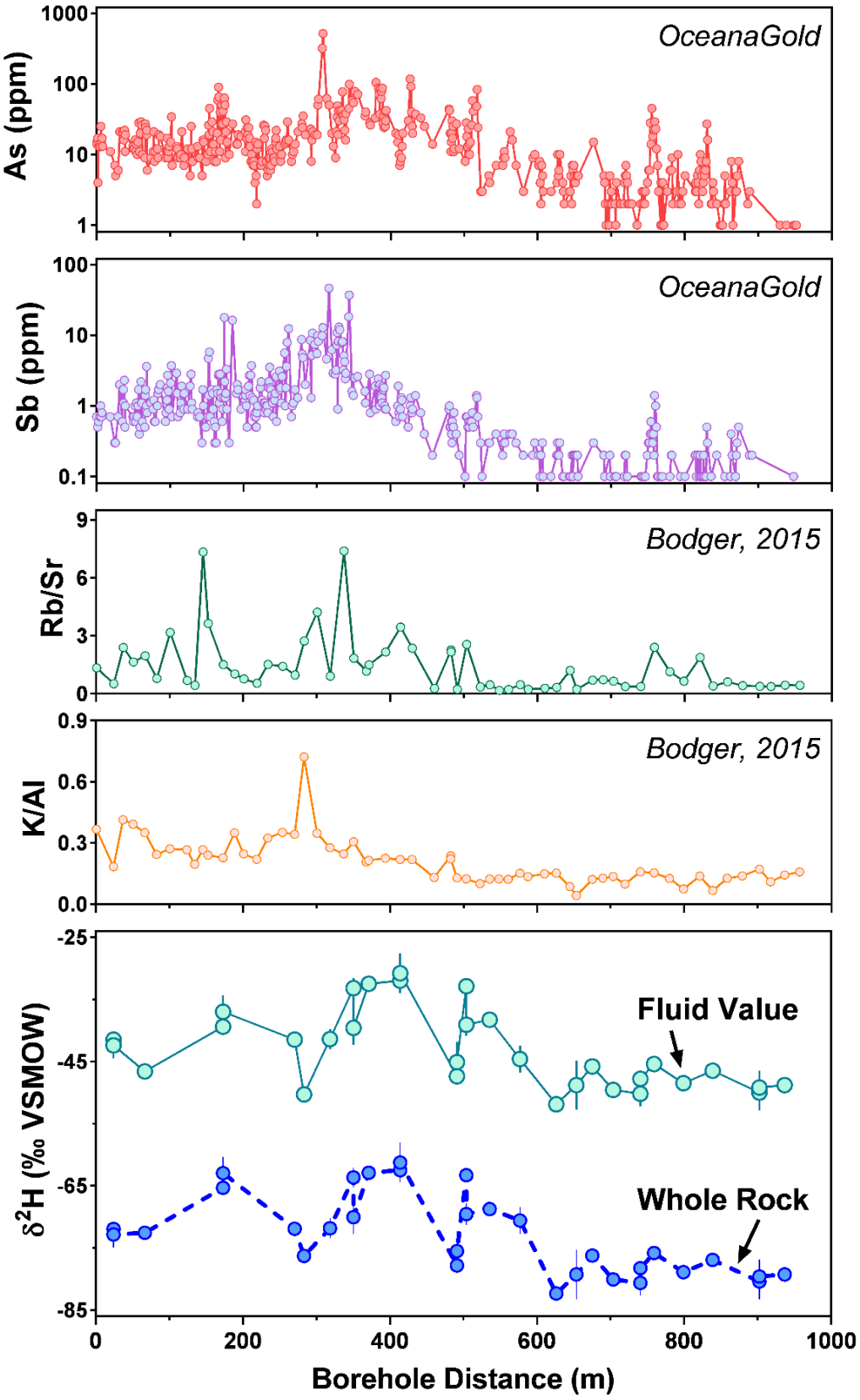
As (ppm)
1000
100
10
1
OceanaGold
Sb (ppm)
100
10
1
0.1
OceanaGold
Rb/Sr
9
6
3
0
Bodger, 2015
K/Al
0.9
0.6
0.3
0.0
Bodger, 2015
δ²H (‰ VSMOW)
-25
-45
-65
-85
Fluid Value
Whole Rock
0
200
400
600
800
1000
Borehole Distance (m)

Figure 6.10: previous page: whole rock δ^2H values were paired with constraints upon clay mineralogy to reconstruct the values of fluid δ^2H over the extent of the UW462 borehole. A progressive decrease in hydrogen isotope values between 500 and 600 m along the borehole coincides with decreased abundance of pathfinder elements (As, Sb), and decrease in the Rb/Sr and K/Al elemental ratios. These results are consistent with lesser degrees of clay alteration moving along the length of the borehole and probably indicate greater volume of upflow over the first ~500-600m.

6.3.6 Hydrogen isotope methodological considerations

Accurate determination of type and relative abundance of hydrous minerals is informative towards reconstruction of palaeofluid properties. However, in many mineral exploration settings, it may not be possible to isolate individual hydrous mineral phases from samples, especially where clays are discreet and intergrown. Spectral analytical techniques, including short wave near infrared (SWIR) spectroscopy, can differentiate between a number of common phyllosilicates (e.g. illite, smectite, chlorite, kaolinite, pyrophyllite) and calc-silicate (e.g. epidote) minerals. SWIR and other infrared tools can be paired with in situ compositional measurements made using portable XRF. The δ^2H tool developed here, as well as new innovative thermogravimetric analysers (TGA), paired with laser spectroscopy instruments (e.g. Bauska et al., 2017; Oerter et al., 2017), may support better characterization of the relative contribution of different fluids in low grade alteration areas around mineral deposits.

6.4 CARBONATE RESULTS AND INTERPRETATION

6.4.1 Carbonate textures

Carbonate was visually logged in hand sample and identified in pulp by reactivity with HCl. Carbonate veins were observed, ranging in thickness from <1 mm to 5-10 mm (Figure 6.11). The presence of replacement carbonate in core samples was identified by reaction with dilute HCl. Cathodoluminescence proved to be highly effective towards highlighting calcite alteration textures (Figure 6.12). Vein calcite is frequently microcrystalline, but notable examples of bladed calcite, a boiling

texture, are present (Figure 6.12). Bladed calcite is observed in samples drilled within 50 m of major mineralized Au-Ag containing veins at the Correnso deposit. Evidence of carbonation reactions is also widespread, with frequent examples of partial to complete replacement of plagioclase by calcite.

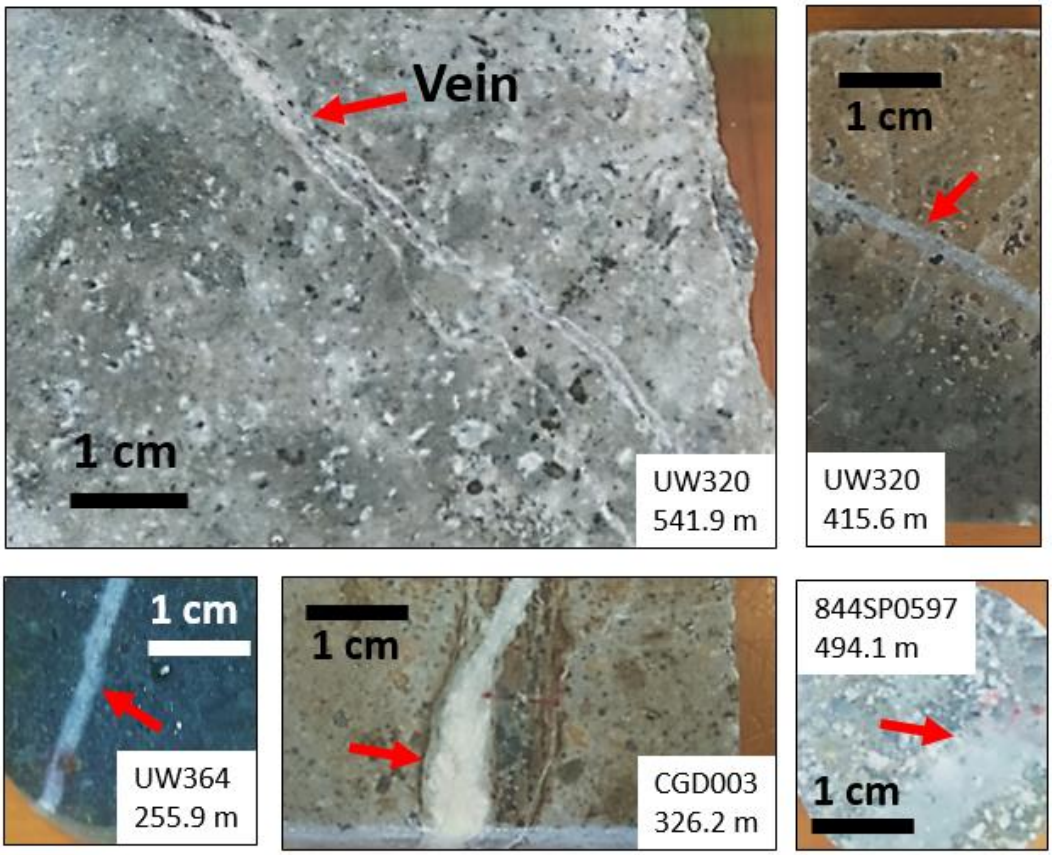

Figure 6.11: examples of calcite vein textures in hand sample at Waihi. Red arrows denote calcite veins.

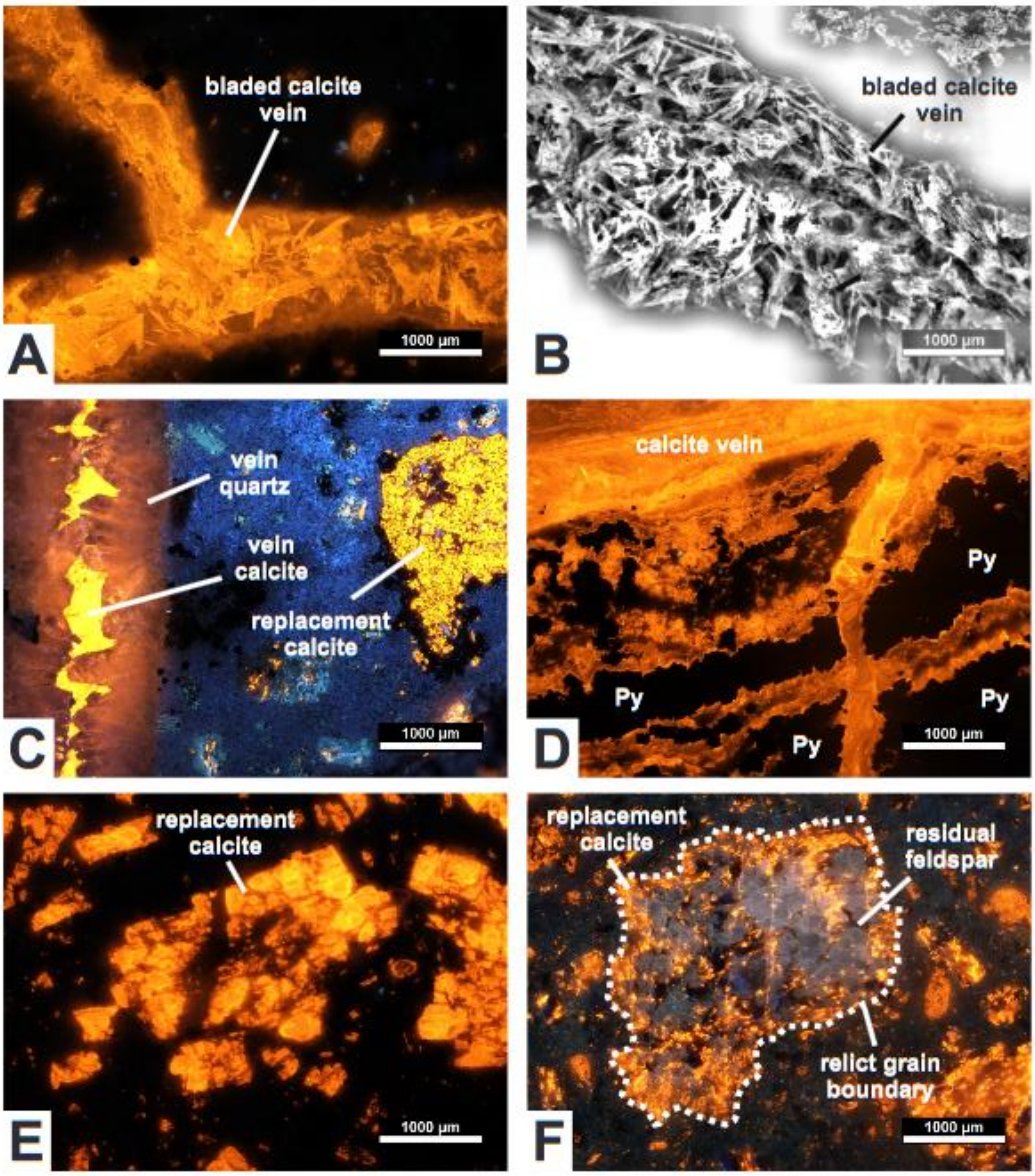

Figure 6.12: cathodoluminescence images of carbonate at Waihi. Calcite is common in propylitic areas surrounding the Martha and Correnso ore zones, occurring in veins (Panels A-D) and replacing feldspar grains (Panels C, E, F). Hydrothermal calcite veins presenting bladed textures (Panels A and B) indicate of boiling conditions. Enhanced contrast is used in CorelDraw® to visualize calcite grain boundaries (B). Veins containing quartz + calcite were evident under CL (C). The presence of sulphides (e.g. pyrite) was confirmed within select calcite veins (D). Partial replacement of feldspar is illustrated, where calcite haloes surround remnant plagioclase grains (F). Higher intensity alteration results in complete replacement of feldspars by carbonate (E, F).

Carbonate content

The amount of carbonate in samples ranges from less than 1 to 55 %, and is 5 % on average. The carbonate percentage, determined by acid digestion during isotope analysis, is closely correlated with carbon content (Figure 6.13). Given the low starting carbon abundance in andesite and rhyolite host rock at Waihi, the majority of carbon in the deposit appears to have been added by hydrothermal carbonation reactions, which generated secondary replacement calcites.

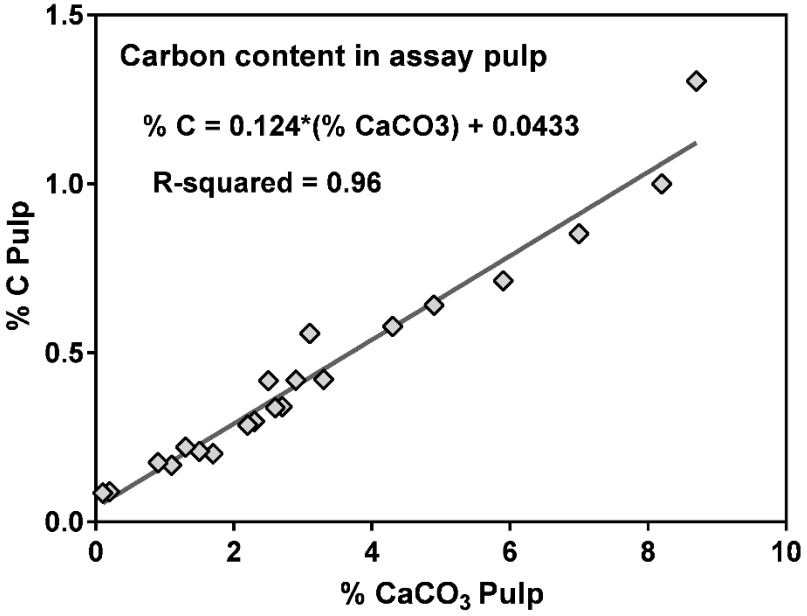

Figure 6.13: correlation between carbonate content determined during OA-ICOS analyses and measured carbon content in assay pulp. A slope of ~0.12 indicates carbon in altered volcanic host rock (e.g. andesite, rhyolite) at Waihi is present as carbonate. Carbon content (% C) was determined in a prior study (e.g. Geraghty, 2016), using an Elemental Analyser (EA).

6.4.2 Carbonate isotope results

Carbonate isotope results at Waihi are presented in Figures 6.14-6.15. Results are summarised in Table 6.4. An archive of analytical data for boreholes is provided in Appendix D. $\delta^{13}C$ ranges from -12.2 to -0.1 ‰ VPDB, and is -8.0 ‰ on average. $\delta^{18}O$ ranges from 0.8 to 23.8 ‰ and is 7.8 ‰ on average. Carbon and oxygen isotope results in assay pulp, veins, and replacement carbonates are similar (Figure

6.15). Low temperature hydrothermal calcite precipitating from groundwaters, or at the surface, occurs in boreholes near Favona veins (UW373, UW67) with $\delta^{18}O$ in excess of 20 ‰ (Table 6.4).

Table 6.4: Carbonate isotope results summarized at Waihi

Borehole	N. Samples	Value range[1]	$\delta^{13}C$ ‰ VPDB	$\delta^{18}O$ ‰ VSMOW	$CaCO_3$[2] Wt. %
WAIHI	189	Mean	-8.0	7.8	4.9
		+	-0.1	23.8	54.7
		-	-12.2	0.8	0.1
UW462	52	Mean	-7.3	8.8	4.7
		+	-4.0	16.5	11.9
		-	-11.7	3.2	0.8
844SP0597	35	Mean	-8.3	5.8	7.3
		+	-6.1	19.8	54.7
		-	-11.7	2.8	0.7
UW364	14	Mean	-7.5	5.7	6.3
		+	-3.2	10.7	9.9
		-	-8.3	0.8	2.6
UW320	36	Mean	-8.7	5.9	4.3
		+	-6.8	9.2	9.9
		-	-10.3	2.8	1.1
CGD003	8	Mean	-8.7	7.2	2.5
		+	-7.9	9.6	3.6
		-	-10.8	5.0	1.2
UW348	18	Mean	-9.2	6.6	3.2
		+	-7.4	10.1	8.2
		-	-12.2	4.5	0.1
UW373	15	Mean	-8.4	12.2	3.3
		+	-6.9	23.8	7.7
		-	-9.7	4.7	0.6
UW67	6	Mean	-2.1	21.2	8.0
		+	-0.1	22.1	9.3
		-	-3.8	20.3	5.9
UW208	5	Mean	-9.7	6.2	3.2
		+	-8.3	9.6	8.2
		-	-11.9	4.2	1.5

[1] Maximum (+) and minimum (-)values
[2] Carbonate content in whole rock assay pulp

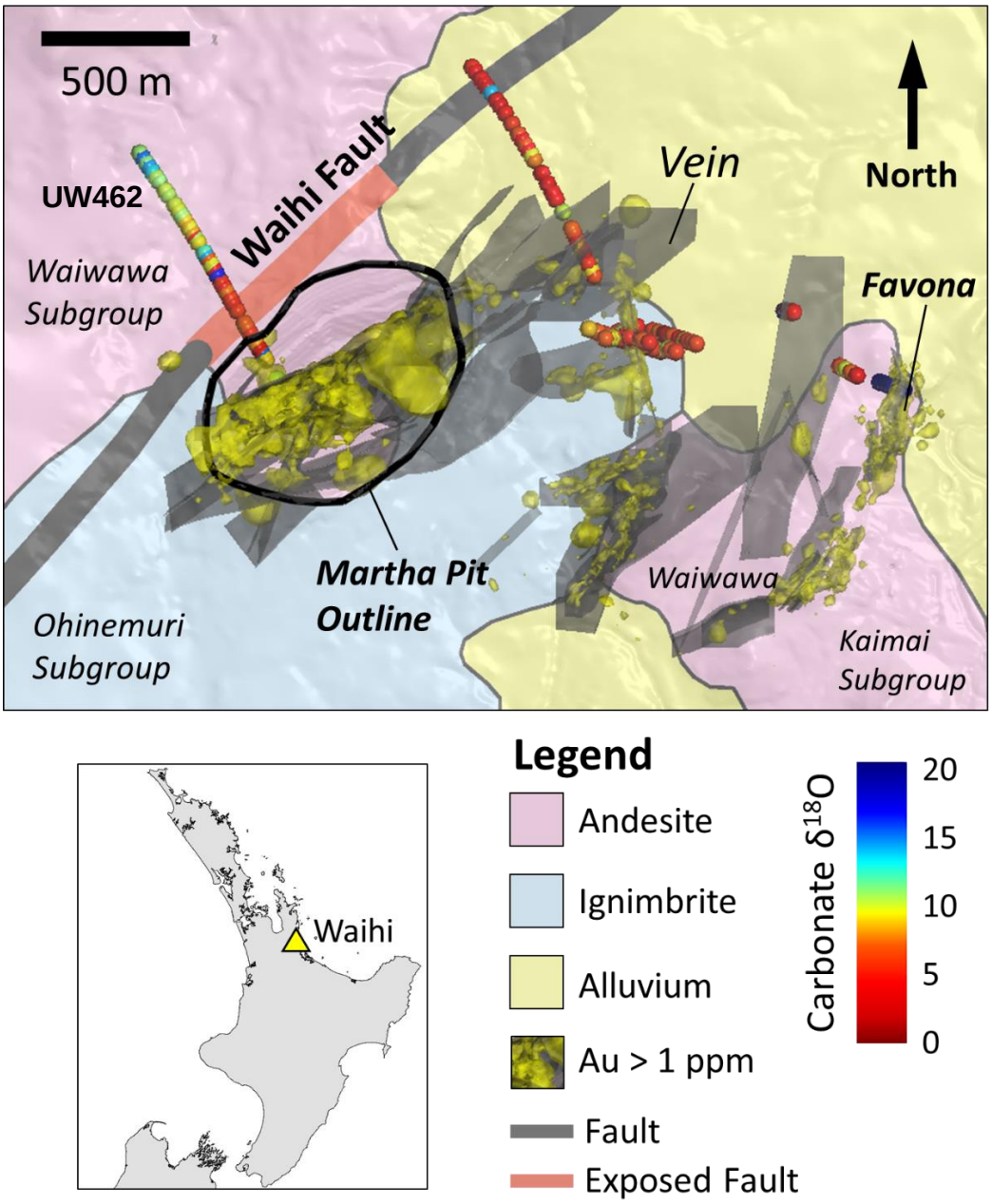

Figure 6.14: spatial context of calcite oxygen isotope results at Waihi. Mineral $\delta^{18}O$ values decrease near Au-Ag mineralised areas, and increase NW of the Waihi Fault. Principal vein and breccia structures shown in grey. Vein and Au assay data from OceanaGold exploration database. Geologic units and fault trace from QMAP project.

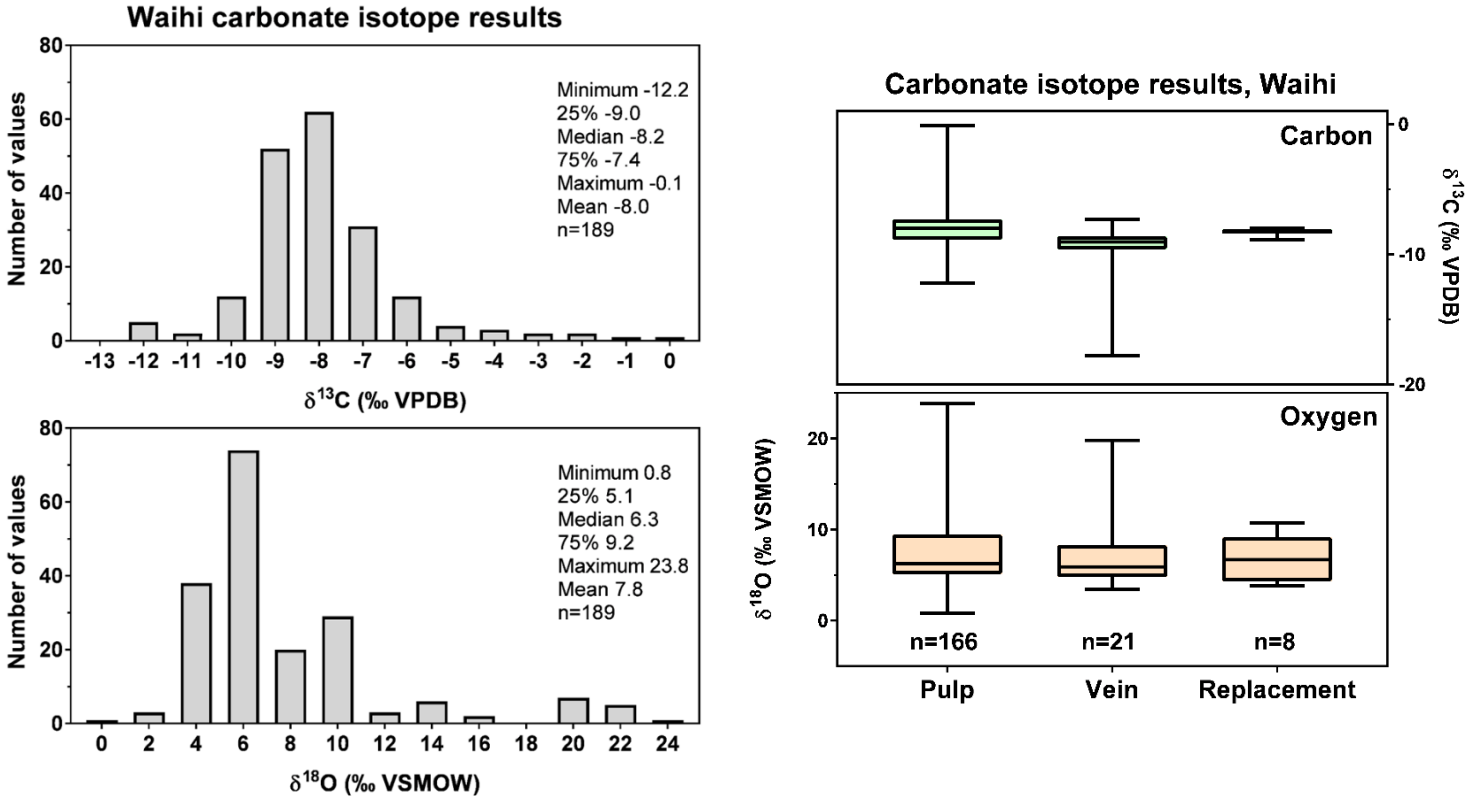

Figure 6.15: Left panel: calcite $\delta^{13}C$ and $\delta^{18}O$ results at Waihi measured by OA-ICOS. Right panel: Comparison of calcite isotope measurements in whole rock assay pulps, veins, and wall rock replacement phenocrysts. Box plots enclose 25-75 percentile values, with median values shown as lines. Four vein and two replacement calcite samples are included from Chapter 5 (i.e. Mering et al., 2018). Results overlap indicating that the H_2O and CO_2 involved in propylitic alteration and fracture filling veins are broadly similar.

6.4.3 Interpretation of carbon and oxygen isotope variability in calcite

At Waihi, the majority of calcite surrounding the Martha, Correnso, and some Favona veins is of hydrothermal origin with values overlapping constraints from geothermal systems and epithermal ore deposits across the North Island. Oxygen and carbon isotope data are plotted relative to hydrothermal calcite at other TVZ and CVZ sites in Figure 6.16. Shallow areas of the Favona deposit contain presentations of both high temperature (low $\delta^{18}O$) calcite, and extremely late stage, or posthydrothermal, calcite. Calcite exceeding 20 ‰, with $\delta^{13}C$ values higher than -4 ‰ imply formation from a low temperature groundwater or extremely late stage, relatively cool hydrothermal fluid.

The modal range for $\delta^{13}C$ at Waihi (-9 to -7 ‰) is consistent with a dominantly magmatic origin, similar to values observed in calcites measured in modern New Zealand geothermal fields (-10 to -4 ‰) in prior studies (e.g. Clayton and Steiner, 1975; Simmons and Christenson, 1994; Horton et al., 2014; Mering et al., 2018). Carbon isotope values at Waihi, and in TVZ geothermal carbonates, often exhibit values below the typical range of mantle CO_2 (-6 to -2 ‰), consistent with some degree of organic contribution (Ohmoto and Rye, 1979; Javoy et al., 1986; Djouka-Fonkwé et al., 2012). Calcite $\delta^{13}C$ significantly below -10 ‰ indicates incorporation of isotopically depleted organic material sourced from either the greywacke basement or interbedded siltstones within the deposit (Brathwaite and Faure, 2002).

Carbonate results are also interpreted alongside mineral-fluid fractionation trends, which take into account the combined effect of CO_2, H_2O, and temperature upon the $\delta^{18}O$ and $\delta^{13}C$ in samples (Figure 6.17). Isotopic C-O covariation plots have been applied elsewhere in geothermal and ore deposit studies (e.g. Zheng, 1990; Simmons and Christenson, 1994; Simmons et al., 2000). In Figure 6.17, temperatures reflect established calcite-water fractionation relationships for oxygen and calcite-CO_2 for carbon (Ohmoto and Rye, 1972; Kim and O'Neil, 1997). Calculations were carried out assuming mineral precipitation from a fluid with $\delta^{18}O_{H2O}$ and $\delta^{13}C_{CO2}$ of -5.7 ‰ and -9.7 ‰, respectively. These values were determined from clumped isotope measurements of vein calcite at Waihi presented in the previous chapter, and are similar to fluid values applied for similar

calculations at the nearby Golden Cross deposit (Simmons et al., 2000). Although the choice of oxygen isotope fractionation factor (e.g. O'Neal et al., 1969 vs. Kim and O'Neil, 1997) will inevitably shift the reconstructed temperature value, it is possible to distinguish between higher and lower temperature calcite using this approach.

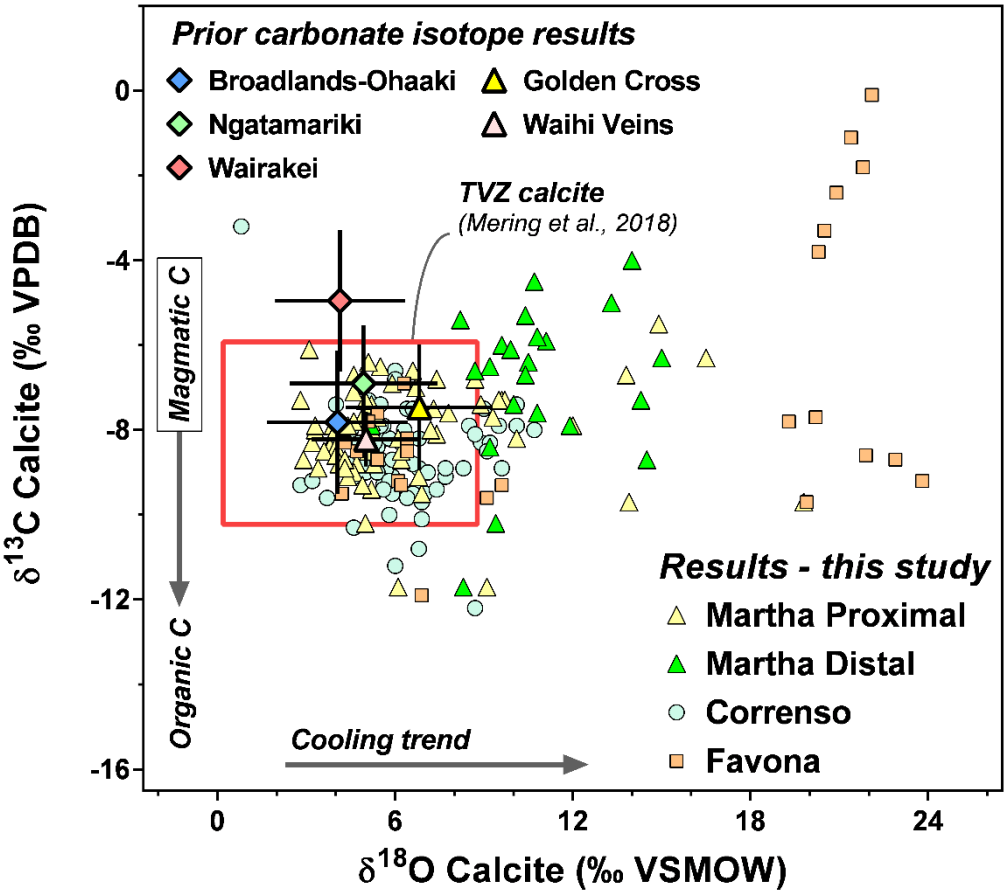

Figure 6.16: $\delta^{13}C$-$\delta^{18}O$ plot of calcite at Waihi. The value range of calcite measured in geothermal scale reported in Chapter 5 (i.e. Mering et al., 2018) is denoted by the red box. Measurements from prior studies are reported for Broadlands Ohaaki (Simmons and Christenson, 1994), Ngatamariki (Horton et al., 2015), Wairakei (Clayton and Steiner, 1975), Golden Cross (Simmons et al., 2000), and Waihi upflow veins (Brathwaite and Faure, 2002). A narrow range of $\delta^{13}C$ values for the majority of samples implicates a magmatic source for CO_2 in the system, with possible organic contribution in some samples.

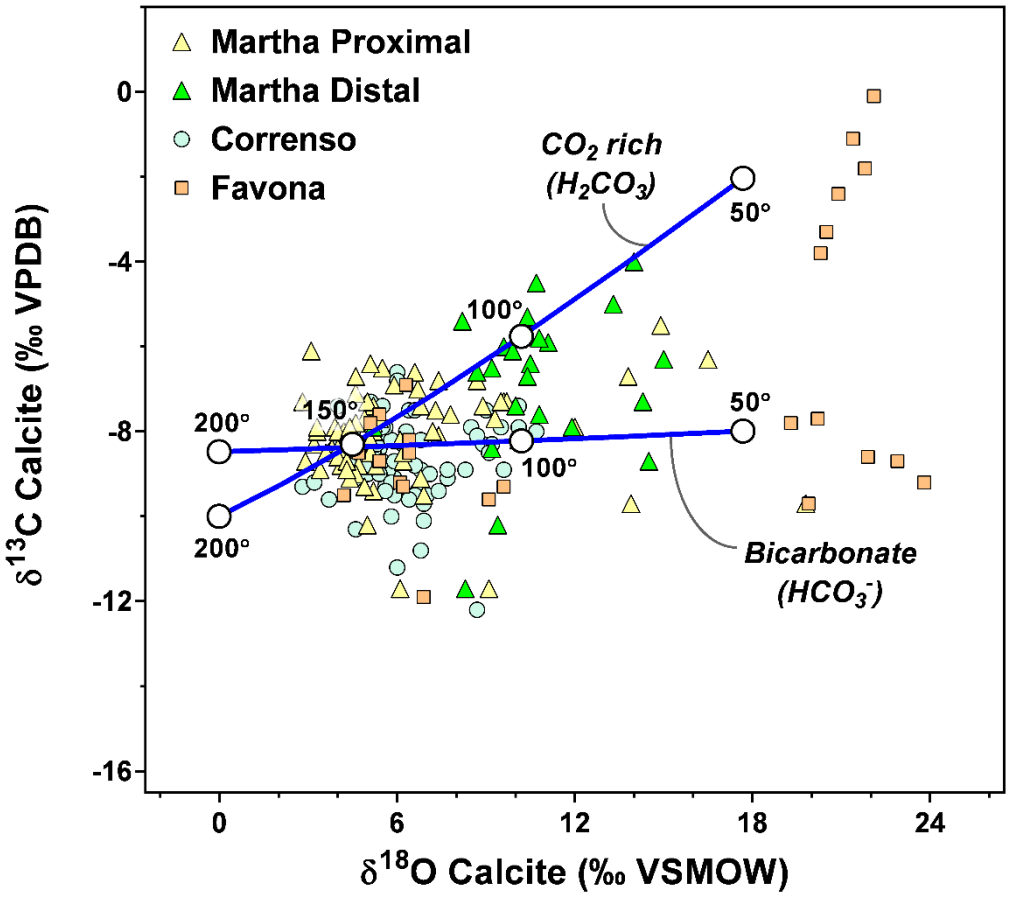

Figure 6.17: trends for $\delta^{13}C$ and $\delta^{18}O$ covariation for samples precipitated from either a CO_2 rich steam heated fluid, or bicarbonate type water. Calculations are made using the following fractionation factors: calcite-CO_2 (Ohmoto and Rye, 1979), calcite-bicarbonate (Deines et al., 1974), and calcite-H_2O (Kim and O'Neil, 1997). Mineral isotope trends are calculated for fluid with a water $\delta^{18}O$ value of -5.7 ‰ and CO_2 with $\delta^{13}C$ of -9.7 ‰ determined from clumped isotope constraints at Waihi (i.e. Mering et al., 2018).

6.4.4 Carbonate abundance and temperature

Oxygen isotope values in calcite at Waihi reflect alteration intensity, where higher whole rock carbonate content relates to lower $\delta^{18}O$ (Figure 6.18). The average $\delta^{18}O$ value for samples containing less than 2 weight percent carbonate is 12.2±5.6 ‰, while sections of core for which the carbonate fraction exceeds 2 percent have an average $\delta^{18}O$ of 7.0±3.9 ‰. The apparent trend of retrograde temperature solubility for calcite is well defined in modern geothermal systems (Simmons and Christenson, 1994; Simmons et al., 2000). From an exploration standpoint, measurement of carbonate abundance in pulp may represent a low-cost qualitative

measure wall-rock alteration intensity. One Favona borehole (UW67) is an outlier to this trend, reflecting significant groundwater involvement near the surface or supergene conditions. The $\delta^{18}O$ results measured in UW67 are similar to values of carbonate accumulating at the surface at 20 °C at the Broadlands-Ohaaki geothermal field (Simmons and Christenson, 1994).

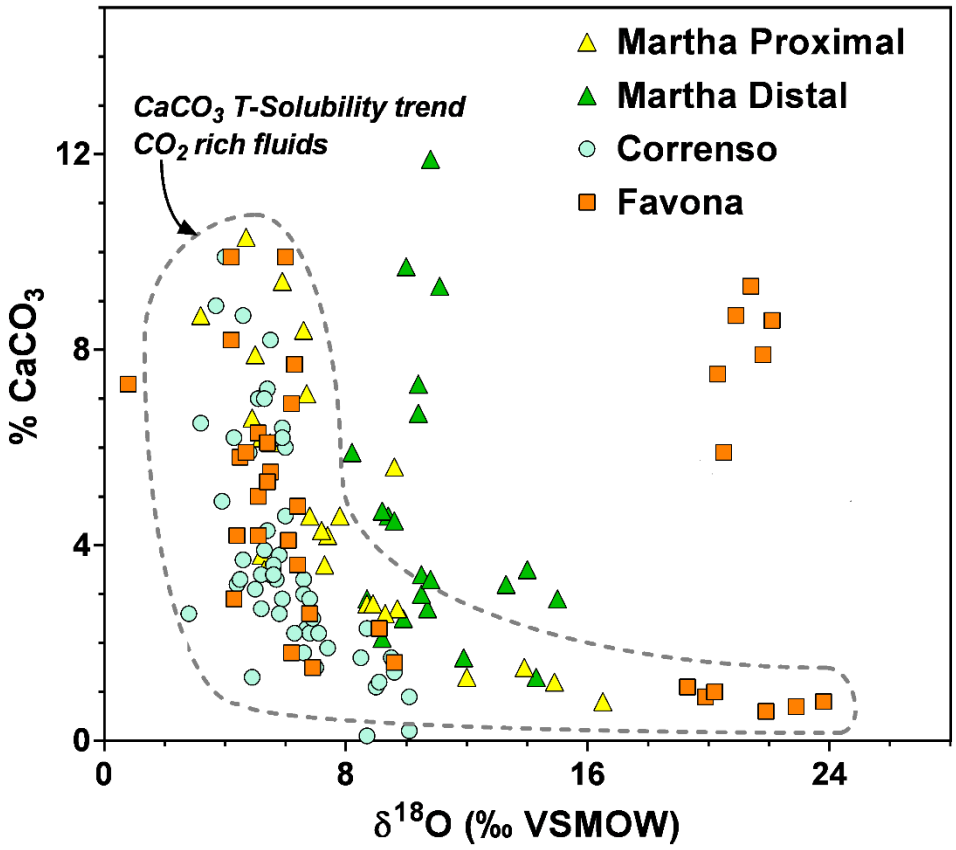

Figure 6.18: calcite $\delta^{18}O$ plotted against carbonate abundance (% $CaCO_3$) in assay pulps at Waihi. Elevated abundance of calcite in samples with lower $\delta^{18}O$ implies that oxygen isotopes track alteration intensity in areas where fluid pH is alkaline.

6.4.5 Thermal profile at Waihi from carbonate isotope constraints

Carbonate stable isotopes may represent an effective tool for distinguishing between calcite forming near hotter mineralized areas, and calcite that is not associated with significant convective fluid flow. Carbonate oxygen isotope results were paired with clumped isotope constraints (Mering et al., 2018) to develop a thermal profile for the UW462 borehole, exhibited previously for $\delta^{2}H$ (Figure 6.19). From 430 to 980 m, the $\delta^{18}O$ carbonate value gradually increases reaching a mean

value of 10-15 ‰ at the distal end. Elevated $\delta^{18}O$ for distal carbonates are interpreted to reflect lower temperature. Carbonate clumped isotope results measured within 500 m of the Martha vein record temperatures between 160 and 174 °C. Calcite veins distal to Martha (UW462, ~500-1000m) record relatively low temperatures (50-120 °C), as determined by clumped isotope thermometry (Mering et al., 2018). A lateral decrease in temperature moving away from mineralised upflow areas of ~134 °C/km is reconstructed from carbonate data (Figure 6.19). This is similar to horizontal gradients observed in modern geothermal systems on the North Island of New Zealand (e.g. Broadlands-Ohaaki), where temperatures vary from below 100 to 300 °C over distances of less than 1 km (Simmons and Christenson, 1994). For perspective on scale, a temperature profile for the Broadlands-Ohaaki geothermal field is superimposed over the extent of the Waihi deposit in Figure 6.19 after Simpson and Mauk (2007).

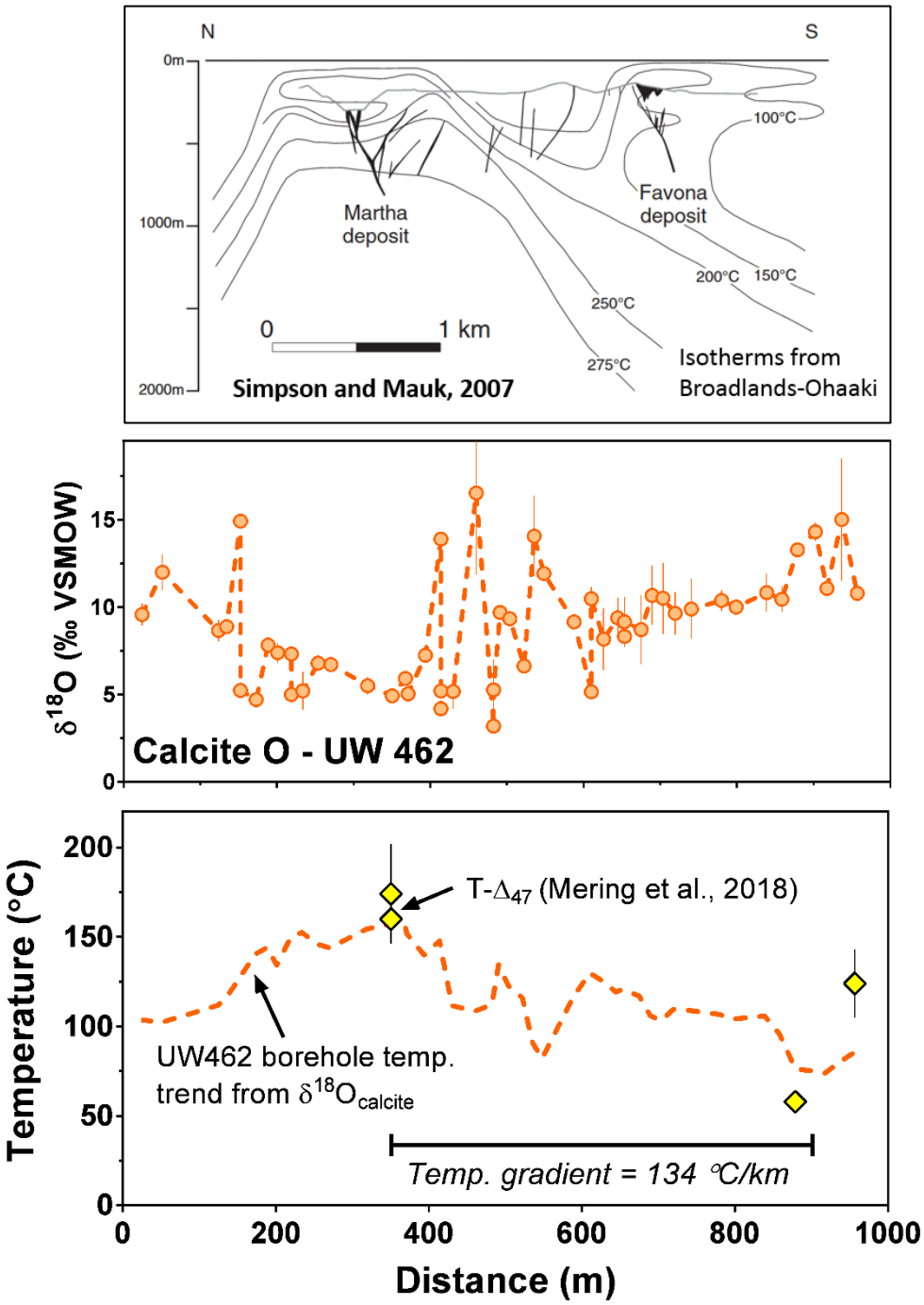

Figure 6.19: carbonate oxygen isotope thermometry at Waihi, defined by clumped isotope constraints. Upper panel: isotherms from Broadlands-Ohaaki geothermal field superimposed over the extent of the Waihi-Favona deposit (Simpson and Mauk, 2007). Middle panel: carbonate $\delta^{18}O$ across the UW462 borehole at Waihi. Lower panel: UW462 borehole temperature plot reconstructed using carbonate clumped isotope constraints.

6.4.6 Comparison to TVZ geothermal systems

In a carbonate generating mineral deposit, where the host rock is dominantly silicate, $\delta^{18}O_{calcite}$ enables approximate characterisation of thermal architecture. Figure 6.20 provides a compilation of carbonate oxygen isotope data, paired with temperature constraints from Waihi, Golden Cross, and several geothermal areas, measured in prior studies (Simmons and Christenson, 1994; Simmons et al., 2000; Mering et al., 2018). In Figure 6.20, $\delta^{18}O$ correlates linearly with measured temperature (R^2 = 0.59), although this analysis does not take into account differences in fluid $\delta^{18}O$ between Miocene Au-Ag deposits and the modern TVZ. Nevertheless, it is apparent that temperature is the primary driver of carbonate mineral $\delta^{18}O$ variation in both CVZ epithermal systems and modern geothermal systems in the TVZ thought to be analogues to low-sulphidation Au-Ag deposits (Simmons and Browne, 2000; Rowland and Simmons, 2012). Carbonate oxygen isotopes, paired with clumped isotope and/or fluid inclusion homogenization temperatures, have promise towards providing enhanced resolution of the structural and thermal aspects that drive fluid circulation.

The mineralising events in epithermal systems are short-lived, but evaluation of fluid flow and metal transport in geothermal fields in the TVZ indicate that thermal activity in a given area is typically sustained on an order of 10-100 ka (Rowland and Simmons, 2012). While calcite likely precipitated both in and out of phase with precious metals at Waihi, and other epithermal areas within the Hauraki goldfields, the oxygen isotope values from carbonate minerals are interpreted to reflect the thermal structure. Modelling of continental hydrothermal systems provide some idea of the spatial and temporal stability of magmatic plumes associated with metal deposits (Bickle and McKenzie, 1987; Ingebritson et al., 2010; Weis et al., 2012). Figure 6.21 provides illustration of temperature vs. depth relationships around a modelled epithermal deposit over 20 ka (Ingebritson et al., 2010), and the location of the 400 °C isotherm relative to a porphyry intrusion over 90 ka (Weis et al., 2012). Model simulations indicate that stable isotherms are established on timescales ~10-100 ka (e.g. Ingebritsen et al., 2010; Weis et al., 2012). As the thermal plume collapses, isotherms contract downward but largely retain symmetry. Thus, at Waihi, and likely other neutral-pH low sulphidation deposits, carbonate $\delta^{18}O$ has the potential to define isotherms with zones of propylitic alteration, with

the caveat that temperatures recorded may be lower than main-stage ore conditions, reflecting the waning stages of hydrothermal circulation.

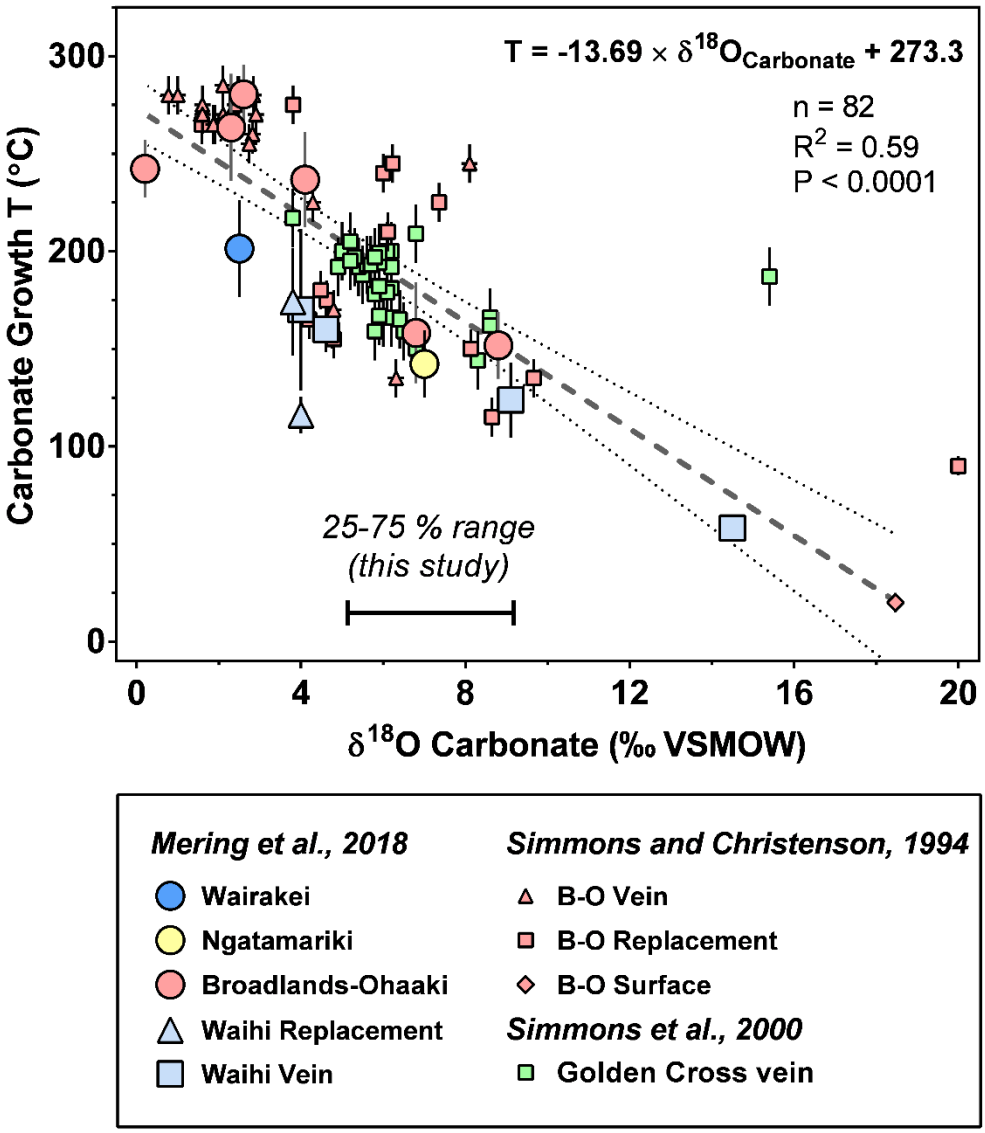

Figure 6.20: comparison of carbonate mineral $\delta^{18}O$ and temperature values at Waihi, Golden Cross, and modern TVZ geothermal areas. The mineral $\delta^{18}O$ and growth temperatures for carbonate in both TVZ geothermal areas and CVZ epithermal deposits are closely correlated. Temperature values from Mering et al. (2018) were determined by clumped isotope thermometry. Values from the Broadlands-Ohaaki geothermal fields are direct temperature measurements of well fluid (Simmons and Christenson 1994). Temperature constraints from Golden Cross were made using fluid inclusion (T_h) methodology (Simmons et al., 2000).

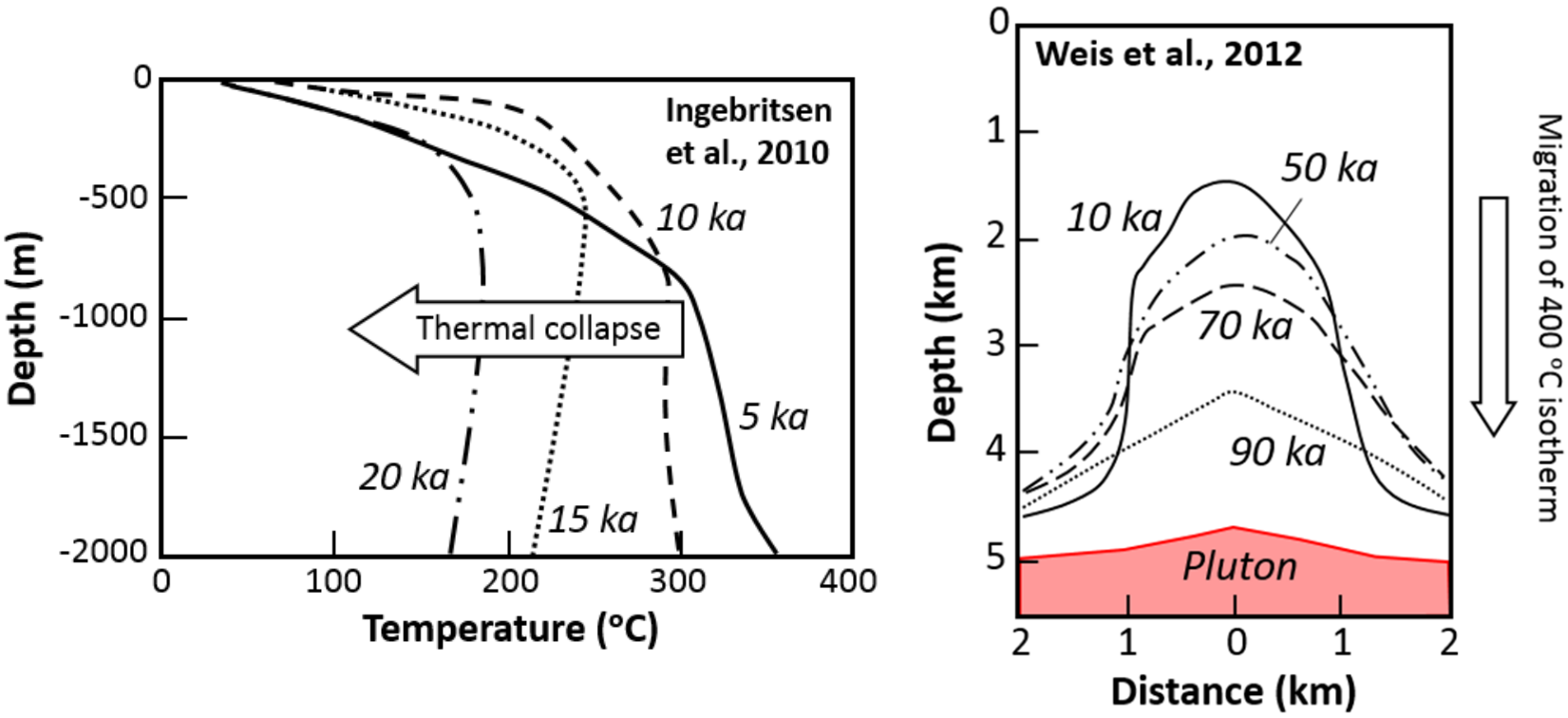

Figure 6.21: two model results for continental hydrothermal systems. Left panel: temperature-depth results for an epithermal model (Ingebritsen et al., 2010). Right panel: depiction of the location of a 400 °C isotherm in a porphyry, relative to a magmatic plume over 90 ka (Weis et al., 2012).

6.5 CONCLUSIONS

The results reported here demonstrate the effectiveness of OA-ICOS, and comparable laser spectrometers, for measurement of isotopic signals in clay minerals and carbonates in hydrothermal settings. The δ^2H method utilised here is capable of rapidly characterising whole rock δ^2H anomalies in assay pulps and mineral separates. Hydrogen isotope analyses, with coupled constraints upon fluid $\delta^{18}O$, allow for assessment of whether the isotopic makeup of primary fluid is changing, by excluding effects of water-rock exchange. Mineral δ^2H is useful for fingerprinting paleo latitude or altitude of source fluids, as evidenced by results from Comstock, which were ~60 ‰ lower for δ^2H, relative to Waihi and Karangahake. It is apparent that mineral δ^2H has greater utility towards understanding mixing in systems where fluids are isotopically distinct. Porphyries, where both magmatic and meteoric waters are significantly involved in alteration, are potentially useful settings for applying δ^2H (e.g., Dilles et al., 1992; Djouka-Fonkwé et al., 2012). This may be especially true in higher latitude areas, where there is significant offset in δ^2H between magmatic and meteoric reservoirs.

At Waihi, calcite $\delta^{18}O$ records temperature variation within the propylitic zone. A significant correlation of increasing $\delta^{18}O$ in assay pulp with decreasing percent carbonate is consistent with temperature control upon calcite solubility (e.g. retrograde calcite solubility). In ore deposits such as Waihi, where $\delta^{18}O$ variation in carbonate appears to reflect the thermal regime, laser spectroscopy may be applied to rapidly generate paleotemperature data relevant to mineral exploration.

Historic exploration at Waihi, and across the Hauraki goldfield region, demonstrate that economic grade epithermal veins are widespread within larger alteration footprints. However, identification of Au-Ag deposits has often been serendipitous. The discovery of the Correnso vein system in the 2000s, within 1 km of the Martha and Favona deposits, and recent exploration at the nearby Wharekirauponga (WKP) prospect imply that within areas that have been mined historically high grade discoveries are still likely. Rapid optical stable isotope methods provide a new approach to identify higher temperature zones with greater precious metal mineralisation potential.

CHAPTER VII

Concluding Remarks

7.1 REVIEW OF SCOPE

In this thesis, new strategies are developed to measure stable isotope ratios in hydrous minerals and carbonates with critical application focus on hydrothermal ore deposits and geothermal fields. The body of research presented here makes use of mass spectrometric and laser spectroscopic techniques to measure $\delta^{2}H$, $\delta^{13}C$, $\delta^{18}O$, and carbonate clumped isotopes (Δ_{47}). Recommendations for applying techniques in mineral deposit investigations are highlighted by evaluation of signals in multiple settings, including: epithermal, modern geothermal, skarn, and carbonate base metal. In Chapter 1, three areas of research inquiry are identified which encompass:

(i) Laser spectroscopy method development
(ii) Testing of carbonate clumped isotope thermometry in geothermal fields and hydrothermal ore deposits
(iii) Application of stable isotope techniques ($\delta^{2}H$, $\delta^{13}C$, $\delta^{18}O$, Δ_{47}) to evaluate temperature and fluid source in epithermal areas

The primary conclusions relating to each area, and associated research questions, are summarized below.

Area 1: Measuring $\delta^{2}H$ and $\delta^{18}O$ in hydrous minerals by laser spectroscopy

> ***Q 1.1:*** *What is the best achievable precision, accuracy, and measurement speed for $\delta^{2}H$ and $\delta^{18}O$ in hydrous minerals using an OA-ICOS platform?*

Q 1.2: *How do the OA-ICOS methods developed here compare to established IRMS approaches?*

Q 1.3: *How can laser spectroscopic measurement of hydrous mineral isotope signals aid ore deposit investigations?*

An OA-ICOS method was developed to measure δ^2H and $\delta^{18}O$ in phyllosilicates, hydrous sulphates, and multimineralic whole rock assay pulps. The δ^2H methodology presented in Chapter 3 is equal to TC/EA-IRMS in terms of speed and precision, but considerably lower in cost. Samples are measured in 2-3 minute acquisition cycles at average precisions 1.1 ‰. Materials, excluding biotite, were calibrated to within 1.5 ‰ of IRMS-measured δ^2H values. Biotite δ^2H measurements were more positive than established values, inferred to be due to partial reduction of evolved waters by Fe in the high temperature dehydroxylation apparatus. Recommendations are provided for overcoming redox interference for measurements of biotite, and other ferrous materials, by thermal dehydroxylation. This work represents the first hydrogen isotope measurements made by a laser spectroscopy system for serpentine, muscovite, sericite, talc, and biotite.

Oxygen isotope results are reported in Chapter 4 for measurements on microvolumes of water (0.25-0.5 μL), gypsum hydration water, and the hydroxyl component of phyllosilicate minerals. Thermal dehydroxylation laser spectroscopy has the potential to provide useful constraints on internal oxygen isotope fractionation in clay minerals (e.g. Bechtel and Hornes, 1990). Preliminary OA-ICOS measurements reported in this thesis of $\delta^{18}O_{OH}$ in kaolinite and muscovite, paired with established whole-mineral $\delta^{18}O$ values, are consistent with other studies (e.g. Bechtel and Hornes, 1990; Seligman and Bindeman, 2019). Continued refinement of this approach should be carried out to define the relationship between fluid $\delta^{18}O$, temperature, and internal fractionation between Si-O and OH in hydrothermal alteration minerals. If useful correlations between these parameters can be identified using OA-ICOS, the resulting method may provide a new approach for constraining the oxygen isotope value of fluids in hydrothermal settings. Significantly, this would provide a safe and low-cost alternative to fluorination for quantifying $\delta^{18}O$ signatures in clay minerals.

Measurements of water vapour by OA-ICOS indicate precisions of 0.1 to 0.2 ‰ are potentially achievable; however, hydrous mineral $\delta^{18}O_{OH}$ was measured at relatively low precision (~0.2 to 2.0 ‰). In comparison, modern IRMS setups typically measure $\delta^{18}O$ at precisions of ~0.1-0.3 ‰. The majority of uncertainty in measurement of $\delta^{18}O_{OH}$ stems from the thermal dehydroxylation setup, where there is the potential for exchange with other oxygen reservoirs (e.g. minor dead leaks), or interference by ferrous materials. Additional work investigating optimum carrier gas conditions, dehydration-dehydroxylation temperature, grain size effects, and redox interference will likely improve analytical performance.

The $\delta^{2}H$ OA-ICOS techniques developed in Chapters 3-4 should be useful towards identifying potential for fluid mixing between reservoirs (e.g. magmatic, meteoric, basinal brines, seawater). Hydrogen isotope analyses, coupled with constraints upon fluid $\delta^{18}O$ derived from water or paragenetically related carbonate, allow for assessment of whether the fluid composition is static, or has become variably shifted by exchange with host rock. The speed (2-3 minutes), and low cost of measurement, enables high resolution exploration datasets in individual boreholes (10-100 measurements), deposits (100-1000 measurements), and across districts (100s to > 1000 measurements) to be made. The low cost of the hardware developed here should make such measurement available to a variety of potential academic and commercial users.

Area 2: Clumped isotope thermometry in hydrothermal investigations

> ***Q 2.1:*** *What is the sensitivity of clumped isotope reconstructions relative to other temperature constraints in geothermal fields and ore deposits (e.g. fluid inclusions, clay mineralogy)?*
>
> ***Q 2.2:*** *Where should Δ_{47} be applied to address gaps in knowledge in terms of reconstructing thermal history?*

In Chapter 5, the first carbonate clumped isotope measurements for epithermal (Waihi), carbonate hosted (Mount Isa), and skarn (Antamina) deposits are reported. These results suggest that clumped isotope thermometry has the potential to provide new constraints on fluid sources and temperatures associated with ore deposit

genesis. Calibration relationships are tested in modern geothermal samples from the Taupo volcanic zone. In general, clumped isotope temperatures overlap fluid inclusion and downhole well temperature measurements in TVZ geothermal wells, highlighting the potential for the method to identify temperature gradients in hydrothermal systems up to ~300 °C. In geothermal-epithermal settings, clumped isotopes enable differentiation between carbonate forming near hotter upflow conduits, which convey metal-rich fluids or energy resources (i.e. geothermal), and lower temperature areas peripheral to upflow. In settings where fluid sources (i.e. magmatic vs. meteoric) are unresolved, clumped isotopes provide new capability to determine fluid $\delta^{18}O$, overcoming a problem which has undermined interpretation of carbonate isotope data in hydrothermal settings for more than 60 years (Engel et al, 1958).

In this work, areas for methodological improvement are identified that should improve application of clumped isotope measurement in future ore deposit studies. There is a need for customized sample preparation systems that prevent reset of the clumped isotope signal in CO_2 by exchange with H_2O, during gas purification. Partial reset of clumped isotope signals can be overcome by implementing advanced CO_2 purification techniques that minimize the partial pressure of H_2O vapour in sample preparation systems (e.g. Sakai et al., 2017). Infrared absorption spectrometers provide an alternative platform for clumped isotope analyses (Nelson, 2016; Sakai et al., 2017; Prokhorov et al., 2019). In addition to lower hardware cost, laser instruments potentially reduce issues of contamination imparted by sulphur, hydrocarbon, and chlorocarbon compounds, which are trapped using a Porapak column in standard IRMS based methodology. However, extensive testing of optical platforms in the context of measuring $^{47}CO_2$ liberated from carbonates is yet to occur.

Area 3: Stable isotope approaches in exploration – epithermal case study

> ***Q 3.1:*** *Do explanations of carbonate growth temperature in the TVZ apply to Waihi? Specifically, do $\delta^{13}C$, $\delta^{18}O$, and clumped isotope records at Waihi reflect temperature gradients or fluid composition, and to what extent can isotopic tools be applied to exploration of low sulphidation epithermal deposits?*

Q 3.2: *Do whole rock measurements provide useful constraints upon fluid δ^2H in hydrothermally altered sequences? What factors control fluid δ^2H variation in epithermal deposits?*

This work demonstrates that mapping the distribution, and isotopic values, of carbonates in epithermal areas has potential as a tool for defining isotherms, especially within areas of propylitic alteration. Instances where lower $\delta^{18}O_{carbonate}$ correlates closely with elevated $CaCO_3$ content in samples indicate some degree of temperature control upon carbonate solubility in a CO_2 rich fluid. Paired $\delta^{18}O$ and clumped isotope measurements applied at Waihi demonstrate that low $\delta^{18}O$ calcite in veins and replacement phenocrysts is primarily related to elevated rock temperature. Carbonate-based estimates of thermal regime are useful at temperatures between 100 and 300 °C, where there is overlap of various clay alteration species. The OA-ICOS technique applied in Chapter 6 exemplifies a rapid and low-cost approach for measuring carbonate percentage and isotopic values simultaneously.

The modal $\delta^{13}C$ (-6 to -9 ‰ VPDB) at Waihi is similar to measurements in TVZ geothermal areas (e.g. Simmons and Christenson, 1994). Carbonate $\delta^{13}C$ values in this range indicate a magmatic CO_2 source with potential minor organic contribution. The range of $\delta^{13}C$-$\delta^{18}O$ values for high temperature (> 150 °C) calcite at Waihi overlap measurements in TVZ geothermal wells reported in Chapter 5 and previously in literature (Simmons and Christenson, 1994). Relatively higher $\delta^{13}C$ and $\delta^{18}O$ signatures imply formation from late stage fluids, or post hydrothermal ground water.

Investigation of the hydrogen isotope signatures at three epithermal deposits (Waihi, Karangahake, Comstock) indicate that the interpretation of δ^2H in assay pulps requires quantification of clay alteration assemblages (e.g. illite, smectite, chlorite, kaolinite). With constraints upon mineralogy, results indicate that fluids are derived from meteoric sources at all three sites. In this way, mineral δ^2H is useful towards identifying paleolatitude and elevation in meteoric dominated hydrothermal systems, as well as the potential for seawater mixing. Although not investigated here, δ^2H in minerals around porphyry deposits should reflect either meteoric water, magmatic water, or a mixture. Reinterpretation of experimental data

(e.g. Gilg and Sheppard, 1996), paired with measurements of clay minerals in modern geothermal and basinal settings (e.g. Marumo et al., 1980; Capuano, 1992), may be helpful towards better constraining the temperature component of clay-water δ^2H fractionation.

7.2 FUTURE STUDIES

7.2.1 Isotope contouring from epithermal to porphyry

The OA-ICOS hydrous mineral techniques developed in Chapters 3-4 should be useful towards identifying fluid sources in porphyry deposits (e.g. Sheppard et al., 1971; Dilles et al., 1992). Hydrogen isotope results for hydrous minerals (e.g. clays, hornblende, tourmaline), combined with knowledge of mineral-water fractionation relationships, should enable determination of the fluid types associated with each alteration zone. Interpretations of fluid sources critically depend on offset in the isotopic values of various reservoirs (e.g. magmatic, continental meteoric, seawater). Mixing relationships may be more precisely determined by combining δ^2H with $\delta^{18}O_{OH}$ constraints. Further work defining the mineralogical, temperature, and fluid controls governing $\delta^{18}O_{OH}$ in phyllosilicates is needed, however.

7.2.2 New stable isotope approaches to thermometry in ore deposit studies

In this thesis, clumped isotope thermometry provided demonstrably useful constraints upon carbonate formation temperatures in epithermal, skarn, and carbonate hosted settings. Future work employing carbonate clumped isotopes in hydrothermal investigations should integrate temperatures with U-Pb ages, fluid inclusion homogenization results (T_h), and conventionally measured $\delta^{18}O$ in carbonates. Using the carbonate OA-ICOS approach demonstrated here and elsewhere (e.g. Barker et al., 2013; Beinlich et al., 2019), combined with clumped isotope temperatures collected at regularly spaced intervals, allows for determination of the temperature component of $\delta^{18}O$. Such work permits evaluation of fluid source and water-rock reaction at a deposit to district scale. Clumped isotope temperatures, paired with fluid inclusion measurements, enable evaluation of fluid pressure (e.g. Honlet et al., 2018), allowing one to test for lithostatic or

hydrostatic regimes (e.g. Weis et al., 2012). Combining clumped isotope temperature and U-Pb ages, determined using laser ablation ICP-MS, unlocks potential for thermochronometry (Mangenot et al., 2018), providing a tool to reconstruct pressure-temperature-time (PTt) paths in ore deposits. This work is useful towards understanding the timing and duration of thermal activity, the role of late stage fluids, subsequent exhumation history, and preservation potential of deposits (e.g. Mueller et al., 2004; McInnes et al., 2005). In particular, such approaches should be informative in sediment hosted metal deposits (e.g. Mount Isa, Carlin-type Au).

The advances in mass spectrometry which facilitate measurement of rare "clumped" $^{47}CO_2$ isotopologues also enable highly precise measurement of all three isotopes of oxygen (^{16}O, ^{17}O, ^{18}O) in silicates and carbonates (Sharp et al., 2016; Hayles et al., 2018; Wostbrock et al., 2018). Small divergences from the $\Delta^{17}O$ terrestrial fractionation line indicate that $\delta^{17}O$-$\delta^{18}O$ relationships include a temperature component (θ), where:

$$\alpha(^{17}O/^{16}O) = \theta * \alpha(^{18}O/^{16}O) \quad (7.1)$$

This phenomenon has recently been demonstrated as a single mineral "triple oxygen" thermometer with case studies comparing theory and observations, including measurements of diatoms, and geothermal silica (Sharp et al., 2016; Hayles et al., 2018; Wostbrock et al., 2018). Together, triple oxygen thermometry, and clumped isotope approaches, have considerable potential as robust single mineral thermometers in future ore deposit investigations.

Defining internal oxygen isotope fractionation in clay minerals presents an additional technique by which temperature information may be generated in hydrothermal clay species. The $\delta^{18}O_{OH}$ method described in Chapter 4, represents a potential single mineral thermometer when results are combined with mineral fluorination $\delta^{18}O$ results. However, the lack of reliable thermal dehydroxylation methodology, and inherent technical challenges of operating silicate fluorination lines have limited development of this technique. The rapid thermal dehydroxylation approach presented in Chapters 3-4, and recently published thermogravimetric laser isotope methods (Oerter et al., 2017; Bauska et al., 2017),

provide new avenues for measuring the H and O isotopic values of mineral hydroxyl. Microfluorination using Teflon powder instead of conventional fluorination agents (e.g. ClF_3, BrF_5) has shown promise towards measuring $\delta^{18}O$ in quartz and biogenic silica (Menicucci et al., 2013), but has yet to be successfully applied in other classes of silicate minerals.

7.3 CLOSING REMARKS: TOWARDS AN OPTICAL FUTURE

Historically, the IRMS has been the workhorse of stable isotope science, but over the last decade optical spectroscopy platforms have become increasingly common. Although early laser models had lower precision and greater sample requirements than IRMS counterparts, recent methodological advances have demonstrated marked improvement on these fronts. This is exemplified by 1 ‰ measurement precision of δ^2H in the hydrous mineral methodology in this thesis, and work on carbonates measuring 1 to 100 µg samples at $\delta^{13}C$ and $\delta^{18}O$ precisions better than 0.1 ‰ (e.g. Sakai et al., 2017). While carbonate clumped isotopes and triple oxygen isotopes are typically quantified by IRMS, new laser based platforms show promise towards making these measurements. An optical instrument was recently developed to measure CO_2 clumped isotopes in geothermal and stochastic (1000 °C) gas, and recorded results within error of IRMS measurements (Prokhorov et al., 2019).

This thesis research was carried out with the objective of testing new, and emerging, stable isotope approaches for reconstructing temperature and fluid signals in ore deposits and geothermal fields. Significant findings were presented with respect to measurement of hydrous minerals and carbonates using both laser spectroscopy and IRMS approaches. These findings have useful application to hydrothermal research, and reflect interest across the global community of stable isotope users to develop better laser-based measurement techniques. Judging by the trajectory of advancement from early work by Urey, McCrea and others in the 1950s, followed by development of many standard stable isotope approaches by the 1960s, optical measurements in minerals, including clumped isotopes, should be widespread within the next 10-15 years. The advances to come will be made possible by interdisciplinary collaboration across the Earth sciences, in areas ranging from hydrothermal studies to palaeoceanography and atmospheric science.

APPENDIX A

Quantification of intersample memory using OA-ICOS with focus on rapid δ^2H surveys in ore deposits

DEFINITION OF MEMORY

Intersample memory is a well-documented operational aspect associated with measurement of molecular H_2O by laser spectroscopy (e.g. Penna et al., 2012; Koehler and Wassenaar, 2012; Oerter et al., 2017). In the continuous flow setup documented here for hydrous minerals, memory was evident during the first replicate in a series of measurements. Memory was minimised by shortening the transfer tubing and wrapping it with heat tape. Memory (M), defined elsewhere in literature (Geldern and Barth, 2012; Oerter et al., 2017), is calculated as a percent of the measured isotopic difference of adjacent analyses, relative to the true difference:

$$M\ (\%) = [1 - (\delta_m - \delta_p)/(\delta_f - \delta_p)] * 100 \qquad (A.1)$$

In the above relationship, δ_m is the measured isotopic value for a replicate, δ_p is the previous replicate isotope value, and δ_f is the final isotope value for a group of replicate measurements, as determined as the average of the final two values.

The application of this equation is demonstrated in Figure A.1 and Table A.1 for δ^2H measurements of kaolinite (Georgia Clay) and serpentine (ATG-1, WS-1), where memory is 25-30 % on the first measurement of a given mineral. For the second acquisition of the ATG-1 serpentine standard, the measurement is within error of the final value. Memory is observed on WS-1 through the third replicate. As a general rule, if the absolute value of the δ^2H difference ($\delta_m - \delta_p$) of two adjacent measurements is less than 4 ‰, memory is considered to have been overcome. When working with samples that cover a significant range of values, analysing three replicates may be necessary to overcome the memory effect, as

illustrated in Figure A.1, where the second acquisition of WS-1 is 5.1 ‰ higher than the final value.

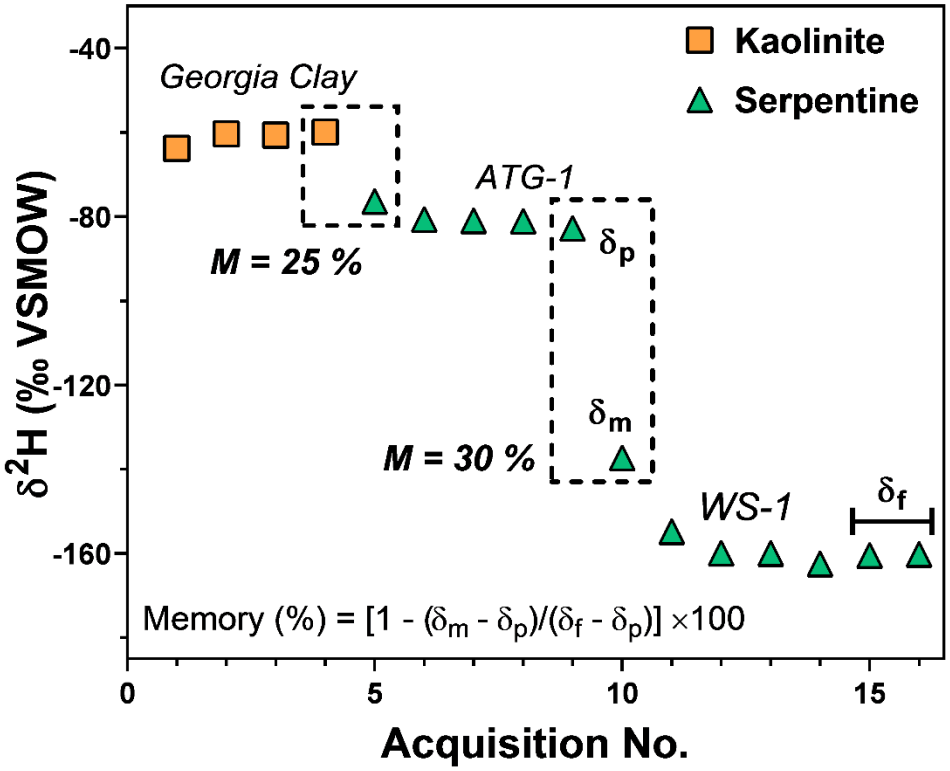

Figure A.1: A memory effect is observed for δ^2H measurements of kaolinite and serpentine mineral separates analysed by thermal dehydroxylation OA-ICOS. Minerals measured here record δ^2H values between -60 and -162 ‰ VSMOW. Memory was overcome by the second or third replicate.

Table A.1: Hydrogen isotope results and calculated memory associated with measuring hydrous minerals over a range of values.

Acq. No.	Mineral	δ^2H (‰ VSMOW)	δ_f	$(\delta_m - \delta_p)$	$(\delta_f - \delta_p)$	M (%)
1	Georgia Clay	-63.8				
2	Georgia Clay	-60.4		3.4	3.5	
3	Georgia Clay	-60.7		-0.3	0.1	
4	Georgia Clay	-60.0	-60.3	0.7	0.4	
5	ATG-1	-76.4		-16.4	-22.0	25
6	ATG-1	-80.7		-4.3	-5.6	23
7	ATG-1	-80.9		-0.3	-1.3	
8	ATG-1	-81.1		-0.2	-1.0	
9	ATG-1	-82.8	-82.0	-1.7	-0.8	
10	WS-1	-137.3		-54.5	-77.5	30
11	WS-1	-154.8		-17.5	-23.1	24
12	WS-1	-159.9		-5.1	-5.6	8
13	WS-1	-160.0		-0.1	-0.4	
14	WS-1	-162.4		-2.5	-0.4	
15	WS-1	-160.5		2.0	2.1	
16	WS-1	-160.2	-160.4	0.2	0.1	

RAPID SURVEY OF ASSAY PULPS IN MINERAL EXPLORATION

In order to achieve rapid throughput, it may be desirable to measure single replicates for a given sample. In Figure A.2, δ^2H results are compared in two boreholes at Waihi (UW 462, UW 85), where samples are measured either as single replicates with no memory correction, or as a groups of 3-4 replicates. At Waihi, where δ^2H is between approximately -60 and -80 ‰ VSMOW (Chapter 5) a memory effect is not strongly expressed in most cases, making similar interpretations possible using either a single or multi replicate approach. This is exemplified by the trend in decreasing δ^2H along latter half of the UW 462 borehole between 450 and 800 m (Figure A.2). Notably, borehole averages of δ^2H using either approach are similar. When deploying the thermal dehydroxylation OA-ICOS technique in a mineral exploration scenario, it should be possible to reconstruct the average δ^2H characteristics of a borehole using a single replicate approach. For extensive characterisation of δ^2H at the deposit scale, a single replicate approach will provide the best spatial coverage at the lowest analytical cost. For samples exhibiting a

significant memory effect, in excess of 5 ‰, an instrument specific correction may be applied. If necessary, anomalous data can subsequently be reanalysed using a multi replicate approach, with memory impacted samples corrected for, or excluded, from sample averages.

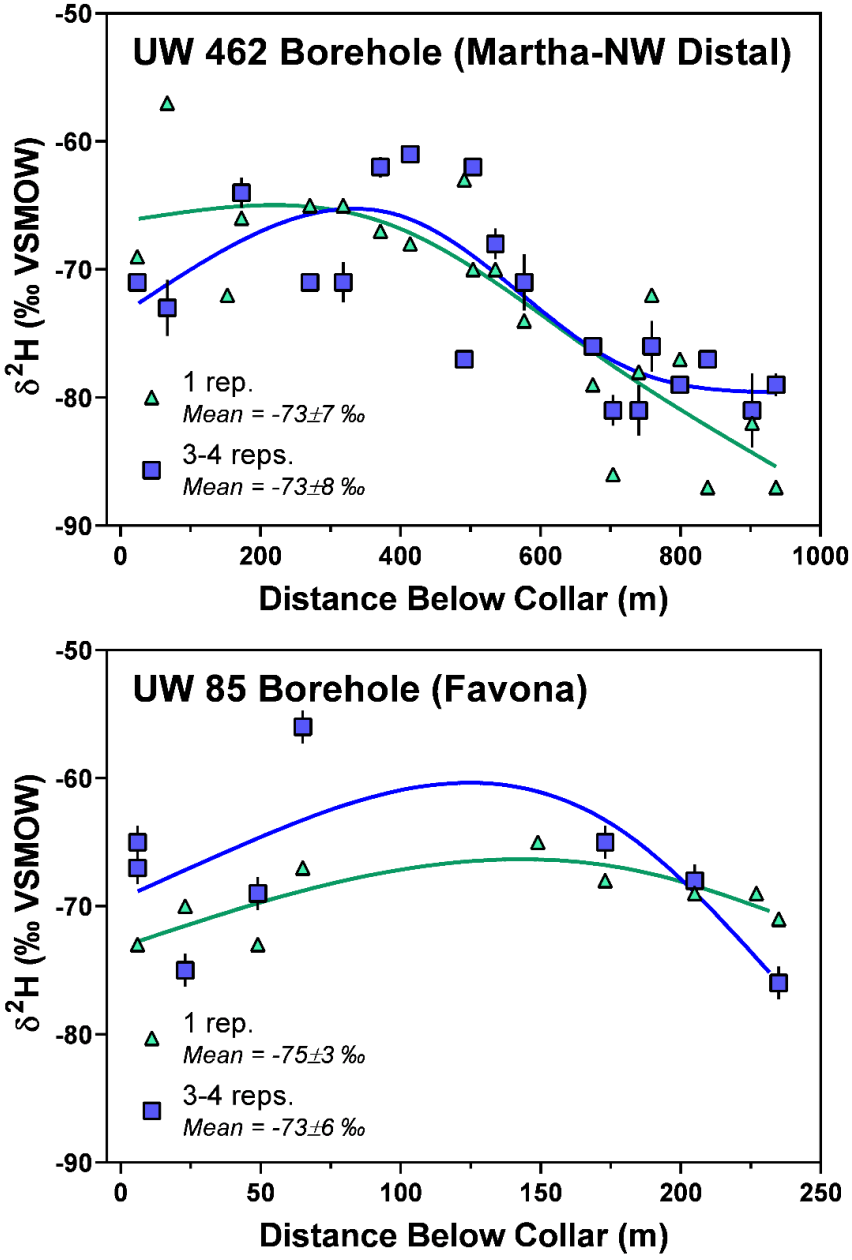

Figure A.2: Comparison of δ^2H collected on whole rock pulps in two boreholes at Waihi using either a single replicate approach (green) or by measuring groups of 3-4 replicates (blue). With the multi replicate approach, the first analysis is discarded and a mean is calculated from the remaining replicates. Borehole fit lines were calculated using a smoothing spline function. Similar trends are observed using either data collection methodology. For a rapid hydrogen isotope survey at the borehole or deposit scale, a single replicate approach will deliver sufficient accuracy. Local variation in samples, evident in an initial survey, may be verified by measuring 2-4 replicates, and excluding memory impacted samples.

APPENDIX B

Clumped isotope sample replicate data

SAMPLE REPLICATE RESULTS

Geothermal and ore deposit samples were typically measured 3-4 times in a randomised rotation. Results reported in Chapter 4 are means of replicates, with uncertainty reported as 1 standard error (1 s.e.). In Table B.1 clumped isotope replicate data is reported for analyses of TVZ, Waihi, Antamina, and Mount Isa carbonates. Additional parameters pertaining to sample preparation (i.e. acid digestion, gas cleanup) and analysis are presented in the digital appendix.

Table B.1: Clumped isotope sample replicate data

Sample	$\delta^{13}C_{min.}$ ‰ VPDB	1 s.e.	$\delta^{18}O_{min.}$ ‰ VPDB	1 s.e.	$\delta^{18}O_{min.}$ ‰ VSMOW	Δ_{47} ‰ CDES	1 s.e.	Δ_{48} ‰
Geothermal, Taupo volcanic zone, North Island, New Zealand								
WK-80	-5.8	0.004	-27.8	0.006	2.3	0.288	0.007	0.110
WK-80	-5.8	0.004	-27.7	0.007	2.4	0.351	0.008	0.676
WK-80	-5.9	0.004	-27.5	0.008	2.6	0.350	0.008	0.463
WK-80	-5.9	0.004	-27.5	0.007	2.6	0.414	0.006	0.220
Ngatamariki-Breccia	-6.5	0.004	-23.3	0.008	6.9	0.317	0.007	0.091
Ngatamariki-Breccia	-6.6	0.004	-23.3	0.007	6.9	0.465	0.006	0.223
Ngatamariki-Breccia	-6.6	0.004	-23.3	0.006	6.9	0.384	0.008	0.123
Ngatamariki-Breccia	-6.6	0.004	-23.1	0.006	7.1	0.466	0.008	0.272
Ngatamariki-Breccia	-6.6	0.004	-23.2	0.008	7.0	0.433	0.007	0.276
Ngatamariki-Breccia	-6.6	0.003	-23.3	0.008	6.9	0.384	0.008	0.587
BR-21-101	-7.1	0.005	-23.5	0.008	6.7	0.433	0.006	0.108
BR-21-101	-7.1	0.004	-23.3	0.007	6.9	0.339	0.007	0.278
BR-21-101	-7.1	0.005	-23.5	0.008	6.7	0.331	0.008	0.081
BR-21-101	-7.2	0.005	-23.3	0.007	6.9	0.435	0.006	0.282
BR-6-15-150	-7.1	0.004	-21.5	0.007	8.8	0.369	0.007	0.208
BR-6-15-150	-7.1	0.004	-21.3	0.007	8.9	0.375	0.008	0.154

Sample	$\delta^{13}C_{min.}$ ‰ VPDB	1 s.e.	$\delta^{18}O_{min.}$ ‰ VPDB	1 s.e.	$\delta^{18}O_{min.}$ ‰ VSMOW	Δ_{47} ‰ CDES	1 s.e.	Δ_{48} ‰
BR-6-15-150	-7.1	0.005	-21.5	0.007	8.8	0.430	0.008	0.018
BR-13-866	-7.8	0.004	-27.4	0.007	2.7	0.292	0.007	-0.003
BR-13-866	-7.9	0.004	-27.5	0.007	2.5	0.307	0.007	0.232
BR-27-400	-9.4	0.004	-26.0	0.007	4.1	0.293	0.008	0.162
BR-27-400	-9.4	0.004	-26.1	0.006	4.1	0.327	0.007	0.172
BR-27-400	-9.4	0.004	-26.0	0.007	4.1	0.348	0.007	0.179
BR-15-1655	-9.4	0.004	-29.8	0.007	0.2	0.308	0.008	0.523
BR-15-1655	-9.5	0.004	-29.8	0.006	0.2	0.313	0.007	0.275
BR-15-1655	-9.5	0.004	-29.8	0.008	0.2	0.338	0.007	0.263
BR-42-Ejecta	-10.2	0.004	-27.7	0.008	2.4	0.352	0.008	1.411
BR-42-Ejecta	-10.2	0.004	-27.8	0.006	2.3	0.258	0.006	0.361
BR-42-Ejecta	-10.2	0.004	-27.8	0.007	2.2	0.324	0.008	0.196
BR-42-Ejecta	-10.2	0.004	-27.6	0.008	2.4	0.297	0.007	0.422
BR-42-Ejecta	-10.2	0.005	-27.9	0.006	2.2	0.307	0.008	0.851

Sample	$\delta^{13}C_{min.}$ ‰ VPDB	1 s.e.	$\delta^{18}O_{min.}$ ‰ VPDB	1 s.e.	$\delta^{18}O_{min.}$ ‰ VSMOW	Δ_{47} ‰ CDES	1 s.e.	Δ_{48} ‰
Waihi, low sulphidation epithermal Au-Ag, North Island, New Zealand								
UW462-BB23V	-9.0	0.003	-25.5	0.008	4.6	0.407	0.007	0.333
UW462-BB23V	-9.0	0.004	-25.6	0.007	4.5	0.375	0.008	0.363
UW462-BB23V	-9.0	0.004	-25.5	0.007	4.6	0.367	0.007	0.230
UW462-879V	-8.6	0.004	-15.8	0.007	14.7	0.565	0.007	0.103
UW462-879V	-8.7	0.004	-15.7	0.007	14.7	0.520	0.007	0.520
UW462-879V	-8.8	0.004	-16.2	0.006	14.2	0.523	0.008	0.414
UW462-BB58V	-17.7	0.005	-20.7	0.007	9.6	0.472	0.006	0.457
UW462-BB58V	-17.8	0.004	-21.6	0.007	8.6	0.420	0.006	0.588
UW462-BB58V	-17.7	0.004	-21.1	0.008	9.1	0.380	0.007	0.881
SP0597-V	-8.0	0.005	-26.1	0.007	4.0	0.390	0.007	0.211
SP0597-V	-8.0	0.004	-26.2	0.008	4.0	0.289	0.008	0.492
SP0597-V	-8.0	0.004	-26.1	0.006	4.0	0.441	0.007	0.416
UW462-BB23R	-8.3	0.005	-26.3	0.007	3.8	0.344	0.006	0.371
UW462-BB23R	-8.4	0.004	-26.5	0.007	3.6	0.425	0.007	0.341
UW462-BB23R	-8.4	0.004	-26.0	0.007	4.1	0.340	0.008	0.592
	-8.0	0.004	-26.2	0.006	3.9	0.421	0.007	0.454

Sample	$\delta^{13}C_{min.}$ ‰ VPDB	1 s.e.	$\delta^{18}O_{min.}$ ‰ VPDB	1 s.e.	$\delta^{18}O_{min.}$ ‰ VSMOW	Δ_{47} ‰ CDES	1 s.e.	Δ_{48} ‰
SP0597-R								
SP0597-R	-8.8	0.004	-25.9	0.007	4.2	0.448	0.007	0.404
Antamina, polymetallic skarn (Cu-Zn), Peru								
4PAA157	0.1	0.004	-16.0	0.006	14.4	0.348	0.007	0.116
4PAA157	0.0	0.005	-16.1	0.007	14.3	0.448	0.007	0.157
4PAA157	0.1	0.004	-16.1	0.007	14.3	0.336	0.007	0.244
4PAA129	-2.1	0.004	-18.3	0.007	12.1	0.372	0.007	0.080
4PAA129	-2.2	0.004	-18.4	0.007	11.9	0.328	0.006	0.164
4PAA129	-2.3	0.005	-18.4	0.007	12.0	0.398	0.007	0.193
4PAA178	-2.6	0.004	-17.7	0.006	12.7	0.299	0.008	0.140
4PAA178	-2.6	0.004	-17.5	0.007	12.8	0.407	0.005	0.188
4PAA178	-2.6	0.004	-17.6	0.006	12.7	0.419	0.007	0.251
4PAA219	-10.6	0.004	-16.9	0.007	13.5	0.514	0.006	1.312
4PAA219	-10.7	0.005	-17.0	0.007	13.4	0.409	0.006	0.295
4PAA219	-10.7	0.005	-17.0	0.007	13.4	0.461	0.007	0.469
4PAA219	-10.6	0.004	-17.0	0.007	13.4	0.309	0.007	0.215
4PAA119	1.9	0.005	-7.5	0.007	23.2	0.395	0.007	0.092
4PAA119	1.9	0.005	-7.5	0.007	23.1	0.328	0.006	0.214

Sample	$\delta^{13}C_{min.}$ ‰ VPDB	1 s.e.	$\delta^{18}O_{min.}$ ‰ VPDB	1 s.e.	$\delta^{18}O_{min.}$ ‰ VSMOW	Δ_{47} ‰ CDES	1 s.e.	Δ_{48} ‰
3PAA273	0.9	0.004	-14.8	0.008	15.7	0.341	0.006	1.215
3PAA273	0.8	0.004	-15.0	0.007	15.4	0.380	0.007	0.124
3PAA273	0.7	0.004	-14.9	0.007	15.6	0.399	0.007	0.091
2PAG172	2.5	0.004	-6.5	0.007	24.3	0.250	0.007	-0.055
2PAG172	2.5	0.004	-6.4	0.007	24.3	0.336	0.008	0.312
2PAG172	2.5	0.004	-6.5	0.008	24.3	0.264	0.007	-0.247
Mount Isa, carbonate hosted (Pb-Zn, and Cu), Queensland, Australia								
ISA105621150V	-5.3	0.004	-18.6	0.007	11.7	0.257	0.007	0.232
ISA105586A150V	-5.5	0.004	-17.6	0.006	12.8	0.291	0.007	0.369

APPENDIX C

Hydrogen isotope results

In Tables C.1-C.3, δ^2H results and sample water contents are presented for Waihi, Karangahake, and Comstock. All data was collected using the OA-ICOS method presented in Chapter 2. Water was liberated from samples at 945 °C. Samples were calibrated to the VSMOW scale using the mineral reference standards developed in Chapter 2. Water content in samples was determined from yield functions developed by measuring variable amounts of Kga-1b kaolinite. Expanded results tables that include replicate data, VSMOW calibration equations, bias correction, and sample water content calculations are provided in the digital archive.

Table C.1: Hydrogen isotope results – Waihi. Sample intervals reflect distance below drill collar.

Borehole	Sample interval (m)	Type	δ^2H ‰ VSMOW	1σ	% H_2O
844SP0597	38.85	Pulp	-69.53	1.0	1.8
844SP0597	91.6	Pulp	-73.80	0.3	3.5
844SP0597	91.6	Clay Separate	-72.14	0.2	5.5
844SP0597	128.7	Pulp	-69.07	1.4	1.8
844SP0597	141	Pulp	-69.45	0.8	2.8
844SP0597	158.4	Pulp	-68.45	1.2	2.6
844SP0597	204.35	Pulp	-69.28	0.4	3.1
844SP0597	249.4	Pulp	-69.91	1.4	2.8
844SP0597	297.5	Pulp	-72.22	1.4	3.3
844SP0597	323.8	Pulp	-66.91	0.3	3.5
844SP0597	323.8	Clay Separate	-70.20	1.0	6.0
844SP0597	348.85	Pulp	-71.58	1.4	3.2
844SP0597	379.8	Pulp	-72.67	1.4	2.5
844SP0597	399.55	Pulp	-65.54	1.4	3.0
844SP0597	399.55	Clay Separate	-67.16	0.1	5.1
844SP0597	452.85	Pulp	-69.72	1.2	2.3
844SP0597	514.3	Pulp	-69.59	1.4	3.3
844SP0597	557.35	Pulp	-71.16	1.4	2.8
844SP0597	679.7	Pulp	-69.60	1.4	2.1
844SP0597	737	Pulp	-72.41	1.4	2.2
844SP0597	737	Clay Separate	-74.22	1.5	5.6
844SP0597	761	Pulp	-73.07	1.2	1.7

Borehole	Sample interval (m)	Type	δ^2H ‰ VSMOW	1σ	% H_2O
844SP0597	779.2	Pulp	-69.77	0.9	2.7
844SP0597	822.2	Pulp	-68.94	0.1	2.3
844SP0597	852	Pulp	-70.08	1.4	2.3
UW462	24	Pulp	-71.97	0.0	2.8
UW462	24	Clay Separate	-72.86	2.1	6.0
UW462	66.6	Pulp	-72.57	0.2	1.9
UW462	173	Pulp	-65.35	1.2	2.9
UW462	173	Clay Separate	-62.96	2.6	5.7
UW462	270.5	Pulp	-71.93	0.4	2.3
UW462	283	Clay Separate	-76.31	1.2	5.1
UW462	318.4	Pulp	-71.86	1.6	2.5
UW462	350.5	Pulp	-63.66	1.6	2.4
UW462	350.5	Clay Separate	-70.06	2.7	5.4
UW462	371.2	Pulp	-62.93	0.8	3.0
UW462	413.85	Pulp	-62.49	0.7	3.2
UW462	413.85	Clay Separate	-61.27	3.2	5.6
UW462	491	Pulp	-77.82	0.7	1.8
UW462	491	Clay Separate	-75.53	3.2	3.7
UW462	503.7	Pulp	-63.31	0.4	3.9
UW462	503.7	Clay Separate	-69.56	1.8	7.3
UW462	535.5	Pulp	-68.77	1.2	3.4
UW462	576.6	Pulp	-70.59	2.2	3.4
UW462	626	Clay Separate	-82.33	1.2	6.8
UW462	653.4	Pulp	-79.27	4.0	4.9
UW462	675	Pulp	-76.24	0.3	3.9
UW462	703.5	Pulp	-80.10	1.2	4.0
UW462	740.5	Pulp	-80.65	2.0	2.2
UW462	740.5	Clay Separate	-78.27	1.1	4.6
UW462	758.9	Pulp	-75.83	1.0	2.7
UW462	799.1	Pulp	-78.92	0.2	4.4
UW462	838.8	Pulp	-76.94	0.7	4.5
UW462	902.3	Pulp	-80.43	2.9	2.8
UW462	902.3	Clay Separate	-79.62	2.7	5.5
UW462	936.6	Pulp	-79.27	0.9	3.5
UW208	19	Pulp	-67.70	1.0	1.6
UW208	63	Pulp	-65.60	1.0	2.8
UW208	85	Pulp	-63.98	1.0	3.4
UW208	105	Pulp	-66.47	1.0	3.7
UW208	115	Pulp	-67.14	1.0	3.4
UW208	139	Pulp	-61.73	0.7	2.8
UW208	154	Pulp	-66.13	1.0	3.1
UW208	157	Pulp	-67.97	1.0	3.6
UW208	167	Pulp	-67.23	1.0	4.0
UW208	225	Pulp	-65.30	1.0	2.6

Borehole	Sample interval (m)	Type	δ^2H ‰ VSMOW	1σ	% H_2O
UW208	249	Pulp			4.2
UW208	269	Pulp			3.2
UW208	295	Pulp			3.2
UW213	87	Pulp	-61.10	1.9	2.3
UW213	87	Clay Separate	-67.59	1.2	6.0
UW213	113	Pulp	-63.85	0.4	3.3
UW213	155	Pulp	-68.55	3.2	2.6
UW213	207	Pulp	-64.03	1.0	2.5
UW213	251	Pulp	-62.67	0.6	2.8
UW221	29	Pulp	-64.86	3.2	2.6
UW221	55	Pulp	-61.70	3.2	1.9
UW221	99	Pulp	-63.81	2.0	2.8
UW221	141	Pulp	-61.33	3.2	4.0
UW221	185	Pulp	-58.86	3.2	4.1
UW221	215	Pulp	-63.90	2.2	1.2
UW221	230	Pulp	-67.16	3.2	2.5
UW320	208.25	Pulp			3.4
UW320	208.25	Pulp	-73.43	1.5	3.1
UW320	267.4	Pulp			2.3
UW320	267.4	Pulp	-73.44	0.9	2.6
UW320	308.8	Pulp	-71.30	1.0	2.3
UW320	308.8	Pulp	-74.48	0.5	2.6
UW320	340.9	Pulp	-70.33	1.0	1.8
UW320	340.9	Pulp	-73.86	0.4	2.1
UW320	362.25	Pulp	-71.85	1.0	2.3
UW320	376.85	Pulp	-69.57	1.0	2.2
UW320	397	Pulp	-69.37	1.0	3.0
UW320	397	Pulp	-73.51	0.3	3.1
UW320	415.6	Pulp	-70.04	1.0	2.4
UW320	430.6	Pulp	-68.00	1.0	2.5
UW320	430.6	Pulp	-73.65	2.3	2.6
UW320	474	Pulp			2.3
UW320	474	Pulp	-75.14	0.3	2.6
UW320	481.9	Pulp	-70.52	1.0	1.9
UW320	523.8	Pulp	-71.98	1.0	1.9
UW320	523.8	Pulp	-75.58	0.7	2.1
UW320	559.1	Pulp	-73.36	1.0	2.0
UW320	613.5	Pulp	-71.06	1.0	1.8
UW320	613.5	Pulp	-73.64	0.4	1.9
UW373	101	Pulp			4.1
UW373	101	Pulp	-54.03	0.5	3.6
UW373	107	Pulp			3.4

Borehole	Sample interval (m)	Type	δ^2H ‰ VSMOW	1σ	% H_2O
UW373	107	Pulp	-58.70	1.0	3.8
UW373	113	Pulp	-61.81	1.0	3.8
UW373	119	Pulp	-62.69	1.0	3.4
UW373	119	Pulp	-51.52	5.8	3.5
UW373	127	Pulp	-61.60	1.0	3.4
UW373	127	Pulp	-52.57	6.2	4.0
UW373	133	Pulp	-58.47	2.1	2.2
UW373	133	Pulp	-59.80	1.0	2.5
UW373	139	Pulp			3.6
UW373	145	Pulp	-64.69	1.0	3.7
UW373	145	Pulp	-55.68	1.5	3.5
UW67	45	Pulp	-59.26	1.3	2.4
UW67	184	Pulp	-59.49	3.2	2.4
UW67	191	Clay Separate	-69.74	1.2	5.1
UW67	216	Pulp	-62.34	3.2	2.8
UW67	266	Pulp	-60.02	2.2	2.7
UW79	55	Clay Separate	-74.48	1.2	2.9
UW79	135	Clay Separate	-71.29	1.2	7.2
UW85	6	Pulp			4.6
UW85	6	Pulp	-60.94	5.7	3.9
UW85	6	Pulp	-66.64	1.9	3.3
UW85	23	Pulp	-74.13	1.0	1.7
UW85	23	Pulp	-75.09	0.5	1.8
UW85	49	Pulp	-75.41	1.0	2.6
UW85	49	Pulp	-69.03	2.8	2.6
UW85	65	Pulp			2.3
UW85	65	Pulp	-60.42	1.4	3.1
UW85	65	Pulp	-51.15	1.1	2.4
UW85	149	Pulp	-67.93	1.0	1.1
UW85	173	Pulp	-70.18	1.0	2.9
UW85	173	Pulp	-65.16	0.6	3.1
UW85	205	Pulp	-71.35	1.0	3.5
UW85	205	Pulp	-67.65	0.2	3.5
UW85	227	Pulp	-71.02	1.0	3.5
UW85	235	Pulp	-72.62	1.0	2.9
UW85	235	Pulp	-75.49	1.7	3.0

Table C.2: Karangahake hydrogen isotope results. Sample numbers are from Simpson et al., 2019.

Sample	Type	δ^2H ‰ VSMOW	1σ	% H_2O
57491	Clay Separate	-74.5	1.2	5.5
57493	Clay Separate	-71.3	1.2	7.0
57495	Clay Separate	-67.0	1.2	6.3
57496	Clay Separate	-76.1	1.2	4.3
57499	Clay Separate	-77.9	1.2	4.9
57501	Clay Separate	-75.2	1.2	6.1
57504	Clay Separate	-75.3	1.2	5.0
57505	Clay Separate	-78.9	1.2	5.4
57507	Clay Separate	-75.3	1.2	5.6
57510	Clay Separate	-74.1	1.2	4.8
57515	Clay Separate	-79.3	1.2	4.6
57518	Clay Separate	-77.5	1.2	4.7
57519	Clay Separate	-69.9	1.2	4.8
57526	Clay Separate	-75.5	1.2	5.0
57535	Clay Separate	-77.4	1.2	4.5
57545	Clay Separate	-70.2	1.2	5.1
57547	Clay Separate	-74.1	1.2	5.0
57548	Clay Separate	-61.5	1.2	4.7
57551	Clay Separate	-75.5	1.2	5.6
57555	Clay Separate	-76.6	1.2	5.8
57568	Clay Separate	-72.5	1.2	5.6
57569	Clay Separate	-78.0	1.2	6.3
57570	Clay Separate	-71.0	1.2	7.4
57574	Clay Separate	-76.1	1.2	4.8
57581	Clay Separate	-69.1	1.2	5.4
57584	Clay Separate	-73.2	1.2	5.8
57598	Clay Separate	-72.2	1.2	3.5
57602	Clay Separate	-65.9	1.2	2.4

Table C.3: Comstock hydrogen isotope results. Sample numbers are from the Smithsonian, described in the supplemental data of Criss and Champion (1998).

Sample	Type	δ^2H ‰ VSMOW	1σ	% H_2O
71638	Pulp	-128.5	1.2	2.4
71639	Pulp	-133.5	1.2	7.2
71390	Pulp	-125.8	1.2	1.6
71598	Pulp	-131.4	1.2	2.7
71603	Pulp	-159.7	1.2	3.6
71643	Pulp	-136.3	1.2	2.5
71612	Pulp	-134.0	1.2	1.7
71424	Pulp	-121.4	1.2	1.4
71619	Pulp	-131.7	1.2	2.5
71642	Pulp	-128.7	1.2	3.2
71647	Pulp	-131.2	1.2	2.6
71570	Pulp	-134.4	1.2	3.1

APPENDIX D

Waihi carbonate isotope results

In Table D.1, $\delta^{13}C$, $\delta^{18}O$, and carbonate content measurements are presented for boreholes at Waihi. All data was collected following the general approach presented in Barker et al. (2011, 2013). Samples were acidified using 102 % orthophosphoric acid in exetainer vials at 72 °C. Sample CO_2 was transferred from exetainers to the OA-ICOS analyser using a needle autosampler, via a dry ice ethanol slush trap to remove H_2O. Sample gas was measured for 30 second intervals as a trapped pulse, or in continuous flow, following a peak area integration approach similar to that presented in Chapter 2. Calibration and yield standards indicate that either approach generates comparable data. Expanded results tables, which include calibration standards, are provided in the digital archive.

Table D.1: OA-ICOS carbonate isotope data collected at Waihi.

Borehole	Interval (m)	Sample Type	n	$\delta^{13}C$ ‰ VPDB	1σ	$\delta^{18}O$ ‰ VSMOW	1σ	% $CaCO_3$ Pulp
UW462	24.0	Pulp	3	-7.3	0.4	9.6	0.6	5.6
UW462	50.8	Pulp	2	-7.9	0.6	12.0	1.0	1.3
UW462	123.8	Pulp	3	-6.8	0.9	8.7	0.6	2.8
UW462	134.5	Pulp	2	-7.4	0.9	8.9	0.1	2.8
UW462	152.6	Pulp	1	-5.5	0.9	14.9	0.3	1.2
UW462	152.6	Vein	1	-9.4	0.3	5.2	0.3	
UW462	173.0	Pulp	2	-8.8	1.7	4.7	0.5	10.3
UW462	188.5	Pulp	2	-7.6	0.7	7.8	0.4	4.6
UW462	201.0	Pulp	3	-8.1	0.4	7.4	0.6	4.2
UW462	219.0	Pulp	2	-7.5	1.8	7.3	0.3	3.6
UW462	219.0	Vein	1	-10.2	0.3	5.0	0.3	
UW462	233.8	Pulp	3	-7.4	1.2	5.2	1.1	6.2
UW462	253.6	Pulp	2	-7.4	0.6	6.8	0.3	4.6
UW462	270.5	Pulp	1	-7.0	0.9	6.7	0.3	7.1
UW462	318.4	Pulp	3	-6.5	0.3	5.5	0.5	6.1
UW462	350.5	Pulp	1	-7.7	0.3	4.9	0.3	6.6
UW462	367.6	Pulp	1	-6.9	0.9	5.9	0.3	9.4
UW462	371.2	Pulp	1	-7.3	0.9	5.0	0.3	7.9
UW462	393.7	Pulp	1	-8.0	0.9	7.2	0.3	4.3
UW462	413.9	Pulp	1	-9.7	0.3	13.9	0.3	1.5
UW462	413.9	Vein	1	-8.0	0.3	4.2	0.3	
UW462	413.9	Replacement	1	-8.0	0.3	5.2	0.3	
UW462	430.0	Pulp	3	-7.8	1.1	5.2	1.0	3.8

Borehole	Interval (m)	Sample Type	n	$\delta^{13}C$ ‰ VPDB	1σ	$\delta^{18}O$ ‰ VSMOW	1σ	% $CaCO_3$ Pulp
UW462	460.0	Pulp	2	-6.3	0.4	16.5	4.6	0.8
UW462	482.5	Pulp	1	-8.3	0.9	3.2	0.3	8.7
UW462	482.5	Pulp	2	-8.8	0.8	5.3	1.7	3.5
UW462	491.0	Pulp	1	-7.3	0.4	9.7	0.1	2.7
UW462	503.7	Pulp	1	-7.7	0.4	9.3	0.1	2.6
UW462	522.4	Pulp	1	-6.6	0.9	6.6	0.3	8.4
UW462	535.5	Pulp	2	-4.0	1.9	14.0	2.3	3.5
UW462	548.2	Pulp	2	-7.9	0.8	11.9	0.2	1.7
UW462	587.5	Pulp	2	-6.5	0.6	9.2	0.4	2.1
UW462	610.0	Vein	1	-7.9	0.3	5.2	0.3	
UW462	610.0	Pulp	2	-6.4	1.6	10.5	0.7	3.4
UW462	626.0	Pulp	2	-5.4	0.0	8.2	1.8	5.9
UW462	644.5	Pulp	2	-10.2	2.3	9.4	1.2	4.6
UW462	653.4	Vein	1	-11.7	0.3	8.3	0.3	
UW462	653.4	Pulp	2	-8.4	1.3	9.2	1.4	4.7
UW462	675.0	Pulp	2	-6.6	2.5	8.7	2.0	2.9
UW462	689.3	Pulp	3	-4.5	2.8	10.7	1.7	2.7
UW462	703.5	Pulp	2	-6.4	1.5	10.5	2.0	3.0
UW462	719.5	Pulp	2	-6.0	1.7	9.6	1.2	4.5
UW462	740.5	Pulp	2	-6.1	1.6	9.9	1.7	2.5
UW462	780.0	Pulp	4	-6.7	0.2	10.4	0.6	7.3
UW462	799.1	Pulp	2	-7.4	1.1	10.0	0.1	9.7
UW462	838.8	Pulp	4	-7.6	1.8	10.8	1.1	11.9
UW462	858.4	Pulp	3	-5.3	1.2	10.4	0.7	6.7

Borehole	Interval (m)	Sample Type	n	$\delta^{13}C$ ‰ VPDB	1σ	$\delta^{18}O$ ‰ VSMOW	1σ	% $CaCO_3$ Pulp
UW462	879.0	Pulp	1	-5.0	0.9	13.3	0.3	3.2
UW462	902.3	Pulp	2	-7.3	0.1	14.3	0.5	1.3
UW462	917.4	Pulp	1	-5.9	0.4	11.1	0.1	9.3
UW462	936.6	Pulp	2	-6.3	1.0	15.0	3.5	2.9
UW462	956.9	Pulp	3	-5.8	1.6	10.8	0.5	3.3
UW364	79.9	Replacement	1	-8.2	0.3	5.7	0.3	
UW364	100.0	Pulp	2	-6.6	1.3	6.0	1.9	9.9
UW364	125.2	Pulp	2	-7.3	0.7	5.1	1.6	6.3
UW364	138.7	Replacement	1	-8.3	0.3	8.9	0.3	
UW364	146.9	Pulp	1	-8.1	0.6	4.2	0.4	9.9
UW364	170.7	Pulp	1	-8.0	0.6	4.4	0.4	4.2
UW364	208.3	Pulp	2	-8.3	1.3	6.2	1.8	6.9
UW364	248.9	Pulp	1	-3.2	0.6	0.8	0.4	7.3
UW364	255.9	Pulp	1	-7.5	1.5	6.4	0.8	
UW364	285.1	Pulp	3	-8.2	2.6	6.8	1.0	2.6
UW364	319.9	Pulp	2	-7.4	1.3	5.5	2.0	5.5
UW364	414.4	Pulp	1	-8.0	0.6	4.5	0.4	5.8
UW364	427.0	Pulp	2	-8.2	0.4	5.1	1.0	5.0
UW364	427.0	Replacement	1	-8.0	0.3	10.7	0.3	
844SP0597	6.3	Pulp	1	-11.7	1.5	6.1	0.8	
844SP0597	6.3	Vein	1	-9.7	0.3	19.8	0.3	
844SP0597	10.3	Pulp	2	-8.2	0.5	5.1	1.8	5.8

Borehole	Interval (m)	Sample Type	n	$\delta^{13}C$ ‰ VPDB	1σ	$\delta^{18}O$ ‰ VSMOW	1σ	% $CaCO_3$ Pulp
844SP0597	25.5	Pulp	1	-11.7	1.5	9.1	0.8	
844SP0597	53.0	Pulp	1	-8.5	0.4	5.1	0.4	8.2
844SP0597	91.6	Pulp	1	-7.9	0.6	3.9	0.4	6.8
844SP0597	106.8	Vein	1	-9.3	0.3	4.9	0.3	
844SP0597	106.8	Pulp	1	-7.8	0.3	4.6	0.3	54.7
844SP0597	141.0	Pulp	1	-9.5	0.4	6.9	0.4	2.7
844SP0597	141.0	Vein	1	-8.8	0.3	4.1	0.3	
844SP0597	171.3	Pulp	1	-8.7	0.4	6.2	0.1	5.3
844SP0597	184.0	Pulp	1	-9.1	0.4	6.8	0.4	5.8
844SP0597	249.4	Pulp	1	-8.2	0.4	10.1	0.4	2.6
844SP0597	297.5	Pulp	2	-7.1	0.6	4.6	1.2	4.3
844SP0597	316.8	Pulp	1	-9.1	0.3	4.4	0.3	6.4
844SP0597	323.8	Pulp	1	-9.1	0.3	4.4	0.3	5.6
844SP0597	360.2	Pulp	1	-8.0	0.4	3.3	0.4	6.1
844SP0597	399.6	Pulp	1	-8.5	0.3	3.6	0.3	7.5
844SP0597	452.9	Pulp	1	-6.8	0.6	7.4	0.4	4.9
844SP0597	472.5	Vein	1	-7.3	0.3	9.5	0.3	
844SP0597	494.7	Pulp	1	-7.9	0.4	4.4	0.4	4.7
844SP0597	514.3	Pulp	1	-8.5	0.3	6.2	0.3	3.0
844SP0597	537.9	Pulp	1	-8.6	0.4	4.0	0.4	8.9
844SP0597	537.9	Vein	1	-8.9	0.3	3.4	0.3	
844SP0597	557.4	Pulp	2	-8.2	1.9	6.1	0.1	1.9
844SP0597	601.6	Pulp	1	-7.7	0.4	5.4	0.4	5.9
844SP0597	645.9	Pulp	1	-6.7	0.4	4.6	0.4	8.4

Borehole	Interval (m)	Sample Type	n	$\delta^{13}C$ ‰ VPDB	1σ	$\delta^{18}O$ ‰ VSMOW	1σ	% $CaCO_3$ Pulp
844SP0597	679.7	Pulp	1	-6.1	0.6	3.1	0.4	7.2
844SP0597	702.2	Pulp	1	-8.7	0.4	2.9	0.4	8.5
844SP0597	737.0	Pulp	1	-6.7	0.4	13.8	0.4	0.7
844SP0597	761.0	Pulp	1	-7.3	0.6	2.8	0.4	7.9
844SP0597	779.2	Pulp	1	-7.9	0.3	3.3	0.3	4.7
844SP0597	796.8	Pulp	1	-8.7	0.4	4.3	0.4	4.4
844SP0597	833.3	Pulp	1	-8.9	0.4	4.3	0.4	5.6
844SP0597	852.0	Pulp	2	-6.4	0.5	5.1	1.4	6.3
UW320	226.0	Pulp	1	-7.9	0.3	8.5	0.3	1.7
UW320	267.4	Pulp	2	-9.4	0.2	6.7	2.2	2.3
UW320	267.4	Vein	1	-9.1	0.3	7.7	0.3	
UW320	272.0	Pulp	1	-8.4	0.6	5.4	0.4	7.2
UW320	272.0	Vein	1	-8.7	0.3	6.4	0.3	
UW320	308.8	Pulp	1	-7.6	0.4	5.1	0.4	7.0
UW320	328.2	Replacement	1	-8.9	0.3	7.7	0.3	
UW320	330.7	Pulp	1	-9.1	0.6	5.9	0.4	2.9
UW320	340.9	Pulp	1	-10.3	0.6	4.6	0.4	3.7
UW320	376.9	Pulp	1	-8.9	0.6	5.7	0.4	3.3
UW320	397.0	Pulp	1	-8.5	0.4	5.2	0.4	2.7
UW320	397.0	Replacement	1	-8.3	0.3	9.2	0.3	
UW320	399.8	Pulp	2	-8.3	0.2	5.3	1.0	3.9
UW320	415.6	Pulp	1	-9.6	0.4	3.7	0.4	8.9
UW320	415.6	Vein	1	-9.7	0.3	6.9	0.3	

Borehole	Interval (m)	Sample Type	n	$\delta^{13}C$ ‰ VPDB	1σ	$\delta^{18}O$ ‰ VSMOW	1σ	% $CaCO_3$ Pulp
UW320	425.8	Pulp	1	-8.9	0.4	6.8	0.4	2.2
UW320	430.6	Pulp	1	-8.7	0.6	5.5	0.4	3.4
UW320	430.6	Pulp	2	-7.5	1.8	6.6	1.6	3.3
UW320	465.8	Pulp	1	-9.3	0.4	2.8	0.4	2.6
UW320	474.0	Pulp	1	-9.5	0.3	7.0	0.3	1.5
UW320	480.5	Pulp	1	-9.3	0.3	5.6	0.3	3.5
UW320	481.2	Pulp	1	-9.4	0.3	7.4	0.3	1.9
UW320	481.9	Pulp	1	-10.0	0.3	5.8	0.3	2.6
UW320	483.5	Pulp	1	-8.8	0.6	4.4	0.4	3.2
UW320	501.2	Pulp	1	-7.5	0.4	9.0	0.4	1.1
UW320	517.0	Pulp	1	-9.2	0.4	3.2	0.4	6.5
UW320	523.8	Pulp	1	-8.0	0.6	4.3	0.4	6.2
UW320	523.8	Pulp	1	-8.7	0.3	5.9	0.3	6.4
UW320	559.1	Pulp	1	-7.7	0.4	5.3	0.4	7.0
UW320	561.6	Pulp	1	-6.8	0.6	6.0	0.4	4.6
UW320	562.7	Vein	1	-9.3	0.3	5.9	0.3	
UW320	562.7	Pulp	1	-9.1	0.3	4.6	0.3	8.7
UW320	564.4	Pulp	3	-7.4	3.3	4.0	0.6	9.9
UW320	581.6	Pulp	3	-8.1	2.2	8.7	3.0	2.3
UW320	607.2	Pulp	1	-8.4	0.3	3.9	0.3	4.9
UW320	613.5	Pulp	2	-8.2	0.1	5.8	0.4	3.8
CGD003	215.1	Pulp	2	-8.8	0.0	6.6	0.5	3.0
CGD003	230.0	Pulp	1	-8.5	0.3	9.1	0.3	1.2

Borehole	Interval (m)	Sample Type	n	$\delta^{13}C$ ‰ VPDB	1σ	$\delta^{18}O$ ‰ VSMOW	1σ	% $CaCO_3$ Pulp
CGD003	244.8	Pulp	2	-7.9	2.5	9.5	0.8	1.7
CGD003	250.8	Pulp	2	-10.8	3.2	6.8	0.5	2.9
CGD003	321.3	Pulp	2	-9.0	1.5	5.0	1.1	3.1
CGD003	326.2	Pulp	2	-8.0	0.5	5.2	0.1	3.4
CGD003	333.9	Pulp	1	-8.9	0.3	9.6	0.3	1.4
CGD003	343.4	Pulp	2	-7.9	0.3	5.6	0.9	3.6
UW373	103.0	Pulp	1	-8.5	0.3	4.7	0.3	5.9
UW373	105.0	Pulp	2	-8.7	2.0	5.4	0.7	6.1
UW373	109.0	Pulp	1	-6.9	0.4	6.3	0.4	7.7
UW373	111.0	Pulp	1	-7.6	0.3	5.4	0.3	5.3
UW373	113.0	Pulp	1	-8.2	0.3	6.4	0.3	3.6
UW373	115.0	Pulp	3	-7.8	0.8	19.3	4.3	1.1
UW373	119.0	Pulp	2	-9.2	1.3	23.8	0.8	0.8
UW373	121.0	Pulp	2	-9.7	3.1	19.9	2.1	0.9
UW373	123.0	Pulp	1	-9.2	0.3	6.1	0.3	4.1
UW373	129.0	Pulp	1	-8.5	0.3	6.4	0.3	4.8
UW373	131.0	Pulp	1	-9.6	0.3	9.1	0.3	2.3
UW373	133.0	Pulp	1	-7.7	0.4	20.2	0.4	1.0
UW373	139.0	Pulp	2	-8.7	0.4	22.9	0.7	0.7
UW373	141.0	Pulp	1	-7.8	0.3	5.1	0.3	4.2
UW373	145.0	Pulp	1	-8.6	0.3	21.9	0.3	0.6
UW67	150.0	Pulp	1	-0.1	0.3	22.1	0.3	8.6

Borehole	Interval (m)	Sample Type	n	$\delta^{13}C$ ‰ VPDB	1σ	$\delta^{18}O$ ‰ VSMOW	1σ	% $CaCO_3$ Pulp
UW67	170.0	Pulp	2	-2.4	2.1	20.9	1.6	8.7
UW67	210.0	Pulp	1	-1.8	0.3	21.8	0.3	7.9
UW67	230.0	Pulp	2	-1.1	0.2	21.4	1.6	9.3
UW67	250.0	Pulp	2	-3.8	3.9	20.3	0.4	7.5
UW67	280.0	Pulp	1	-3.3	0.3	20.5	0.3	5.9
UW348	84.9	Pulp	1	-7.9	0.4	5.5	0.4	8.2
UW348	109.9	Pulp	1	-8.0	0.4	6.3	0.4	2.2
UW348	122.3	Pulp	1	-7.4	0.3	10.1	0.3	0.2
UW348	217.4	Pulp	2	-8.8	0.7	4.9	1.2	1.3
UW348	250.0	Pulp	1	-9.5	0.3	6.6	0.3	1.8
UW348	254.2	Pulp	2	-9.0	0.2	5.4	0.7	4.3
UW348	254.7	Vein	1	-9.6	0.3	6.4	0.3	
UW348	258.7	Pulp	2	-11.2	1.7	6.0	2.0	6.0
UW348	267.1	Pulp	1	-9.5	0.3	5.9	0.3	6.2
UW348	279.0	Pulp	1	-9.0	0.3	7.1	0.3	2.2
UW348	285.5	Vein	1	-8.9	0.3	8.3	0.3	
UW348	295.9	Pulp	1	-10.1	0.3	6.9	0.3	2.5
UW348	295.9	Vein	1	-9.2	0.3	5.8	0.3	
UW348	314.4	Pulp	1	-9.0	0.4	4.5	0.4	3.3
UW348	333.9	Pulp	1	-8.3	0.4	4.8	0.4	5.9
UW348	352.7	Pulp	1	-7.9	0.3	10.1	0.3	0.9
UW348	358.7	Pulp	1	-12.2	0.3	8.7	0.3	0.1
UW348	374.55	Pulp	1	-9.4	0.3	5.6	0.3	3.4

Borehole	Interval (m)	Sample Type	n	$\delta^{13}C$ ‰ VPDB	1σ	$\delta^{18}O$ ‰ VSMOW	1σ	% $CaCO_3$ Pulp
UW208	93	Pulp	1	-8.3	0.3	4.3	0.3	2.9
UW208	123	Pulp	1	-11.9	0.3	6.9	0.3	1.5
UW208	151	Pulp	2	-9.3	0.1	9.6	0.8	1.6
UW208	177	Pulp	2	-9.3	0.4	6.2	0.5	1.8
UW208	179	Pulp	1	-9.5	0.3	4.2	0.3	8.2

REFERENCES

Affolter, S., Fleitmann, D., Leuenberger, M., 2014. New online method for water isotope analysis of speleothem fluid inclusions using laser absorption spectroscopy (WS-CRDS). Clim. Past. 10, 1291–1304. https://doi.org/10.5194/cp-10-1291-2014

Arehart, G.B., Donelick, R.A., 2006. Thermal and isotopic profiling of the Pipeline hydrothermal system: Application to exploration for Carlin-type gold deposits. Journal of Geochemical Exploration 91, 27–40.

Arribas Jr, A., 1995. Characteristics of high-sulfidation epithermal deposits, and their relation to magmatic fluid. Mineralogical Association of Canada Short Course 23, 419–454.

Baer, D.S., Paul, J.B., Gupta, M., O'Keefe, A., 2002. Sensitive absorption measurements in the near-infrared region using off-axis integrated-cavity-output spectroscopy. Appl Phys B 75, 261–265. https://doi.org/10.1007/s00340-002-0971-z

Banner, J.L., Hanson, G.N., 1990. Calculation of simultaneous isotopic and trace element variations during water-rock interaction with applications to carbonate diagenesis. Geochimica et Cosmochimica Acta 54, 3123–3137. https://doi.org/10.1016/0016-7037(90)90128-8

Barker, S.L., Dipple, G.M., 2019. Exploring for Carbonate-Hosted Ore Deposits Using Carbon and Oxygen Isotopes. Ore Deposits: Origin, Exploration, and Exploitation 185–207.

Barker, S.L., Dipple, G.M., Hickey, K.A., Lepore, W.A., Vaughan, J.R., 2013. Applying stable isotopes to mineral exploration: Teaching an old dog new tricks. Economic Geology 108, 1–9.

Barker, S.L.L., Dipple, G.M., Dong, F., Baer, D.S., 2011. Use of Laser Spectroscopy To Measure the 13C/12C and 18O/16O Compositions of Carbonate Minerals. Anal. Chem. 83, 2220–2226. https://doi.org/10.1021/ac103111y

Barker, S.L.L., Hood, S., Hughes, R.M., Richards, S., 2019. The lithogeochemical signatures of hydrothermal alteration in the Waihi epithermal district, New Zealand. New Zealand Journal of Geology and Geophysics 0, 1–18. https://doi.org/10.1080/00288306.2019.1651345

Barker, S.L.L., Dipple, G.M., Hickey, K.A., Lepore, W.A., Vaughan, J.R., 2013. Applying Stable Isotopes to Mineral Exploration: Teaching an Old Dog New Tricks. Economic Geology 108, 1–9. https://doi.org/10.2113/econgeo.108.1.1

Bauer, K.K., Vennemann, T.W., 2014. Analytical methods for the measurement of hydrogen isotope composition and water content in clay minerals by TC/EA. Chemical Geology 363, 229–240. https://doi.org/10.1016/j.chemgeo.2013.10.039

Bauska, T.K., Walters, G., Gázquez, F., Hodell, D.A., 2018. Online Differential Thermal Isotope Analysis of Hydration Water in Minerals by Cavity Ringdown Laser Spectroscopy. Anal Chem 90, 752–759.

https://doi.org/10.1021/acs.analchem.7b03136

Bechtel, A., Hoernes, S., 1990. Oxygen isotope fractionation between oxygen of different sites in illite minerals: a potential single-mineral thermometer. Contributions to Mineralogy and Petrology 104, 463–470.

Becker, G.F., 1882. Geology of the Comstock Lode and the Washoe District, with Atlas. U.S. Government Printing Office.

Beinlich, A., Barker, S.L.L., Dipple, G.M., Gupta, M., Baer, D.S., 2017. Stable Isotope (δ13C, δ18O) Analysis of Sulfide-Bearing Carbonate Samples Using Laser Absorption Spectrometry. Economic Geology 112, 693–700. https://doi.org/10.2113/econgeo.112.3.693

Beinlich, A., Barker, S.L.L., Dipple, G.M., Hansen, L.D., Megaw, P.K.M., 2019. Large-Scale Stable Isotope Alteration Around the Hydrothermal Carbonate-Replacement Cinco de Mayo Zn-Ag Deposit, Mexico. Economic Geology 114, 375–396. https://doi.org/10.5382/econgeo.2019.4635

Bell, T.H., 1983. Thrusting and duplex formation at Mount Isa, Queensland, Australia. Nature 304, 493–497. https://doi.org/10.1038/304493a0

Bergman, S.C., Huntington, K.W., Crider, J.G., 2013. Tracing paleofluid sources using clumped isotope thermometry of diagenetic cements along the Moab Fault, Utah. Am J Sci 313, 490–515. https://doi.org/10.2475/05.2013.03

Bernasconi, S.M., Müller, I.A., Bergmann, K.D., Breitenbach, S.F.M., Fernandez, A., Hodell, D.A., Jaggi, M., Meckler, A.N., Millan, I., Ziegler, M., 2018. Reducing Uncertainties in Carbonate Clumped Isotope Analysis Through Consistent Carbonate-Based Standardization. Geochemistry, Geophysics, Geosystems 0. https://doi.org/10.1029/2017GC007385

Bethke, P. M., Rye, R.O., 1979. Environment of ore deposition in the Creede mining district, San Juan Mountains, Colorado; Part IV, Source of fluids, from oxygen, hydrogen, and carbon isotope studies. Economic Geology 74, 1832–1851. https://doi.org/10.2113/gsecongeo.74.8.1832

Bickle, M.J., McKenzie, D., 1987. The transport of heat and matter by fluids during metamorphism. Contributions to Mineralogy and Petrology 95, 384–392.

Bigeleisen, J., Perlman, M.L., Prosser, H.C., 1952. Conversion of Hydrogenic Materials to Hydrogen for Isotopic Analysis. Anal. Chem. 24, 1356–1357. https://doi.org/10.1021/ac60068a025

Bodger, B., 2015. Andesite volcanic facies and hydrothermal alteration in the subsurface peripheral to existing Waihi mine workings (Thesis). University of Waikato.

Bonifacie, M., Calmels, D., Eiler, J.M., Horita, J., Chaduteau, C., Vasconcelos, C., Agrinier, P., Katz, A., Passey, B.H., Ferry, J.M., Bourrand, J.-J., 2017. Calibration of the dolomite clumped isotope thermometer from 25 to 350°C, and implications for a universal calibration for all (Ca, Mg, Fe)CO3 carbonates. Geochimica et Cosmochimica Acta 200, 255–279. https://doi.org/10.1016/j.gca.2016.11.028

Booden, M.A., Smith, I.E.M., Mauk, J.L., Black, P.M., 2012. Geochemical and isotopic development of the Coromandel Volcanic Zone, northern New Zealand, since 18 Ma. Journal of Volcanology and Geothermal Research

219–220, 15–32. https://doi.org/10.1016/j.jvolgeores.2012.01.005

Bottinga, Y., Javoy, M., 1975. Oxygen isotope partitioning among the minerals in igneous and metamorphic rocks. Reviews of Geophysics 13, 401–418. https://doi.org/10.1029/RG013i002p00401

Bowen, G.J., 2019. The Online Isotopes in Precipitation Calculator, version 3.1. URL http://www.waterisotopes.org

Bowman, J.R., Willett, S.D., Cook, S.J., 1994. Oxygen isotopic transport and exchange during fluid flow: One-dimensional models and applications. American Journal of Science;(United States) 294.

Boyabat, N., Özer, A.K., Bayrakçeken, S., Gülaboğlu, M.Ş., 2004. Thermal decomposition of pyrite in the nitrogen atmosphere. Fuel Processing Technology 85, 179–188. https://doi.org/10.1016/S0378-3820(03)00196-6

Brand, W.A., Assonov, S.S., Coplen, T.B., 2010. Correction for the 17O interference in δ(13C) measurements when analyzing CO2 with stable isotope mass spectrometry (IUPAC Technical Report). Pure and Applied Chemistry 82, 1719–1733. https://doi.org/10.1351/PAC-REP-09-01-05

Brathwaite, R.L., Christie, A.B., 1996. Geology of the Waihi Area: Part Sheets T13 and U13; Scale 1: 50 000. Institute of Geological & Nuclear Sciences Limited.

Brathwaite, R.L., Faure, K., 2002. The Waihi Epithermal Gold-Silver-Base Metal Sulfide-Quartz Vein System, New Zealand: Temperature and Salinity Controls on Electrum and Sulfide Deposition. Economic Geology 97, 269–290. https://doi.org/10.2113/gsecongeo.97.2.269

Brenan, J.M., McDonough, W.F., 2009. Core formation and metal–silicate fractionation of osmium and iridium from gold. Nature Geosci 2, 798–801. https://doi.org/10.1038/ngeo658

Brenna, J.T., Corso, T.N., Tobias, H.J., Caimi, R.J., 1997. High-precision continuous-flow isotope ratio mass spectrometry. Mass Spectrom Rev 16, 227–258. https://doi.org/10.1002/(SICI)1098-2787(1997)16:5<227::AID-MAS1>3.0.CO;2-J

Briggs, R.M., Houghton, B.F., McWilliams, M., Wilson, C.J.N., 2005. 40Ar/39Ar ages of silicic volcanic rocks in the Tauranga-Kaimai area, New Zealand: Dating the transition between volcanism in the Coromandel Arc and the Taupo Volcanic Zone. New Zealand Journal of Geology and Geophysics 48, 459–469. https://doi.org/10.1080/00288306.2005.9515126

Burgener, L., Huntington, K.W., Hoke, G.D., Schauer, A., Ringham, M.C., Latorre, C., Díaz, F.P., 2016. Variations in soil carbonate formation and seasonal bias over >4 km of relief in the western Andes (30°S) revealed by clumped isotope thermometry. Earth and Planetary Science Letters 441, 188–199. https://doi.org/10.1016/j.epsl.2016.02.033

Butterman, W.C., Amey, E., 2005. Mineral Commodity Profiles -- Gold. U.S. Geological Survey Open-File Report 02-303 66.

Buzon, M., 2016. Talc Characterization: A Provenance Study. University of Idaho.

Cameron, E., Hamilton, S., Leybourne, M., Hall, G., McClenaghan, B., 2004. Finding deeply buried deposits using geochemistry | Geochemistry:

Exploration, Environment, Analysis. Geochemistry: Exploration, Environment, Analysis 4, 7–32.

Capuano, R.M., 1992. The temperature dependence of hydrogen isotope fractionation between clay minerals and water: Evidence from a geopressured system. Geochimica et Cosmochimica Acta 56, 2547–2554. https://doi.org/10.1016/0016-7037(92)90208-Z

Cathles, L.M., 1993. Oxygen isotope alteration in the Noranda mining district, Abitibi greenstone belt, Quebec. Economic Geology 88, 1483–1511. https://doi.org/10.2113/gsecongeo.88.6.1483

Census.gov, 2019. [WWW Document]. URL https://www.census.gov/en.html

Chiba, H., Chacko, T., Clayton, R.N., Goldsmith, J.R., 1989. Oxygen isotope fractionations involving diopside, forsterite, magnetite, and calcite: Application to geothermometry. Geochimica et Cosmochimica Acta 53, 2985–2995. https://doi.org/10.1016/0016-7037(89)90174-9

Christenson, B.W., Mroczek, E.K., Kennedy, B.M., van Soest, M.C., Stewart, M.K., Lyon, G., 2002. Ohaaki reservoir chemistry: characteristics of an arc-type hydrothermal system in the Taupo Volcanic Zone, New Zealand. Journal of Volcanology and Geothermal Research 115, 53–82. https://doi.org/10.1016/S0377-0273(01)00309-2

Christie, A.B., Simpson, M.P., Brathwaite, R.L., Mauk, J.L., Simmons, S.F., 2007. Epithermal Au-Ag and Related Deposits of the Hauraki Goldfield, Coromandel Volcanic Zone, New Zealand. Economic Geology 102, 785–816. https://doi.org/10.2113/gsecongeo.102.5.785

Clayton, R.N., Friedman, I., Graf, D.L., Mayeda, T.K., Meents, W.F., Shimp, N.F., 1966. The origin of saline formation waters: 1. Isotopic composition. Journal of Geophysical Research 71, 3869–3882. https://doi.org/10.1029/JZ071i016p03869

Clayton, R.N., Mayeda, T.K., 1963. The use of bromine pentafluoride in the extraction of oxygen from oxides and silicates for isotopic analysis. Geochimica et Cosmochimica Acta 27, 43–52. https://doi.org/10.1016/0016-7037(63)90071-1

Clayton, R.N., O'Neil, J.R., Mayeda, T.K., 1972. Oxygen isotope exchange between quartz and water. Journal of Geophysical Research 77, 3057–3067.

Clayton, R.N., Steiner, A., 1975. Oxygen isotope studies of the geothermal system at Wairakei, New Zealand. Geochimica et Cosmochimica Acta 39, 1179–1186.

Cline, J.S., Hofstra, A.H., Muntean, J.L., Tosdal, R.M., Hickey, K.A., 2005. Carlin-type gold deposits in Nevada: Critical geologic characteristics and viable models. Economic Geology 100th anniversary volume 451, 484.

Coleman, M.L., Shepherd, T.J., Durham, J.J., Rouse, J.E., Moore, G.R., 1982. Reduction of water with zinc for hydrogen isotope analysis. Analytical Chemistry 54, 993–995.

Coplen, T.B., 2011. Guidelines and recommended terms for expression of stable-isotope-ratio and gas-ratio measurement results. Rapid communications in mass spectrometry 25, 2538–2560.

Coplen, T.B., 1988. Normalization of oxygen and hydrogen isotope data.

Chemical Geology: Isotope Geoscience section 72, 293–297. https://doi.org/10.1016/0168-9622(88)90042-5

Coplen, T.B., Kendall, C., Hopple, J., 1983. Comparison of stable isotope reference samples. Nature 302, 236.

Craig, H., 1961. Isotopic Variations in Meteoric Waters. Science 133, 1702–1703. https://doi.org/10.1126/science.133.3465.1702

Craig, H., 1957. Isotopic standards for carbon and oxygen and correction factors for mass-spectrometric analysis of carbon dioxide. Geochimica et Cosmochimica Acta 12, 133–149. https://doi.org/10.1016/0016-7037(57)90024-8

Criss, R.E., Champion, D.E., Horan, M.F., 1988. Oxygen isotope map of the fossil hydrothermal system in the Comstock Lode mining district, Nevada. US Geol. Surv. Circ. 1035, 11–13.

Criss, R.E., Taylor Jr, H.P., 1986. Meteoric-hydrothermal systems. Reviews in Mineralogy 16, 373–424.

Criss, R.E., Taylor, H.P., 1979. Isotopic evidence for the relationship of large-scale Eocene meteoric-hydrothermal systems to mineral deposits and cauldron subsidence in the Idaho batholith labs. I: American Institute of Mining Metallurgical Engineers, in: Technical Program, Fall Meeting. p. 24.

Criss, R.E., Taylor Jr, H.P., 1983. An 18O/16O and D/H study of Tertiary hydrothermal systems in the southern half of the Idaho batholith. Geological Society of America Bulletin 94, 640–663.

Criss, R.E., Champion, D.E., McIntyre, D.H., 1985. Oxygen isotope, aeromagnetic, and gravity anomalies associated with hydrothermally altered zones in the Yankee Fork mining district, Custer County, Idaho. Economic Geology 80, 1277–1296. https://doi.org/10.2113/gsecongeo.80.5.1277

Criss, R.E., Fleck, R.J., Taylor, H.P., 1991. Tertiary meteoric hydrothermal systems and their relation to ore deposition, northwestern United States and southern British Columbia. Journal of Geophysical Research: Solid Earth 96, 13335–13356. https://doi.org/10.1029/91JB00640

Criss, R.E., Gregory, R.T., Taylor, H.P., 1987. Kinetic theory of oxygen isotopic exchange between minerals and water. Geochimica et Cosmochimica Acta 51, 1099–1108. https://doi.org/10.1016/0016-7037(87)90203-1

Criss, R.E., Singleton, M.J., Champion, D.E., 2000. Three-Dimensional Oxygen Isotope Imaging of Convective Fluid Flow around the Big Bonanza, Comstock Lode Mining District, Nevada. Economic Geology 95, 131–142. https://doi.org/10.2113/gsecongeo.95.1.131

Crocket, J.H., 1991. Distribution of gold in the Earth's crust, in: Gold Metallogeny and Exploration. Springer US, pp. 1–36. https://doi.org/10.1007/978-1-4613-0497-5_1

De Groot, P.A., 2004. Handbook of stable isotope analytical techniques. Elsevier.

Defliese, W.F., Lohmann, K.C., 2015. Non-linear mixing effects on mass-47 CO2 clumped isotope thermometry: Patterns and implications. Rapid Communications in Mass Spectrometry 29, 901–909. https://doi.org/10.1002/rcm.7175

Deines, P., Langmuir, D., Harmon, R.S., 1974. Stable carbon isotope ratios and the existence of a gas phase in the evolution of carbonate ground waters. Geochimica et Cosmochimica Acta 38, 1147–1164.

Dempsey, D.E., Simmons, S.F., Archer, R.A., Rowland, J.V., 2012. Delineation of catchment zones of geothermal systems in large-scale rifted settings. Journal of Geophysical Research 117. https://doi.org/10.1029/2012JB009515

Dennis, K.J., Affek, H.P., Passey, B.H., Schrag, D.P., Eiler, J.M., 2011. Defining an absolute reference frame for 'clumped' isotope studies of CO2. Geochimica et Cosmochimica Acta 75, 7117–7131. https://doi.org/10.1016/j.gca.2011.09.025

Dennis, K.J., Schrag, D.P., 2010. Clumped isotope thermometry of carbonatites as an indicator of diagenetic alteration. Geochimica et Cosmochimica Acta 74, 4110–4122. https://doi.org/10.1016/j.gca.2010.04.005

Dennis, P.F., Myhill, D.J., Marca, A., Kirk, R., 2018. Clumped isotope evidence for episodic, rapid flow of fluids in a mineralized fault system in the Peak District, UK. Journal of the Geological Society jgs2016-117. https://doi.org/10.1144/jgs2016-117

Dilles, J.H., 2007. D/H via TCEA on minerals - musc vs biot. ISOGEOCHEM Archives.

Dilles, J.H., Solomon, G.C., Taylor, H.P., Einaudi, M.T., 1992. Oxygen and hydrogen isotope characteristics of hydrothermal alteration at the Ann-Mason porphyry copper deposit, Yerington, Nevada. Economic Geology 87, 44–63. https://doi.org/10.2113/gsecongeo.87.1.44

Dipple, G.M., Ferry, J.M., 1992. Metasomatism and fluid flow in ductile fault zones. Contr. Mineral. and Petrol. 112, 149–164. https://doi.org/10.1007/BF00310451

Djouka-Fonkwé, M.L., Kyser, K., Clark, A.H., Urqueta, E., Oates, C.J., Ihlenfeld, C., 2012. Recognizing Propylitic Alteration Associated with Porphyry Cu-Mo Deposits in Lower Greenschist Facies Metamorphic Terrain of the Collahuasi District, Northern Chile—Implications of Petrographic and Carbon Isotope Relationships. Economic Geology 107, 1457–1478. https://doi.org/10.2113/econgeo.107.7.1457

Douglas, P.M.J., Affek, H.P., Ivany, L.C., Houben, A.J.P., Sijp, W.P., Sluijs, A., Schouten, S., Pagani, M., 2014. Pronounced zonal heterogeneity in Eocene southern high-latitude sea surface temperatures. PNAS 201321441. https://doi.org/10.1073/pnas.1321441111

Eaton, G.F., Criss, R.E., Champion, D.E., 1998. The Becker Collection, Comstock Lode, Nevada: A compilation of historical notes and recent data. Rep. UCRL-ID 130195, 108.

Engel, A.E.J., Clayton, R.N., Epstein, S., 1958. Variations in isotopic composition of oxygen and carbon in Leadville limestone (Mississippian, Colorado) and in its hydrothermal and metamorphic phases. The Journal of Geology 66, 374–393.

Eiler, J.M., 2011. Paleoclimate reconstruction using carbonate clumped isotope thermometry. Quaternary Science Reviews 30, 3575–3588. https://doi.org/10.1016/j.quascirev.2011.09.001

Eiler, J.M., 2007. “Clumped-isotope” geochemistry—The study of naturally-occurring, multiply-substituted isotopologues. Earth and Planetary Science Letters 262, 309–327. https://doi.org/10.1016/j.epsl.2007.08.020

Epstein, S., Buchsbaum, R., Lowenstam, H.A., Urey, H.C., 1953. Revised Carbonate-Water Isotopic Temperature Scale. Geological Society of America Bulletin 64, 1315–1326. https://doi.org/10.1130/0016-7606(1953)64[1315:RCITS]2.0.CO;2

Escalante, A., Dipple, G.M., Barker, S.L.L., Tosdal, R., 2010. Defining trace-element alteration halos to skarn deposits hosted in heterogeneous carbonate rocks: Case study from the Cu–Zn Antamina skarn deposit, Peru. Journal of Geochemical Exploration 105, 117–136. https://doi.org/10.1016/j.gexplo.2010.04.011

Essene, E.J., Peacor, D.R., 1995. CLAY MINERAL THERMOMETRY- A CRITICAL PERSPECTIVE. Clays and Clay Minerals 43, 540–553.

Evans, N.P., Turchyn, A.V., Gázquez, F., Bontognali, T.R.R., Chapman, H.J., Hodell, D.A., 2015. Coupled measurements of δ18O and δD of hydration water and salinity of fluid inclusions in gypsum from the Messinian Yesares Member, Sorbas Basin (SE Spain). Earth and Planetary Science Letters 430, 499–510. https://doi.org/10.1016/j.epsl.2015.07.071

Faure, K., Matsuhisa, Y., Metsugi, H., Mizota, C., Hayashi, S., 2002. The Hishikari Au-Ag Epithermal Deposit, Japan: Oxygen and Hydrogen Isotope Evidence in Determining the Source of Paleohydrothermal Fluids. Economic Geology 97, 481–498. https://doi.org/10.2113/gsecongeo.97.3.481

Ferry, J.M., Gerdes, M.L., 1998. Chemically Reactive Fluid Flow During Metamorphism. Annual Review of Earth and Planetary Sciences 26, 255–287. https://doi.org/10.1146/annurev.earth.26.1.255

Gázquez, F., Mather, I., Rolfe, J., Evans, N.P., Herwartz, D., Staubwasser, M., Hodell, D.A., 2015. Simultaneous analysis of 17O/16O, 18O/16O and 2H/1H of gypsum hydration water by cavity ring-down laser spectroscopy. Rapid Commun. Mass Spectrom. 29, 1997–2006. https://doi.org/10.1002/rcm.7312

Geatches, D., 2011. Clay minerals and their gallery guests: an ab initio investigation into their interactions. Durham University.

Giggenbach, W.F., 1980. Geothermal gas equilibria. Geochimica et Cosmochimica Acta 44, 2021–2032. https://doi.org/10.1016/0016-7037(80)90200-8

Giggenbach, W.F., 1981. Geothermal mineral equilibria. Geochimica et Cosmochimica Acta 45, 393–410.

Giggenbach, W.F., 1992a. Magma Degassing and Mineral Deposition in Hydrothermal Systems along Convergent Plate Boundaries. Economic Geology, Society of Economic Geologists Bulletin 97, 1927–1944.

Giggenbach, W.F., 1992b. Isotopic shifts in waters from geothermal and volcanic systems along convergent plate boundaries and their origin. Earth and Planetary Science Letters 113, 495–510. https://doi.org/10.1016/0012-821X(92)90127-H

Giletti, B.J., 1986. Diffusion effects on oxygen isotope temperatures of slowly cooled igneous and metamorphic rocks. Earth and Planetary Science Letters 77, 218–228. https://doi.org/10.1016/0012-821X(86)90162-7

Gilg, H.A., Sheppard, S.M.F., 1996. Hydrogen isotope fractionation between kaolinite and water revisited. Geochimica et Cosmochimica Acta 60, 529–533. https://doi.org/10.1016/0016-7037(95)00417-3

Girard, J.-P., Savin, S.M., 1996. Intracrystalline fractionation of oxygen isotopes between hydroxyl and non-hydroxyl sites in kaolinite measured by thermal dehydroxylation and partial fluorination. Geochimica et Cosmochimica Acta 60, 469–487.

Gonfiantini, R., 1984. Advisory Group Meeting on Stable Isotope Reference Samples for Geochemical and Hydrological Investigations: IAEA, Vienna, 19-21 September 1983: Report to the Director General. International Atomic Energy Agency.

Graham, C.M., Viglino, J.A., Harmon, R.S., 1987. Experimental study of hydrogen-isotope exchange between aluminous chlorite and water and of hydrogen diffusion in chlorite. American Mineralogist 72, 566–579.

Grim, R.E., 1962. Clay mineralogy: the clay mineral composition of soils and clays is providing an understanding of their properties. Science 135, 890–898.

Gupta, P., Noone, D., Galewsky, J., Sweeney, C., Vaughn, B.H., 2009. Demonstration of high-precision continuous measurements of water vapor isotopologues in laboratory and remote field deployments using wavelength-scanned cavity ring-down spectroscopy (WS-CRDS) technology. Rapid Commun. Mass Spectrom. 23, 2534–2542. https://doi.org/10.1002/rcm.4100

Hamilton, A.R., Campbell, K.A., Rowland, J.V., Barker, S., Guido, D., 2018. Characteristics and variations of sinters in the Coromandel Volcanic Zone: application to epithermal exploration. New Zealand Journal of Geology and Geophysics 1–19.

Hamza, M.S., Epstein, S., 1980. Oxygen isotopic fractionation between oxygen of different sites in hydroxyl-bearing silicate minerals. Geochimica et Cosmochimica Acta 44, 173–182. https://doi.org/10.1016/0016-7037(80)90129-5

Hannan, K.W., Golding, S.D., Herbert, H.K., Krouse, H.R., 1993. Contrasting alteration assemblages in metabasites from Mount Isa, Queensland; implications for copper ore genesis. Economic Geology 88, 1135–1175. https://doi.org/10.2113/gsecongeo.88.5.1135

Hayles, J., Gao, C., Cao, X., Liu, Y., Bao, H., 2018. Theoretical calibration of the triple oxygen isotope thermometer. Geochimica et Cosmochimica Acta 235, 237–245.

Haynes, D.W., Cross, K.C., Bills, R.T., Reed, M.H., 1995. Olympic Dam ore genesis; a fluid-mixing model. Economic Geology 90, 281–307. https://doi.org/10.2113/gsecongeo.90.2.281

Hedenquist, J.W., Arribas R., A., Gonzalez-Urien, E., 2000. Exploration for Epithermal Gold Deposits, in: Hagemann, S.G., Brown, P.E. (Eds.), Gold in 2000. Society of Economic Geologists, p. 0.

https://doi.org/10.5382/Rev.13.07

Hedenquist, Jeffrey W., Browne, P.R., 1989. The evolution of the Waiotapu geothermal system, New Zealand, based on the chemical and isotopic composition of its fluids, minerals and rocks. Geochimica et Cosmochimica Acta 53, 2235–2257.

Hedenquist, J.W., Lowenstern, J.B., 1994. The role of magmas in the formation of hydrothermal ore deposits. Nature 370, 519–527. https://doi.org/10.1038/370519a0

Heinrich, C.A., Andrew, A.S., Wilkins, R.W.T., Patterson, D.J., 1989. A fluid inclusion and stable isotope study of synmetamorphic copper ore formation at Mount Isa, Australia. Economic Geology 84, 529–550. https://doi.org/10.2113/gsecongeo.84.3.529

Heinrich, C.A., Walshe, J.L., Harrold, B.P., 1996. Chemical mass transfer modelling of ore-forming hydrothermal systems: current practise and problems. Ore Geology Reviews, The Conjunction of Processes Resulting in the Formation of Orebodies 10, 319–338. https://doi.org/10.1016/0169-1368(95)00029-1

Henley, R.W., Ellis, A.J., 1983. Geothermal systems ancient and modern: a geochemical review. Earth-Science Reviews 19, 1–50. https://doi.org/10.1016/0012-8252(83)90075-2

Hodell, D.A., Turchyn, A.V., Wiseman, C.J., Escobar, J., Curtis, J.H., Brenner, M., Gilli, A., Mueller, A.D., Anselmetti, F., Ariztegui, D., Brown, E.T., 2012. Late Glacial temperature and precipitation changes in the lowland Neotropics by tandem measurement of δ18O in biogenic carbonate and gypsum hydration water. Geochimica et Cosmochimica Acta 77, 352–368. https://doi.org/10.1016/j.gca.2011.11.026

Hoefs, J., Hoefs, J., 2009. Stable isotope geochemistry. Springer.

Honlet, R., Gasparrini, M., Muchez, P., Swennen, R., John, C.M., 2018. A new approach to geobarometry by combining fluid inclusion and clumped isotope thermometry in hydrothermal carbonates. Terra Nova 30, 199–206. https://doi.org/10.1111/ter.12326

Horita, J., 2014. Oxygen and carbon isotope fractionation in the system dolomite–water–CO2 to elevated temperatures. Geochimica et Cosmochimica Acta 129, 111–124. https://doi.org/10.1016/j.gca.2013.12.027

Horton, T.W., Atkinson, L., Oze, C., 2012. Hydrothermal carbonate geochemistry of the Ngatamariki subsurface reservoir, New Zealand, in: Proceedings of the Thirty-Seventh Workshop on Geothermal Reservoir Engineering, Stanford, California. pp. 1–8.

Hughes, R., Barker, S.L.L., 2017. Using portable XRF to infer adularia halos within the Waihi Au-Ag system, New Zealand. Geochemistry: Exploration, Environment, Analysis geochem2016-006. https://doi.org/10.1144/geochem2016-006

Huntington, K.W., Budd, D.A., Wernicke, B.P., Eiler, J.M., 2011. Use of Clumped-Isotope Thermometry To Constrain the Crystallization Temperature of Diagenetic Calcite. Journal of Sedimentary Research 81, 656–669. https://doi.org/10.2110/jsr.2011.51

Huntington, K.W., Wernicke, B.P., Eiler, J.M., 2010. Influence of climate change and uplift on Colorado Plateau paleotemperatures from carbonate clumped isotope thermometry. Tectonics 29. https://doi.org/10.1029/2009TC002449

Ingebritsen, S.E., Manning, C.E., 2010. Permeability of the continental crust: dynamic variations inferred from seismicity and metamorphism. Geofluids 10, 193–205.

Inoue, A., 1995. Formation of Clay Minerals in Hydrothermal Environments, in: Velde, B. (Ed.), Origin and Mineralogy of Clays: Clays and the Environment. Springer Berlin Heidelberg, Berlin, Heidelberg, pp. 268–329. https://doi.org/10.1007/978-3-662-12648-6_7

Jackson, M.J., Scott, D.L., Rawlings, D.J., 2000. Stratigraphic framework for the Leichhardt and Calvert Superbasins: Review and correlations of the pre-1700 Ma successions between Mt Isa and McArthur River. Australian Journal of Earth Sciences 47, 381–403. https://doi.org/10.1046/j.1440-0952.2000.00789.x

Javoy, M., Pineau, F., Delorme, H., 1986. Carbon and nitrogen isotopes in the mantle. Chemical geology 57, 41–62.

Kele, S., Breitenbach, S.F.M., Capezzuoli, E., Meckler, A.N., Ziegler, M., Millan, I.M., Kluge, T., Deák, J., Hanselmann, K., John, C.M., Yan, H., Liu, Z., Bernasconi, S.M., 2015. Temperature dependence of oxygen- and clumped isotope fractionation in carbonates: A study of travertines and tufas in the 6–95 °C temperature range. Geochimica et Cosmochimica Acta 168, 172–192. https://doi.org/10.1016/j.gca.2015.06.032

Kelson, J.R., Huntington, K.W., Schauer, A.J., Saenger, C., Lechler, A.R., 2017. Toward a universal carbonate clumped isotope calibration: Diverse synthesis and preparatory methods suggest a single temperature relationship. Geochimica et Cosmochimica Acta 197, 104–131. https://doi.org/10.1016/j.gca.2016.10.010

Kesler, S.E., Simon, A.C., 2015. Mineral Resources, Economics and the Environment by Stephen E. Kesler. Cambridge University Press. https://doi.org/10.1017/CBO9781139871426

Kesler, S.E., Vennemann, T.W., Frederickson, C., Breithaupt, A., Vazquez, R., Furman, F.C., 1997. Hydrogen and oxygen isotope evidence for origin of MVT-forming brines, southern Appalachians. Geochimica et Cosmochimica Acta 61, 1513–1523. https://doi.org/10.1016/S0016-7037(97)00014-8

Kim, S.-T., O'Neil, J.R., 1997. Equilibrium and nonequilibrium oxygen isotope effects in synthetic carbonates. Geochimica et Cosmochimica Acta 61, 3461–3475. https://doi.org/10.1016/S0016-7037(97)00169-5

Kluge, T., John, C.M., Jourdan, A.-L., Davis, S., Crawshaw, J., 2015. Laboratory calibration of the calcium carbonate clumped isotope thermometer in the 25–250°C temperature range. Geochimica et Cosmochimica Acta 157, 213–227. https://doi.org/10.1016/j.gca.2015.02.028

Koehler, G., Wassenaar, L.I., 2012. Determination of the Hydrogen Isotopic Compositions of Organic Materials and Hydrous Minerals Using Thermal Combustion Laser Spectroscopy. Anal. Chem. 84, 3640–3645. https://doi.org/10.1021/ac3000489

Kotzer, T.G., Kyser, T.K., 1995. Petrogenesis of the Proterozoic Athabasca Basin, northern Saskatchewan, Canada, and its relation to diagenesis, hydrothermal uranium mineralization and paleohydrogeology. Chemical Geology 120, 45–89.

Kyser, K., Barr, J., Ihlenfeld, C., 2015. Applied Geochemistry in Mineral Exploration and Mining. Elements 11, 241–246. https://doi.org/10.2113/gselements.11.4.241

Lambert, S.J., Epstein, S., 1980. Stable isotope investigations of an active geothermal system in Valles Caldera, Jemez Mountains, New Mexico. Journal of Volcanology and Geothermal Research 8, 111–129. https://doi.org/10.1016/0377-0273(80)90010-4

Lechler, A.R., Niemi, N.A., Hren, M.T., Lohmann, K.C., 2013. Paleoelevation estimates for the northern and central proto–Basin and Range from carbonate clumped isotope thermometry. Tectonics 32, 295–316. https://doi.org/10.1002/tect.20016

Lepore, W.A., 2013. Petrophysical and physicochemical controlling parameters on stable isotope depletion patterns in carbonate rocks from auriferous hydrothermal fluid infiltration at the Long Canyon sediment-hosted gold deposit : NE Nevada. University of British Columbia. https://doi.org/10.14288/1.0074052

Lindgren, W., 1933. Mineral deposits. New York and London, McGraw-Hill Book Co.

Lis, G., Wassenaar, L.I., Hendry, M.J., 2008. High-Precision Laser Spectroscopy D/H and 18O/16O Measurements of Microliter Natural Water Samples. Anal. Chem. 80, 287–293. https://doi.org/10.1021/ac701716q

Lloyd, M.K., Eiler, J.M., Nabelek, P.I., 2017. Clumped isotope thermometry of calcite and dolomite in a contact metamorphic environment. Geochimica et Cosmochimica Acta 197, 323–344. https://doi.org/10.1016/j.gca.2016.10.037

Love, D.A., Clark, A.H., Glover, J.K., 2004. The Lithologic, Stratigraphic, and Structural Setting of the Giant Antamina Copper-Zinc Skarn Deposit, Ancash, Peru. Economic Geology 99, 887–916. https://doi.org/10.2113/econgeo.99.5.887

Lu, Y.-C., Song, S.-R., Taguchi, S., Wang, P.-L., Yeh, E.-C., Lin, Y.-J., MacDonald, J., John, C.M., 2018. Evolution of hot fluids in the Chingshui geothermal field inferred from crystal morphology and geochemical vein data. Geothermics 74, 305–318. https://doi.org/10.1016/j.geothermics.2017.11.016

Lu, Y.-C., Song, S.-R., Wang, P.-L., Wu, C.-C., Mii, H.-S., MacDonald, J., Shen, C.-C., John, C.M., 2017. Magmatic-like fluid source of the Chingshui geothermal field, NE Taiwan evidenced by carbonate clumped-isotope paleothermometry. Journal of Asian Earth Sciences, Tectonics, Volcanism and Geo-energy in East Asia 149, 124–133. https://doi.org/10.1016/j.jseaes.2017.03.004

Luetkemeyer, P.B., Kirschner, D.L., Huntington, K.W., Chester, J.S., Chester, F.M., Evans, J.P., 2016. Constraints on paleofluid sources using the clumped-isotope thermometry of carbonate veins from the SAFOD (San

Andreas Fault Observatory at Depth) borehole. Tectonophysics, The role of fluids in faulting and fracturing in carbonates and other upper crustal rocks 690, 174–189. https://doi.org/10.1016/j.tecto.2016.05.024

Lusty, P. a. J., Gunn, A.G., 2015. Challenges to global mineral resource security and options for future supply. Geological Society, London, Special Publications 393, 265–276. https://doi.org/10.1144/SP393.13

Mangenot, X., Gasparrini, M., Rouchon, V., Bonifacie, M., 2018. Basin-scale thermal and fluid flow histories revealed by carbonate clumped isotopes (Δ47) – Middle Jurassic carbonates of the Paris Basin depocentre. Sedimentology 65, 123–150. https://doi.org/10.1111/sed.12427

Marumo, K., Hattori, K.H., 1999. Seafloor hydrothermal clay alteration at Jade in the back-arc Okinawa Trough: mineralogy, geochemistry and isotope characteristics. Geochimica et Cosmochimica Acta 63, 2785–2804. https://doi.org/10.1016/S0016-7037(99)00158-1

Marumo, K., Nagasawa, K., Kuroda, Y., 1980. Mineralogy and hydrogen isotope geochemistry of clay minerals in the Ohnuma geothermal area, Northeastern Japan. Earth and Planetary Science Letters 47, 255–262. https://doi.org/10.1016/0012-821X(80)90041-2

Mauk, J.L., Hall, C.M., Chesley, J.T., Barra, F., 2011. Punctuated evolution of a large epithermal province: The Hauraki goldfield, New Zealand. Economic Geology 106, 921–943.

Mauk, J.L., Skinner, E.G., Fyfe, S.J., Menzies, A.H., Lowers, H.A., Koenig, A.E., 2016. Ore mineralogy and textural zonation in the world-class epithermal Waihi Vein System, Hauraki Goldfield 293–301.

McInnes, B.I.A., Evans, N.J., Fu, F.Q., Garwin, S., 2005. Application of Thermochronology to Hydrothermal Ore Deposits. Reviews in Mineralogy and Geochemistry 58, 467–498. https://doi.org/10.2138/rmg.2005.58.18

McKinney, C.R., McCrea, J.M., Epstein, S., Allen, H.A., Urey, H.C., 1950. Improvements in Mass Spectrometers for the Measurement of Small Differences in Isotope Abundance Ratios. Review of Scientific Instruments 21, 724–730. https://doi.org/10.1063/1.1745698

Meinert, L.D., Robinson, G.R., Nassar, N.T., 2016. Mineral Resources: Reserves, Peak Production and the Future. Resources 5, 14. https://doi.org/10.3390/resources5010014

Menicucci, A.J., Matthews, J.A., Spero, H.J., 2013. Oxygen isotope analyses of biogenic opal and quartz using a novel microfluorination technique. Rapid Commun. Mass Spectrom. 27, 1873–1881. https://doi.org/10.1002/rcm.6642

Mering, J.A., Barker, S.L.L., 2018. Precise Measurement of the Hydrogen Isotope Composition of Phyllosilicates by Continuous Flow Off-Axis Integrated Cavity Output Spectroscopy. Anal. Chem. 90, 2852–2859. https://doi.org/10.1021/acs.analchem.7b04992

Mering, J.A., Barker, S.L.L., Huntington, K.W., Simmons, S., Dipple, G., Andrew, B., Schauer, A., 2018. Taking the Temperature of Hydrothermal Ore Deposits Using Clumped Isotope Thermometry. Economic Geology 113, 1671–1678. https://doi.org/10.5382/econgeo.2018.4608

Mineral Commodity Summaries 2019 (USGS Unnumbered Series), 2019. , Mineral Commodity Summaries. U.S. Geological Survey, Reston, VA.

Mueller, A.G., Nemchin, A.A., Frei, R., 2004. The Nevoria Gold Skarn Deposit, Southern Cross Greenstone Belt, Western Australia: II. Pressure-Temperature-Time Path and Relationship to Postorogenic Granites. Economic Geology 99, 453–478. https://doi.org/10.2113/gsecongeo.99.3.453

Müller, I.A., Fernandez, A., Radke, J., Dijk, J. van, Bowen, D., Schwieters, J., Bernasconi, S.M., 2017. Carbonate clumped isotope analyses with the long-integration dual-inlet (LIDI) workflow: scratching at the lower sample weight boundaries. Rapid Communications in Mass Spectrometry 31, 1057–1066. https://doi.org/10.1002/rcm.7878

Nelson, D.D., 2016. Laser absorption measurement for clumped isotopes.

US9261457B1.

Nesbitt, B.E., 1996. Applications of oxygen and hydrogen isotopes to exploration for hydrothermal mineralization. SEG Newsletter 27.

Nutting, P.G., 1943. Some standard thermal dehydration curves of minerals. US Government Printing Office.

Oerter, E., Singleton, M., Davisson, L., 2017. Hydrogen and oxygen stable isotope signatures of goethite hydration waters by thermogravimetry-enabled laser spectroscopy. Chemical Geology 475, 14–23. https://doi.org/10.1016/j.chemgeo.2017.10.025

Ohmoto, H., 1972. Systematics of Sulfur and Carbon Isotopes in Hydrothermal Ore Deposits. Economic Geology 67, 551–578. https://doi.org/10.2113/gsecongeo.67.5.551

Ohmoto, H., Rye, R., 1972. Isotopes of sulfur and carbon. Geochemistry of hydrothermal ore deposits 509–567.

Ohmoto, H., Rye, R.O., 1974. Hydrogen and Oxygen Isotopic Compositions of Fluid Inclusions in the Kuroko Deposits, Japan. Economic Geology 69, 947–953. https://doi.org/10.2113/gsecongeo.69.6.947

Oliveira, E.M. de, Oliveira, C.M. de, Sala, M.V.B., Montedo, O.R.K., Peterson, M., Oliveira, E.M. de, Oliveira, C.M. de, Sala, M.V.B., Montedo, O.R.K., Peterson, M., 2018. Thermal Behavior of Pyrite in the CO2 and N2 Atmosphere for Obtaining Pyrrhotite: A Magnetic Material. Materials Research 21. https://doi.org/10.1590/1980-5373-mr-2017-0244

O'Neil, J.R., Clayton, R.N., Mayeda, T.K., 1969. Oxygen Isotope Fractionation in Divalent Metal Carbonates. The Journal of Chemical Physics 51, 5547–5558. https://doi.org/10.1063/1.1671982

O'Neil, J.R., Silberman, M.L., 1974. Stable Isotope Relations in Epithermal Au-Ag Deposits. Economic Geology 69, 902–909. https://doi.org/10.2113/gsecongeo.69.6.902

O'Neil, J.R., Taylor, H.P., 1969. Oxygen isotope equilibrium between muscovite and water. Journal of Geophysical Research 74, 6012–6022.

Page, R.W., Bell, T.H., 1986. Isotopic and Structural Responses of Granite to Successive Deformation and Metamorphism. The Journal of Geology 94,

365–379. https://doi.org/10.1086/629035

Penna, D., Stenni, B., Šanda, M., Wrede, S., Bogaard, T.A., Gobbi, A., Borga, M., Fischer, B.M.C., Bonazza, M., Chárová, Z., 2010. On the reproducibility and repeatability of laser absorption spectroscopy measurements for δ2H and δ18O isotopic analysis. Hydrol. Earth Syst. Sci. 14, 1551–1566. https://doi.org/10.5194/hess-14-1551-2010

Penna, D., Stenni, B., Šanda, M., Wrede, S., Bogaard, T.A., Michelini, M., Fischer, B.M., Gobbi, A., Mantese, N., Zuecco, G., 2012. Evaluation of between-sample memory effects in the analysis of δ 2 H and δ 18 O of water samples measured by laser spectroscopes. Hydrology and Earth System Sciences 16, 3925–3933.

Perkins, W.G., 1984. Mount Isa silica dolomite and copper orebodies; the result of a syntectonic hydrothermal alteration system. Economic Geology 79, 601–637. https://doi.org/10.2113/gsecongeo.79.4.601

Plimer, I.R., Elliott, S.M., 1979. The use of Rb/Sr ratios as a guide to mineralization. Journal of Geochemical Exploration 12, 21–34.

Prokhorov, I., Kluge, T., Janssen, C., 2017. Laser spectrometer for CO2 clumped isotope analysis, in: EGU General Assembly Conference Abstracts. p. 5045.

Pruett, R.J., Webb, H.L., 1993. Sampling and analysis of KGa-1B well-crystallized kaolin source clay. Clays and Clay Minerals 41, 514–519.

Qi, H., Gröning, M., Coplen, T.B., Buck, B., Mroczkowski, S.J., Brand, W.A., Geilmann, H., Gehre, M., 2010. Novel silver-tubing method for quantitative introduction of water into high-temperature conversion systems for stable hydrogen and oxygen isotopic measurements. Rapid Commun. Mass Spectrom. 24, 1821–1827. https://doi.org/10.1002/rcm.4559

Qi, H., Coplen, T.B., Olack, G.A., Vennemann, T.W., 2014. Caution on the use of NBS 30 biotite for hydrogen-isotope measurements with on-line high-temperature conversion systems. Rapid Commun. Mass Spectrom. 28, 1987–1994. https://doi.org/10.1002/rcm.6983

Qi, H., Coplen, T.B., Gehre, M., Vennemann, T.W., Brand, W.A., Geilmann, H., Olack, G., Bindeman, I.N., Palandri, J., Huang, L., Longstaffe, F.J., 2017. New biotite and muscovite isotopic reference materials, USGS57 and USGS58, for δ2H measurements–A replacement for NBS 30. Chemical Geology 467, 8999. https://doi.org/10.1016/j.chemgeo.2017.07.027

Reference Materials and Calibration Services [WWW Document], n.d. URL https://isotopes.usgs.gov/lab/referencematerials.html (accessed 5.1.19).

Richards, J.P., 2013. Giant ore deposits formed by optimal alignments and combinations of geological processes. Nature Geoscience 6, 911–916. https://doi.org/10.1038/ngeo1920

P Richet, Y Bottinga, Javoy, and M., 1977. A Review of Hydrogen, Carbon, Nitrogen, Oxygen, Sulphur, and Chlorine Stable Isotope Fractionation Among Gaseous Molecules. Annual Review of Earth and Planetary Sciences 5, 65–110. https://doi.org/10.1146/annurev.ea.05.050177.000433

Robinson, B.W., 1975. Carbon and oxygen isotopic equilibria in hydrothermal calcites. Geochemical Journal 9, 43–46.

Roedder, E., 1984. Fluid inclusion evidence bearing on the environments of gold

deposition. Gold 82, 129–163.

Roedder, E., Bodnar, R.J., 1980. Geologic pressure determinations from fluid inclusion studies. Annual Review of Earth and Planetary Sciences 8, 263–301.

Rowland, J.V., Sibson, R.H., 2004. Structural controls on hydrothermal flow in a segmented rift system, Taupo Volcanic Zone, New Zealand. Geofluids 4, 259–283. https://doi.org/10.1111/j.1468-8123.2004.00091.x

Rowland, J.V., Simmons, S.F., 2012. Hydrologic, Magmatic, and Tectonic Controls on Hydrothermal Flow, Taupo Volcanic Zone, New Zealand: Implications for the Formation of Epithermal Vein Deposits. Economic Geology 107, 427–457. https://doi.org/10.2113/econgeo.107.3.427

Sakai, S., Matsuda, S., Hikida, T., Shimono, A., McManus, J.B., Zahniser, M., Nelson, D., Dettman, D.L., Yang, D., Ohkouchi, N., 2017. High-Precision Simultaneous 18O/16O, 13C/12C, and 17O/16O Analyses for Microgram Quantities of CaCO3 by Tunable Infrared Laser Absorption Spectroscopy. Anal. Chem. 89, 11846–11852. https://doi.org/10.1021/acs.analchem.7b03582

Savin, S.M., 1967. Oxygen and Hydrogen Isotope Ratios in Sedimentary Rocks and Minerals (phd). California Institute of Technology.

Savin, S.M., Epstein, S., 1970. The oxygen and hydrogen isotope geochemistry of clay minerals. Geochimica et Cosmochimica Acta 34, 25–42. https://doi.org/10.1016/0016-7037(70)90149-3

Schauble, E.A., Ghosh, P., Eiler, J.M., 2006. Preferential formation of 13C–18O bonds in carbonate minerals, estimated using first-principles lattice dynamics. Geochimica et Cosmochimica Acta 70, 2510–2529. https://doi.org/10.1016/j.gca.2006.02.011

Schauer, A.J., Kelson, J., Saenger, C., Huntington, K.W., 2016. Choice of 17O correction affects clumped isotope (Δ47) values of CO2 measured with mass spectrometry. Rapid Communications in Mass Spectrometry 30, 2607–2616. https://doi.org/10.1002/rcm.7743

Schimmelmann, A., Sessions, A.L., Mastalerz, M., 2006. Hydrogen Isotopic (d/H) Composition of Organic Matter During Diagenesis and Thermal Maturation. Annual Review of Earth and Planetary Sciences 34, 501–533. https://doi.org/10.1146/annurev.earth.34.031405.125011

Seligman, A.N., Bindeman, I.N., 2019. The δ18O of primary and secondary waters in hydrous volcanic glass. Journal of Volcanology and Geothermal Research 371, 72–85. https://doi.org/10.1016/j.jvolgeores.2018.12.008

Shah, M.T., Ikramuddin, M., Shervais, J.W., 1994. Behaviour of Tl relative to K, Rb, Sr and Ba in mineralized and unmineralized metavolcanics from the Dir area, northern Pakistan. Mineralium Deposita 29, 422–426.

Shanks III, W.C., 2001. Stable isotopes in seafloor hydrothermal systems: vent fluids, hydrothermal deposits, hydrothermal alteration, and microbial processes. Reviews in Mineralogy and Geochemistry 43, 469–525.

Sharp, Z., 2017. Principles of stable isotope geochemistry.

Sharp, Z.D., 1990. A laser-based microanalytical method for the in situ determination of oxygen isotope ratios of silicates and oxides. Geochimica

et Cosmochimica Acta 54, 1353–1357. https://doi.org/10.1016/0016-7037(90)90160-M

Sharp, Z.D., Atudorei, V., Durakiewicz, T., 2001. A rapid method for determination of hydrogen and oxygen isotope ratios from water and hydrous minerals. Chemical Geology 178, 197–210. https://doi.org/10.1016/S0009-2541(01)00262-5

Sharp, Z.D., Gibbons, J.A., Maltsev, O., Atudorei, V., Pack, A., Sengupta, S., Shock, E.L., Knauth, L.P., 2016. A calibration of the triple oxygen isotope fractionation in the SiO2–H2O system and applications to natural samples. Geochimica et Cosmochimica Acta 186, 105–119. https://doi.org/10.1016/j.gca.2016.04.047

Sheppard, S.M.F., Gilg, H.A., 1996. Stable Isotope Geochemistry of Clay Minerals. Clay Minerals 31, 1–24. https://doi.org/10.1180/claymin.1996.031.1.01

Sillitoe, R., Hedenquist, J., 2003. Linkages between volcanotectonic settings, ore-fluid compositions, and epithermal precious-metal deposits. ResearchGate 315–343.

Sillitoe, R.H., 2015. Epithermal paleosurfaces. Miner Deposita 50, 767–793. https://doi.org/10.1007/s00126-015-0614-z

Simon, L., Lécuyer, C., Martineau, F., Robert, F., 2011. Experimental study of D/H fractionation between water and hydrogen gas during the oxidation of Fe-bearing silicates at high temperatures (600 C–1200 C). Central European Geology 54, 81–93.

Simmons, S.F., Brown, K.L., 2007. The flux of gold and related metals through a volcanic arc, Taupo Volcanic Zone, New Zealand. Geology 35, 1099–1102. https://doi.org/10.1130/G24022A.1

Simmons, S.F., Brown, K.L., Browne, P.R.L., Rowland, J.V., 2016a. Gold and silver resources in Taupo Volcanic Zone geothermal systems. Geothermics, Taupo Volcanic Zone Geothermal Systems, New Zealand : Exploration, Science and Development 59, 205–214. https://doi.org/10.1016/j.geothermics.2015.07.009

Simmons, S.F., Brown, K.L., Tutolo, B.M., 2016b. Hydrothermal Transport of Ag, Au, Cu, Pb, Te, Zn, and Other Metals and Metalloids in New Zealand Geothermal Systems: Spatial Patterns, Fluid-Mineral Equilibria, and Implications for Epithermal Mineralization. Economic Geology 111, 589–618. https://doi.org/10.2113/econgeo.111.3.589

Simmons, S.F., Browne, P.R.L., 2000. Hydrothermal Minerals and Precious Metals in the Broadlands-Ohaaki Geothermal System: Implications for Understanding Low-Sulfidation Epithermal Environments. Economic Geology 95, 971–999. https://doi.org/10.2113/gsecongeo.95.5.971

Simmons, S.F., Arehart, G., Simpson, M.P., Mauk, J.L., 2000. Origin of massive calcite veins in the Golden Cross low-sulfidation, epithermal Au-Ag deposit, New Zealand. Economic Geology 95, 99–112.

Simmons, S.F., Christenson, B.W., 1994. Origins of calcite in a boiling geothermal system. Am J Sci 294, 361–400. https://doi.org/10.2475/ajs.294.3.361

Simmons, S.F., White, N.C., John, D.A., 2005. Geological characteristics of epithermal precious and base metal deposits. Economic Geology 29, 485–522.

Simpson, M.P., Christie, A.B., 2019. Hydrothermal alteration mineralogical footprints for New Zealand epithermal Au-Ag deposits. New Zealand Journal of Geology and Geophysics 0, 1–30. https://doi.org/10.1080/00288306.2019.1577278

Simpson, M.P., Gazley, M.F., Stuart, A.G., Pearce, M.A., Birchall, R., Chappell, D., Christie, A.B., Stevens, M.R., 2019. Hydrothermal Alteration at the Karangahake Epithermal Au-Ag Deposit, Hauraki Goldfield, New Zealand. Economic Geology 114, 243–273.

Simpson, M.P., Mauk, J.L., 2007. The Favona Epithermal Gold-Silver Deposit, Waihi, New Zealand. Economic Geology 102, 817–839.

Simpson, M.P., Rosenberg, M.D., Rae, A.J., Bignall, G., Mountain, B.W., Graham, D., Chapell, D., 2014. Insight-into-the-2005-hydrothermal-eruption-at-South-Orakonui-Ngatamariki-Geothermal-Field-New-Zealand-from-calcite-microthermometry.pdf. New Zealand Geothermal Workshop 2014 Proceedings.

Sinclair, W.D., 2007. PORPHYRY DEPOSITS, in: Mineral Deposits of Canada: A Synthesis of Major Deposit-Types, District Metallogeny,the Evolution of Geological Provinces, and Exploration Methods. Geological Association of Canada, Mineral Deposits Division, pp. 223–243.

Skrzypek, G., Ford, D., 2014. Stable Isotope Analysis of Saline Water Samples on a Cavity Ring-down Spectroscopy Instrument. Environ. Sci. Technol. 48, 2827–2834. https://doi.org/10.1021/es4049412

Spörli, K.B., Cargill, H., 2011. Structural evolution of a world-class epithermal orebody: The Martha Hill deposit, Waihi, New Zealand. Economic Geology 106, 975–998.

Sugisaki, R., Jensen, M.L., 1971. Oxygen isotopic studies of silicate minerals with special reference to hydrothermal mineral deposits. Geochemical Journal 5, 7–21.

Sumner, K.K., 2014. Assessing Fracture Connectivity using Stable and Clumped Isotope Geochemistry of Calcite Cements.

Suzuoki, T., Epstein, S., 1976. Hydrogen isotope fractionation between OH-bearing minerals and water. Geochimica et Cosmochimica Acta 40, 1229–1240.

Swain, S.K., Sarangi, S., Srinivasan, R., Sarkar, A., Bhattacharya, S., Patel, S.C., Pasayat, R.M., Sawkar, R.H., 2015. Isotope (C and O) composition of auriferous quartz carbonate veins, central lode system, Gadag Gold Field, Dharwar Craton, India: Implications to source of ore fluids. Ore Geology Reviews 70, 305–320. https://doi.org/10.1016/j.oregeorev.2015.03.020

Swift, W.M., Panek, A.F., Smith, G.W., Vogel, G.J., Jonke, A.A., 1976. Decomposition of Calcium Sulfate: A Review of the Literature. (No. ANL--76-122). Argonne National Lab. (ANL), Argonne, IL (United States).

Taylor, B.E., O'Neil, J.R., 1977. Stable isotope studies of metasomatic Ca-Fe-Al-Si skarns and associated metamorphic and igneous rocks, Osgood

Mountains, Nevada. Contributions to Mineralogy and Petrology 63, 1–49.

Taylor, H.F.W., 1962. Homogeneous and inhomogeneous mechanisms in the dehydroxylation of minerals. Clay Minerals Bulletin 5, 45–55. https://doi.org/10.1180/claymin.1962.005.28.01

Taylor, H.P., 1974. The application of oxygen and hydrogen isotope studies to problems of hydrothermal alteration and ore deposition. Economic geology 69, 843–883.

Taylor, H.P., 1973. O 18/O 16 evidence for meteoric-hydrothermal alteration and ore deposition in the Tonopah, Comstock Lode, and Goldfield mining districts, Nevada. Economic Geology 68, 747–764.

Taylor, H.P., Barnes, H.L., 1997. Oxygen and hydrogen isotope relationships in hydrothermal mineral deposits. Geochemistry of hydrothermal ore deposits 3, 229–302.

Tilling, R.I., Gottfried, D., Rowe, J.J., 1973. Gold Abundance in Igneous Rocks; bearing on Gold Mineralization. Economic Geology 68, 168–186. https://doi.org/10.2113/gsecongeo.68.2.168

Torckler, L.K., 2006. Geology and exploration of the Favona Au-Ag deposit, Waihi, Hauraki goldfield. Australasian Institute of Mining and Metallurgy Monograph 25, 179–184.

Truche, L., Joubert, G., Dargent, M., Martz, P., Cathelineau, M., Rigaudier, T., Quirt, D., 2018. Clay minerals trap hydrogen in the Earth's crust: Evidence from the Cigar Lake uranium deposit, Athabasca. Earth and Planetary Science Letters 493, 186–197.

Urey, H.C., Lowenstam, H.A., Epstein, S., McKINNEY, C.R., 1951. Measurement of Paleotemperatures and Temperatures of the Upper Cretaceous of England, Denmark, and the Southeastern United States. Geological Society of America Bulletin 62, 399–416. https://doi.org/10.1130/0016-7606(1951)62[399:MOPATO]2.0.CO;2

VanDeVelde, J.H., Bowen, G.J., 2013. Effects of chemical pretreatments on the hydrogen isotope composition of 2:1 clay minerals. Rapid Communications in Mass Spectrometry 27, 1143–1148. https://doi.org/10.1002/rcm.6554

Vaughan, J.R., Hickey, K.A., Barker, S.L.L., 2016. Isotopic, Chemical, and Textural Evidence for Pervasive Calcite Dissolution and Precipitation Accompanying Hydrothermal Fluid Flow in Low-Temperature, Carbonate-Hosted, Gold Systems. Economic Geology 111, 1127–1157. https://doi.org/10.2113/econgeo.111.5.1127

Vennemann, T.W., O'Neil, J.R., 1993. A simple and inexpensive method of hydrogen isotope and water analyses of minerals and rocks based on zinc reagent. Chemical Geology 103, 227–234. https://doi.org/10.1016/0009-2541(93)90303-Z

Vikre, P.G., 1989. Fluid-mineral relations in the Comstock Lode. Economic Geology 84, 1574–1613. https://doi.org/10.2113/gsecongeo.84.6.1574

Waring, C.L., Andrew, A.S., Ewers, G.R., 1998. Use of O, C, and S stable isotopes in regional mineral exploration.

Weis, P., Driesner, T., Heinrich, C.A., 2012. Porphyry-Copper Ore Shells Form at Stable Pressure-Temperature Fronts Within Dynamic Fluid Plumes.

Science 338, 1613–1616. https://doi.org/10.1126/science.1225009

Wenner, D.B., Taylor, H.P., 1971. Temperatures of serpentinization of ultramafic rocks based on O 18/O 16 fractionation between coexisting serpentine and magnetite. Contributions to Mineralogy and Petrology 32, 165–185.

Werner, R., Brand, W., 2001. Referencing strategies and techniques in stable isotope ratio analysis. Rapid Commun. Mass Spectrom. 15.

White, N.C., Hedenquist, J.W., 1990. Epithermal environments and styles of mineralization: Variations and their causes, and guidelines for exploration. Journal of Geochemical Exploration 36, 445–474. https://doi.org/10.1016/0375-6742(90)90063-G

White, N.C., Hedenquist, J.W., 1995. Epithermal gold deposits: styles characteristics and exploration. SEG newsletter 23, 9–13.

Wilkinson, J.J., Chang, Z., Cooke, D.R., Baker, M.J., Wilkinson, C.C., Inglis, S., Chen, H., Bruce Gemmell, J., 2015. The chlorite proximitor: A new tool for detecting porphyry ore deposits. Journal of Geochemical Exploration 152, 10–26. https://doi.org/10.1016/j.gexplo.2015.01.005

Winkelstern, I.Z., Kaczmarek, S.E., Lohmann, K.C., Humphrey, J.D., 2016. Calibration of dolomite clumped isotope thermometry. Chemical Geology 443, 32–38. https://doi.org/10.1016/j.chemgeo.2016.09.021

Wostbrock, J.A.G., Sharp, Z.D., Sanchez-Yanez, C., Reich, M., van den Heuvel, D.B., Benning, L.G., 2018. Calibration and application of silica-water triple oxygen isotope thermometry to geothermal systems in Iceland and Chile. Geochimica et Cosmochimica Acta 234, 84–97. https://doi.org/10.1016/j.gca.2018.05.007

Yeh, H.-W., 1980. D/H ratios and late-stage dehydration of shales during burial. Geochimica et Cosmochimica Acta 44, 341–352.

Young, D.J., 2016. High Temperature Oxidation and Corrosion of Metals.

Elsevier.

Zhang, L., 2000. Stable isotope investigation of a hydrothermal alteration system; Butte porphyry copper deposit. Oregon State University.

Zheng, Y.-F., 1993. Calculation of oxygen isotope fractionation in hydroxyl-bearing silicates. Earth and Planetary Science Letters 120, 247–263. https://doi.org/10.1016/0012-821X(93)90243-3

Zheng, Y.-F., 1990. Carbon-oxygen isotopic covariation in hydrothermal calcite during degassing of CO2. Mineral. Deposita 25, 246–250. https://doi.org/10.1007/BF00198993

Zheng, Y.-F., Hoefs, J., 1993. Carbon and oxygen isotopic covariations in hydrothermal calcites. Mineral. Deposita 28, 79–89. https://doi.org/10.1007/BF00196332

Zhu, Y., An, F., Tan, J., 2011. Geochemistry of hydrothermal gold deposits: A review. Geoscience Frontiers 2, 367–374. https://doi.org/10.1016/j.gsf.2011.05.006